Mechanisms controlling Gadolinium, Rhenium, and Selenium sequestration under the oxygen-depleted condition

Leydy Carolina Guida Manrique

THÈSE

Pour obtenir le grade de

DOCTEUR DE L'UNIVERSITÉ GRENOBLE ALPES

École doctorale : STEP - Sciences de la Terre de l'Environnement et des Planètes
Spécialité : Sciences de la Terre et de l'Environnement
Unité de recherche : Institut des Sciences de la Terre

Mécanismes contrôlant la séquestration du gadolinium, du rhénium et du sélénium dans des conditions de faible teneur en oxygène

Mechanisms controlling gadolinium, rhenium, and selenium sequestration under the oxygen-depleted condition

Présentée par :

Leydy Carolina GUIDA MANRIQUE

Direction de thèse :

Laurent CHARLET PROFESSEUR EMERITE, Université Grenoble Alpes	Directeur de thèse
Anthony CHAPPAZ PROFESSEUR, Central Michigan University	Co-directeur de thèse

Rapporteurs :

Guillaume MORIN
DIRECTEUR DE RECHERCHE, CNRS délégation Paris Centre
Delphine VANTELON
CHARGEE DE RECHERCHE HDR, Synchrotron SOLEIL

Thèse soutenue publiquement le **30 avril 2024**, devant le jury composé de :

Guillaume MORIN, DIRECTEUR DE RECHERCHE, CNRS délégation Paris Centre	Président
Delphine VANTELON, CHARGEE DE RECHERCHE HDR, Synchrotron SOLEIL	Rapporteure
Alexandra GOURLAN, MAITRESSE DE CONFERENCES HDR, Université Grenoble Alpes	Examinatrice
Kristina KVASHNINA, PROFESSEUR, Helmholtz-Zentrum Dresden-Rossendorf	Examinatrice

Invités :

Jean-Marc Greneche
DIRECTEUR DE RECHERCHE EMERITE, Institut des Molécules et Matériaux du Mans (IMMM CNRS UMR 6283)
Alexandre DICKSON
PROFESSEUR, Royal Holloway University

Para ti, mamá

Acknowledgements

First, I would like to express my sincere gratitude to Dr. Guillaume Morin, Dr. Delphine Vantelon, Dr. Alexandre Gourlan, and Dr. Kristina Kvashina for agreeing to be part of the examination committee for my thesis. I am thankful to the members of my thesis jury for their interest and time you expend with my doctoral defence. I would also like to thank you for your corrections and advice for the improvement of this manuscript.

I would like to express my gratitude to my primary supervisor, Professor Laurent Charlet, for providing me with the chance to pursue this project, for his endless support, and for always being available to hear or answer any queries I may have. Being his student has been an extraordinary opportunity that I would repeat without hesitation. I would also like to thank my co-supervisor, Professor Anthony Chappaz, for his scientific insights and for meticulously mentoring this thesis. This work would not have been possible without the guidance of my two supervisors. I am grateful for their support and for introducing me to the exciting world of geochemistry; ISTerre and STARLAB laboratories. I owe you an immense gratitude.

During these past few years, I have had the privilege of being part of the ISTerre community, growing personally and professionally, and immersing myself in the vibrant energy and passion for understanding nature that characterises the Institute's members. I would like to express my heartfelt gratitude to all those who have helped me along the way. Aude, thank you for always bringing a smile to my face and making lab work enjoyable; Delphine and Martine for their unwavering support and making me feel at home; Nathaniel for his tireless help, discussions and guidance through the experiments; and Simona for her invaluable assistance in the lab. I would also like to thank Valerie, Sabine, Sylvain and Rachel for their assistance with sample analysis, and Dr Plunian, Dr Thomas, Dr Doan, Jean-Marc Nicole, Clementine and the administration team for their support in all the processes involved in the enrollment and follow-up of a doctoral program. I would like to express my sincere gratitude to Carlos Heredia, Dr Martinez-Fernandez, Dr Kazi Tani, Dr Poulain, Dr Wang, Dr Ding, Dr Pierangeli, Carlos Heredia, Djamilatou Dabre and all my colleagues for creating a friendly and productive working environment and participating in enriching discussions.

I am grateful to the ROBL and FAME beamline groups at ESRF for their training and support in my studies, with special thanks to Dr Schenoist, Dr Prieur, Dr Roßberg and Dr Rovezzi. A very special thanks to Dr Greneche for introducing me to the Mössbauer technique, patiently answering my questions, explaining results, and supporting my thesis and professional endeavours. Gracias por permitirme conocer mi país de otra manera y por tenerle tanto cariño. I would like to thank Dr Gloter for welcoming me to the lab, helping me with the STEM-EELS measurements, and engaging me in enlightening conversations. Thanks to Dr Menguy, for your assistance with the TEM measurements.

I would like to express my gratitude to my second advisor Anthony for the warm welcome I received from you, your research group, and your family during my time in Mount Pleasant. I am particularly thankful for the introduction to Dr. Grant, Marcelo Prianti and Aurelie for their invaluable help and guidance with my research. I would also like to extend a special thanks to Wendy, Dr. Lemke, Becky, and Darcy, who made my stay in US unforgettable. I would like to express my gratitude to Dr. Alex Dickson and his research group for their kind welcome and support during my time in their new laboratory at RHUL last autumn. It was a delightful experience to train and interact with you all.

Last but not least, I want to give a heartfelt thank to my Colombian and French friends, my family, my aunt, my mother, my father and my beloved for supporting, guiding and embracing me throughout this journey. Thank you all for years of care and love. This would not have been possible without you.

Vous remerciez ne sera jamais assez… ¡Gracias por tanto!

Summary

Trace elements, despite their scarcity (less than 100 parts per million) on Earth, serve diverse purposes: some act as micronutrients, while others, known as critical metals, possess unique industrial and medical applications. In oxygen-deprived natural aquatic systems electron transfers involve biogeochemical reactions catalyzed by iron, sulfur and trace elements. Understanding their reactivity in these environments remains a challenge. My Ph.D. research focus on filling this knowledge gap concerning three specific elements (rhenium (Re), selenium (Se), and gadolinium (Gd)). They exist in various chemical aqueous species in water: monovalent anion (perrhenate, ReO_4^-), divalent anion (selenate, $SeO_4^{2-}$and selenite, SeO_3^{2-}) or cation (Gadolinium, Gd^{3+}). Rhenium is a critical metal, while selenium is a bioessential element at low levels, and becomes toxic in higher concentrations. Gadolinium is a rare earth element and a critical metal as well, due to its wide use as a contrast agent in magnetic resonance imaging (MRI).

These elements are most concentrated in marine sediments formed in oxygen-deprived environments. Common mineral phases include pyrite (FeS_2) and magnetite (Fe_3O_4) depending on sulfide content in those environments, and origin (autogenic vs. detritic, e.g., from volcanic rocks) of the particles. My research, presented across four chapters, investigates surface reduction (Re(VII), Se(VI) and Se(IV)) and the sorption (Gd(III)) processes on/into magnetite and pyrite particles. Employing various analytical methods such as XAFS spectroscopy, STEM-EELS spectro microscopie and MC-ICP-MS, our study reveals distinct reactive pathways. Re(VII) reacts with sulfidic water to form Re(III, IV, V)$_2S_7$ nanoparticles, while at lower concentrations Re is reduced and incorporated into particles, in different pathways characterized by less isotopic fractionation with pyrite than with magnetite. We also show that pyrite nanoparticles reduce Se(VI) and Se(IV), down to surface Se(0) or structure Se(-I) depending on whether adsorption or co-precipitation occurs. Lastly, Gd substitutes for Fe(III) in magnetite nanoparticles up to 5% Fe substitution by Gd. We attempt to unify the affinity behaviour of these and other trace elements with anoxic Fe-bearing sediments in the light of the hard and soft acids and bases principle.

The study provides new insights into the mechanisms that govern the sequestration of metals and metalloids in sedimentary settings. The significance of this research lies in its relevance to contemporary scientific and technological endeavours, particularly in understanding how processes in Fe and sulfidic systems work like trace elements, Fe and S mobility, mass balance in the global sedimentary cycles to the exploration, mining and recycling of potential repositories of metals. Furthermore, it enhances our current understanding of the use of palaeoenvironmental proxies to reconstruct the Earth's formation. Finally, this study also has implications for the treatment of nuclear waste and pollution, particularly in the management of selenium (Se) and gadolinium (Gd) contamination.

Sommaire

Les éléments traces, malgré leur rareté (moins de 100 parties par million) sur Terre, ont des fonctions diverses : certains agissent comme des micronutriments, tandis que d'autres, connus sous le nom de métaux critiques, possèdent des applications industrielles et médicales uniques. Dans les systèmes aquatiques naturels privés d'oxygène, les transferts d'électrons impliquent des réactions biogéochimiques catalysées par le fer, le soufre et les oligo-éléments. Comprendre leur réactivité dans ces environnements reste un défi. Mes recherches de doctorat visent à combler cette lacune en ce qui concerne trois éléments spécifiques (rhénium (Re), sélénium (Se) et gadolinium (Gd)). Ils existent sous différentes formes chimiques dans l'eau : anion monovalent (perrhenate, ReO_4^-), anion divalent (sélénate, SeO_4^{2-} et sélénite, SeO_3^{2-}) ou cation (gadolinium, Gd^{3+}). Le rhénium est un métal critique, tandis que le sélénium est un élément bioessentiel à de faibles niveaux et devient toxique à des concentrations plus élevées. Le gadolinium est une terre rare et un métal critique, en raison de sa large utilisation comme agent de contraste dans l'imagerie par résonance magnétique (IRM).

Ces éléments sont plus concentrés dans les sédiments marins formés dans des environnements privés d'oxygène. Les phases minérales communes comprennent la pyrite (FeS_2) et la magnétite (Fe_3O_4) en fonction de la teneur en sulfure dans ces environnements et de l'origine (autogène ou détritique, par exemple à partir de roches volcaniques) des particules. Mes recherches, présentées dans quatre chapitres, portent sur les processus de réduction de surface (Re(VII), Se(VI) et Se(IV)) et de sorption (Gd(III)) sur/dans les particules de magnétite et de pyrite. En utilisant diverses méthodes analytiques telles que la spectroscopie XAFS, la microscopie STEM-EELS et la MC-ICP-MS, notre étude révèle des voies réactives distinctes. Le Re(VII) réagit avec l'eau sulfurée pour former des nanoparticules de Re(III, IV, V)$_2S_7$, tandis qu'à des concentrations plus faibles, le Re est réduit et incorporé dans les particules, selon des voies différentes caractérisées par un fractionnement isotopique moindre avec la pyrite qu'avec la magnétite. Nous montrons également que les nanoparticules de pyrite réduisent Se(VI) et Se(IV), jusqu'à Se(0) en surface ou Se(-I) en structure, selon qu'il y a adsorption ou coprécipitation. Enfin, le Gd se substitue au Fe(III) dans les nanoparticules de magnétite jusqu'à 5% de substitution du Fe par le Gd. Nous tentons d'unifier le comportement d'affinité de ces éléments et d'autres éléments traces avec les sédiments anoxiques contenant du Fe à la lumière du principe des acides et bases durs et mous.

L'étude fournit de nouvelles informations sur les mécanismes qui régissent la séquestration des métaux et des métalloïdes dans les milieux sédimentaires. L'importance de cette recherche réside dans sa pertinence pour les efforts scientifiques et technologiques contemporains, en particulier pour comprendre le fonctionnement des processus dans les systèmes Fe et sulfurés, comme les éléments traces, la mobilité du Fe et du S, l'équilibre de masse dans les cycles sédimentaires globaux, l'exploration, l'exploitation minière et le recyclage des dépôts potentiels de métaux. En outre, elle améliore notre compréhension actuelle de l'utilisation des proxys paléoenvironnementaux pour reconstruire la formation de la Terre. Enfin, cette étude a également des implications pour le traitement des déchets nucléaires et de la pollution, en particulier pour la gestion de la contamination par le sélénium (Se) et le gadolinium (Gd).

Table of contents

Introduction

Trace elements are ubiquitous on Earth despite their low abundance (less than 100 parts per million). Some can either be essential or toxic to organisms, while others display unique properties for industrial and medical applications. The European Union and the USA list many trace elements as critical metals. The biogeochemistry of trace elements in natural aquatic systems in oxic environments is usually well understood while where oxygen is absent (less than 1 µM O_2), so-called anoxic environments, due to a complex interaction of biological, chemical and physical processes are much less understood. In particular, their reactions with iron and sulphur, in a solid or aqueous form are poorly understood, although Fe(II) and S(-I) or (-II) are among the main electron transfers at the Earth's surface and many processes governing the reactivity of certain trace elements in ferruginous and sulfidic aquatic environments remain unclear. The goal of my Ph.D. research project is to fulfill this knowledge gap focusing on three unique trace elements: Rhenium (Re), selenium (Se), and gadolinium (Gd).

Rhenium is a recognised critical metal. It is mainly used in high-temperature superalloys to manufacture jet engine turbine blades and platinum-rhenium catalysts for the petrochemical industry. In water, Re is present as a monovalent anion (perrhenate ion, ReO_4^-) and due to its mono-charge is poorly immobilised electrostatically at water mineral interfaces. Selenium is a bioessential metalloid at low concentrations but toxic at high concentrations. Se in the metallurgical industry is used to produce electrolytic manganese and as an additive in the steel manufacturing process. It is a pollutant from coal mining and nuclear waste disposal sites. In water, Se is present in divalent aqueous forms (selenate, SeO_4^{2-} or selenite, SeO_3^{2-} ions). Selenite and especially selenate adsorb weakly to pyrite, making it difficult to characterise their interactions. Rhenium and Selenium have been used as a paleo-redox proxy to study ancient environments to be developed. Gadolinium is a rare critical metal, soluble and highly toxic as a free cation (Gd^{3+}). It is an emerging contaminant because of its wide use as a contrast agent in magnetic resonance imaging (MRI).

Marine rocks such as black shales, basalts, or deep oceanic sediments contain the highest concentrations of Re, Se, and Gd and are formed in anoxic environments. These elements have been transported from land after physical weathering and are concentrated in these rocks as the result of early diagenesis. The most common mineralogical phases in these geological environments are pyrite (FeS_2) in sulphide-rich environments and magnetite (Fe_3O_4) in within iron-rich environment, though the later can be of detrital origin coming from volcanic igneous rocks. Magnetite or pyrite can immobilise Re, Se and Gd by adsorption, by co-precipitation during mineral formation, or by co-adsorption with iron (Fe(II)) and/or sulphur (S(-II)). Some specific questions about the mechanistic process of immobilisation of these elements with pyrite and magnetite remain to be answered. For example, to the best of our knowledge, no study has directly investigated the co-precipitation of Re, although this appears to be the most important mechanism for its sequestration. The reduction of Se(VI) to Se(0) involves the transfer of six electrons and the breaking of four oxygen bonds. As a consequence, Se reductive sorption is very slow. Interactions between selenite and iron sulfide minerals have been extensively studied. However, it is still not entirely clear whether Se is coprecipitated in pyrite or reduced and precipitated on the pyrite surface. Incorporation of Gd(III) into the nanomagnetite structure may be possible due to charge similarity with Fe(III), but this has not been proven and needs to be evaluated before significant medical applications can be developed.

The first focus of my PhD project deals with the geochemical process that can be used to purify water from Re, Se and Gd. I investigated these processes in ferruginous and sulphidic conditions by an experimental approach. This thesis studies the surface-reduction processes of Re(VII) (as a model metallic oxidant) and Se(VI, IV) on magnetite and pyrite and the incorporation of Gd(III) in magnetite lattices. Various methods were used to characterize these experimental systems: STEM-EELS, XRD, ^{57}Fe Mössbauer spectrometry, XAFS spectroscopy, colourimetric analysis, ICP-AES, and MC-ICP-MS. My thesis consists of four chapters. The first chapter introduces through a literature review and in a strict chemical framework (the hard & soft acid & base principle), why some trace elements have a better affinity for sulfur atoms in anoxic environments. The second chapter presents an experimental study of the speciation of Re in sulfidic water. My third chapter shows based on a series of adsorption and co-precipitation experiments, how to enhance the bonding of Re with magnetite and pyrite solids. The last chapter focuses on Se and Gd geochemistry and their interactions with magnetite and pyrite minerals when buried under anoxic conditions.

This PhD research sheds new light on the study of palaeoenvironments, critical metal recycling, mining processes, biomaterial development, and nuclear waste management. The new results suggest that the addition of S(-II) or Fe(II) enhances the removal of Re(VII) and Se(VI) in anoxic waters, which could be used as a treatment to trap these elements from polluted waters or mining effluents. Furthermore, the incorporation of Se or Re into the stoichiometric structure of pyrite or magnetite may prove to be an effective water treatment, as this approach has the potential to minimise the mobility of precipitated and reduced species. On the other hand, this study represents a significant advance in our understanding of the ancient processes leading to the accumulation of rhenium and selenium in pyrite and magnetite in anoxic environments. This study reveals pathways involving oxyanion reduction to Re(VI), Re(IV), Se(0) and Se(-I), as well as reductive adsorption, Se and Re incorporation into the pyrite lattice, and sulphide precipitation, providing a valuable basis for complementing Re and Se isotopic studies in both natural and experimental samples to deepen our understanding of the mechanisms elucidated here and to capture the occurrence of anoxic events ranging from modern times to the gradual oxygenation of the Earth in the past. Lastly, the characterisation of the trace elements enriched particles is also useful for biomedical applications. The magnetite nanoparticle with Gd trapping (or substitution) has great potential in medical applications by preventing the release of Gd, a theragnostic agent, into the cytoplasm or nucleus of targeted cells. The use of this novel composite is also environmentally friendly as it can be easily recovered from urine by sedimentation or magnetic separation and then recycled.

Chapter 1: Oxyanions in sulfidic environment

Oxyanions HSAB behaviour: Thiolation, mineral ores, criticality and paleoenvironmental implications

Carolina Guida[†a,b,c], Laurent Charlet[†a]*, Alex Dickson[d] and Anthony Chappaz[b]*

[a] *Univ. Grenoble Alpes, Univ. Savoie Mont Blanc, CNRS, IRD, Univ. Gustave Eiffel, ISTerre, 38000 Grenoble, France.*
[b] *STARLAB, Earth & Atmospheric Sciences, Central Michigan University, Mount Pleasant, Michigan 48859, USA.*
[c] *Grupo geología médica y forense, Universidad Nacional de Colombia, Apartado Aéreo, Bogotá, Colombia.*
[d] *Department of Earth Sciences, Royal Holloway University of London, Egham, Surrey TW20 0EX, UK.*
[†] Equal first authors
* Corresponding author. E-mail address: anthony.c@cmich.edu & charlet38@gmail.com

1.1 Introduction

Trace elements are present in the Earth's crust in small amounts (less than 100 parts per million), with unique properties for industrial and medical applications and environmental and biological processes (Hooda, 2010). They can be toxic to organisms when their levels exceed safe thresholds, while others are essential but can be harmful in high concentrations (Hooda, 2010; Osamu, 2004). Alternatively, many trace elements are now listed as critical metals by national and regional governments such as the United States, European Union, Japan, Australia and Canada (Graedel et al., 2022). In environments with low oxygen levels (less than 1 µM), known as anoxic environments, the biogeochemical cycles of trace elements are influenced by a complex interaction of biological, chemical, and physical processes that affect both the water column and the sediment-water (Canfield and Thamdrup, 2009; Middelburg and Levin, 2009; Rubalcaba et al., 2020). The sulfur cycle happens in a sulfidic zone defined as the region where measurable ΣS^{2-} exists after iron and sulfate (SO_4^{2-}) reduction dominates (Hlohowskyj et al., 2021a).

Metals, metalloids, and non-metals exist in different forms, such as sulfides, oxides, or carbonates, depending on the cation's affinity with sulfur, oxygen, or carbonate ions (Pearson, 1997). Sulfide minerals like pyrite are formed in anoxic environments through sulfur reduction, and they are the primary source of many metals and essential ore minerals (Lottermoser, 2010; Vaughan, 2005). However, mining these resources can expose sulfides to an oxygenated environment, producing acid mine drainage (AMD) and releasing non-commercial trace elements and heavy metals into the environment, significantly impacting ecosystems and human health.

The toxicity of trace elements to living organisms depends, on the nature of their metal ion, which is closely linked, among other factors, to the redox environmental conditions (Kinraide and Yermiyahu, 2007). In sulfide-rich environments, trace elements bind with sulfur ligands and exist in low-soluble and low oxidation states, making them less available for ingestion and, therefore, less toxic. However, exposure to oxygen can lead to the oxidative dissolution of these sulfide minerals and

the release of metals as free ions or oxyanions in water, rendering them significantly more toxic as organisms can ingest them. The toxicity becomes more complex inside the organism because the physiological effects depend on the type and strength of the new binding of metals to biological materials enzymes (Kinraide and Yermiyahu, 2007). Some exceptional toxicities are attributable to the complexation of these "heavy metal" sulfur-rich enzymes.

Redox-sensitive metals (RSMs) or chemicals that show changes in the redox state and solubility with or without oxygen are used as lacustrine and marine palaeo-proxies to study pollution, ocean oxygen levels, productivity and circulation over geological time scales (O'Connor et al., 2022). The behaviour of RSMs varies for each specific element when exposed to euxinic conditions. For example, Molybdenum (Mo), Tungsten (W) and Rhenium (Re) form thiolate species in sulfidic waters as $MoO_{4-x}S_x^-$, $WO_{4-x}S_x^{2-}$ and $ReO_{4-x}S_x^-$ (Helz and Dolor, 2012; Hlohowskyj et al., 2021b). In the case of Re and W, however, thiolation occurs in the presence of high concentrations of dissolved sulphide, in contrast to Mo. However, the literature does not provide any evidence of thiolation for chromium (Cr), and selenium (Se), which are also used to track anoxia (Janssen et al., 2023; Kipp et al., 2020). These species exhibit greater reactivity and are more likely to concentrate in anoxic deposits (Helz, 2022; Robbins et al., 2016) evidenced in various sediments records (Dellwig et al., 2019; Helz and Adelson, 2013; Morford and Emerson, 1999).

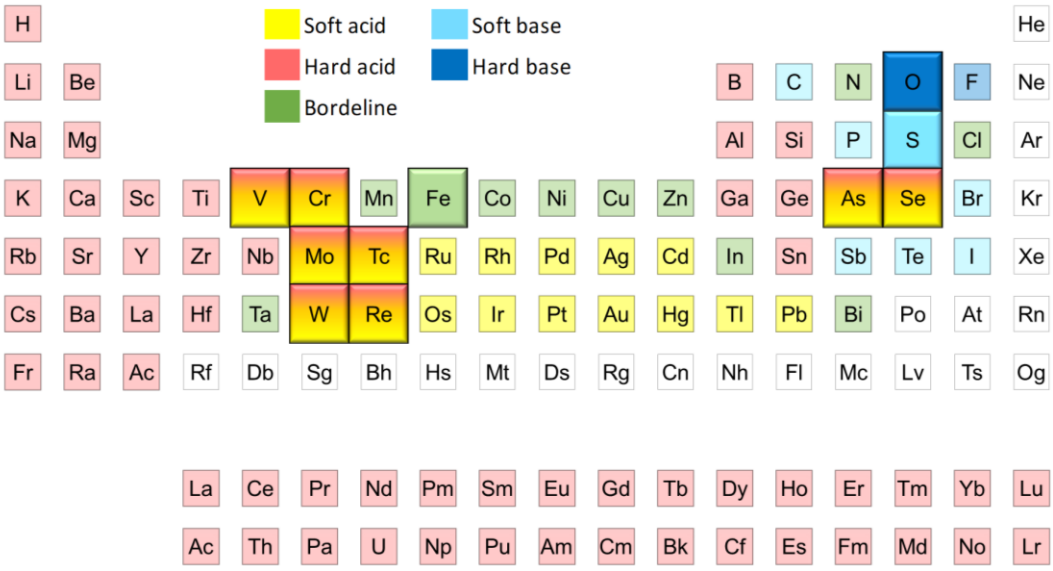

Figure 1 Determination of the oxyanions of interest and classification of the elements as acid or base following the HSAB theory (Wulfsberg, 1987).

Metal or metalloids geochemistry in depleted oxygen water is intricately shaped by their distinct chemical and thermodynamic attributes, as well as their affinity for ligands such as sulfide and oxygen (Sposito, 1981). Although there is a vast amount of literature on the subject, publications on oxyanions are limited, and their geochemistry is still poorly understood (Müller et al., 1994, 1981; Planer-Friedrich et al., 2020). This review focuses on specific RSMs: two metalloids—Selenium and Arsenic—and six metals—Rhenium, Technetium, Chromium, Vanadium, Molybdenum and Tungsten (See Figure 1). We first provide a brief description of the occurrence and aqueous chemistry in the environment. Then, we provide an overview of the current literature on their interaction with iron sulfide minerals. Finally, we connect observations about the reactivity of these elements in sulfidic

water, using the HASB principle. This study aims to improve our understanding of the factors that govern the reactivity of oxyanions in aquatic environments.

1.2 Environmental occurrence

The different oxidation states of the eight conservative elements of interest in this review determine their reactivity, mobility and solubility under different environmental conditions. In aqueous environments, these elements at near-neutral pH, oxidized species are expected to be present as oxyanions (primarily $H_2AsO_3^{2-}$, $H_2VO_4^-$, $HAsO_4^{2-}$, MoO_4^{2-}, $HSeO_3^{2-}$, WO_4^{2-}, CrO_4^{2-}, SeO_4^{2-}, ReO_4^{2-} and TcO_4^{2-}) (See Figure 2). These elements occur naturally from atmospheric deposition, marine aerosols produced by the bursting of sea surface bubbles, tephra and ash from volcanic activity, emissions from hydrothermal vents and the weathering of shales. Anthropogenic sources include mining, industry and the burning of fossil fuels. These elements are also reduced and immobilised by interaction with iron oxyhydroxides, sulphides, clays and organic matter; solids typically present in anoxic aquatic environments. The main concentrations of these elements in different compartments of the Earth are shown in Table 1.

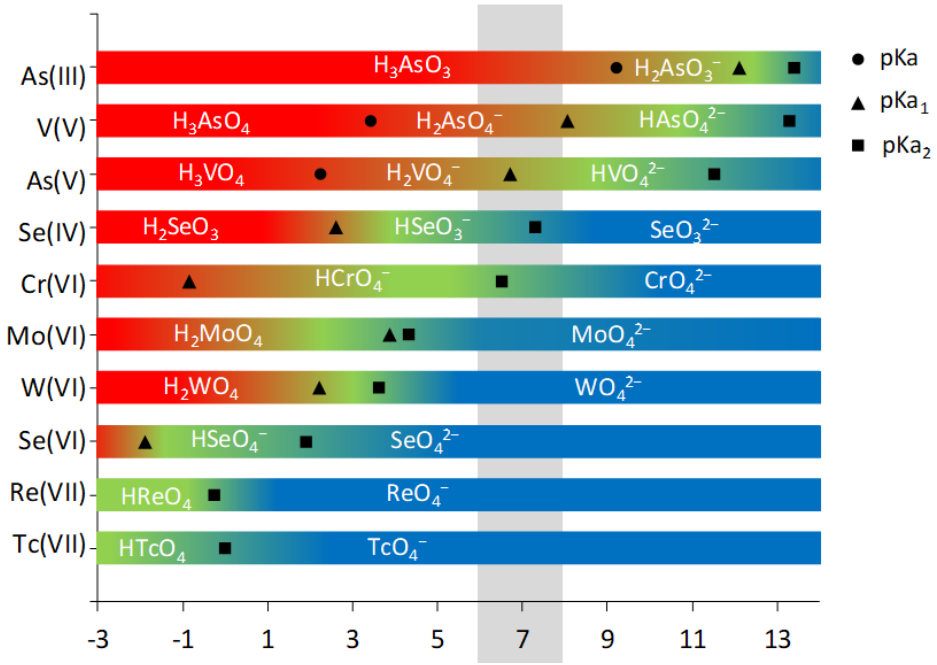

Figure 2 Species distribution diagram of oxyanions according to pH

Table 1 Se, As, V, Mo, W and Re concentrations in different earth compartments.

Element	Upper crustal average Earth - mg/kg [a]	Global black shales - mg/kg [b]	Carbonaceous shales - mg/kg [c]	Soils - mg/kg	Rivers - ng/kg	Ocean - ng/kg	Other references
Se	50	6 +/- 1.7	8 +/- 0.8	0.005 - 1200	71.06 - 718.54	39.48 - 181.61	(Cutter and Cutter, 2001; Gebreeyessus and Zewge, 2018; Mason et al., 2018)
As	1.5	27 +/-03	34 +/- 6	4.4 - 9.3	250 - 2.24x10^8	5.60 - 11240.00	(Boyle and Jonasson, 1973; Kabata-Pendias, 2000)
V	107	200 +/- 10	99 +/- 23	18 - 115	25.47 - 2271.99	1528.25 - 1884.84	(Emerson and Huested, 1991; Kabata-Pendias, 2000; Shiller and Boyle, 1987; Sohrin et al., 1989)
Mo	1.5	18 +/- 3	16 +/- 7	1.3 - 2.8	479.70 - 959.40	9594.00 - 10361.52	(Emerson and Huested, 1991; Hlohowskyj et al., 2021a; Kabata-Pendias, 2000; C. Miller et al., 2011; Sohrin et al., 1987)
W	2	2.4 +/- 1.9	8.1 +/- 1.2	0.68 - 2.7	3.68 – 189171.36	7.54 - 12.32	(Kurzweil et al., 2021; Sohrin et al., 1989)
Re	0.0004	0.2 +/- 0.2	0.5 +/- 0.5	0.000018 - 0.00477	2.09	7.42 - 7.58	(Anbar et al., 1992; Dickson et al., 2020; C. Miller et al., 2011; Tagami and Uchida, 2008)

*Values are taken from (McLennan, 2001) for a, (Ketris and Yudovich, 2009) for b and (Ketris and Yudovich, 2009) for c.

1.2.1 Selenium

Selenium (Se) exhibits a diverse range of oxidation states, spanning from -II to +VI, with Se(-II), Se(-I), Se(0), Se(IV) and Se(VI) being the prevailing forms in natural settings (Fordyce, 2013). The average Se concentration in the upper crust is 50 mg/kg (McLennan, 2001), while carbonate shales contain 8 ± 0.8 mg/kg, and black shales contain 6 ± 1.7 mg/kg (Ketris and Yudovich, 2009). Volcanic emissions contribute 400 to 9000 metric tons per year (mt/a) of Se to the atmosphere, with nearly equal amounts originating from continental sources (about 150 to 5250 mt/a) (Wen and Carignan, 2007). Additionally, various industries release anthropogenic Se into natural waters through activities such as coal mining, glassmaking, irrigation, pigment production, petroleum refining, coal combustion, and radioactive waste disposal plants (Cao et al., 2014; Etteieb et al., 2021; Fernández-Martínez and Charlet, 2009). Notably, radioactive waste disposal leads to significant emissions of the radioisotope ^{79}Se, a byproduct produced in nuclear power plants. In well-oxygenated waters, predominant Se species are the oxyanions: selenate [$Se(VI)O_4^{2-}$] prevails, while in hypoxic water, selenite [$Se(IV)O_3^{2-}$] and biselenite [$HSe(IV)O_3^-$] dominate (Belzile et al., 2000; Mason et al., 2018). Se(VI) and Se(IV) can undergo sequestration through adsorption and reduction reactions, ultimately resulting in Se(0), Se(-I), and Se(-II) forms with low solubility due to interactions with various minerals such as clay, iron oxyhydroxides, and iron sulfide and natural organic matter (Perrone et al., 2015; Scheinost and Charlet, 2008a). In seawater, the average world concentration of Se in the surface water is 39.48 ng/kg, and deep ocean concentrations (>3,000 m) are 181.61 ng/kg (Mason et al., 2018), with a mean residence time of the deep ocean about 1100 years (Fernández-Martínez and Charlet, 2009). The typical Se concentration for the rivers ranges between 71.06 to 718.54 ng/kg (Cutter and Cutter, 2001). Selenium concentrations vary widely, from 0.005 to 1200 mg/kg, higher in soils of more recent volcanic origins (Gebreeyessus and Zewge, 2018). Certain plant species can uptake and process Se as selenate ions through sulfate transporters (El-Ramady et al., 2016). For human dietary needs, Se intake ranging from 50 to 400 micrograms per day (µg/day) is considered essential and beneficial (WHO, 1996). However, excessive Se intake, reaching 800 µg/day, can harm aquatic life, leading to deformities, reduced reproductive rates, and increased mortality (Balistrieri and Chao, 1990).

1.2.2 Arsenic

Arsenic (As) is also a metalloid prevalent in Earth's crust at a concentration of 1.5 mg/kg (McLennan, 2001) and exists in both inorganic and organic forms, exhibiting four valence states: -III, 0, +III, and +V (Wang et al., 2023). Among these, trivalent arsenic – As(III) and pentavalent arsenic – As(V) are widely distributed in natural waters, displaying solubility across a broad spectrum of pH and E_H conditions (Duker et al., 2005). In oxygenated waters characterised by elevated E_H values, arsenates ($H_3As(V)O_4$, $H_2As(V)O_4^-$, $HAsO_4^{2-}$, and $As(V)O_4^{3-}$) remain stable. Conversely, arsenite species thrive under mildly reducing conditions: $H_3As(III)O_3$, $H_2As(III)O_3^-$, and $Has(III)O_3^{2-}$. Under anaerobic conditions, microorganisms in soil can reduce arsenite to arsine (AsH_3) (Duker et al., 2005). Soluble arsenic species settle mainly as insoluble sulfides or metallic arsenic within sediments. The processes involved in arsenic sequestration are co-precipitation, adsorption and epitaxial attachment of crystals with manganese (oxy)hydroxide, iron, organic matter and sulfur minerals. Prominent arsenic-sulfide minerals encompass orpiment (As_2S_3) and arsenopyrite (FeAsS), which may manifest in specific hot spring precipitates (Suess and Planer-Friedrich, 2012) and sulpho-salt tetrahedrite-tennantite ($(Cu,Fe,Zn,Cd,Bi,Hg,Ag)_{12}(Sb,As, Bi)4S_{13}$) (Boyle and Jonasson, 1973). In particular, concentrated arsenic

samples are linked to coal associated with pyrite minerals, exhibiting levels of up to 6000 mg/kg (Boyle and Jonasson, 1973). In unpolluted river waters, typical arsenic concentrations usually display levels between 250 and 2.24x10^8 ng/kg (Boyle and Jonasson, 1973). In contrast, seawater's mean arsenic concentration slightly surpasses freshwater due to the influence of marine hydrothermal fluids, hovering around a range of 5.6 to 11240 ng/kg.

1.2.3 Rhenium

The metal Rhenium (Re) presents oxidation states ranging from +I to +VII. In aqueous systems, the most stable oxidation states of Re are +VII with the highly soluble perrhenate [ReO_4^-] and in a less soluble form under anoxic conditions +IV (Duckworth et al., 2021). Re primarily enters the oceans through the weathering of continental crust, with only about 30% attributed to human activities, such as fossil fuels, fuel processing catalysts, brake liners, jet engines, and road dust. In terrestrial environments, Rhenium upper crustal average is 0000.4 mg/kg (McLennan, 2001). Re concentrates near roadways, reaching values as high as 0.000018 to 0.00477 mg/kg in Japanese soils (Tagami and Uchida, 2008). In seawater, Re concentrations were recorded at around 7.58 ± 0.25 ng/kg in the South Atlantic Ocean (Dickson et al., 2020) and 7.42 +/- 0.04 ng/kg in the Pacific Ocean (Anbar et al., 1992). It has an oceanic residence time of approximately 720000 years (C. A. Miller et al., 2011). The average Re concentration in river systems is estimated at 2.09 ng/kg as a pre-industrial calculated concentration (Colodner et al., 1995; C. Miller et al., 2011). Potential sinks for Re include the dissolved river flux, shales and sulfide minerals as FeS_2, $CuFeS_2$, AsFeS, MoS_2, ReS_2, ReS_3, $CuReS_4$, $Re_4Mo_2CuFeS_{11}$ and hydrothermal vents on the ocean floor, where Re(IV) complexes are found in chloride-bearing solutions and the precipitation of ReS_2 in the presence of sulfur in laboratory experiments (Xiong and Wood, 2002, 1999). In carbonate and black shales, the Re average concentration is about 0.5 ± 0.5 and 0.2 ± 0.1 mg/kg, respectively (Ketris and Yudovich, 2009). Re has been observed to bioaccumulate in brown algae (>10000 ng/kg) taken up in ReO_4^- form as an accidental side effect of its extraordinary iodine accumulation (Helz and Dolor, 2012; Tagami and Uchida, 2008).

1.2.4 Vanadium

Vanadium (V), another metal, exist in various oxidation states, including -1, 0, +2, +3, +4, and +5. In natural environments, vanadium (+5) and vanadium (+4) are prevalent under oxidizing and moderately reducing conditions (Huang et al., 2015). Vanadium (+3) is found in anoxic environments and is relatively immobile and insoluble, readily oxidizing to higher states in oxygen. Vanadium upper crustal average earth content is 107 mg/kg (McLennan, 2001). The higher V concentrations are found in global black and carbonaceous shales with 200 ± 10 and 99 ± 23 mg/kg, respectively (Ketris and Yudovich, 2009). In soils, the concentration varies between 18 to 115 mg/kg (Kabata-Pendias, 2000). Within aquatic environments, the dissolved concentration of V is in rivers about 25.47 to 2271.99 ng/kg (Shiller and Boyle, 1987) and in the open ocean, averaging 1528.25 to 1884.84 ng/kg (Emerson and Huested, 1991). At neutral pH, the dominant aqueous species of V(V) are the phosphate-like mononuclear vanadate oxyanions $H_nVO_{4n}^{-3}$ (Wanty and Goldhaber, 1992; Wehrli and Stumm, 1989), under acidic conditions is VO^{2+}, and in highly alkaline conditions VO_4^{3-} (Huang et al., 2015). The natural contributions yield an estimated 37000 mt/a of vanadium added to the atmosphere (Duce and Hoffman, 1976). The budget for anthropogenic V emissions to the atmosphere is estimated at 85941 mt/a, far exceeding that of natural V emissions (Hope, 2008). Vanadium exists in soils in various forms, including dissolved in soil solution, retained in soil particles, associated with organic matter, bound or

substituted for common transition elements in clay minerals, oxides, hydroxides, silicates, and infrequent sulfides (Shaheen et al., 2019). Adsorption onto metal oxide minerals involves inner-sphere bidentate complexes for vanadyl ions and monodentate complexes for vanadate ions. Notably, particulate vanadium displays limited mobility except under conditions of high acidity and remains the most available form for plants (Huang et al., 2015).

1.2.5 Molybdenum

Molybdenum (Mo) is an essential trace element for human, animal and plant health and has played an important part in the evolution of life on Earth (Smedley and Kinniburgh, 2017). Mo has formal oxidation states from -II to VI. However, IV, V and VI are the most important in the environment. Under oxic conditions, dissolved Mo is dominated by the relatively unreactive tetrahedral $Mo(VI)O_4^{2-}$ ion. Protonated forms, $HMoO_4^-$ and H_2MoO_4, are found at pH < 5 though even here, $HMoO_4^-$ is rarely dominant. In open marine water, Mo occurs in concentrations of 9594 to 10361.52 ng/kg (Bruland et al., 2014), with a long residence time in the oceans of 400000 years (C. Miller et al., 2011). Rivers supply most of Mo to the oceans, up to 19958 mt/a, mainly by the weathering of continental material (Smedley and Kinniburgh, 2017). World rivers present a concentration of 479.70 to 959.40 (Hlohowskyj et al., 2021a; C. Miller et al., 2011). Estimates of its upper crustal abundance have been put at around 1.5 mg/kg (McLennan, 2001). The average black and carbonaceous shale Mo contents have been estimated from around 18 +/- 3 and 16 +/- 7 mg/kg, respectively (Ketris and Yudovich, 2009). The principal ore mineral of Mo is molybdenite (MoS_2), a silvery black Mo(IV) mineral. Non-contaminated soils typically have Mo contents of 1.3 to 2.8 mg/kg (Kabata-Pendias, 2000).

1.2.6 Tungsten

Tungsten (W) has a diversity of oxidation states between -2 to +6. Tungstate $W(VI)O_4^{2-}$ is the principal form as soluble species in oxic environments, and as a solid substance, metal tungsten – W and oxides of tungsten like WO_2, W_2O_5 and WO_3 are predominant(Koutsospyros et al., 2006). Because the ability to polymerise is common for elements in Groups V and VI of the periodic table, tungstates tend to polymerize to form isopolytungstates under even slightly acidic conditions. Under alkaline solutions, the monomeric state is stable. In the open sea, specifically in the NW Pacific Ocean, the tungsten concentration is about 7.54 - 12.32 ng/kg (Kurzweil et al., 2021; Sohrin et al., 1989) with a moderately long residence time between 14000 to 61000 years (Kurzweil et al., 2021; Sohrin et al., 1987). In rivers, the W concentration measure is about 3.68 – 189171.36 ng/kg and in hydrothermal fluids, about 40.44 - 22612.32 ng/kg (Johannesson et al., 2000; Kishida et al., 2004; Kurzweil et al., 2021). Notably, in sulfidic groundwater, geothermal fluids, and euxinic marine waters, the dissolved W concentration increase relative to oxic marine waters (Cui et al., 2020). The Earth's upper crustal average concentration of tungsten is 2 mg/kg (McLennan, 2001), and the enriched minerals containing W are scheelite ($CaWO_4$) and wolframite ($[Fe/Mn]WO_4$). W exhibits a stronger affinity for ferromanganese oxides/oxyhydroxides in anoxic marine sediments (100 mg/kg) and less affinity with sulfide minerals(Cui et al., 2020; Kashiwabara et al., 2013). In global black and carbonaceous shales, concentrations are 2.4 ± 1.9 and 8.1 ± 1.2 mg/kg, respectively (Ketris and Yudovich, 2009). W concentrations in surface soils are 0.68 to 2.7 mg/kg (Senesil et al., 1999).

1.3 Aqueous chemistry in sulfidic waters

Previous studies have shown that the oxyanions MoO_4^{2-}, ReO_4^-, TcO_4^-, AsO_3^{3-}, AsO_4^{3-}, WO_4^{2-}, and VO_4^{3-}, can undergo a chemical transformation where one or more oxygen atoms are replaced by sulfur atoms, resulting in the formation of thiometalates anions (Müller et al., 1981). In these anions, sulfur acts as a multidentate chelating agent, forming multiple bonds with the metal or metalloid ion and creating a more stable and reactive metal-ligand complex. The conditions essential for producing thiometalate anions can differ based on the specific metal or metalloid involved and the characteristics of sulfide waters like pH and the ratio between [ΣS^{2-}] and the metal/metalloid concentration. Some of these oxyanions can thiolate in sulphur-poor waters while others have only been observed in sulphur-rich conditions. Sulfide waters can be categorized into three distinct sulfidic zones, determined by the overall concentration of reduced sulfur [ΣS^{2-}] in the water. These zones are a weak sulfidic zone, characterized by [ΣS^{2-}] falling within the range of 0.2 µM to 15 µM; the moderate sulfidic zone, spanning 15 µM to 600 µM; and the highly sulfidic zone, where concentrations exceed 600 µM (Cui et al., 2021).

The phenomenon of thiolation has been extensively researched in experimental settings and natural waters for elements such as As, Mo, V, Re, and W. Studies involving Re, Tc, Cr and V are exceptions in natural water contexts. Various techniques are commonly employed for identifying and quantifying thiospecies in diverse sample types, including synthetic, environmental, geological, and biological samples. These techniques encompass ultraviolet-visible (UV-Vis) spectroscopy, atomic absorption spectrometry (AAS), atomic fluorescence spectrometry (AFS), inductively coupled plasma mass spectrometry (ICPMS), and electrospray ionization mass spectrometry (ESMS), as referenced. These methods are utilized either independently or in combination with different separation techniques, which include ion chromatography (IC), ion-pair chromatography (IPC), ion-exchange chromatography (AEC), reverse phase ion pair chromatography (RP-IPC), high-performance liquid chromatography (HPLC), gas chromatography (GC), capillary electrophoresis (CE), and supercritical fluid chromatography (SFC) (Diemann and Müller, 1970; Herath et al., 2018, 2018; Lohmayer et al., 2015; Müller et al., 1994, 1981; Planer-Friedrich et al., 2020; Ranade et al., 1970; Vorlicek and Helz, 2002; Weiss et al., 1988). UV-Vis spectroscopy is commonly used in laboratory settings to identify thiometalates for Re, Mo, and W. However, the experiments are conditional and must be developed at millimolar concentration levels.

1.3.1 Metalloids: Se and As

Based on our experience, no evidence of selenate thiolation has been observed using the UV-vis detection method. This observation is consistent with no findings of ligand exchange of Se(VI) in previous studies. Conversely, for selenite, there is well-documented fast reductive precipitation at neutral pH in the first 30 minutes (Jung et al., 2016) and in the presence of sulfide concentrations in the range of S/Se ratios from 0.6 to 11.5, rather than thiolation phenomena.

The behaviour of thioarsenates ($AsS_XO_{4-X}^{3-}$, with X ranging from 1 to 4) has been examined in various environmental conditions in previous studies. Thioarsenates are generated through a multi-step process involving the deprotonation of arsenite in aqueous sulfide (H_2S). For arsenate, this ion becomes thiolated, forming dithioarsenate. This process has been extensively studied in laboratory settings, revealing its feasibility under specific conditions: H_3AsO_3 concentration of 91 µM, H_2S/HS^- ratio of 5000 µM, and a neutral pH (Stauder et al., 2005).

Observations in natural settings emphasize arsenic's inclination to become thiolated when sulfide availability is limited relative to metal(loid) concentrations. in sulfidic geothermal waters, all four thioarsenate species are prevalent, comprising a significant portion of the arsenic speciation landscape, often exceeding 80% of total As content (Planer-Friedrich et al., 2020, 2007). In natural waters, several mechanisms are proposed for the thioarsenates. A first mechanism suggests initial trithioarsenite as the primary reaction product. Subsequently, under oxic conditions, trithioarsenite undergoes voluntary oxidation, leading to the formation of di- and tri-thioarsenate compounds. Another pathway involves the oxidation of arsenite by elemental sulfur (S°), contributing to the formation of thioarsenate species (Wallschläger and Stadey, 2007). Alternatively, a further route suggested is the oxidation of arsenite by mycobacteria to arsenate (Wu et al., 2017). This arsenate then reacts with sulfide, forming thioarsenate compounds.

The thioarsenates exhibit notable stability against transformation under alkaline pH conditions. Research by Thilo et al. (1970) suggests that thioarsenates remain stable in solution through proton binding to AsO-sites (Thilo et al., 1970). However, the presence of AsSH groups destabilizes thioarsenates, causing the precipitation of arsenic sulfide. Experimental findings demonstrate that di- and trithioarsenate first transform into arsenite before precipitating (Kumar et al., 2020). Monothioarsenate remains stable across the pH spectrum, while dithioarsenate converts to arsenite below pH 4 and initiates this transition at pH 7 (Planer-Friedrich and Wallschläger, 2009). Tetrathioarsenate transforms into trithioarsenate at pH 11.9, further changing to a mixture of arsenite and trithioarsenate at pH 5.6. At pH levels below 5, the arsenic-sulfur compounds precipitate (Rochette et al., 2000). The sulfide particulate mechanism formation is not fully understood and could involve sulfur donors like elemental sulfur and polysulfides acting as redox partners for As. In scenarios where there are elevated S:As ratios and high sulfide concentrations, the significance of intermediate As-S species notably diminishes at a pH value of 4. During this condition, sulfide stimulates the precipitation of arsenic. At pH 7, precipitation does not occur, so the specific S:As ratio becomes unimportant (Rochette et al., 2000).

Arsenites can form trivalent thiospecies ($AsS_XO_{3-X}^{3-}$, with X ranging from 1 to 3), particularly when a surplus of SH^- is present compared to OH^-. Notably, among these species, only trithiolated variants have undergone analytical confirmation. Detecting thioarsenites in natural water samples at environmentally relevant low concentrations remains a challenge because the methods have yet to be developed. However, it is crucial to acknowledge that thioarsenites exhibit remarkable vulnerability to oxidation, implying that their presence in natural waters is very low probable, even when considering minute oxygen traces. On the other hand, several soluble arsenic-sulfide complexes, such as di- and trithioarsenite monomers as well as dimeric and trimeric arsenic-sulfur complexes have been described or suggested during orpiment (As_2S_3) dissolution (Rochette et al., 2000).

1.3.2 Transition metals: Cr, W, Re, Tc, Mo, and V

To our knowledge, no thiolation species have been identified for the hazardous hexavalent chromium as CrO_4^{2-} and $HCrO_4^-$(Stefánsson et al., 2015). Thus, based on sedimentary evidence, Cr appears to have a greater affinity for ferruginous waters than for sulphidic waters.The transition metals W, Tc, Re, Mo, and V also demonstrated susceptibility to thiolation. However, the potential for vanadium to form thiolation species in natural sulfidic waters is not definitively established. Some literature references allude to the presence of thiovanadates (Diemann and Müller, 1970; Müller et al., 1994, 1981; Ranade et al., 1970), yet recent experimental and natural measurements do not

provide substantial support for this claim. Instead, existing evidence points toward complexation rather than reduction of Vanadate when interacting with certain biological thiols (Crans et al., 2010). In line with experimental conditions outlined by Ranade, reactions are fast, with significant changes occurring within the initial 6-minute timeframe.

Between Mo and W, thyomolybdates ($MoO_xS_{4-x}^{2-}$) form more rapidly than thiotungstates ($WO_xS_{4-x}^{2-}$) (Müller et al., 1981) and Mo need less sulfide concentration than W to form. Aqueous speciation modelling demonstrates that tungstate and molybdate dominate in the weakly sulfidic zone, WO_4^{2-} and thiomolybdates are present in the moderately sulfidic zone, and thiotungstates and MoS_4^{2-} govern in the strongly sulfidic zone (Cui et al., 2021). Therefore, the behaviour of W and Mo is different in sulphidic waters: dissolved W concentrations increase while dissolved Mo concentrations decrease (Cui et al., 2020). These variations in W and Mo concentrations also may be attributed to differences in the particle reactivity of thiotungstate and thiomolybdate species. Thiotungstates exhibit lower particle reactivity in sulfidic waters, whereas tungstates demonstrate high reactivity with Mn oxides and Fe-hydroxides (Kurzweil et al., 2021).

For Re, UV-vis spectra show that concentrations of the order of millimolar Re can form ReO_3S^- at a molar ratio of 1:1 (Re:S) (Ferrier, 2014). At higher levels of $\sum S^{2-}$, equilibrated solutions at pH values between 6 and 10 have been observed to contain $ReOS_3^-$ and ReS_4^- (Helz and Dolor, 2012). However, the formation of thioperrhenates is much slower at alkaline pH. Once ReS_4^- has been identified, Re-S colloid formation is reported. Vorlicek et al, (2015) identify thioperrhenates from solutions with initial experimental conditions of the order of micromolar using the RP-ICP-MS method. Regarding Tc, the single study only identified the formation of the first thiospecie at different Tc:S ratios (1:1 to 1:4) (Ferrier, 2014). It seems that after TcO_4^- exchanges an oxygen with a sulphur, TcO_3S^- becomes highly unstable and reactive, reducing and/or polymerizing into a technetium oxosulfide species such as $Tc_2O_5S^-$, $Tc_2O_4S^{2-}$, $Tc_2O_3S^{3-}$ and $Tc_2S_5O^-$.

1.4 Oxides, sulfides and iron sulfide minerals

Solids connect trace elements that circulate within the Earth's interior to weathering and biogeochemical processes on the surface. They usually appear as an accessory component of minerals. This phenomenon can be explained by the low concentration of these elements in the Earth's crust and their tendency to disperse in response to acidity and oxygen levels. Below is a brief compilation of trace element occurrences in three types of rocks: oxides, sulfides, and iron sulfide minerals.

1.4.1 Oxides

When Re and Tc undergo combustion in an oxygen-rich environment, Re_2O_7 or Tc_2O_7 oxides are produced. Despite both heptoxides being volatile, ReO_3 remains inert. Both ReO_2 and TcO_2 oxides exhibit distorted rutile structures. However, Tc(IV) oxide is the most stable, as ReO_2 can decompose under specific conditions (Earnshaw and Greenwood, 1997). In nature, Re_2O_7 is believed to occur naturally in uranium (U) deposits (Petersen et al., 1957).

Molybdenum oxide minerals result from the weathering of molybdenum-bearing deposits. The most common molybdenum oxides include molybdite (MoO_3), wulfenite ($PbMoO_4$), ferrimolybdite ($Fe_2(MoO_4)_3.nH_2O$), powellite ($CaMoO_4$), ilsemannite ($Mo_3O_8.nH_2O$), and lindgrenite ($Cu_3(MoO_4)_2(OH)_2$)

(Smedley and Kinniburgh, 2017). Molybdates, characterized by their soft and brittle nature, often occur alongside chemically analogous tungstate minerals.

Similar to Re, Tc and Mo, selenium oxyanions can exist in certain minerals but exhibit instability under oxidizing conditions, leading to their transformation into soluble species. Several mentioned minerals containing Se(VI) and Se(IV) include marthozite ($Cu(UO_2)_3(SeO_3)_2O_2{\cdot}8H_2O$), mandarinoite ($Fe_2(SeO_3)_3{\cdot}6H_2O$), carlosruizite ($K_6Na_4Na_6Mg_{10}(SeO_4)_{12}(IO_3)_{12}{\cdot}12H_2O$), prewittite ($KPb_{1.5}ZnCu_6O_2(SeO_3)_2Cl_{10}$), and nicksobolevite ($Cu_7(SeO_3)_2O_2Cl_6$) (Krivovichev et al., 2019). Two selenium oxide minerals, SeO_3 and SeO_2, are reported in the literature. The latter, known as Downeyite, is the only one found naturally. It forms acicular crystals from gases escaping through vents on culm banks in the anthracite region of Pennsylvania (Finkelman and Mrose, 1977).

For As, common arsenic oxide minerals include scorodite ($FeAsO_4{\cdot}2H_2O$), amorphous ferric arsenate, arseniosiderite ($Ca_2Fe_3(AsO_4)_3O_2{\cdot}3H_2O$), yukonite ($Ca_7Fe_{12}(AsO_4)_{10}(OH)_{20}{\cdot}15(H_2O)$), and pharmacosiderite ($KFe_4(AsO_4)_3(OH)_4{\cdot}(6\text{-}7)H_2O$) and for As(III), claudetite (As_2O_3), arsenolite (As_2O_3), picropharmacolite ($Ca_4Mg(AsO_3OH)_2(AsO_4)_211H_2O$) and tooeleite ($Fe_6(AsO_3)_4(SO_4)(OH)_44H_2O$) (Juillot et al., 1999; Morin et al., 2003). These minerals are the result of oxidation of arsenic-bearing minerals. Among these secondary minerals, scorodite is the most abundant variety due to its higher stability in near-surface environments (Blowes et al., 2003).

Among the elements studied, only W and Cr have as principal mineral ore oxides. The most common ores of W are found almost exclusively in oxide-rich tungsten minerals, either as scheelite ($CaWO_4$) or wolframite ($[Fe/Mn]WO_4$) (Koutsospyros et al., 2006). The two main naturally occurring oxides are chromite ($FeCr_2O_4$) and crocoite ($PbCrO_4$) (Barnhart, 1997). Vanadium occurs mainly in oxide and hydroxide minerals where it replaces Fe and Al due to the size and charge of its species. The most important source of mined vanadium is titaniferous magnetite, which is primarily produced as a byproduct of iron and titanium mining. In magnetite, vanadium occurs mostly as V(III), with minor V(IV) occupying octahedral sites (Balan, 2006). Vanadate (VO_4^{3-}) ore minerals are associated with low-temperature, non-sulfidic mineralization in Southern Africa (Boni et al., 2007). The minerals found in these areas include mottramite ($PbCu(VO_4)(OH)$), descloizite ($(Pb,Zn)_2VO_4(OH)$), and vanadinite ($Pb_5(VO_4)_3Cl$).

1.4.2 Sulfides

The most common minerals containing arsenic are arsenic sulfides, such as arsenopyrite (FeAsS), realgar (As_4S_4), and orpiment (As_2S_3) (Drewniak and Sklodowska, 2013). These minerals are formed only under high-temperature conditions in the Earth's crust and are found in hydrothermal and magmatic ore deposits. In contrast, nanostructures of As_2S_3 are observed to form in anoxic, sulfide-rich waters with high S:As ratios (20:1), low pH and low temperature. Experimental studies have shown that arsenate reduction by hydrogen sulfide is rapid and conforms to a second-order kinetic model at pH 4, compared to pH 7 (Rochette et al., 2000). In fact, at an initial sulfide-arsenate ratio of 100:1, essentially no reduction was observed after 7 days. For Se, earlier studies have shown that selenite can precipitate with sulphide to form selenium-sulphur compounds, commonly represented by the formula SeS_2 (Hageman et al., 2017; Jung et al., 2016; Pettine et al., 2012). These particles are composed of eight rings of variable composition (Se_nS_{8-n}), where n ranges between 2.5 and 3 (Geoffroy and Demopoulos, 2011).

Regarding Re and Tc, metal oxide formations are more common than sulfide formations, although sulfides tend to occur at lower oxidation states. Both elements can form MS_2 and M_2S_7 (M=Re or Tc), while Re can also form ReS_3 (Peacock, 1966). Formed at high temperatures, MS_2 compounds are isostructural, with monoatomic S^{2-} units and trigonal prismatic coordination of the metal in a layered lattice structure (Earnshaw and Greenwood, 1997). The Re_2S_7 materials lose sulfur at higher temperatures (Schwarz et al., 2004). Rhenium sulfide is a rare mineral often found in Russia, Mongolia and Greece (Berzina et al., 2005; Voudouris et al., 2009). The Kudriavy volcano yielded the purest naturally occurring rhenium sulfide in 1994 with an intermediate composition of rheniite (ReS_2) and Re_2S_3 (Korzhinsky et al., 1994).

The elements Mo and W exhibit similarities to Tc and Re like their sulfides (Peacock, 1966). Molybdenite (MoS_2) is the primary ore mineral of Mo. Mo(IV) sulfide materials include Mo_6S_8, Mo_2S_3, MoS_6, and $Mo_{15}S_1$ (Afanasiev, 2008). Additionally, amorphous sulfur-rich sulfides such as MoS_3, MoS_4, MoS_5, and MoS_6 with an oxidation state close to V can be formed at low temperatures, unlike Mo(IV) sulfides that are formed above 300°C (Chappaz et al., 2008; Mohajerin et al., 2016). Additionally, mineralised areas may contain ore minerals such as galena (PbS) and sphalerite (ZnS), which offer ample opportunity for binding chalcophilic Mo (Smedley and Kinniburgh, 2017). In the case of W, the only secondary mineral reported is tungstenite (WS2), which has a structure very similar to molybdenite (Wells and Butler, 1917).

There is limited information available on vanadium sulfides, with references to the existence of two natural minerals and various synthetic materials: patronite (VS_4) described as $V(IV)(S_2^{2-})_2$, Colimaite (K_3VS_4), V_2S_5, VS, V_3S and VS_6, VS_2, and V_2S_3 (Liu et al., 2020). The scarcity of findings regarding V sulfide minerals can be attributed to their high solubility, which suggests that they may have served as a source of vanadium to the environment during the Archean and Proterozoic eras (Moore et al., 2020).

Chromium sulphides are not commonly found in the literature. Rare minerals such as Brezinaite (Cr_3S_4), Caswellsilverite ($NaCrS_2$), Cuprokalinite ($CuCr_2S_4$), Grojovskyite ($CuCrS_2$), Joegoldsteinite ($MnCr_2S_4$), Kalinite ($ZnCr_2S_4$) and Murchisite (Cr_5S_6) ("Mindat.org," n.d.). Synthetic Cr(III) sulphides with the formula Cr_2S_3 are also known. These are generally non-stoichiometric compounds with a formula range from CrS to $Cr0.6_7S$ (Jellinek, 1957)

1.4.3 Iron sulfide minerals

The formation and presence of authigenic iron sulphide minerals, such as pyrite (FeS_2) and its metastable precursors like mackinawite (FeS) and a poorly-ordered FeS mineral, are well-documented in geological studies (Rickard and Luther, 2007). In environments characterized by strong reducing conditions, thiomolybdates exhibit preferential sorption to sulphide minerals, particularly amorphous FeS and pyrite, potentially overshadowing sorption to oxides (Smedley and Kinniburgh, 2017). The sorption behaviour of molybdate (MoO_4^{2-}) and tetrathiomolybdate (MoS_4^{2-}) onto pyrite (FeS_2) is influenced by pH, with maximum sorption occurring under acidic conditions (pH 4 to 5), analogous to oxides and clays (Freund et al., 2016). Notably, MoS_4^{2-} exhibits slightly weaker sorption compared to MoO_4^{2-}, especially at higher pH levels (Smedley and Kinniburgh, 2017). Notably, a $FeMoS_4$ phase with similar reactivity as pyrite has been identified, suggesting its potential role in elemental cycling (Cui et al., 2021; Vorlicek et al., 2018; Vorlicek and Helz, 2002). W species form strong inner-sphere complexes on pyrite surfaces and can incorporated into pyrite (Cui et al., 2021).

Observations in natural pyrite show contain Se, As, W, V, and Mo (Large et al., 2014; Manceau et al., 2020). Recent studies have shown that Mackinawite and Pyrite are capable of reducing V(V) to V(III) (Haase et al., 2024). Pyrite enhances V(V) sorption through both adsorption at acidic pH levels and coprecipitation mechanisms (Baya et al., 2022; Cui et al., 2023). Previous studies also reported experimental confirmation that pyrite can incorporate Se, As, V, and Mo within the thousand ppm wt. range (Baya et al., 2022; Guida et al., 2023; Pape et al., 2017). Experimental studies have shown that 'fresh' pyrites exhibit high adsorption reactivity towards As (Sun et al., 2012), Se(IV) (Kang et al., 2011; Mitchell et al., 2013), Re (Wang et al., 2020), and Tc (Rodríguez et al., 2020). However, Se(VI) shows very little reactivity.

Mackinawite has been studied in As(III) and As(V) sorption experiments. The results suggest that both forms of arsenic dominantly form an outer-sphere complex on the surface of FeS (Wolthers et al., 2005). Other studies have demonstrated the efficient removal of Tc(VII) (Livens et al., 2004), Re(VII) (Kilber et al., 2024) and Se(IV) (Scheinost and Charlet, 2008a) through sorption on mackinawite. This results in the reduction of Tc(VII) to Tc(IV), Re(VII) to Re(IV), and Se to Se(0). However, the reactivity of Se(VI) was low, although higher than that observed with pyrite (Han et al., 2011; Mitchell et al., 2013). Through co-precipitation, mackinawite shows high reactivity with Tc(VII) and Re(VII) (Wharton et al., 2000).

1.5 Oxyanion thiolation and the Hard and Soft Acid-Base (HSAB) theory

In the Hard and Soft Acid-Base (HSAB) theory, hard Lewis acids tend to combine with hard Lewis bases, and soft acids prefer soft bases. The hydrosulfide ion is categorised as a soft base, implying a natural tendency to form complexes with soft acids. Consequently, metals possessing soft acidic properties are expected to bind effectively with sulfur. The classification of ions of hard and soft acid or base is based on a variety of chemical properties (Wulfsberg, 1987), summed up into two parameters the Softness Misono parameter and the Absolute Hardness parameter proposed by Misono, 1967 and Pear & Pearson, 1983, respectively (Misono et al., 1967; Parr and Pearson, 1983). The Softness Misono parameter was derived from the relationship between charge (n), ionic radius (r_i), and the ionisation potential from the neutral atom to the given oxidised state (I_n). This parameter, denoted Y, is defined by the following equation:

$$Y = 10\left(\frac{I_n}{I_{n+1}}\right)\left(\frac{r_i}{\sqrt{n}}\right)$$

Oxyanions typically exhibit hard behaviour, as evidenced by their attraction to OH^- sites in oxide or hydroxide minerals (Sposito, 1981). However, it has been observed that the characteristics of these species are not homogeneous in phenomena such as sulfur-ligand, reduction, and precipitation when exposed to environments with high concentrations of sulfur without oxygen. The behaviour of these species in sulphide chemistry can be explained by the strength of the acidic character of the central metal. Figure 3 provides a comparison of the ionic radii, ionisation potential, and softness parameter (Y) values for metal ions involved in oxyanions of interest. The figure illustrates that Vanadium (V), Arsenic (As), Molybdenum (Mo), Tungsten (W), Technetium (Tc), and Re exhibit a less hard acidic character in their higher redox state compared to Chromium (Cr) and Se. This may explain why there is more experimental evidence and natural thiospecies occurrence for the former oxyanions than for Se and Cr. Thiolation can be explained as the result of a reaction between a hard acid (HA),

such as Se or Cr, bound to a hard base (HB), represented by O^{2-}, and a soft base (SB), represented by S^{2-} ions. The arrow indicates the direction in which the reaction is more favourable.

(1) $HAHB^{-}_{(aq)} + SB^{-}_{(aq)} \leftarrow HASB^{-}_{(aq)} + HB^{-}_{(aq)}$

(2) $SAHB^{-}_{(aq)} + SB^{-}_{(aq)} \rightarrow SASB^{-}_{(aq)} + HB^{-}_{(aq)}$

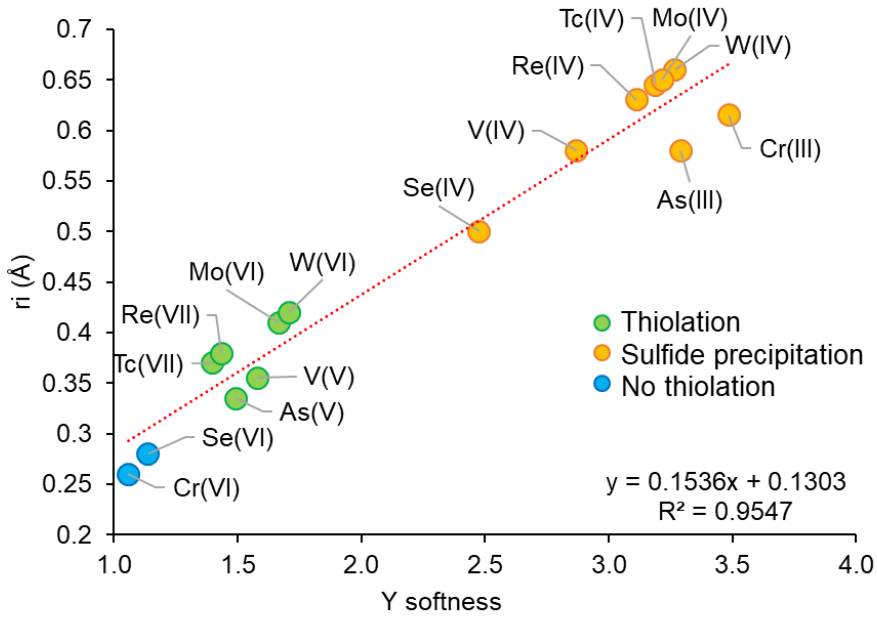

Figure 3 Comparative analysis of ionic radii and softness parameter (Y) values among metal ions in oxyanions and in sulfide precipitates (V, As, Mo, W, Tc, Re, Cr and Se).

The Hardness parameter is dependent on the ionisation potential and electron affinity values of each element. Currently, data on the electron affinity of trace elements relevant to this study are unavailable at different oxidation states, making it impossible to accurately calculate the Hardness parameter.

In general, the transition metals in the first row can be classified as hard acids that are most stable when complexed with first-row ligands of reactive non-metals, such as oxygen (Ahrland, 1973). Soft acids, typically second and third-row transition metals with a +1 or +2 charge and filled or nearly filled d orbitals available for π bonding, form stable compounds with second-row or subsequent row ligands, such as sulfur. However, chemical elements on the left side of the d-block in the periodic table tend to act as hard acids in their higher oxidation states (Pearson, 1963). While metals with high oxidation states tend to form oxyanions, the same metals with lower oxidation states have a softer acid character and thus tend to bind S.

The metals studied in this research fall within the borderline region between distinct O and S acceptors. This is partially due to the numerous oxidation states that lead to fluctuating chemistry. The higher oxidation states exhibit more O-binding character, which is consistent with the hard-hard bonding typically observed between M(V, VI,VII) (M=V, Re, Mo, W, Tc, Cr) and first-row ligands nitrogen N, O, or F. As is typical of hard acids, these metal ions bind more tightly to their electrons and have empty outer orbitals that are ready to accept electrons from π-donors such as N, O or F. Perrhenate, tungstate, and molybdate ions can bond with S, making them less hard than the other metals. Among the d-block elements investigated in this study, Cr, Tc, and V are the smallest, more compact and less

polarisable when compared to the other metals. According to HSAB theory, this makes them the most stable acceptors when complexed with hard O ligands, as the ionic radius is the primary parameter influencing the softness value. This physical property can explain why the O of the oxyanion species of these metals is not easily exchanged with the soft base S^{2-}.

All of the lower valence metals exhibit a softer character due to the extra d-electrons available to form dative π bonds, which are covalent bonds where one atom provides both electrons. Typically, to be classified as S acceptors, five electrons are required to remain in an outer shell and be more delocalised. As a result, they can easily donate electron density to ligands such as S. The sulfide metals that contain fewer sulfur atoms are the most stable. These sulfides coincide with the metals that have the lowest degree of oxidation. Generally, they are formed at high temperatures. The sulfides formed at low temperatures for Mo, W, V, and Cr precipitate in the form of MS_3, M_2S_3, and MS_4. For Re and Tc, they form M_2S_7 colloids. The reduction of these shapeless sulfides occurs quickly through likely intramolecular redox processes, followed by polymerization with the S species.

Se and As, elements of p-block, undergo multiple electron transfer reactions while Se(VI) and As(V) will be harder and prefer O bonds than Se(IV) and As(III). The higher valence state fits the parameters of a hard acid with its relatively small size and high charge. It will also follow the trends of hard acids, such as bonding with halides in the preferential order of I < Br < Cl < F (Juniku, 2004). At lower oxidation states (III or IV, respectively), the core is softer and will prefer soft base ligands as donors (Bandoli et al., 2006). Selenate (SeO_4^{-2}) has an ionic radius smaller than AsO_4^{-3} and less ionic charge density. Consequently, SeO_4^{-2} can be expected to follow the same HSAB trends as As(V) but with a stronger and harder base framework, and will accordingly react more readily with hard acids.

1.6 Conclusions

Previous research has demonstrated that certain oxyanions—MoO_4^{2-}, ReO_4^{-}, TcO_4^{-}, AsO_3^{3-}, AsO_4^{3-}, WO_4^{2-}, and VO_4^{3-}—are capable of sulfur substitution, resulting in the formation of thiometalate anions. Sulfur serves as a multidentate chelating agent, leading to the creation of stable and reactive metal-ligand complexes. Additionally, these compounds contribute to the formation of various sulfide minerals in environments abundant in sulfide. Iron sulfides, such as pyrite and mackinawite, exhibit high reactivity under reducing conditions, effectively adsorbing and incorporating elements such as Se, As, W, V, and Mo. The specific conditions required for the formation of thiometalate complexes, nanoparticles, or sorption complexes with iron minerals depend on the characteristics of the metal/metalloid and the sulfide-rich water environment. The stability or propensity of the metal/metalloid to bond with sulfur atoms can be predicted by applying the Hard and Soft Acid-Base (HSAB) theory. In this theory, transition metals exhibit varying acid character based on their oxidation state, with reducing species being softer and thus more compatible with the soft base sulfur. We also show that V, As, Mo, W, Tc and Re have a less hard acidic character in their higher redox state, when compared to Cr and Se suggesting why there is more experimental evidence and natural thiospecies formation for the first above-mentioned oxyanions than for Se and Cr. This understanding provides valuable insights into the behavior of metal-ligand interactions in sulfide-rich environments and offers a framework for predicting the formation of complex mineral species. Building upon this knowledge, the next chapter delves into the examination of these reactivity phenomena within an anoxic environment, contrasting two conditions: a low sulfidic system (ferruginous conditions) and a high sulfidic environments. Specifically, we investigate the reactivity of the oxyanions ReO_4^{-} and SeO_4^{2-} and compare their chalcophilic behavior with the lanthanide gadolinium. According to the HSAB theory, gadolinium's hard character renders this cation poorly reactive in sulfidic environments.

Chapter 2: Re speciation and reduction in anoxic waters

Rhenium geochemistry under sulfidic conditions: When does sulfide act as both ligand and reducing agent?

Carolina Guida [1,2,3], Anthony Chappaz [2], Alejandro Fernandez-Martinez[1], Nicolas Menguy[4], Damien Prieur[5], Andreas C. Scheinost[5] and Laurent Charlet[1]

[1] Univ. Grenoble Alpes, Univ. Savoie Mont Blanc, CNRS, IRD, Univ. Gustave Eiffel, ISTerre, 38000 Grenoble, France

[2] STARLAB, Central Michigan University, Mount Pleasant, Michigan, U.S.A.

[3] Grupo geología médica y forense, Universidad Nacional de Colombia. Apartado Aéreo, Bogotá, Colombia.

[4] Sorbonne Université, Muséum National d'Histoire Naturelle, IRD, Institut de minéralogie, de Physique des Matériaux et de Cosmochimie (IMPMC UMR CNRS 7590), F-75005, Paris, France.

[5] The Rossendorf Beamline at ESRF, 71 Avenue des Martyrs, 38043 Grenoble, France and HZDR Institute of Resource Ecology, 01328 Dresden, Germany.

Correspondence and requests for materials should be addressed to AC (email: anthony.c@cmich.edu) or to LC (email: charlet38@gmail.com)

Abstract

The critical element, Rhenium (Re), is highly soluble as perrhenate ion (VII) - ReO_4, and little soluble in reduced form as rhenium (IV) oxide - $ReO_{2(s)}$ or rhenium (IV) sulfide $ReS_{2(S)}$. The mechanism leading to the Re deposits is not precise, but critical to explain the Re cycle in Earth's history and present-day engineering processes. In sulfide presence, the oxyanion perrhenate is transformed by a step-wise O atom substitution by S atoms, forming thioperrhenate species ($Re(VII)O_{4-x}S_x^{-}$), and then Re is reduced, but the latter pathway is unknown. Using different spectroscopic methods such as UV-vis, XANES, and EXAFS on liquid samples, and XRD, DLS, and TEM on solid samples, we show that Re, after being thiolated, is reduced to form Re(IV)-S nanoparticles, whose kinetics and morphology depends on the Re initial concentration and the initial pH. This research enhances our understanding of Re as a redox proxy and the effectiveness of recovering Re from wastewater, hydrometallurgical solutions, or sulfide ores.

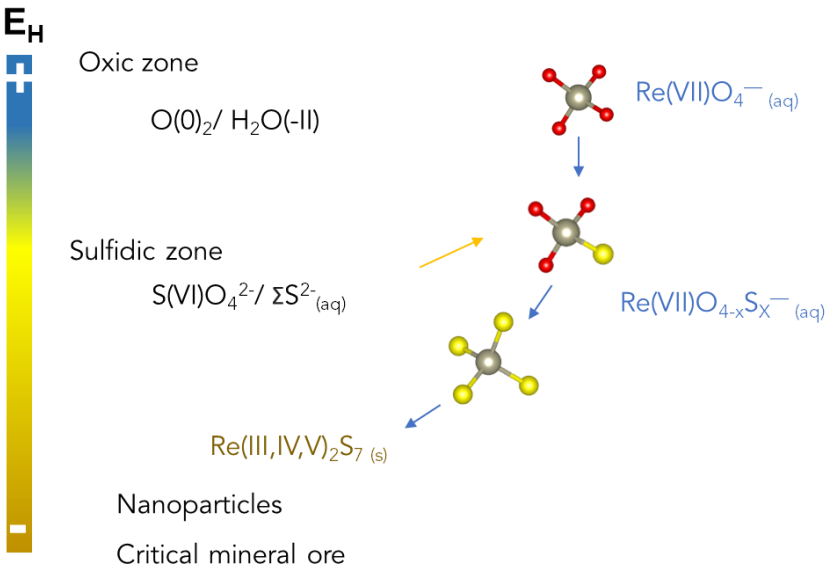

2.1 Introduction

The oxygen-sulfur interface is a fascinating world with implications from the ancient past to the present day (Lu et al., 2020; Pósfai and Dunin-Borkowski, 2006). Understanding sulfur chemistry is crucial for gaining insights into ancient environments, oceanic and atmospheric chemistry, the origin of life, the ore mineral formation, critical element technological uses (Graedel et al., 2022) and climate change (Grégoire et al., 2021). In modern times, oxygen depletion and rising sulfide levels are common in water bodies, such as the coastal and open oceans or dam reservoirs, in response to global eutrophication and hypoxia. These changes are often lethal to aquatic life and can disrupt biogeochemical cycles (Grégoire et al., 2021). In cellular redox chemistry, sulfide ligand affinity is critical in biological pathways for cellular functioning and the survival of life in the aggressive oxidizing environmental conditions of the present-day Earth (Palumaa, 2009). Besides, sulfide is also relevant in constructing molecule libraries for functional materials, chemical biology, and drug discovery (Cao et al., 2020; Del Corso et al., 2002; Fang et al., 2018).

Rhenium (Re) is a highly valuable and critical metal in various high-tech industries (Shen et al., 2021a) due to its exceptional properties, including a high melting point (3182 °C), density (21.02 $g.cm^{-3}$), and resistance to heat and wear (Lunk et al., 2021; Neikov et al., 2019). It is mainly mined in Chile, the United States, and Poland. Recovered from dust in lead smelters and from copper mining (Lunk et al., 2021), global annual production is around 50 tons. Historically expensive due to limited availability, recycling efforts have contributed to a reduction in price, with about 28 tons recycled in 2022, with the United States as a leading producer (Graedel et al., 2022; Polyak, 2023). Re is mainly used in nickel-based superalloys between 3 to 6%, constituting 80% of production, enhancing strength and preventing creep failure at high temperatures (Lunk et al., 2021; Wu et al., 2022). Additionally, it serves as a catalyst, with applications like bimetallic platinum-rhenium catalysts in petroleum reforming for lead-free gasoline production. Re finds also extensive applications including enhancing other alloys, in diverse electronic devices (Neikov et al., 2019), photodetectors and photocatalysis for water, making it a potential candidate for clean energy production (Hämäläinen et al., 2018; Liu et al., 2016).

In medicine, the biocompatibility of Re holds great capability for different uses in implants(Lunk et al., 2021), diagnosis[15] and treatment of various cancers (Tu and Denizot, 2007). This

significance is due to the ^{188}Re (half-life 17 h) and ^{186}Re (half-life 89 h) radioisotopes properties and to the Re resemblance in charge and size between iodate and the radioactive and hazardous pertechnetate ions used in diagnosing and treating thyroid cancer (Dadachova et al., 2002; Shinto and Knapp, 2017; Zuckier et al., 2004). These artificial isotopes emit beta particles effective in targeting and destroying tumour cells, particularly those up to 2 mm in solid tumours (Lunk et al., 2021), while also emitting gamma particles suitable for imaging.

Re can provide information about oxidation reactions during chemical weathering (Dellinger et al., 2020; Hilton et al., 2014; Zondervan et al., 2023) and the extent of low-oxygen depositional environments in lakes and oceans (Bennett and Canfield, 2020; Dickson et al., 2020; Helz, 2022; Helz and Adelson, 2013; Sheen et al., 2018) similar to Mo, a widely recognized paleo-redox proxy (Hlohowskyj et al., 2021a; Vorlicek et al., 2015). Re is a trace metal sensitive to redox conditions with a high affinity to sulfide ions. In geological depositories, the highest Re concentrations are found in sulfide-rich euxinic settings in black shales (Brumsack, 2006) as a reduced form. To explain how Re is transformed from the geochemically inert perrhenate ($Re(VII)O_4^-$) anion, present at concentrations of approximately 40 pM (Anbar et al., 1992) in modern oxygenated oceans, to reduce sulfide minerals, the geochemical pathway involves not only metal precipitation but other preliminary phenomena. When sulfide is present in solution, the oxyanion perrhenate transforms in two steps. The O atoms surrounding the Re can be substituted by S atoms, forming presumable via ligand substitution thioperrhenate species ($Re(VII)O_{4-x}S_{x-}$)(Helz and Dolor, 2012; Müller et al., 1981; Tossell, 2005). Subsequently, sulfur reduces Re and precipitates it in particulate sulfide forms. Although numerous studies have explored Re thiolation and the characterization of rhenium sulfides, yet the transition from thiolation species to solid crystallization remains unclear. Existing research on the synthesis and properties of various Re sulfides (Re_2S_7, ReS_4, ReS_3, ReS_2) deviates from neutral natural conditions; for instance, Re_2S_7 precipitates in highly acidic environments (Briscoe et al., 1931; Hibble and Walton, 1996), and ReS_2 forms at elevated temperatures (Brauer, 1975). The exact nature and structures of heptasulphides are controversial and unknown, and information regarding the kinetic dependence of particle size growth on pH or Re/S saturation is absent.

In our study, we prepare solutions with different concentrations of Re (range between 5 to 22.2mM) and a high sulfide concentration (100 and 500mM) at three initial pH: 6, 7, and 8. Re(VII) is gradually thiolated and precipitated by S atoms, forming $Re_2S_{7(s)}$ particles. We observe that nucleation occurs just after starting the ligand exchange process. We characterize for the first time the reduction pathway and grow Re-S nanoparticles from a few nanometers to tens of nanometers. The discovery of this reaction pathway helps to expand our understanding of the geochemistry of the sulfur-rhenium system and the stability and bioavailability of rhenium species in past and present natural environments, as well as in environments relevant to clean energy production, electronic, pharmaceutical, biological, and recycling and mining industries. Furthermore, by considering the reductive mineralization of Re on a near-atomic scale level, this work opens the field to new studies in trace elements crystallization in highly oversaturated sulfidic environments.

2.2 Results

2.2.1 Re speciation in sulfidic water: thiolation without reduction

2.2.1.1 pH effect

Previous works study the possibility of sulfur ligand exchange to dictate Re speciation in sulfidic waters (Helz and Dolor, 2012; Müller et al., 1981; Tossell, 2005; Vorlicek et al., 2015). Procedures to investigate the substitution of O by S atoms in perrhenate molecules include UV-vis spectra (Helz and Dolor, 2012; Tossell, 2005) and, in a sophisticated and more precise way, reverse phase ion pair chromatography (RC-IPC) (Vorlicek et al., 2015). In the present study, we employed UV-vis spectra to corroborate the thioperrhenate species formation in comparison with previous experimental (Helz and Dolor, 2012) and theoretical (Tossell, 2005) measurements in which two kinetically stable species were identified: ReO_3S^- and ReS_4^-. A solution with 5mM Re concentration and 100mM $\sum S^{2-}$ is a suitable experimental condition to follow the thiolated species formation over time (Figure S 1). In 5 mM Re solutions, absorbance increases at wavelengths 298, 350, and 505 nm, similar to previous studies (Helz and Dolor, 2012). The formation of ReO_3S^- species measured at 298 and 350nm precedes ReS_4^-, followed at 505 nm. After 1 week, all baseline UV-vis spectra present a slope and lifting characteristic of light scattering due to colloid formation (Helz and Dolor, 2012) with a more pronounced effect observed at pH 6 and 8.

The concentrations of ReO_3S^- and ReS_4^- appear to be influenced by pH. The abundance of thio species increased significantly one week after preparation at pH 6, compared to pH 7 and 8. The evidence of this was provided by absorbance measurements in the three spectrum picks. UV-vis spectra at pH 8 exhibited lower absorbances in comparison to pH 6 and pH 7. Temporal variations were present in the pH solution as well (Figure S 2). The sample initially stabilised at pH 6 showed the most significant increase (pH 7.0), reflecting a difference of 0.9 units. The solutions that were originally pH 7 and pH 8 were raised to pH 7.4 and 8.6, with a difference of 0.4 units for pH 7 and 0.5 units for pH 8.

2.2.1.2 Influence of S:Re molar ratios

To assess the impact of varying concentrations and ratios of sulfur and rhenium species on thiolation reactions, we meticulously prepared eight distinct solutions. Systematic adjustments were made in ratios of S^{2-} and ReO_4^- concentrations, ranging from 0.5 to 50. All solutions were adjusted to an initial pH of 7, and the equilibration period was set at one week. Figure 4 displays the UV-vis spectra of each solution. The solution with a 0.5 ratio exhibited no speciation. A distinctive peak at 298 nm was observed in the 1:1 ratio UV-vis spectra which suggests primarily ReO_3S^- production. Solutions with ratios between 5 and 20 displayed three distinct peaks associated with thioperrhenate species, with a ratio of 20 exhibiting the highest absorbance peaks. In contrast, solutions containing 10, 20, and 22.2mM of Re, mixed with 500mM S^{2-}, exhibited strong absorption across all UV-vis wavelengths. This intense absorption rendered the identification of thiolated species peaks impossible. Regarding pH, interestingly, a significant increase is identified for solutions with a radius of more than 20. The final pH for these solutions varied between 9.3 and 11.1 unities.

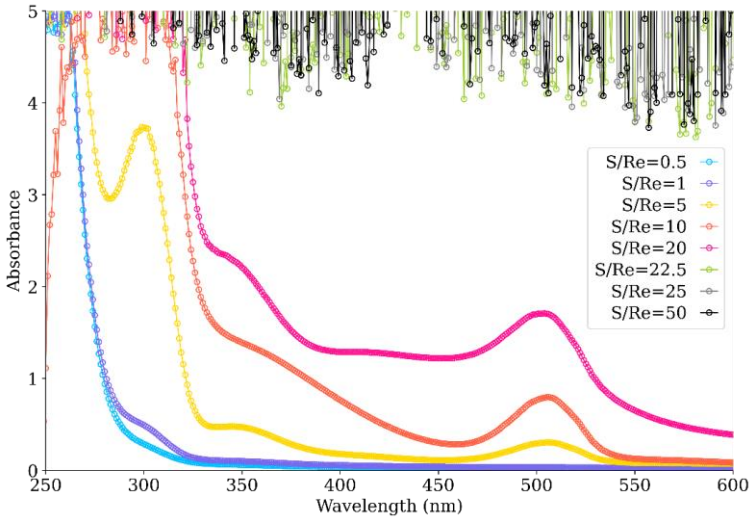

Figure 4 The UV-vis spectra were recorded at various equilibrium times following the reaction between 0.005 to 0.0222 M $NaReO_4$ and 0.005 to 0.5 M $Na_2S{\cdot}9H_2O$, with the initial pH adjusted to 7. The analysis revealed three distinct absorption peaks, providing clear evidence for the formation of thioperrhenate species. Specifically, peaks were observed at 298 and 350 nm, corresponding to ReO_3S^-, and at 505 nm, indicative of ReS_4^- formation. Those wavelengths agree well with previously published theoretical and experimental studies.

2.2.2 XANES and EXAFS results: Re reduction by -HS ligands

X-ray absorption near-edge spectroscopy spectra (XANES) at the Re L-III edge is a diagnostic tool to assess the symmetry and coordination of Re ions. Furthermore, it has a high sensitivity to changes in oxidation state, which allows it to distinguish between Re(IV) and Re(VII) states. Figure S 3 displays the reference fingerprints used to interpret sample spectra. Between all references studied, the reference XANES spectra white line for Sodium Pherrenate (VII) ($NaReO_4$) shifts by 1.5 eV compared to standard Rhenium oxide (IV) (ReO_2), by 2.6 eV compared to ET_4NReS_4-(VII) and by 3.1 eV to ReS_2-(IV) powder. Another XANES feature that can distinguish Re cluster coordinates with S or O atoms is the width of the peak and its general shape. The peak becomes narrower when Re is reduced and bonds with an S.

Following the synthesis proposed in previous studies (Bernhardt and Herbst-Irmer, 2020; Wiley and Sons, 2002), we synthesized Et_4NReS_4 and Re_2S_7 as XANES and EXAFS references. For Et_4NReS_4 XANES calculation was performed with the Finite Difference Method Near Edge Structure (FDMNES) code (Bunău and Joly, 2009; Guda et al., 2015) using the CIF published by Bernhardt and Herbs-Irmer (2020) and was compared to Et_4NReS_4 spectra (Figure S 4). In general, XANES characteristics indicate a white energy line of two references (for Re_2S_7 10539.1 eV and 10539.8 eV for Et_4NReS_4) similar to ReS_2 (10539.6 eV) but with a broader and slightly different peak shape.

Alternately, the Fast Fourier transform (FFT) of Extended X-ray Absorption Fine Structures (EXAFS) spectra for the standard materials revealed information about the distance and coordination number that allows us to identify the local chemistry of the solutions analyzed. Table S1 contains data about the crystal structure of the reference compounds collected from various bibliographic sources. We observed a shorter length of 1.7Å is present for Re(VII) coordinated with 4 oxygens, followed by 2.0Å for Re(IV) coordinated with 6 oxygens (Wharton et al., 2000). For sulfide references, the longest distance of 2.3Å is for Re(IV), Re(V) and Re(VI) coordinated with 6 sulfides for ReS_2, ReS_4 and Re_2S_7 (Hibble and Walton, 1996; *Materials Data on $NaReO_4$ by Materials Project*, 2020; Schwarz et al., 2004; Wharton et al., 2000). The Re-S bond distance for the only reference with four-sulphur atoms coordinated Re(VII) (ET_4NReS_4) is 2.1Å (Bernhardt and Herbst-Irmer, 2020).

Table 2 EXAFS Parameters and interatomic distances calculated for Re(VII) and HS— solution samples.

Sample	Path	N [a]	R [b] [Å]	σ^2 [c] [Å^2]	ΔE_0 [d] [eV]	S_0^2 [e]	R-factor
5mM_pH7_1w / S/Re=20	Re-O.1	4.2 (0.5)	1.71 (0.009)	0.003[a]	9.4[a]	1[a]	0.09
R-range: 1.15:4							
5mM_pH7_3w	Re-O.1	3.7 (0.5)	1.71 (0.010)	0.003[a]	9.9[a]	1[a]	0.07
R-range: 1.15:4							
5mM_pH7_5w	Re-O.1	3.9 (0.4)	1.71 (0.008)	0.003[a]	9.6[a]	1[a]	0.07
R-range: 1.15:4							
10mM_pH6_1w	Re-O.1	3.6 (0.4)	1.7 (0.008)	0.003[a]	9.9[a]	0.9[a]	0.07
R-range: 1.15:4							
10mM_pH6_5w	Re-O.1	1.6 (0.8)	1.7 (0.038)	0.003[a]	3[a]	1[a]	0.07
R-range: 1.15:4	Re-S.1	2.3 (0.5)	2.3 (0.502)	0.003[a]	3[a]	1[a]	
	Re-Re.1	1.8 (1.0)	2.7 (0.964)	0.003[a]	3[a]	1[a]	
10mM_pH7_1w / S/Re=50	Re-O.1	0.6 (0.6)	1.7 (0.073)	0.003[a]	7.3[a]	0.8[a]	0.07
R-range: 1.15:4	Re-S.1	3.9 (0.6)	2.4 (0.011)	0.003[a]	7.3[a]	0.8[a]	
	Re-Re.1	1.8 (1.2)	2.8 (0.039)	0.003[a]	7.3[a]	0.8[a]	
10mM_pH7_5w	Re-O.1	1.3 (1.0)	1.6 (0.060)	0.003[a]	4.2[a]	0.8[a]	0.07
R-range: 1.15:4	Re-S.1	2.6 (2.2)	2.2 (0.063)	0.003[a]	4.2[a]	0.8[a]	
	Re-S.2	2.2 (2.0)	2.4 (0.087)	0.003[a]	4.2[a]	0.8[a]	
	Re-Re.1	1.9 (1.8)	2.7 (0.056)	0.003[a]	4.2[a]	0.8[a]	
10mM_pH8_1w	Re-O.1	1.3 (1.0)	1.6 (0.060)	0.003[a]	1.4[a]	1[a]	0.04
R-range: 1.15:4	Re-S.1	2.6 (2.2)	2.2 (0.063)	0.003[a]	1.4[a]	1[a]	
10mM_pH8_5w	Re-O.1	1.7 (0.4)	1.7 (0.019)	0.003[a]	5.2[a]	1[a]	0.04
R-range: 1.15:4	Re-S.1	2.6 (0.4)	2.4 (0.011)	0.003[a]	5.2[a]	1[a]	
	Re-Re.1	0.9 (0.8)	2.8 (0.054)	0.003[a]	5.2[a]	1[a]	
S/Re=22.5	Re-O.1	2.6 (0.3)	1.7 (0.009)	0.003[a]	3[a]	0.8[a]	0.04
R-range: 1.15:4	Re-S.1	2.7 (0.3)	2.3 (0.007)	0.003[a]	3[a]	0.8[a]	
	Re-Re.1	0.5 (0.5)	2.7 (0.066)	0.003[a]	3[a]	0.8[a]	
S/Re=25	Re-O.1	1.3 (0.4)	1.7 (0.027)	0.003[a]	3.7[a]	0.8[a]	0.02
R-range: 1.15:4	Re-S.1	4.2 (0.9)	2.3 (0.009)	0.005 (0.001)	3.7[a]	0.8[a]	
	Re-Re.1	1.8 (0.8)	2.8 (0.025)	0.003[a]	3.7[a]	0.8[a]	
Nanoparticles	Re-S.1	4.0 (0.3)	2.3 (0.006)	0.003[a]	2.5[a]	0.7[a]	0.02
R-range: 1.25:3	Re-Re.1	1.4 (0.8)	2.8 (0.037)	0.003[a]	2.5[a]	0.7[a]	
Re_2S_7	Re-S.1	3.6 (0.2)	2.4 (0.004)	0.003[a]	7.3[a]	0.7[a]	0.02
R-range: 1.65:4	Re-Re.1	2.0 (0.5)	2.8 (0.015)	0.003[a]	7.3[a]	0.7[a]	
ET_4ReS_4	Re-S.1	4[a]	2.3 (0.008)	0.004 (0.001)	10[a]	0.7[a]	0.04
R-range: 1.55-3							
ReS_2	Re-S.1	6[a]	2.4 (0.007)	0.003[a]	4.7 (0.9)	0.7[a]	0.01
R-range: 1:3	Re-Re.1	3[a]	2.8 (0.012)	0.003 (0.001)	4.7 (0.9)	0.7[a]	
$NaReO_4$	Re-O.1	3.6 (0.1)	1.7 (0.009)	0.003 (0.001)	8.5[a]	0.8[a]	0.05
R-range: 1.1:3	Re-O.1	2.0 (0.5)	3.0 (0.056)	0.009 (0.010)	8.5[a]	0.8[a]	

[a]Coordination number for single paths. [b]Interatomic distance. [c]Debye−Waller factor, fixed value. [d]Shift of energy threshold, fixed value. [e]Passive electron reduction factor, fixed value.

Samples prepared with 10 mM Re show a noticeable presence of colloids. These colloids, as discussed below, have nano sizes which cannot be removed by filtration with 0.22 nm filters or

centrifugation. For the interpretation of the XANES and EXAFS spectra, we considered the proportion of colloids that flocculated after adding 40 mM $MgCl_2$. Interpreting XANES spectra (Figure 5), in samples containing less than 30% nanoparticles, the solution signal is predominant. When the colloidal concentration is between 30% and 70%, the spectra show a combination of signals. However, when the concentration exceeds 70%, the solid signal becomes dominant. The references used as representatives of aqueous species are $ET_4NReS_{4(s)}$ and $NaReO_{4(s)}$. In solutions where colloids are predominant, the $Re_2S_{7(s)}$ reference is typically used. We do not consider $ReS_{2(s)}$ as it forms at high temperatures, which is not the case in our experiment.

The end-product at 1, 3 and 5 weeks in sulfide super saturated liquid samples with 5, 10, 20 and 22.2 mM Re concentrations were analyzed from Re L_3-edge XANES and EXAFS. For 5 mM Re and 100mM $\sum S^{2-}$ solution samples at 1, 3, and 5 weeks of equilibrium time, XANES (Figure S 5) and EXAFS (Figure S 6) spectroscopy showed mostly similar white line and form features with $NaReO_4$ reference and coordination with O atoms. The application of linear fitting combinations to the reference material yielded no successful results. However, the XANES features analysis qualitatively may indicate progressive ligand exchange by hydrosulfide ions rather than just a reduction to Re(IV), as evidenced by the samples with the highest equilibrium time and S/Re ratio shift to the left and shape peak with similarities to Re-S references. In contrast, the optimal fit for the FFT of the 5mM samples indicates only coordination with oxygen atoms, as observed in $NaReO_4$ powder (Table 2).

The XANES results show no reduction for 1 week at all pH and all times pH6. More ReS_4^- formation can be observed for pH6 samples with longer periods. Samples adjusted at pH 7 and 8 after 3 weeks seem to have been reduced and coordinated with sulfur atoms. The FFT of the EXAFS spectra for these samples support an increasing Re coordination to sulfur atoms over time and show dependence on the initial pH and sulfide to Re(VII) concentration ratio (Figure S 7). The Re–S bond distance determined in this study (2.2-2.4 Å) is similar to that reported in the literature for $Re_xS_{x(s)}$ minerals (2.3-2.4 Å, respectively). Like XANES results, the samples equilibrated at 5 weeks and adjusted at pH7, pH6, and pH8 show more coordination with sulfur than oxygen atoms. For pH7 sample, the coordination number and interatomic distance are similar to those observed for $Re_xS_{x(s)}$ solids (Table 2).

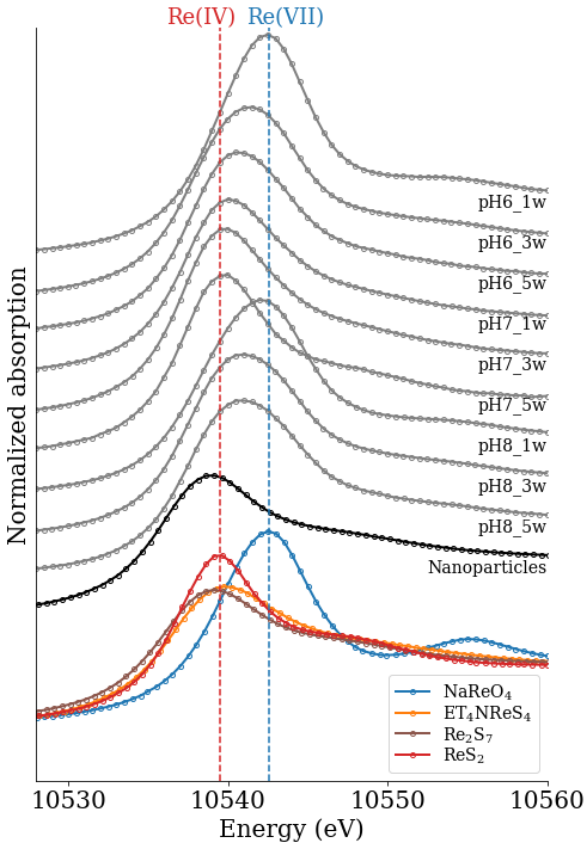

Figure 5 Rhenium L_3-edge XANES for samples with 10mM ReO_4^- and 500mM S^{2-} with three equilibration periods: 1, 3 and 5 weeks. Spectra of Re experiments at pH6, pH 7, pH8 (gray lines), the nanoparticles floculated after 5 weeks (black line) and the standard spectra used for analysis (blue, orange, brown and red lines).

Four samples with varying S/Re ratios were equilibrated at pH7 and analyzed using XANES and EXAFS spectroscopy. The results of the EXAFS analysis, like those of the XANES analysis, indicate that the reduction and complexation kinetics of the Re-S system are significantly influenced by the S/Re ratio (Figure S 8). Figure 6 displays the EXAFS results, showing a higher S/Re ratio with more sulphur atoms coordinated to the central Re atom. All of the samples analysed in this study contain less than 30% nanoparticles, except for the sample with an S/Re ratio of 25, which has 37%. Additionally, this sample exhibits a more rapid increase in pH level after three days than the other samples (refer to Figure S 2).

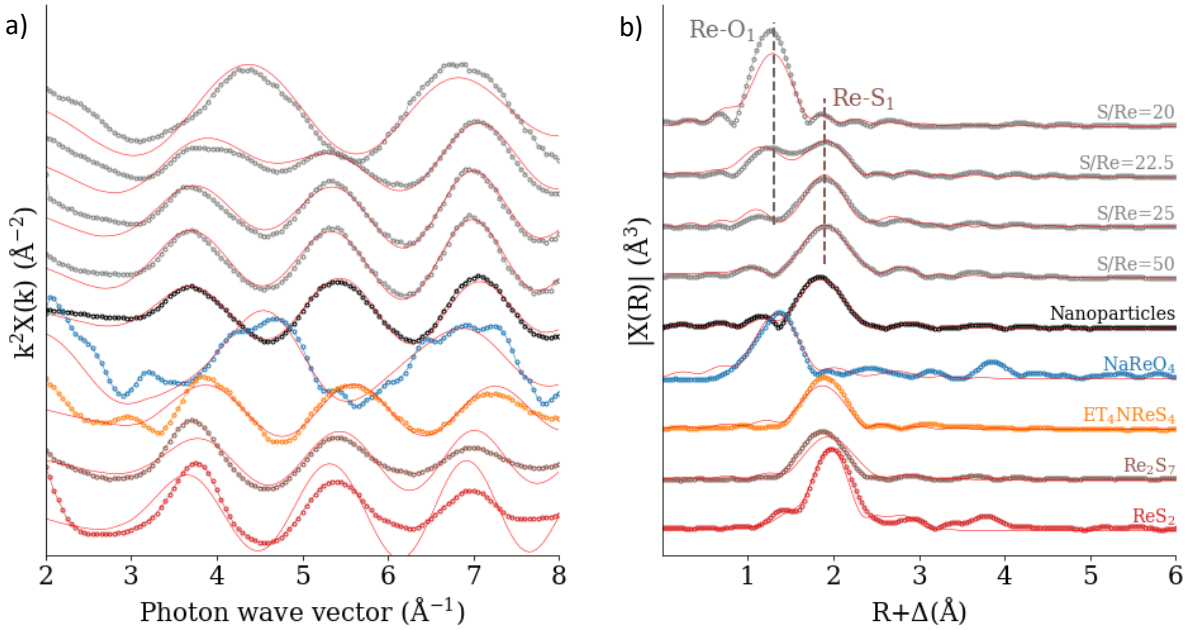

Figure 6 a. Rhenium L-III-edge k_2-weighted chi functions EXAFS spectra (a) and its Fourier transform magnitudes (b) of 5 (S/Re=50), 20 (S/Re=25), 22.5 (S/Re=22.2) and 10mM (S/Re=20) Re(VII) sulfide solutions. All solutions were equilibrated at pH=7 and were measured at 1 week.

2.2.3 Perrhenate thiolation and Re sulfide nucleation

2.2.3.1 Nanoparticle flocculation

Inorganic rhenium sulfide polymers are small and hydrophilic, allowing them to pass through 0.02 µm filters. According to Helz and Dolor (2012), these polymers can remain suspended in solutions for extended periods, depending on experimental conditions. The colloids were flocculated using $MgCl_2$, and the measurements of the remaining Re in solution for the experiments with 5 mM (S/Re=20) and 10 mM Re (S/Re=50) are presented in Figure S 9.

The formation of colloidal particles is affected by the starting pH, S/Re ratio, and ionic strength. The percentage of nanoparticles present at different S/Re ratios varied in pH7 solutions that were allowed to equilibrate for one week: 6% at 20 (µ=0.30 mol/L), 27% at 22.5 (µ=1.09 mol/L), 37% at 25 (µ=1.08 mol/L), and 15% at 50 (µ=1.07 mol/L). A larger percentage of nanoparticles was observed in solutions with a higher ionic strength. Experiments with a S/Re ratio of 20 showed minimal Re consumption (less than 1.2 mM in 5 weeks) during colloid formation compared to S/Re=50 samples. At an S/Re ratio of 20, it seemed that pH 7 and 8 produced more particles than pH 6. However, the observed pH differences are within the margin of error. After five weeks, around 70% of the total rhenium was consumed at pH values 7 and 8, whereas only 14% was consumed at pH 6. Particle production ceased one week later at this pH.

2.2.3.2 XANES and EXAFS

The redox state and atom coordination of amorphous nanoparticles were determined by analysing XANES and EXAFS measurements (Figure 5). The sample exhibits identical XANES features when compared with the Re_2S_7 reference. The flocked colloids appear to share a chemical environment with Re_2S_7, which, according to previous studies, presents an oxidation state between 3.5, 4, and 5

(Hibble and Walton, 1996; Schwarz et al., 2004). The EXAFS spectra show an interatomic distance of Re-S_1 path to 2.3 and 4-coordinate sulfur atoms in the first shell.

2.2.3.3 DLS measurements

Dynamic light scattering (DLS) was used to identify and characterise the morphology of Re particles. The study analysed 10 mM Re samples at initial pH values of 6, 7, and 8 (refer to Figure 8) and three solutions with varying $\sum S^{2-}/ReO_4^-$ ratios (refer to Figure S 10). Nanoparticles were formed and their hydrodynamic size was found to be dependent on the initial pH. After 5 weeks, all three solutions showed a slightly wider nanoparticle size distribution (24-75 nm). At pH 6, the distribution was achieved more rapidly, as observed after 3 weeks. The smallest particle sizes were observed at a S/Re ratio of 50, which also resulted in the lowest percentage of suspended solids post-flocculation (15%).

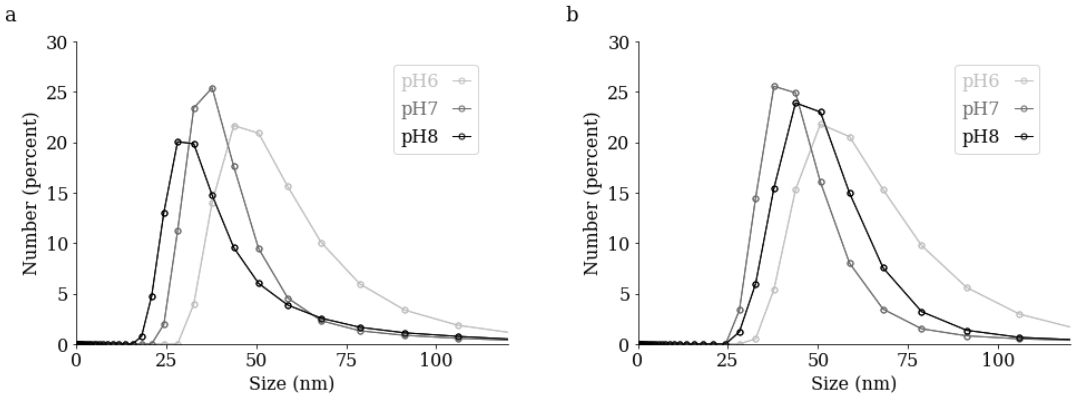

Figure 7 Results of number distribution after dynamic light scattering (DLS) analysis to determine the hydrodynamic size of nanoparticles formation at different times and initial pH. The samples measured correspond to three reactors: 10mM ReO_4^-, 500mM $\sum S^{2-}$ and 100mM NaCl with an initial pH of 6, 7, and 8. The measurements in panel a) are taken after 3 weeks, while in panel b) they are taken after 5 weeks equilibrium time.

2.2.3.4 TEM observations

The nanoparticles of rhenium sulfide were analysed after being deposited on a TEM grid and flocculated with 30 mM $MgCl_2$ using Scanning Transmission Electron Microscopy (STEM) and Field Emission Scanning Electron Microscopy (FESEM), respectively. A nanoscale particle was observed in TEM, with an interatomic distance of 2.3 Å between two rows of atoms. This value corresponds to the sulfur-to-rhenium distances found in Re_2S_7, ReS_4, and ReS_2 crystal structures (Table S1). The FIB-SEM images showed that the Re-S particles, precipitated with $MgCl_2$, formed thick flakes that were randomly oriented concerning the substrate plane. These aggregates had a 2D structure deposition on a substrate that corresponds to NaCl and $Mg(OH)_2$ crystals, as identified through XRD and PDF analysis.

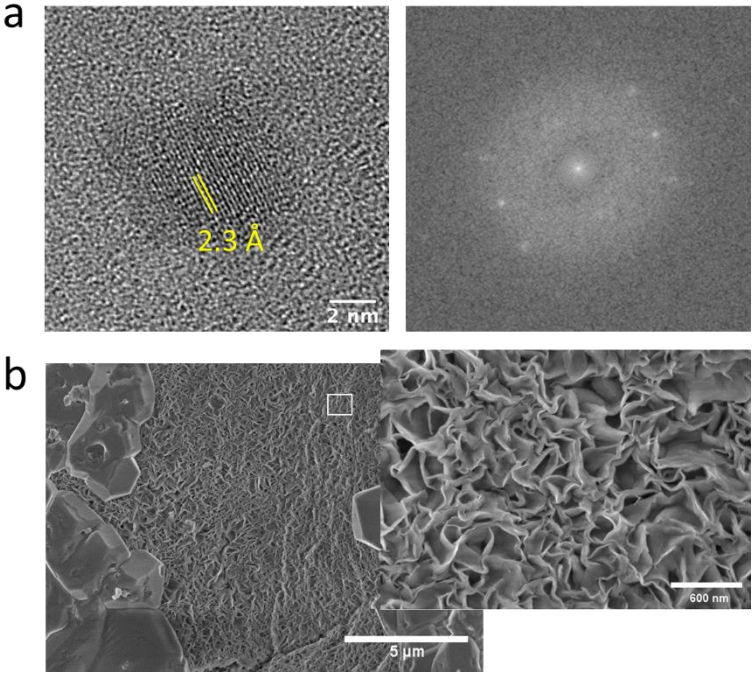

Figure 8 Rhenium sulfide nanoparticles deposited in two ways to microscopy imaging observations. a) TEM image of a nanoparticle after evaporation of a 10mM Re thiolation solution at an initial pH of 7 following a 5-week equilibrium period. b) FESEM images of rhenium sulfide nanofilms after flocculation and precipitation with 30mM $MgCl_2$.

2.3 Discussion: Removal mechanism of Re(VII) in sulphidic water

XANES, EXAFS, DLS, and TEM results allow us to study the Re_2S_7 nanophase formation mechanism, including step-wise valence state and morphological transition from $Re(VII)O_4^-$ ligand exchange and reduction by sulfide ions. We evidenced that sulfide replaces oxygen in $Re(VII)O_4^-$ molecule to form $Re(VII)S_{4-x}O_x^-$ species, while $Re(VII)S_2O_2^-$ and $Re(VII)S_3O^-$ UV-vis spectra did not detect and are probably metastable species. After thiolation, sulfur and rhenium precipitate together, and Re(VII) is reduced to Re(V), Re(IV) or Re(3.5). How fast the nanoparticles form seems to depend on the formation of the thiometalate species, and both phenomena depend on the initial experimental conditions, such as pH, rhenium-to-sulfur concentration ratio and ionic strength.

The transformation rates of thiolation species were highly pH-dependent and increased with increasing solution pH. Among the three pHs studied, we observed that Re ligand exchange and reduction of the more concentrated solution is fast at pH=7 and pH=8 but does not occur at pH=6. However, the thiolation and growth of the nanoparticles were faster at pH=6. We know that the solution should have low OH^- ions to form thiolation (Harmer and Sykes, 1980), and thus high concentrations of H^+. The H^+ protonates oxygen atoms within the oxyanion and assists the thiolation and reduction processes, in which an OH^- is substituted by a nucleophilic HS^-. As H_2S pK_a is 6.99, the solution below pH=7 becomes saturated with H_2S, and part of sulfur is volatilized, leading to less HS^- present to react with ReO_4^-. That is confirmed by the saturation index of $H_2S_{(g)}$ computed by Phreeqc code. Thus an optimum pH between 6 and 7 is observed for perrhenate thiolation, where H_2S degassing and OH^- competition are limited. Regarding the second factor that plays a role in rhenium sequestration, we identified that the higher the sulfur concentration and the lower the perrhenate concentration, the faster the Re is reduced and the particles are formed. The Re(VII) reduction mechanism is probably associated with reactive thioperrhenate species, which sulfide can more easily further reduce. Previous research indicates that the rhenium chalcogenide cluster may have a

structure consisting of the metal with a mixture of possible sulphur oxidation states, including S_X^{2-} polysulphide and disulphide ligands S_2^{2-}, following an internal redox process. Therefore, a new pathway could be introduced for the Re-S particle formation in a system at low temperatures in aqueous solutions:

(1) $ReO_4^-{}_{(aq)} + HS^-{}_{(aq)} + H^+ \rightarrow ReO_3S^-{}_{(aq)} + H_2O$

(2) $ReO_3S^-{}_{(aq)} + 3HS^-{}_{(aq)} + H^+ \rightarrow ReS_4^- + 3H_2O$

(3) $H^+ + 2\ ReS_4^- \rightarrow Re_2S_7 + HS^-$

Observations of crystalline growth from solution suggest that crystallisation occurs through particle attachment (De Yoreo et al., 2015). Small nanoparticles were detected through DLS, FIB-SEM, and TEM measurements, followed by stable prenucleation cluster aggregation and subsequent 2D film particle crystallization. A correlation was observed between the initial pH, the ionic strength, and the free energy barrier for solid nucleation. The kinetics of Re-S nanoparticle formation can be increased at higher alkaline pH levels and ionic strength, as the system can reach the energy barrier more rapidly. On the other hand, in acidic pH, the Re_2S_7 nanoparticles seem to aggregate faster (Figure 9).

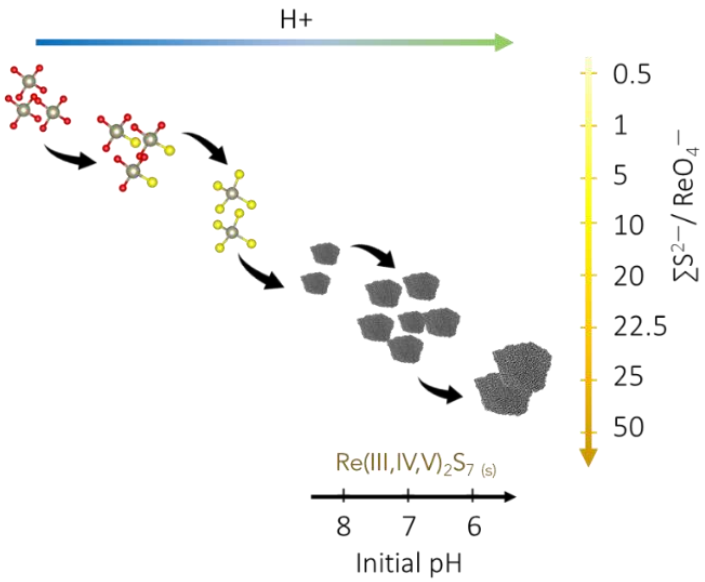

Figure 9 Conceptual model of Re(VII) thiolation and reduction by HS^-

2.4 Environmental, engineering and medical implications

In deep waters without oxygen, such as the Black Sea (Colodner et al., 1995; Helz, 2022), rhenium concentrations decrease with depth. Solid Re is commonly found in sulfide mineral ores, such as the reduced-mineralized Kupferschiefer in Poland, which may have originated from sulfide precipitation in the deep anoxic waters of the ancient Zechstein Sea (Foltyn et al., 2022). Previous articles have identified a high concentration of Re correlating with high levels of Fe and total organic carbon in rock nuclei with an age of 2495 ± 14 Ma (Kendall et al., 2015). Given that the Proterozoic oceans were rich in sulphur it is highly likely that the origin of Re in these sediments is due to the chemistry of extreme sulphidic environments. The reported findings, which include the observation of the transient valence state and thick flake structure, enhance our understanding of a potential pathway for the reductive mineralization of Re_2S_7. This detailed mechanistic understanding of particle

formation can refine fate and transport models of rhenium in extreme anoxic and sulfide environments, such as those found in brines, geothermal waters, black smokers, hypersaline sulfidic lakes, deep sea, and acid mining waters. This research contributes to the understanding of Re accumulation in ore deposits, Re mobility in contaminated environments, and modern and past Re accumulation in sulfidic ocean and lake sediments.

The conditions that can accelerate or impede Re sequestration with sulfide, as previously discussed, can be critical factors in the separation of rhenium from other metals such as Cu, Mo or W in mining metal recovery and metal recycling, or in improving classical Re extraction methods by pyrometallurgical and hydrometallurgical means. Primary rhenium is usually extracted from molybdenum sulfide and copper sulfide ores. The recovery process involves wet scrubbing or leaching the ore mineral with water after roasting it in the air. Subsequently, rhenium is isolated through selective adsorption or solvent extraction, and aqueous extracts finally precipitate as NH_4ReO_4 crystals. Recycling rhenium, for instance, from WRe wire scrap, involves air oxidation at 900°C. At this temperature, tungsten solidifies and rhenium transforms into a volatile species ($Re_2O_{7(g)}$). Rhenium is precipitated through evaporative crystallization and then re-reduced to rhenium metal, similar to primary rhenium recovery. However, these methods result in significant energy consumption and SO_2 emissions. To improve this process, the addition of a chemical precipitation step can be beneficial. Sulfide precipitation, in particular, offers a less expensive means of separating rhenium from other trace metals. A previous study demonstrated that in an alkaline solution, sulfide precipitates rhenium, whereas molybdenum requires acidification to precipitate (Müller and Lande, 1933). Tungsten may exhibit similar behaviour to Mo as it is less calcophilic than Re. Additionally, the direct production of Re_2S_7 nanoparticles as the final product can have practical applications in industries such as hydrogen production catalysts or electronic devices.

Future in situ experiments with systematic observations of the crystallization process are required to obtain more precise information about the dynamic migration, orientation, and attachment of nanoparticles to gain insight into crystal growth. Future studies on the toxicity of Re should take into account its affinity for sulfide ions, the potential risk of particulate accumulation, and the effects of the interaction between the ^{188}Re radionuclide used in medicine and biological hydrogen sulfide (H_2S), which is the third endogenous gasotransmitter produced by four enzymatic pathways in mammals from L-cysteine and homocysteine (Augsburger and Szabo, 2020; Wu et al., 2018).

To the best of our knowledge, this is the first study to provide a detailed characterisation of the particulate Re formation in sulfidic waters. The present work may serve as a fertile ground for research on the reduction and mineralisation of thiometalates in reducing and sulfidic environments, with broad technological and industrial application relevance. These processes are fundamental in geological and biological processes.

2.5 Supplementary information

2.5.1 Methods

2.5.1.1 Materials

Sodium perrhenate, 99.99%, Sodium sulfide nonahydrate, ≥99.99 %, and Sodium chloride, ≥99.5 %, were obtained from Sigma-Aldrich. Sodium hydroxide was acquired from Roth, and Hydrochloric acid, 37 % Extra Pure, SLR, from Fisher Chemical.

All solutions were prepared with 18.2 MΩ/cm Millipore water boiled and cooled by bubbling nitrogen gas. The degassed water was stored inside the glove box, where for the first 12 hours, the inert atmosphere was continuously bubbled. All recipients were soaked in 10% and 2% HNO_3 and ultrapure deionized water for at least 24 hours and rinsed three times with deionized water before use. All experiments were performed at room temperature in a COY Laboratory Products glove box, type A, filled with 97% N_2 and 3% H_2, with oxygen partial pressure controlled below 1 ppm. Duplicate experiments were performed in a Jacomex glove box filled with Ar (O_2<5 ppm).

2.5.1.2 Thiolated solutions

Inside an anaerobic chamber, stock solutions of 1 M ΣS^{2-}, 1 M Sodium Chloride, and 0.1 M Perrhenate were prepared. All solutions were filtered with a syringe filter 0.22 µm pore size and repacked. The ΣS^{2-} stock solution is made with transparent $Na_2S.9H_2O$ crystals previously washed at least three times with ultrapure deoxygenated water. From the stock solutions, different reactors are prepared at three concentrations: 5, 10, and 20 mM ReO_4^-. A concentration of 100 mM ΣS^{2-} is adjusted for 5 mM Re solutions; for the 10 and 20 mM Re solutions is added 500 mM ΣS^{2-} is added. The 5 and 10 mM ReO_4^- solutions are adjusted to pH=6, 7, and 8, and the 20 mM solution is adjusted to pH=7 with 10 and 1 M HCl. Each pH value was set with a VWR pH110 pH meter.

2.5.1.3 UV-VIS spectra

UV-vis spectra are measured to identify the speciation of perrhenate in sulfuric waters. Typical peaks of the absorption spectra of thioperrhenate ions ($ReO_nS_{4-n}^-$) were taken from Helz and Dolor, 2012. At the glovebox, 2 mL of thiolation solutions are sampled at a specific time with a kinetic approach and filled 12 mm square polystyrene cuvettes with a lid. Ultraviolet-visible spectra were recorded on an Agilent Cary 300 UV-VIS spectrophotometer using deionized water as the blank solution in the 200 nm and 800 nm light path range.

2.5.1.4 Zetasizer Nano

The cuvettes used for UV-vis measurements are also measured in Zetasizer to identify and follow colloid formation. Dynamic light scattering experiments were performed using a Malvern Zetasizer Nano at ISTerre, Grenoble, France. Light scattering measurements were performed at 25 °C with the intensity autocorrelation function calculated from 12 measurements at 10-second intervals.

2.5.1.5 TEM

A few millilitres of samples were placed in plastic vials, filled with 10 mL of ethanol, sealed with parafilm, and removed from the glovebox for 5 minutes for redistribution in an ultrasonic bath. These dilute suspensions were drop-casted on pure carbon, 200 mesh Cu TEM grids and dried. The samples were transferred for TEM measurement under anoxic conditions and were in contact with air only for a few minutes during mounting on the microscope sample holder. TEM observations were performed on a Jeol JEM 2100F microscope, operating at 200 kV, equipped with a Schottky emitter, a Jeol detector with an ultra-thin window to detect light elements and a scanning TEM (STEM) device.

2.5.1.6 FESEM

Structural observations of Re-S nanoparticles were performed using a ZEISS Ultra Plus field emission scanning electron microscope (FESEM) with an accelerating voltage of 3 kV. The ReS_2 films were deposited on electrically conductive double-sided carbon tape placed on the support. Before measurement, the sample was metallized with Au.

2.5.1.7 XANES and EXAFS spectroscopy

Re L-III edge X-ray Absorption Near-Edge Structure (XANES) and Extended X-Ray Absorption Fine Structure (EXAFS) were collected at the Rossendorf beamline operated by Helmholtz-Zentrum Dresden Rossendorf (HZDR, Germany). Inside of glove box, an aliquot of liquid samples was used to fill Kapton-sealed holders, then stored in mylar bags, heat-sealed, and transported anaerobically to the station in jars filled with O_2-free nitrogen. All data collection is performed in a closed-cycle He cryostat with the atmosphere at 15 K to avoid photon-induced oxidation and to limit thermal disorder. XANES and EXAFS data were collected in fluorescence mode, and Re-references were measured in a transmission mode with an 18-element solid-state Germanium detector (Ultra-LEGe, GUL0055, Mirion Technologies). The monochromator was calibrated using simultaneous measurement of Ta-foil at L_3-edge energy at 9881 eV. The data collected was processed with the open-source software ATHENA program and ARTEMIS software package. Theoretical backscattering paths were calculated by FEFF to perform the fit in back-transformed reciprocal space.

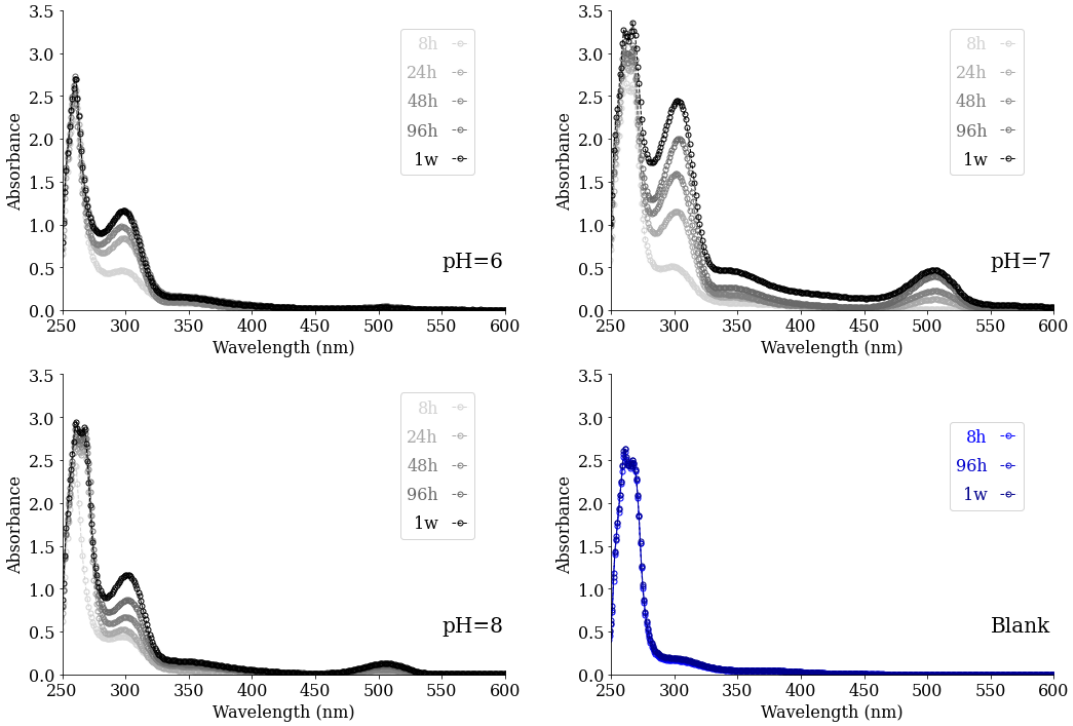

Figure S 1 UV-vis spectra at different equilibrium times after reaction between 0.005 M NaReO4 with 0.1 M $Na_2S.9H_2O$ and initial pH adjusted at pH=6, 7 and 8. The three absorption peaks observed indicate the formation of thioperrhenates species: ReO_3S^- at 298 and 350 nm and ReS_4^- at 505 nm. Those wavelengths agree well with previously published theoretical and experimental studies.

Table S1 EXAFS parameters and interatomic distances compiled from the bibliography of principal solids that can be relevant for the study.

	Crystal structure	Oxidation state	Atom	Crystallography		EXAFS		References
				CN	R [Å]	CN	R [Å]	
$NaReO_4$	Tetragonal ($I4_1/a$)	7	Re-O_1	4	1.8			(*Materials Data on NaReO4 by Materials Project*, 2020)
ReO_2	Orthorhombic (Pbcn)	4	Re-O_1	2	1.7	4	2.0	(*Materials Data on NaReO4 by Materials Project*, 2020; Wharton et al., 2000)
			Re-O_2	4	1.7	-	-	
			Re-Re_1	2	1.9	2	2.6	
			Re-Re_2	4	2.1	4	3.7	
			Re-Re_3	4	2.1	4	3.8	
ReS_2	Triclinic ($\bar{P}1$)	4	Re-S_1	2	2.3			(*Materials Data on NaReO4 by Materials Project*, 2020; Wharton et al., 2000)
			Re-S_2	2	2.4			
			Re-S_3	2	2.5			
			Re-S_1	6	2.4	6	2.4	(Hibble et al., 1999)
			Re-Re_1	3	2.8	3	2.8	
			Re-S_1	6	2.4	6	2.4	(Schwarz et al., 2004)
			Re-Re_1	3	2.8	3	2.8	
ReS_4	Amorphous crystals	5/6	Re-S_1			5	2.3	(Schwarz et al., 2004)
			Re-Re_1			3	2.8	
Et_4NReS_4	Monoclinical (P21) at 285K and hexagonal (P63mc) at 296K Orthorhombic (Pnma)	7	Re-S_1	4	2.1			(Bernhardt and Herbst-Irmer, 2020; Do et al., 1985)
Re_2S_7	Amorphous crystals	3.5/ 4/ 5	Re-S_1			4	2.4	(Müller et al., 1994; Wharton et al., 2000)
			Re-Re_1			2	2.8	
			Re-S_1			5	2.3	(Hibble et al., 1999)
			Re-Re_1			3	2.7	
			Re-S_1			6	2.3	(Schwarz et al., 2004)
			Re-Re_1			2	2.8	

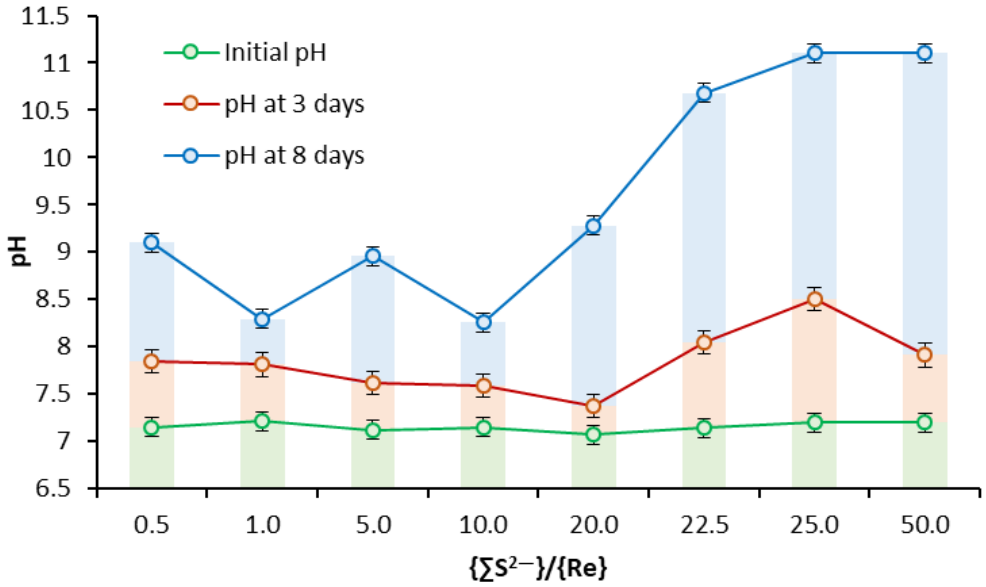

Figure S 2 pH measured at two equilibrium times: 3 and 8 days after adjusting an initial pH of 7 for different solutions with ratios between S and Re concentrations varying between 0.5 and 50.

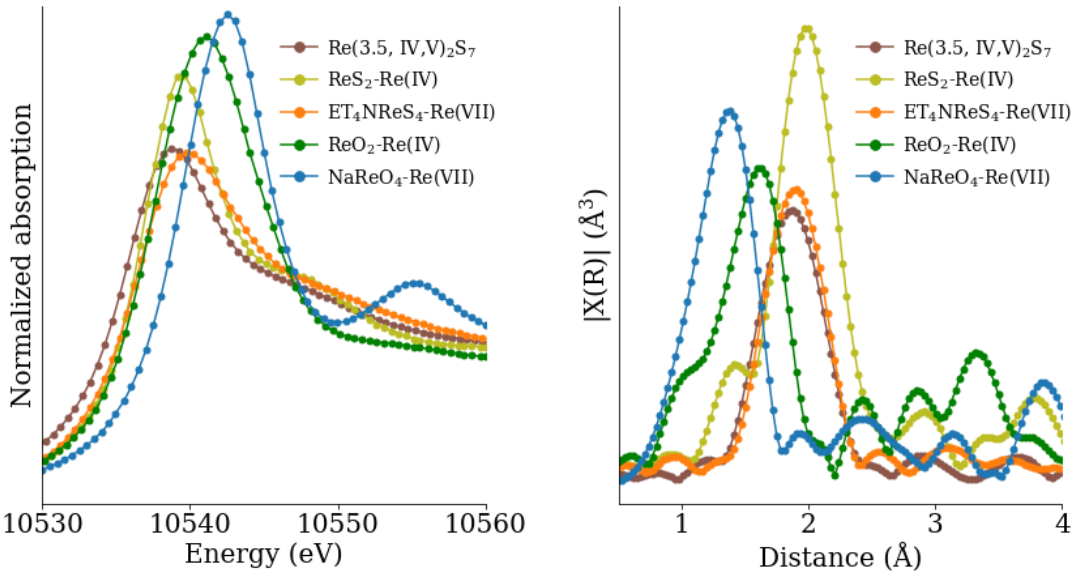

Figure S 3 Rhenium L-III-edge XANES (a) and Fourier transform magnitudes of EXAFS (b) references.

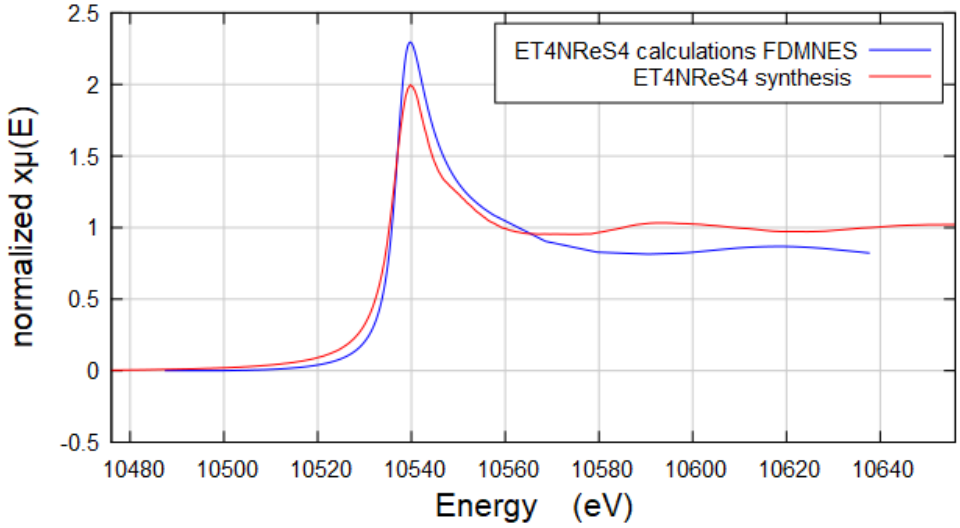

Figure S 4 Xanes spectra of the ET4NReS4 synthesis compared to the spectra obtained from FDMNES calculations using the published CIF structure.

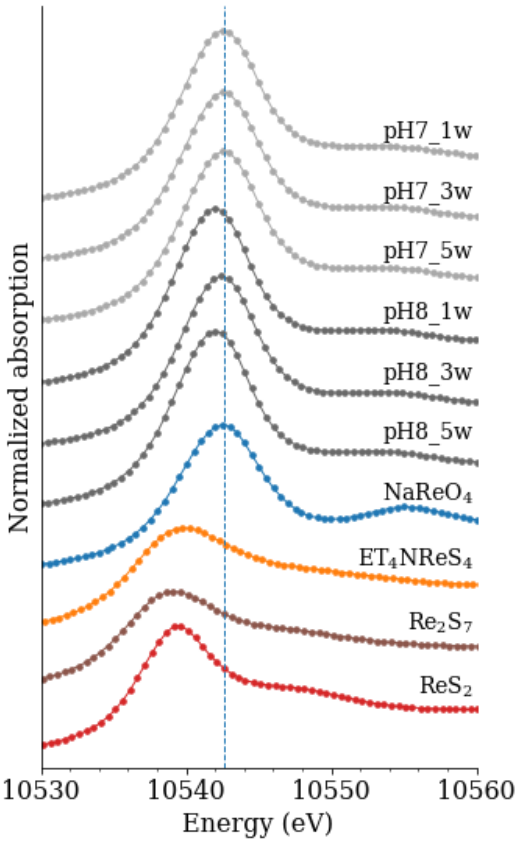

Figure S 5 Rhenium L3-edge XANES conducted on samples with 5mM ReO_4^- and 100mM S^{2-} adjusted at pH 7 (green line) and pH8 (black line) equilibrated over 1, 3, and 5 weeks.

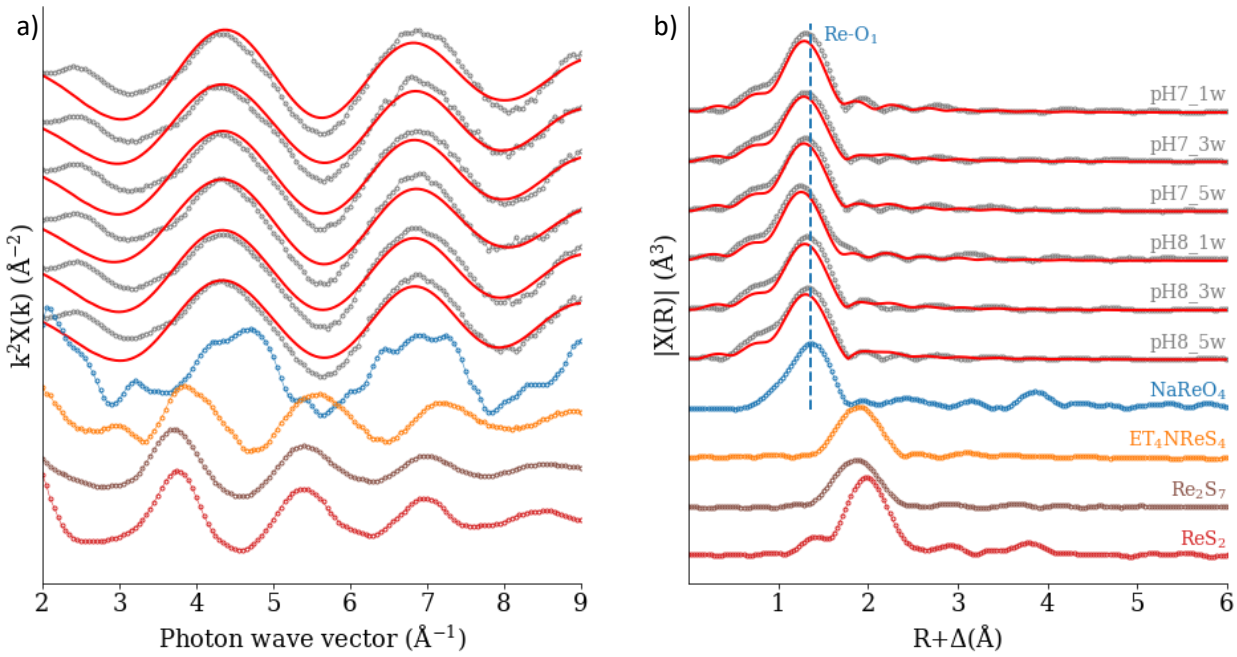

Figure S 6 Rhenium L_3-edge EXAFS for samples with 5mM ReO_4^- and 100mM S^{2-} with three equilibration periods: 1, 3 and 5 weeks at pH 7 and 8 and its Fourier transform magnitudes (b).

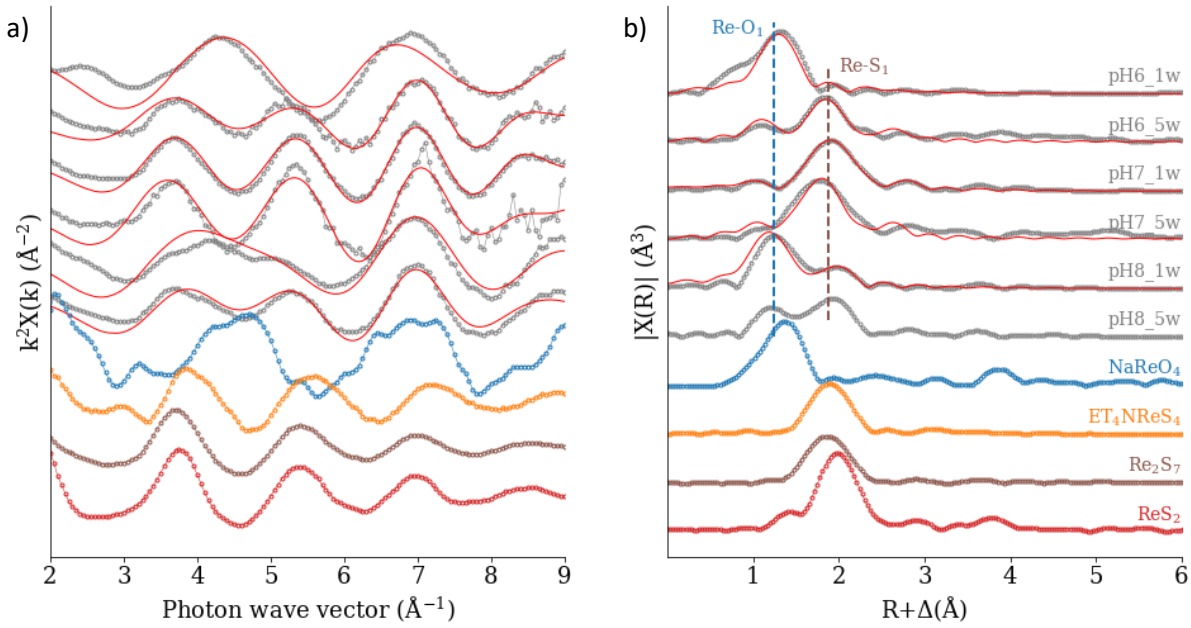

Figure S 7 Rhenium L_3-edge EXAFS for samples with 10mM ReO_4^- and 500mM S^{2-} equilibrated at three initial pH values: 6, 7 and 8 (a) and its Fourier transform magnitudes (b).

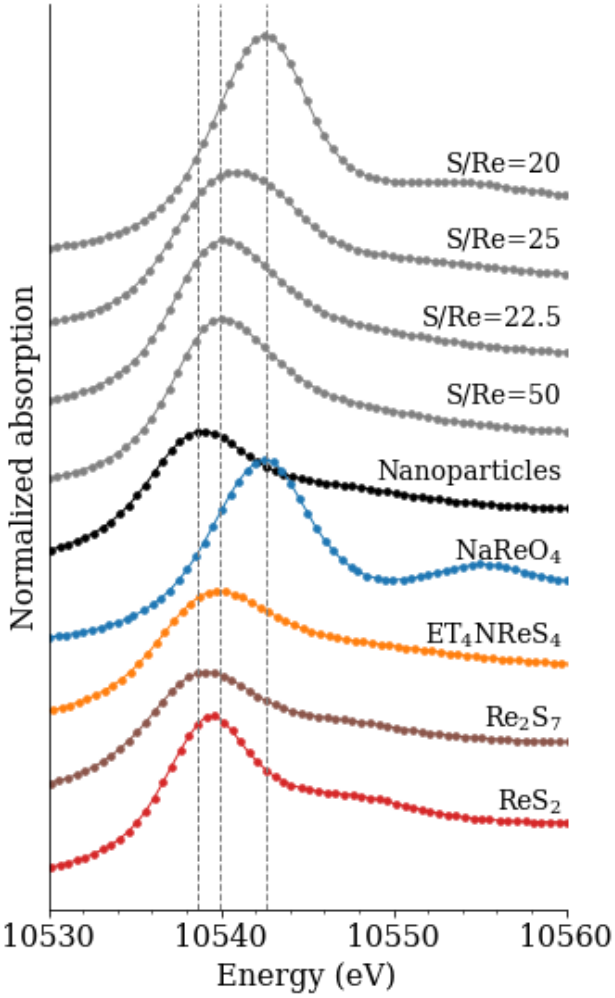

Figure S 8 Rhenium L_3-edge XANES for samples with different ReO_4^- and S^{2-} concentrations equilibrated at pH7 and during 1 week.

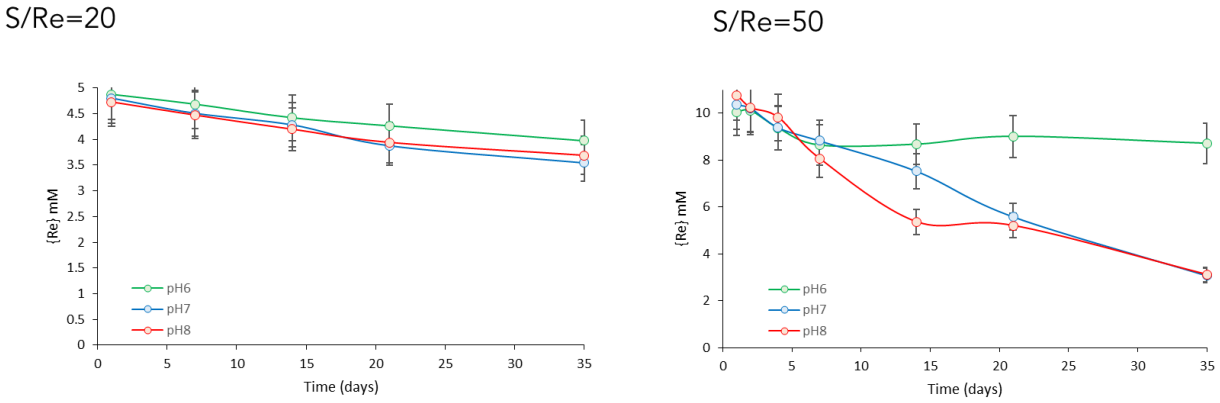

Figure S 9 Measurement of Re remaining in solution during colloid formation at two different molar S:Re ratios.

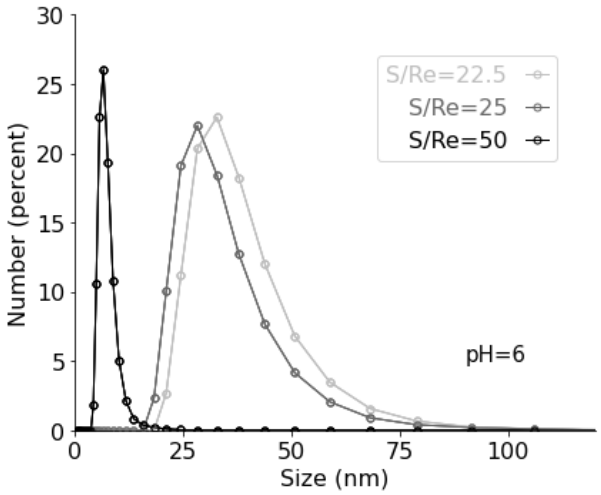

Figure S 10 The hydrodynamic size of nanoparticle formation at different molar S:Re ratios was determined by dynamic light scattering (DLS) analysis. The results of number distribution were obtained from samples measured after 1 week of equilibrium time.

Chapter 3: Interpreting the geochemistry of Re in anoxic buried sediments: Rhenium bonding with magnetite and Pyrite

This chapter consists of two sections, each containing distinct papers that are currently being prepared. The first section presents the results of the investigation into the adsorption and coprecipitation of Rhenium by magnetite. This section is presented as a brief report for submission to the Proceedings of the National Academy of Sciences (PNAS). The second section is dedicated to a manuscript that explains the interactions between Re and pyrite. This manuscript is currently being prepared for future submission.

3.1 Isotopic fractionation, reduction and structure of Rhenium at the water magnetite interface

Carolina Guida[a,b,c], Anthony Chappaz[b]*, Alex Dickson[d], Alexandre Gloter[e], Jean-Marc Greneche[f], Agnieszka Poulain[a], Damien Prieur[g,h], Andreas C. Scheinost[g,h], Laurent Charlet[a]*

Author affiliations: *[a]Univ. Grenoble Alpes, Univ. Savoie Mont Blanc, CNRS, IRD, Univ. Gustave Eiffel, ISTerre, 38058 Grenoble, France, [b]STARLAB, Central Michigan University, 48859 Mount Pleasant, Michigan, USA, [c]Grupo geología médica y forense, Universidad Nacional de Colombia, 111321 Bogotá, Colombia, [d]Department of Earth Sciences, Royal Holloway University of London, Egham, Surrey TW20 0EX, UK, [e]Laboratoire de Physique des Solides, Batiment 510, CNRS UMR 8502, Universite Paris Sud XI, 91405 Orsay, France, [f]Institut des Molécules et Matériaux du Mans, (IMMM CNRS UMR 6283), Le Mans Université, F-72085 Le Mans, France, [g]The Rossendorf Beamline at ESRF, 71 avenue des Martyrs, 38043 Grenoble, France and [h]HZDR Institute of Resource Ecology, 01328 Dresden, Germany.*

*To whom correspondence may be addressed.

Email: charlet38@gmail.com or anthony.c@cmich.edu

Abstract

Anoxic sediments are known sinks for redox-sensitive trace elements such as rhenium (Re). Rhenium oxidation state, bonding and the fractionation of its stable isotopes ^{187}Re and ^{185}Re are indices of redox changes in the depositional environment of the sediments. Understanding the Re sequestration process in anoxic conditions is essential for to use Re as a redox tracer in the present ocean, and for tracking past oxygenation of the earth and weathering of organic carbon-rich rocks. Here we study the mechanisms behind the Re trapping by magnetite at different pH values and concentrations using a range of analytical techniques such as powder X-ray absorption spectroscopy (XAS), Electron Energy Loss Spectroscopy (EELS) and Scanning Transmission Electron Microscopy (STEM). Results show that Re may be incorporated into a mineral structure via co-precipitation mechanisms. The $\delta^{187}Re/^{185}Re$ isotopic ratio is a possible fingerprint of such mechanism and can be used to track formation and weathering in basaltic rocks in which magnetite is an important Fe pool. Using magnetite as a model for ferruginous environments, this study sheds light on particle reactivity and on the geochemistry of Re in euxinic waters.

3.1.1 Introduction

Iron (Fe) is the main redox-active element at the earth's surface driving a global electron transfer flux of 3.5×10^{12} mol/year in various redox reactions (Stumm and Sulzberger, 1992). In nature, iron exists mainly as Fe(II) and Fe(III), with Fe(II) being more soluble and abundant in bioavailable forms. Iron solid phases include hydroxides, oxides, sulfides, sulfates, phosphates, and silicates. Among them, magnetite is widely found and an easily recognizable mineral in various rocks and sediments of different ages, making it crucial for petrogenetic and geochemical studies.

Redox-sensitive trace elements are used to follow the understanding of Earth's oxygenation and carbon rock weathering, influencing CO_2 emissions. Specifically, the metal rhenium (Re) has been used as a paleo-redox proxy to track redox conditions in oceans (Dellinger et al., 2023; Kendall et al., 2015; Rooney et al., 2014; Zondervan et al., 2023), and as an analogue to radioactive waste Technetium (Tc) to track its reactive transfer in surficial environments (Duckworth et al., 2021; Kim and Boulègue, 2003). Re occurs naturally as two stable isotopes, ^{187}Re and ^{185}Re, composing 63% and 37% respectively of Re in the oceanic crust, and can exhibit significant mass-dependent-and nuclear volume-fractionation following changes in redox environment (Dickson et al., 2020; Miller et al., 2015). In oxidizing conditions, Re(VII) is soluble as ReO_4^- in near-surface waters and continental weathering has the highest isotopic composition. Under reducing conditions, Re(IV) accumulates in marine sediments (Sheen et al., 2018). Depending on the interaction mechanisms with minerals that make up the seabed, Re can change its isotopic composition, be adsorbed, reduced or immobilised within crystal structures.

Here, in this Brief Report, we combined multiple advanced analytical techniques (X-ray absorption near edge structure (XANES), extended X-ray absorption fine structure (EXAFS) aberration-corrected scanning transmission electron microscopy-high angle annular dark field (STEM-HAADF), and $\delta^{187}Re/^{185}Re$ isotopic measurements) to investigate sorption experiments three Re sequestration systems with magnetite across an array of pH values: reductive adsorption (ads.), precipitation (prec.), or incorporation into magnetite mineral (coprec.). These diverse chemical mechanisms are at work in Re trapping processes. Unfortunately, sediments are difficult to analyze spectroscopically due to their low Re concentration, which is often below the detection limit of the various techniques. Our approach connects mechanistic insights with Re stable isotopes fractionation measurements in a natural environment.

3.1.2 Results and discussion

We studied as a function of pH, either adsorption or equilibrium with Fe-Re coprecipitates or Re precipitation. Adsorption isotherm experiments were conducted to determine the pH effect on this sorption, which can be due to the dissolution of magnetite, deprotonation or coprecipitation. We performed precipitation experiments from ferrous solutions with perrhenate concentration equilibrated at different pHs below 7.5 to avoid Fe oxide precipitation. We synthesized Re-doped magnetite using a magnetite precipitation method, where part of Fe(III) was substituted by a specific amount of perrhenate and mixed with the initial Fe solution before the alkalinization step. Our results were interpreted in terms of isotopic fractionation, wet chemistry (Re and Fe(II) removal and extractable Fe(III)) and above mentioned spectroscopic analyses of magnetite samples.

In the adsorption system (ads.), a clear isotopic fractionation is observed both in liquid and solid, compared to -0.04‰ initial composition (Figure 10 A), although less than 20% of Re was adsorbed whatever the equilibrium pH (Figure 10 B) after 2 weeks and adjusting pH twice a week. Adsorbed Fe(II) concentration increased at acidic pH, while extractable Fe(III) precipitated at alkaline pH. Thus, Fe(II)-Re(VII) co-adsorption e.g. via a ternary complex is not responsible for the removal of Re(VII). This implies a multi-step reaction that includes reductive adsorption, formation of ternary complexes, and/or coprecipitation. E_H values recorded during adsorption experiments with magnetite solid samples (-0.144 to 0.289 eV) coincide with the thermodynamically computed Re(VII)/ Re(VI) and Re(VII) / Re(IV) redox boundaries (Figure 10 C). Iron phases do not take part in the control of E_H values.

In Fe(II)-Re(VII) precipitation experiments (Prec.), we obtained between 32-33% Re(VII) and 12-16% Fe(II) removal from aqueous solution after 15 days of equilibrium time for the four pH studies (4 to 7). The ratio of Fe/Re in the precipitated (0.6 to 0.8) is much lower than 3 indicative of a Re reduction down to +VI oxidation state rather than +IV. Indeed, our measured E_H values are located in the Re(VII)/Re(VI) border. Thus, suggesting also reduction to Re(VI).

Almost all of the Re(VII) was removed from the solution in our coprecipitation experiments (coprec.) with a final concentration in solid between 509 to 7949 ppm, i.e. was longer than 90% leaving less than the detection limit in solution. After washing 6 cycles with DIW, the equilibrium pH was ~8 and solid Re exhibited a strong isotopic fractionation.

In accordance with our XANES spectroscopic evidence (Figure 10 D), the adsorption model (Ads.) illustrated the presence of Re(VI)/Re(V) species or a mix between Re(VII)/Re(VI)/Re(IV) phases. The EXAFS data fit very well with the first distance Re-O of the crystallographic structure of $NaReO_4$ - Re(VII) reference (1.72-1.76 Å) and not with the distance within ReO_2 or ReO_3 (2.03 or 1.90 Å, respectively). However, the second and third EXAFS peaks are consistent with ReO_3 crystal structure and in agreement with previous findings associated with sorbed Tc(IV) dimers phases (Kobayashi et al., 2013). Re atoms are visible on the periphery of the particle in the STEM-HAADF images (Figure 10 E). Bright spots are consistently found between the planes containing octahedral sites and some on the Fe octahedral atoms. For Fe(II)-Re(VII) solids (Prec.), we obtained XANES and EXAFS exhibiting features of a ReO_3 crystalline structure based on white line position, XANES shape and the fit of the Fourier transform data (Table 3). Furthermore, the greater reduction for adsorption than for precipitation is still not very clear, but for Fe precipitates the presence of characteristics related to Re(VI) pure phase is evidenced by wet chemistry, XANES and EXAFS spectra. Re atoms are present in the morphology of the precipitates, which are in the form of needles, in a sheet structure and as an amorphous material (Figure 10 G). For our Re-doped magnetite samples, the XANES spectra showed that only Re(IV) is present. The perfect EXAFS fit revealed that the first Re - O path has a 1.95 Å distance followed by Re-Fe. Re-O and Re-Fe distances are similar to Fe-O and Fe-Fe distances found in a magnetite structure (Table 3). These findings suggest for the first time the presence of Re structural, according to our knowledge. The Re structure is also observed in the STEM-HAADF images (Figure 10 F). The bright spots associated with the Re-atom columns are identified at sites where Fe is octahedral in the crystalline magnetite structure.

The isotopic ratio measured after digestion and column purification revealed longer Re fractionation for adsorption and coprecipitation solid samples (-0.6 vs -0.2 ‰) than during Re(VII)-Fe(II) precipitation experiments (Figure 10 A). We have confirmed previous ab initio calculations that show reduced Re species have isotopic values lower than those of ReO_4^- (Miller et al., 2015).

Present results are consistent to Tc(VII) slow adsorption and coprecipitation with magnetite (Liu et al., 2012; Marshall et al., 2014; Pearce et al., 2012) where just after 2 months Tc appears to be completely reduced (Yalçıntaş et al., 2016). When Tc(VII) was reacted with Fe(II) aqueous in a previous study (Zachara et al., 2007), there was a possible initial oxidation of Fe(II), followed by further interactions between Tc and Fe(II) with hydrolyzed Fe(III) clusters and other precursors of Fe(III) precipitates. It appears that the kinetic reactivity of Fe(II)-Fe(III) colloids with Tc increases during the final stage. Our observations support this interpretation. We noted that the Fe(II)-Re(VII) batch solution only became turbid after ageing for 10 days, followed by a faster formation of a more solid suspension. On the other hand, evidence suggests that Tc(IV) can be incorporated not only into magnetite but also into other iron oxide minerals, with Tc(IV) octahedrally coordinated within the relevant crystal structure, directly substituting for Fe(III). Like Tc(IV), Re(IV) has a crystallographic ratio close to the 6-atom coordinated Fe(III) (Fe= 0.78 Å and Re=0.77 Å) (Pearce et al., 2014; Shannon, 1976).

In summary, our findings demonstrated that adsorption was pH-independent, the Fe(II) role is not the only one responsible for Re removal and solids presented no pure Re phase (Re(VI, V and IV). Our Fe(II) precipitation solid samples show less isotopic fractionation than adsorption or coprecipitation and a pure Re(VI) phase. Finally, our coprecipitation experimental approach promoted major isotopic fractionation, complete reduction and retention of Re thus could be explained by the substitution of Fe(III) to Re(IV) in the magnetite lattice. The structural mechanism presented here can guide the formulation of hypotheses regarding sorption behavior on metal-iron oxide structures. Those insights can be used in complementary environment studies to follow Fe biogeochemical reactions in complete anoxia or suboxia (Fe(II) versus Fe(II)/Fe(III) minerals) and help to precise kinetic redox processes (slow adsorption/precipitation time versus fast co-precipitation). The isotopic composition values measured here in a ubiquitous mineral commonly found in marine sediments can improve the evaluation of the Re isotopic mass balance in the modern ocean and the geological past. The study of Re as a redox proxy represents valuable information for understanding natural deoxygenation phenomena like Proterozoic ocean oxygenation or weathering of Carboniferous rocks.

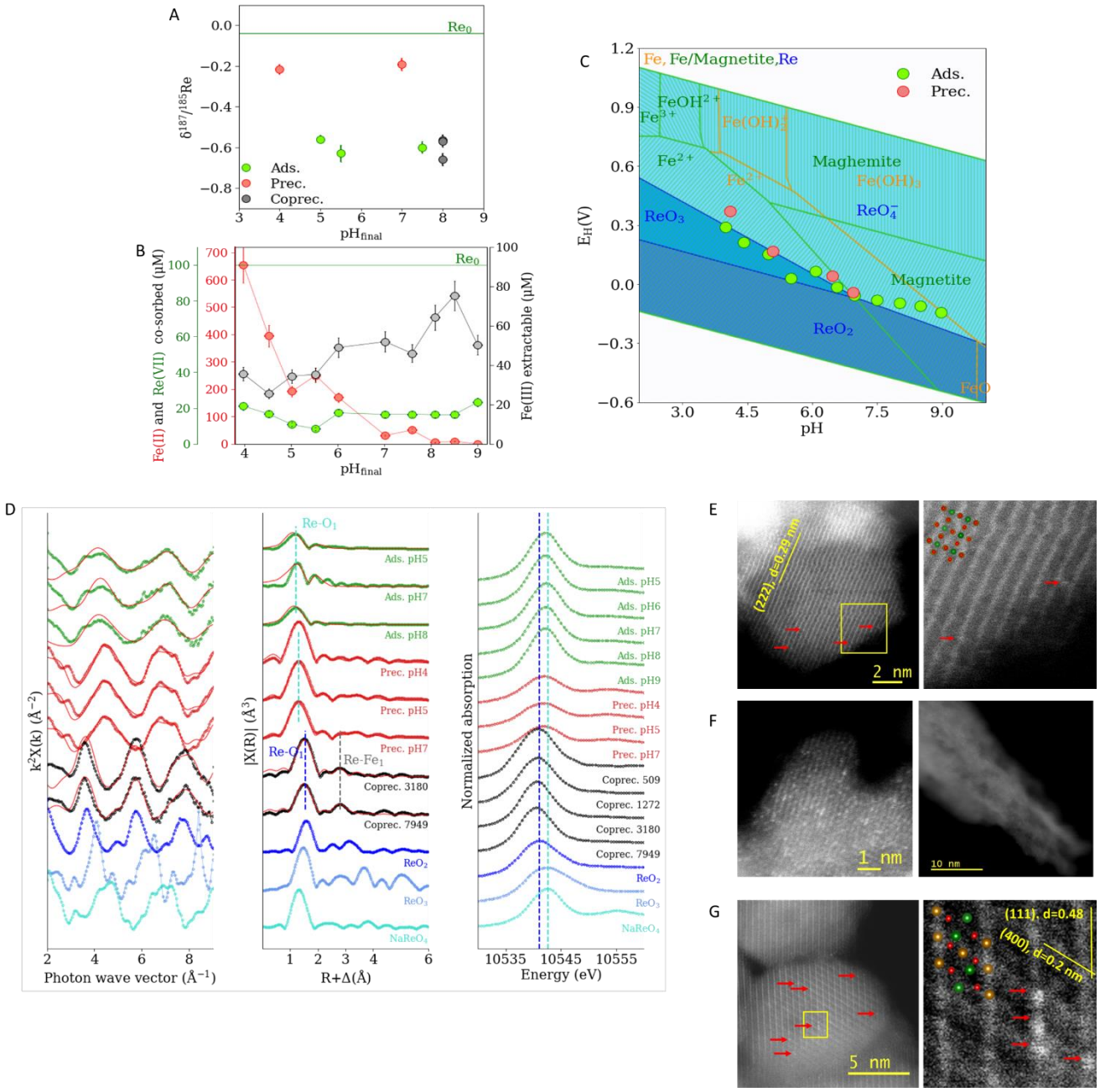

Figure 10. **A**. Re isotope compositions for selected samples for the three systems studied. Dashed line indicate the mean isotopic composition of $NaReO_4$ initial solution used for preparing experiments. **B**. Sorbed measurement of total Re(VII) (green circle), Fe(III) (black circle) and Fe(II) (red circle) after 24 h equilibrium time with nanomagnetite at different pHs between 4 and 9. The initial Re concentration is 100 μM and the solid concentration is 2 g/L. The error bar corresponds to 0.1 pH measuring precision and 5% of the standard error of ICP-AES and UV-VIS. **C**. E_H-p_H values collected in Re(VII) adsorption and precipitation experiments plotted in the Fe-O-H and Re-O E_H-P_H diagramas. Panel **D** shows k_2-weighted chi functions EXAFS spectra and its Fourier transform magnitudes of Re L_3-EXAFS spectra of samples with Re(VII) adsorbed on magnetite (green circle), precipitated with Fe(II) (red circle) and doped magnetite (black circle). On the right side, rhenium L3-edge XANES for sample systems. Red lines represent the fit for EXAFS. The standard spectra used for XANES and EXAFS analysis are plotted in blue tones. STEM-HAADF images of Ads. pH7(**E**), Prec. pH7(**F**) and (**G**) Coprec. 7949 ppm. Second image displays focal Re-atom arrangement after background normalisation to enhance the sharp contrast associated with single or small clusters of Re-atoms (yellow boxes)

Table 3 EXAFS Parameters and interatomic distances calculated for Re(VII) samples

Sample	Path	N [a]	R [b] [Å]	σ^2 [c] [Å^2]	ΔE_0 [d] [eV]	S_0^2 [e]	R-factor
Ads. pH5	Re-O.1	7[a]	1.76 (0.023)	0.012 (0.003)	0[a]	0.8[a]	0.144
R-range: 1-4	Re-O.2	4[a]	2.03 (0.032)	0.002 (0.003)	0[a]	0.8[a]	
	Re-O.3	24[a]	2.71 (0.080)	0.015 (0.016)	0[a]	0.8[a]	
Ads. pH7	Re-O.1	7[a]	1.74 (0.016)	0.012 (0.002)	0[a]	0.8[a]	0.289
R-range: 1-4	Re-O.2	4[a]	2.04 (0.021)	0.003 (0.002)	0[a]	0.8[a]	
	Re-O.3	24[a]	2.74 (0.046)	0.003[a]	0[a]	0.8[a]	
Ads. pH8	Re-O.1	7[a]	1.74 (0.019)	0.012 (0.002)	0[a]	0.8[a]	0.075
R-range: 1-4	Re-O.2	4[a]	2.04 (0.033)	0.006 (0.004)	0[a]	0.8[a]	
	Re-O.3	24[a]	2.79 (0.119)	0.03[a]	0[a]	0.8[a]	
Prec. pH4	Re-O.1	3.3[a]	1.71 (0.01)	0.001 (0.001)	7.2[a]	0.7[a]	0.023
R-range: 1.15-4	Re-O.2	6[a]	3.01 (0.12)	0.007 (0.024)	7.2[a]	0.7[a]	
	Re-Re.1	6[a]	3.91 (0.06)	0.013 (0.009)	7.2[a]	0.7[a]	
Prec. pH5	Re-O.1	3.0 (0.3)	1.70 (0.01)	0.000[a]	6.1[a]	0.7[a]	0.024
R-range: 1.15-4	Re-O.2	10[a]	2.98 (0.07)	0.003[a]	61[a]	0.7[a]	
	Re-Re.1	6[a]	3.89 (0.05)	0.008 (0.008)	6.1[a]	0.7[a]	
Prec. pH7	Re-O.1	2.8 (0.2)	1.70(0.01)	0.000[a]	6[a]	0.7[a]	0.024
R-range: 1.15-4	Re-O.2	6[a]	2.98 (0.12)	0.003[a]	6[a]	0.7[a]	
	Re-Re.1	6[a]	3.88 (0.04)	0.006 (0.006)	6[a]	0.7[a]	
Coprec. 3180	Re-O.1	5.4 (0.5)	1.96 (0.01)	0.003[a]	3[a]	1[a]	0.026
R-range: 1.3-4	Re-Fe.1	1 (0.5)	2.95 (0.03)	0.000[a]	3[a]	1[a]	
	Re-O.2	12[a]	3.61 (0.04)	0.013 (0.012)	3[a]	1[a]	
	Re-Fe.2	2[a]	3.64 (0.07)	0.032 (0.005)	3[a]	1[a]	
Coprec. 7949	Re-O.1	3.5 (1.2)	1.95 (0.01)	0.000[a]	0[a]	1[a]	0.022
R-range: 1.35-4	Re-Fe.1	1.4 (0.8)	2.99 (0.03)	0.003[a]	0[a]	1[a]	
	Re-O.2	9[a]	3.30 (0.03)	0.003[a]	0[a]	1[a]	
	Re-Fe.2	1[a]	3.40 (0.03)	0.000[a]	0[a]	1[a]	

[a]Coordination number for single paths, fixed value. [b]Interatomic distance. [c]Debye–Waller factor. [d]Shift of energy threshold. [e]Passive electron reduction factor.

3.1.3 Materials and methods

Detailed protocols are provided in Appendix 2 adsorption experiments, XAS, STEM- HAADF and Re isotopy measurements.

3.1.4 Supplementary information

3.1.4.1 Materials and methods

3.1.4.1.1 Chemicals

All solutions were prepared with 18.2 MΩ/cm Millipore water. For mineral synthesis and sorption experiments, water was boiled and cooled by bubbling nitrogen gas. The degassed water was stored inside the glove box. The recipients were soaked in 5% HNO_3 for 24h, cleaned for 10 minutes in an ultrasonic bath, and rinsed thoroughly with deionized water before use. The anoxic experiments were performed at room temperature in a Jacomex glove box filled with Ar (O_2<5 ppm). A pH meter with a pH/°C probe connected to a 1 m cable (VWR pH110) was used to measure the pH, which was calibrated with VWR buffers. For isotopic analysis, all Teflon flasks and pipette tips were carefully cleaned with 10% nitric acid, 5% hydrochloric acid and 18.2 MΩ/cm Millipore water, with a minimum contact time of 24 h for each solution at 70 °C. The acid used was distilled according to strict quality control procedures to ensure precision and accuracy of chemical analysis. The whole procedure, from sample digestion to column Re-cleaning and dilution preparation for isotopic measurements, was carried out in an ultra-clean laboratory.

Sodium perrhenate, 99.99%, sodium sulfide nonahydrate, ≥99.99 %, sodium hydrosulfide hydrate, sulfur, 99.998% trace metals basis, zinc acetate dihydrate, ≥98%, carbon disulfide, anhydrous, 99+%, Sodium chloride, ≥99.5 %, Nitric acid, ≥ 65 %, p.a., ISO, hydrazine hydrate (≥ 95%), iron (II) chloride tetrahydrate (99.99%), iron (III) chloride hexahydrate (≥ 99%), and ammonia solution, 25% (99%), were obtained from Sigma-Aldrich. Sodium hydroxide was acquired from Roth, and Hydrochloric acid, 37 % Extra Pure, SLR, from Fisher Chemical. Isoamyl Alcohol 99% was obtained from Trafalgar Scientific. Anionic resin AG1-X8 (200-400 mesh) was purchased from Bio-Rad Laboratories, W NIST SRM 3163 and $\delta^{187/185}$Re NIST SRM 989 from the NIST store, and RHUL ^{185}Re tracer was provided by Dr Dickson's laboratory.

3.1.4.1.2 Magnetite and Re-doped magnetite synthesis

Magnetite was prepared by slow addition of 25 mL of 0.8 M $FeCl_2$ mixed with 25 mL 1.6 M $FeCl_3$ solution to a volume of 60 mL of 6 M NH_4OH solution (10 mL/1 min). The suspension was stirred for 24 hours, then washed by replacing the supernatant with degassed water six times, vacuum filtered with a 0.22 µm filter, and dried under an anoxic atmosphere. Re-doped nano magnetites were synthesised using the same alkalinisation of aqueous Fe(II) and Fe(III) ions method as above, but by adding a precise amount of 100 mM Re(VII) stock solution to the ferrous/ferric chloride solution before the alkalinisation step. The Fe solution volume was also modified, assuming that Fe(II) reduces Re(VII) to Re(IV) by decreasing the Fe(II) concentration and increasing the Fe(III) concentration. To maintain the stoichiometry of magnetite, the excess Fe(II) added was three times the concentration of Re(VII) and the concentration of Fe(III) was reduced for the same volume of Fe(II) added. The supernatant was separated and acidified with HNO_3 65% before ICP-AES measurements.

3.1.4.1.3 Re(VII) precipitation by Ferrous Iron

Four reactors were made by mixing 9 mL of 100 M Re(VII) stock solution with 21 mL of 72 mM Fe(II) solution. Each batch was adjusted at a different pH between 4 to 7 with some drops of 1M NaOH solution. The pH adjustment was made twice during the 2-week equilibration period. The final pH was 4.1, 5.1, 6.5, and 6.9. EH values were measured in the final solution. The precipitated form was collected and dried after the supernatant was separated. Colorimetry and ICP-AES methods were used to measure the filtrated solution with cellulose-nitrate filters (pore size 0.22 µm).

3.1.4.1.4 Adsorption experiments

Several batch experiments were conducted at pH levels ranging from 4 to 9, including a blank. The initial concentration of Magnetite was set at 2 g/L, and the ionic strength was adjusted to 0.1 M NaCl. Before adding Re(VII) concentration, the pH was adjusted to the desired values by either adding HCl or NaOH. After 24 hours of equilibrium, pH and EH were measured for each sample. Two aliquots of the mixed solution and precipitate were taken, one of 1.35 mL and the other of 10 mL. The latter was filtered through a 0.45 µm filter and divided into two volumes. The first 5 mL volume was stored in an ICP tube for Fe(II) analyses. The second 5 mL volume was acidified with 100 µL of 65% HNO_3 for ICP-AES measurements. The 1.35 mL sample was mixed with 0.15 mL of a 1mM Xylene Orange solution and left to equilibrate for 24 hours. The next day, the sample was filtered, and 2.25 mL of 40 mM HCl was added. The resulting solution was allowed to stand for an additional 24 hours and then measured for Fe(III) concentration. For the remaining batch solution, 100 µM Re(VII) was added. The pH was adjusted three more times during a 20-day equilibrium period. The final pH and EH were also recorded. Subsequently, 1.35 mL samples (for Fe(III) measurements) and 2 x 10 mL samples (for Fe(II) analysis) were taken from all solutions and the same treatment as described above was followed.

3.1.4.1.5 Wet chemical analysis

ICP-AES. Total dissolved Re and Fe concentrations in the supernatant and in some digest coprecipitation samples were determined by inductively coupled plasma atomic emission spectroscopy (ICP-AES, Varian 720 ES) at wavelengths 234.350 nm for Fe and 197.248 nm for Re. 1000 ppm Fe and Re ROTH standards were used to prepare an external calibration with a range of 0.1 ppm - 25 ppm for Fe and Re concentration. Analytical precision (RSD) and recovery (CMS) were determined from replicate analyses (n=5 and n=2, respectively). The RSD calculated of 4.5 ppm standard was 1% for Fe and for Re. The CMS was 100% for Fe and for Re. The detection limits (DLs) for Fe and Re were 0.1 µM and 0.9 µM, respectively. The quantification limits (QLs) for Fe and Re were 0.4 µM and 2.1 µM, respectively.

Inductively Coupled Plasma-Mass Spectrometry (ICP–MS) in RHUL facilities was used for total Re quantitative analyses of solutions and digest solid samples with less than 1 ppm concentration.

Colorimetry. The ferric xylenol orange complex method (Gay et al., 1999) was used to determine the amount of Fe(III) absorbed by iron minerals after Fe(II) oxidation. Fe(II) dissolved before and after the sorption experiments were measured spectroscopically using the O-phenanthroline(Fortune and Mellon, 1938). An Agilent Cary 300 UV-VIS system was used to analyse the samples at 560 nm and 513 nm for Fe(III) and Fe(II) respectively. The DL for Fe(III) was 3.7 µM and for Fe(II) 15.2µM. The QLs were 11.3 µM for Fe(III) and 46.1 µM for Fe(II).

3.1.4.1.6 Re-isotope analysis

For the measurement of Re concentrations, a predetermined amount of solid and liquid samples were weighed into Teflon vials. These samples were then spiked with a solution enriched with ^{185}Re and mixed with 0.1 µL of 37% hydrochloric acid and 0.3 µL of 65% nitric acid. After refluxing to attain equilibrium, they were evaporated and re-dissolved in 0.3 µL of 65% nitric acid. This process was repeated before finally being re-dissolved in 2 mL of 2 M nitric acid. Purification from the matrix was achieved using the alcohol partition procedure recommended by Birck et al., (1997) (Birck et al., 1997). The resulting purified samples were evaporated and then re-dissolved in 0.3 mL of 3% HNO_3.

For isotopic ratio measurements, a small quantity of identical samples (approximately 200-300 ng of Re) was digested following the same procedures as before. However, the spike addition and alcohol step were omitted, and the final re-dissolving occurred in 10 mL 0.5M HNO_3. The purification process involved three anion exchange columns employing AG1X8 resin (200-400 mesh) following the previously detailed procedure (Miller et al., 2009). 2 mL and 200 µL of resin were used for the first and

last columns, respectively. The acid elution protocol(25) for the large column consisted of cleaning and preconditioning with 30 mL of 7.5M HNO_3 and 10 mL of 0.5M HNO_3, followed by sample loading, matrix elution with 20 mL of 0.5M HNO_3, and final elution of Re with 14 mL of 7.5M HNO_3. The sample was then evaporated and diluted with 1 mL of 3% HNO_3 for the small column. Prior to sample elution, the small column was prepared with 6 mL of 7.5M HNO_3 and 1mL of 0.5M HNO_3, followed by matrix elution with 3 mL of 0.5M HNO_3 and Re elution with 6 mL of 3M HNO_3. The final pure Re sample was dried, re-dissolved in 0.3mL of 14M HNO_3, refluxed for two days, dried again, and finally re-dissolved in 1mL of 3% HNO_3 for subsequent measurements.

Concentration and isotope ratios were analyzed using a Neptune Plus MC-ICP-MS (multi-collector inductively coupled plasma mass spectrometer) at Royal Holloway University. To measure ion beams in static mode with 1013 Ω resistors, the Faraday cup configuration of 180W (L3), 182W (L2), 183W (L1), 184W (Axial), 185Re (H1), 185W (H2), 187Re (H3), and 189Os (H4) was employed. Due to the naturally variable ^{187}Os, there is a potential for Os interferences on ^{184}W, ^{186}W, and particularly on ^{187}Re. In order to monitor ^{189}Os, the axial secondary electron multiplier (SEM) is utilized. For instrumental mass bias correction, NIST SRM 3163 is added to each sample. Corrections are made using the W/Re ratio and an exponential mass bias law (Dellinger et al., 2020; Dickson et al., 2020). The recovery of Re is verified by comparing Re concentration measurements acquired with alcohol extraction and the concentration after column, as well as measuring $\delta^{187/185}Re$ NIST SRM 989 standard, which also follows column purification procedure. The isotopic composition of the stock Re solution used in sorption experiments is also determined, and all Re isotope values are presented relative to this measurement.

3.1.4.1.7 Mineral characterization

STEM-HAADF. Structural observations STEM-HAADF (high-angle annular dark field imaging in scanning transmission electron microscope mode) images were collected. The preparation of the sample involved delicately spreading a drop of powder diluted with ethanol onto pure carbon, 200 mesh Cu TEM grids and drying inside the glovebox. The samples were transferred for STEM measurement under anoxic conditions and were in contact with air only for a few minutes during mounting on the microscope sample holder. STEM-EELS measurements were performed in a NION UltraSTEM200 operated at 100 kV and coupled with a high-sensitivity EELS spectrometer. Data was collected from clean GR plates; those that were considered free of contamination and/or visible stray iron (oxyhydr)oxide minerals.

X-ray absorption spectroscopy. Re L-III edge XANES and EXAFS were collected at the Rossendorf beamline of the Helmholtz-Zentrum Dresden Rossendorf (HZDR, Germany). In the glovebox, 50 mg powder samples were filled into capton sealed holders, then stored in mylar bags, heat sealed, and shipped to the station in anaerobic bottles containing O_2-free nitrogen. To avoid photon-induced oxidation and to limit thermal perturbations, all data collection is performed in a closed-cycle He cryostat with the atmosphere at 15 K. XANES and EXAFS data were collected in fluorescence mode, and the Re references were collected in transmission mode with an 18-element solid-state germanium detector (Ultra-LEGe, GUL0055, Mirion Technologies). The monochromator was calibrated by simultaneously measuring Re metal foil at L3 energy 10535 eV. The open-source software ATHENA and the software package ARTEMIS were used to process the collected data. Theoretical backscattering paths were calculated using FEFF to fit in back-transformed reciprocal space (Ravel and Newville, 2005)

3.2 Rhenium reductive adsorption and co-precipitation by pyrite

Carolina Guida [1,2,3], Anthony Chappaz[2*], Alex Dickson[4], German Montes-Hernandez [1], Andreas C. Scheinost[5,6], Laurent Charlet[1*]

[1] Univ. Grenoble Alpes, Univ. Savoie Mont Blanc, CNRS, IRD, Univ. Gustave Eiffel, ISTerre, 38058 Grenoble, France
[2] STARLAB, Central Michigan University, 48859 Mount Pleasant, Michigan, USA
[3] Grupo geología médica y forense, Universidad Nacional de Colombia, 111321 Bogotá, Colombia.
[4] Department of Earth Sciences, Royal Holloway University of London, Egham, Surrey TW20 0EX, UK.
[5] The Rossendorf Beamline at ESRF, 71 avenue des Martyrs, 38043 Grenoble, France
[6] HZDR Institute of Resource Ecology, 01328 Dresden, Germany.
[*] Corresponding author. E-mail address: charlet38@gmail.com & anthony.c@cmich.edu

3.2.1 Introduction

The metal rhenium (Re) has played a crucial role in elucidating important processes in nature, such as the oxygenation of the Earth (Kendall et al., 2015) and the weathering of organic carbon rocks, which act as a source of CO_2 emissions to the atmosphere(Hilton et al., 2014; Zondervan et al., 2023). This has been facilitated by the Re redox that controls its mobility. Under oxidising conditions, Re(VII) exhibits high solubility and mobility in water, existing primarily as the perrhenate anion, ReO_4^-, found in near-surface water within the oxidative weathering zone. Conversely, Re(IV) predominates under reducing conditions and tends to accumulate in marine sediments as a precipitate or adsorb onto oxide or sulphide phases present on the surfaces of iron and organic carbon minerals. Thus, elevated aqueous Re concentrations may indicate a transient increase in continental oxidative weathering, possibly related to increased atmospheric O_2, while subsequent declines may show a return to lower redox conditions. Re also occurs naturally in two stable isotopes, ^{187}Re and ^{185}Re, composing 63% and 37% respectively. Studies suggest a potential isotopic fractionation of up to 1.5‰ between various Re species, especially ReO_4^- found in seawater(Dickson et al., 2020). The removal of Re with lower isotopic composition into marine sediments might influence global seawater isotopes over time, hinting at Re isotopes as tracers for ocean redox.

The perrhenate oxyanion shows long residence times. In general, the highest concentrations of Re are found in marine rocks (Bennett and Canfield, 2020). These are either the result of early diagenesis or have been transported from land after physical weathering. Enrichments of this metal have been studied in black shales such as the Mount McRae Shale (Hamersley Basin, Western Australia) and in deep oceanic sediments (Nameroff et al., 2002). The most common mineralogical phase in these geological environments is pyrite (FeS_2).

Rhenium is often considered a close chemical analogue of Technetium (Tc) (7) due to their similar ionic radii, 0.77 Å for Re(IV) and 0.79 Å for Tc(IV) in octahedral coordination(Shannon, 1976), and shared chemical properties, including redox states and affinities with the reduce S and Fe species. Previous studies have demonstrated the effectiveness of Fe(II)-bearing sulfides in removing Tc(VII) and Re(VII) from solution through reductive adsorption or precipitation (Kilber et al., 2024; Wang et al., 2020; Wharton et al., 2000). These studies observed the reduction of M(VII) (where M=Tc or Re) sorbed on fresh pyrite and mackinawite to M(IV), and identified the presence of Fe(II) in solution as a key factor. The incorporation of Re into stable mineral phases, such as iron sulfides, provides a pathway for sequestering this element with potential immobilization. Helz (2022) proposed co-precipitation with Fe-Mo-S phases as a primary mechanism of sequestration in anoxic settings(Helz, 2022). Although numerous investigations have focused on elucidating the mechanism(s) involved in the capture of Re and its analogue Tc, they remain poorly understood. To the best of our knowledge, no studies have been carried out directly investigating the co-precipitation of Re with pyrite, although this seems to be the most important mechanism in its sequestration. No comparative studies have been conducted to determine which mechanism is more efficient between adsorption and coprecipitation.

Theoretical models of equilibrium Re isotope fractionation factors indicate a link between oxidation state and ligand strength(Miller et al., 2015). However, no research has been made to corroborate this theory with an experimental approach and this assumption has not been demonstrated. This study aimed to characterize the mechanism(s) of ReO_4^- reaction with pyrite through different pH values. We have combined geochemical data with quantitative powder X-ray absorption spectroscopy (XAS) and the $\delta^{187}Re/^{185}Re$ isotopic ratio to thoroughly characterize the fate of Re reduction adsorption and incorporation with pyrite mineral in an atomic scale bonding environment.

3.2.2 Materials and methods

3.2.2.1 Chemicals

All solutions were prepared with 18.2 MΩ/cm Millipore water. For mineral synthesis and sorption experiments, water was boiled and cooled by bubbling nitrogen gas. The degassed water was stored inside the glove box. The recipients were soaked in 5% HNO_3 for 24h, cleaned for 10 minutes in an ultrasonic bath, and rinsed thoroughly with deionized water before use. The anoxic experiments were performed at room temperature in a Jacomex glove box filled with Ar (O_2<5 ppm). A pH meter with a pH/°C probe connected to a 1 m cable (VWR pH110) was used to measure the pH, which was calibrated with VWR buffers. For isotopic analysis, all Teflon flasks and pipette tips were carefully cleaned with 10% nitric acid, 5% hydrochloric acid and 18.2 MΩ/cm Millipore water, with a minimum contact time of 24 h for each solution at 70 °C. The acid used was distilled according to strict quality control procedures to ensure precision and accuracy of chemical analysis. The whole procedure, from sample digestion to column Re-cleaning and dilution preparation for isotopic measurements, was carried out in an ultra-clean laboratory.

Sodium perrhenate, 99.99%, sodium sulfide nonahydrate, ≥99.99 %, sodium hydrosulfide hydrate, sulfur, 99.998% trace metals basis, zinc acetate dihydrate, ≥98%, carbon disulfide, anhydrous, 99+%, Sodium chloride, ≥99.5 %, Nitric acid, ≥ 65 %, p.a., ISO, hydrazine hydrate (≥ 95%) and iron (III) chloride hexahydrate (≥ 99%), were obtained from Sigma-Aldrich. Sodium hydroxide was acquired from Roth, and Hydrochloric acid, 37 % Extra Pure, SLR, from Fisher Chemical. Isoamyl Alcohol 99% was obtained from Trafalgar Scientific. Anionic resin AG1-X8 (200-400 mesh) was purchased from Bio-Rad Laboratories, W NIST SRM 3163 and $\delta^{187/185}$Re NIST SRM 989 from the NIST store, and RHUL ^{185}Re tracer was provided by Dr Dickson's laboratory.

3.2.2.2 Pyrite and Re-doped pyrite synthesis

Pure pyrite was synthesized using the reductive coprecipitation method. In brief 125 mL of 0.08M of $FeCl_3.6H_2O$ solution was added drop by drop into 125 mL of 0.32 M $Na_2S.9H_2O$ and 0.02 M S solution (10 mL/1 min). Then, 10 M HCl solution drops were added to adjust a pH value of ~4. The final solution was placed in a non-stirred pressure reactor and heated at 160°C for 4 h. After cooling, the FeS_2 precipitate was decanted and washed by replacing the supernatant with 0.2 M HCl solution three times, followed by carbon disulfide and acetone, to remove residual sulfur entirely from the solid surface. All the washing solutions were in contact with pyrite for a minimum of an hour. Finally, the suspension was washed, vacuum filtered through a 0.22 µm filter with degassed water, dried in an anaerobic chamber and stored in degassed ultrapure water at 100 g/L solid concentration.

Re-doped pyrite synthesis was inspired by the method proposed by Diener and Neumann (2011)(Diener and Neumann, 2011). 60 mL of 0.15 HS^- solution received a specific volume of 0.01 M Re(VII) stock solutions before being mixed with 60 mL of 0.05 M Fe(III) solution. Then, 1 M NaOH solution drops were added to adjust the pH value to ~4 and the final solution was agitated for five days. The Re coprecipitated with pyrite was cleaned and dried, just like pure pyrite. Re-pyrite samples were synthesized with final concentrations of 17.5, 50, 125, 250, 375, and 500 µM for Re(VII). The supernatant was analyzed for elemental and isotopic properties before being acidified with 100 µL of 65 % HNO_3.

3.2.2.3 Adsorption experiments

Several batch experiments were conducted at pH levels ranging from 4 to 9, including a blank. The initial concentration of pyrite was set at 2 g/L, and the ionic strength was adjusted to 0.1 M NaCl.

Before adding Re(VII) concentration, the pH was adjusted to the desired values by either adding HCl or NaOH. After 24 hours of equilibrium, pH and E_H were measured for each sample. Two aliquots of the mixed solution and precipitate were taken, one of 1.35 mL and the other of 10 mL. The latter was filtered through a 0.45 µm filter and divided into two volumes. The first 5 mL volume was stored in a tube with 100 µL of a 100 mM Zinc acetate dihydrate (ACZn) stock solution for Fe(II) and ΣS(-II) analyses (for pyrite reactors). The second 5 mL volume was acidified with 100 µL of 65% HNO_3 for ICP-AES measurements. The 1.35 mL sample was mixed with 0.15 mL of a 1mM Xylene Orange solution and left to equilibrate for 24 hours. The next day, the sample was filtered, and 2.25 mL of 40 mM HCl was added. The resulting solution was allowed to stand for an additional 24 hours and then measured for Fe(III) concentration. For the remaining batch solution, 100 µM Re(VII) was added. The pH was adjusted three more times during a 20-day equilibrium period. The final pH and E_H were also recorded. Subsequently, 1.35 mL samples (for Fe(III) measurements) and 2 x 10 mL samples (for Fe(II) and ΣS(-II) analyses) were taken from all solutions and the same treatment as described above was followed.

3.2.2.4 Wet chemical analysis

3.2.2.4.1 ICP-AES

Total dissolved Re and Fe concentrations in the supernatant and in some digest coprecipitation samples were determined by inductively coupled plasma atomic emission spectroscopy (ICP-AES, Varian 720 ES) at wavelengths 234.350 nm for Fe and 197.248 nm for Re. 1000 ppm Fe and Re ROTH standards were used to prepare an external calibration with a range of 0.1 ppm - 25 ppm for Fe and Re concentration. Analytical precision (RSD) and recovery (CMS) were determined from replicate analyses (n=5 and n=2, respectively). The RSD calculated of 4.5 ppm standard was 1% for Fe and for Re. The CMS was 100% for Fe and for Re. The detection limits (DLs) for Fe and Re were 0.1 µM and 0.9 µM, respectively. The quantification limits (QLs) for Fe and Re were 0.4 µM and 2.1 µM, respectively.

Inductively Coupled Plasma-Mass Spectrometry (ICP–MS) in RHUL facilities was used for total Re quantitative analyses of solutions and digest solid samples with less than 1 ppm concentration.

3.2.2.4.2 Colorimetry

The ferric xylenol orange complex method(Gay et al., 1999) was used to determine the amount of Fe(III) absorbed by iron minerals after Fe(II) oxidation. Fe(II) and S(-II) dissolved before and after the sorption experiments were measured spectroscopically using the O-phenanthroline(Fortune and Mellon, 1938) and methylene blue methods(Cline, 1969) respectively. The 10 mM ΣS(-II) stock solution for UV-vis curve calibration was analysed by sodium thiosulphate titration. An Agilent Cary 300 UV-VIS system was used to analyse the samples at 560 nm, 513 nm and 670 nm for Fe(III), Fe(II) and ΣS(-II) respectively. The DL for Fe(III) was 3.7 µM, for Fe(II) 15.2µM and for ΣS(-II) 0.5 µM. The QLs were 11.3 µM for Fe(III), 46.1 µM for Fe(II) and 1.5 µM for ΣS(-II).

3.2.2.5 Re-isotope analysis

For the measurement of Re concentrations, a predetermined amount of solid and liquid samples were weighed into Teflon vials. These samples were then spiked with a solution enriched with ^{185}Re and mixed with 0.1 µL of 37% hydrochloric acid and 0.3 µL of 65% nitric acid. After refluxing to attain equilibrium, they were evaporated and re-dissolved in 0.3 µL of 65% nitric acid. This process was repeated before finally being re-dissolved in 2 mL of 2 M nitric acid. Purification from the matrix was achieved using the alcohol partition procedure recommended by Birck et al., (1997)(Birck et al., 1997). The resulting purified samples were evaporated and then re-dissolved in 0.3 mL of 3% HNO_3.

For isotopic ratio measurements, a small quantity of identical samples (approximately 200-300 ng of Re) was digested following the same procedures as before. However, the spike addition and alcohol step were omitted, and the final re-dissolving occurred in 10 mL 0.5M HNO_3. The purification process involved three anion exchange columns employing AG1X8 resin (200-400 mesh) following the previously detailed procedure(Miller et al., 2009). 2 mL and 200 µL of resin were used for the first and last columns, respectively. The acid elution protocol(Miller et al., 2009) for the large column consisted of cleaning and preconditioning with 30 mL of 7.5M HNO_3 and 10 mL of 0.5M HNO_3, followed by sample loading, matrix elution with 20 mL of 0.5M HNO_3, and final elution of Re with 14 mL of 7.5M HNO_3. The sample was then evaporated and diluted with 1 mL of 3% HNO_3 for the small column. Prior to sample elution, the small column was prepared with 6 mL of 7.5M HNO_3 and 1mL of 0.5M HNO_3, followed by matrix elution with 3 mL of 0.5M HNO_3 and Re elution with 6 mL of 3M HNO_3. The final pure Re sample was dried, re-dissolved in 0.3mL of 14M HNO_3, refluxed for two days, dried again, and finally re-dissolved in 1mL of 3% HNO_3 for subsequent measurements.

Concentration and isotope ratios were analyzed using a Neptune Plus MC-ICP-MS (multi-collector inductively coupled plasma mass spectrometer) at Royal Holloway University. To measure ion beams in static mode with 10^{13} Ω resistors, the Faraday cup configuration of 180W (L3), 182W (L2), 183W (L1), 184W (Axial), 185Re (H1), 185W (H2), 187Re (H3), and 189Os (H4) was employed. Due to the naturally variable ^{187}Os, there is a potential for Os interferences on ^{184}W, ^{186}W, and particularly on ^{187}Re. In order to monitor ^{189}Os, the axial secondary electron multiplier (SEM) is utilized. For instrumental mass bias correction, NIST SRM 3163 is added to each sample. Corrections are made using the W/Re ratio and an exponential mass bias law(Dellinger et al., 2020; Dickson et al., 2020). The recovery of Re is verified by comparing Re concentration measurements acquired with alcohol extraction and the concentration after column, as well as measuring $\delta^{187/185}$Re NIST SRM 989 standard, which also follows column purification procedure. The isotopic composition of the stock Re solution used in sorption experiments is also determined, and all Re isotope values are presented relative to this measurement.

3.2.2.6 Mineral characterization

3.2.2.6.1 XRD

All synthesized minerals underwent purity checks through X-ray powder diffraction (XRD) utilizing a Bruker D8 diffractometer. The diffractometer used Cu radiation (λ = 1.54 Å) and a SolX Si(Li) solid-state detector. A step size of 0.026° was implemented, and XRD patterns were collected using an air-tight polymethyl methacrylate (PMMA) sample holder with a transparent dome to evade any potential oxidation in the 20° to 70° 2-theta range at room temperature. The lattice parameters and average crystallite sizes for all samples were calculated by utilizing the Debye-Scherrer equation and the Profex software(Doebelin and Kleeberg, 2015) with a free lattice parameter.

3.2.2.6.2 RAMAN Spectroscopy

Raman spectroscopy was used to monitor the direct nucleation of pure pyrite synthesis for 4 hours. The sampling rate was one Raman spectrum per minute. The Raman spectra were collected with a Raman RXN1 from Kaiser Optical Systems with an exposure time of 3 seconds. The spectra were averaged over three scans.

3.2.2.6.3 SEM and FESEM

Structural observations SEM images were collected with a Scanning Electron Microscope with 16 kV at ISTerre, Grenoble, France. The imaging method utilized backscattered electrons (BSE) and secondary electrons (SE). Several solid samples were additionally analyzed via a ZEISS Ultra Plus FESEM, which utilized an accelerating voltage of 3 kV at IPG, INP Grenoble. The preparation of the sample

involved delicately spreading a small amount of powder onto an electrically conductive carbon tape placed on the mount. The sample was metallized with Au before the measurement took place.

3.2.2.6.4 X-ray absorption spectroscopy

Re L-III edge XANES and EXAFS were collected at the Rossendorf beamline of the Helmholtz-Zentrum Dresden Rossendorf (HZDR, Germany). In the glovebox, 50 mg powder samples were filled into capton sealed holders, then stored in mylar bags, heat sealed, and shipped to the station in anaerobic bottles containing O_2-free nitrogen. To avoid photon-induced oxidation and to limit thermal perturbations, all data collection is performed in a closed-cycle He cryostat with the atmosphere at 15 K. XANES and EXAFS data were collected in fluorescence mode, and the Re references were collected in transmission mode with an 18-element solid state germanium detector (Ultra-LEGe, GUL0055, Mirion Technologies). The monochromator was calibrated by simultaneously measuring Re metal foil at L3 energy 10535 eV. The open source software ATHENA and the software package ARTEMIS were used to process the collected data. Theoretical backscattering paths were calculated using FEFF to fit in back-transformed reciprocal space(Ravel and Newville, 2005).

3.2.3 Results and discussion

The pyrite employed in this study (Figure 11) constitutes a highly pure mineralogical phase (>90%). Raman spectra were recorded during the synthesis, delineating the emergence of a metastable phase associated with FeS composition until the formation of pyrite (See Figure 12). Based on Fe(II) and ∑S(-II) solution concentrations measured across titration experiments within a pH range of 4 to 9, this pyrite exhibits lower solubility compared to the freshly synthesized pyrite in the study by Wang et al. (2020). EH values were measured in reactors both before and after the addition of Re(VII). No significant difference was observed between the two values (Figure 13). Interestingly, experiments conducted at low pH (>6) show a slight reduction in EH. Re adsorption was nearly negligible, with less than 0.1% being adsorbed by pyrite over a 15-day equilibrium period. Furthermore, no discernible difference in adsorption was noted among reactors balanced at different pH levels (Figure 14). This contrasts significantly with previous studies, possibly due to the absence of metastable FeS mineral phases in the pyrite used here, which also appears to be much less soluble than the other "fresh" pyrite employed.

Regarding coprecipitation experiments, all Re was effectively removed from the solution. XANES spectra exhibit similarities with the reference Re_2S_7, which corresponds to nanoparticles resulting from the combination of perrhenate with sodium sulfide, acidified with pure HCl (Figure 15). Therefore, the white line and the shape of the spectra indicate reduction of Re and coordination with sulphur atoms. Meanwhile, with regard to the EXAFS spectra, the optimal fit was achieved by modelling the coordination and distances of the Fe-S (N=6, 2.2 Å) and Fe-Fe (N=12, 3.8 Å) atoms of the pyrite structure. The final fit indicates that the central atom is coordinated with six sulfur atoms at a distance of 2.3 Å, which resembles the coordination observed in the references ReS_2, Re_2S_7 and ET_4NReS_4. The second layer corresponds to Fe atoms at a distance of 3.9 Å (Table 4). This EXAFS fit provides evidence that Re may be incorporated into the pyrite structure, replacing an Fe atom.

The isotopic composition ratio of $^{187/185}$Re measured in the solids obtained from adsorption and coprecipitation experiments shows no significant difference (Figure 16). Additionally, the values of the two systems measured in solids do not significantly differ from the solution containing the remaining Re.

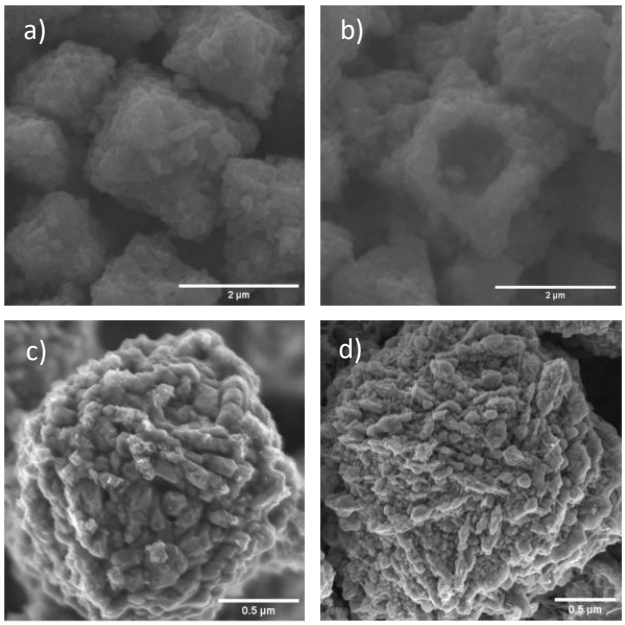

Figure 11 SEM and FESEM images of pyrite used for Re adsorption experiments (panels a and b) and Re doped pyrite solids with 3104 ppm (panel c) and 3.1 % (panel d).

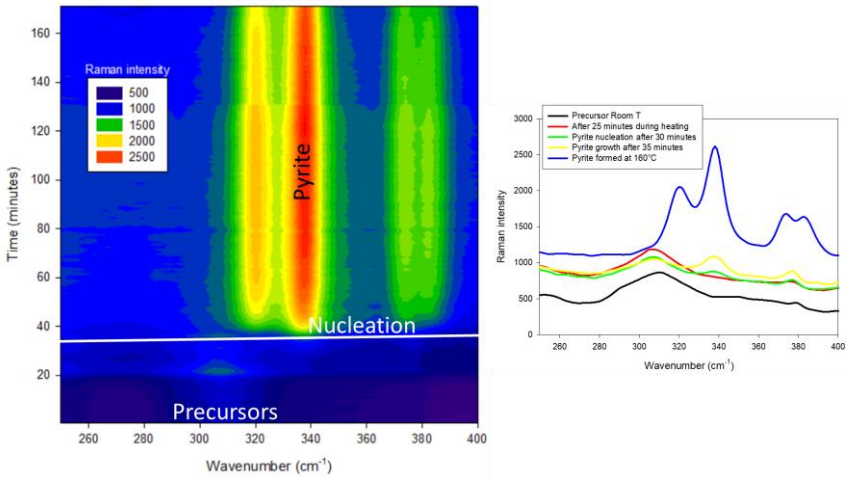

Figure 12 Left: Time-lapse Raman spectroscopy monitoring of the direct nucleation of pyrite (raw Raman spectra between 0 and 180 min). Right: Selected spectra showing the evolution of the pyrite peak (shape, intensity, and position) at different times.

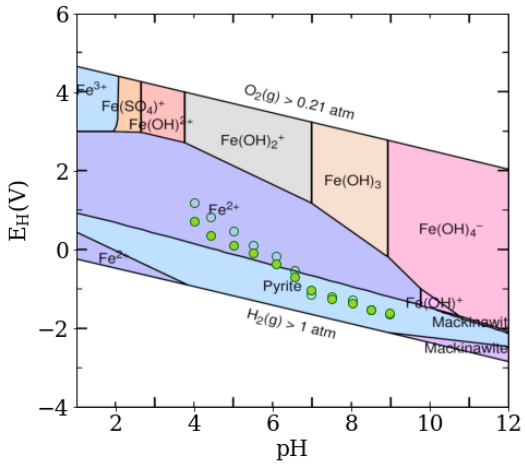

Figure 13 EH-pH values collected in Re(VII)-pyrite experiments plotted in the Fe-O-H (a) and Fe-S-O-H (b) EH-pH diagrams.

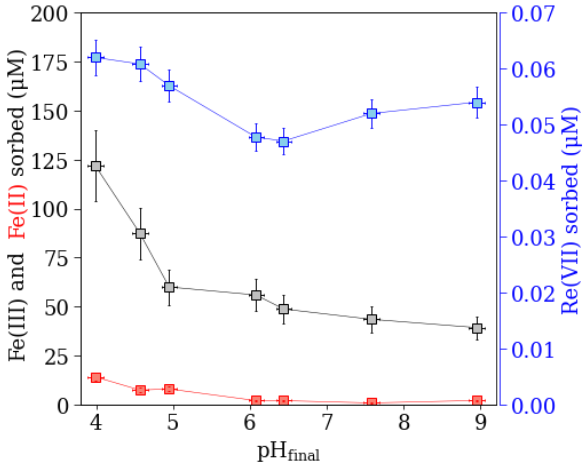

Figure 14 Sorbed measurement of total Re(VII) (blue circle), Fe(III) (black circle) and Fe(II) (red circle) after 24 h equilibrium time with pyrite at different pHs between 4 and 9. The initial Re concentration is 100 µM and the solid concentration is 2 g/L. The error bar corresponds to 0.1 pH measuring precision and 5% of the standard error of ICP-AES and UV-VIS.

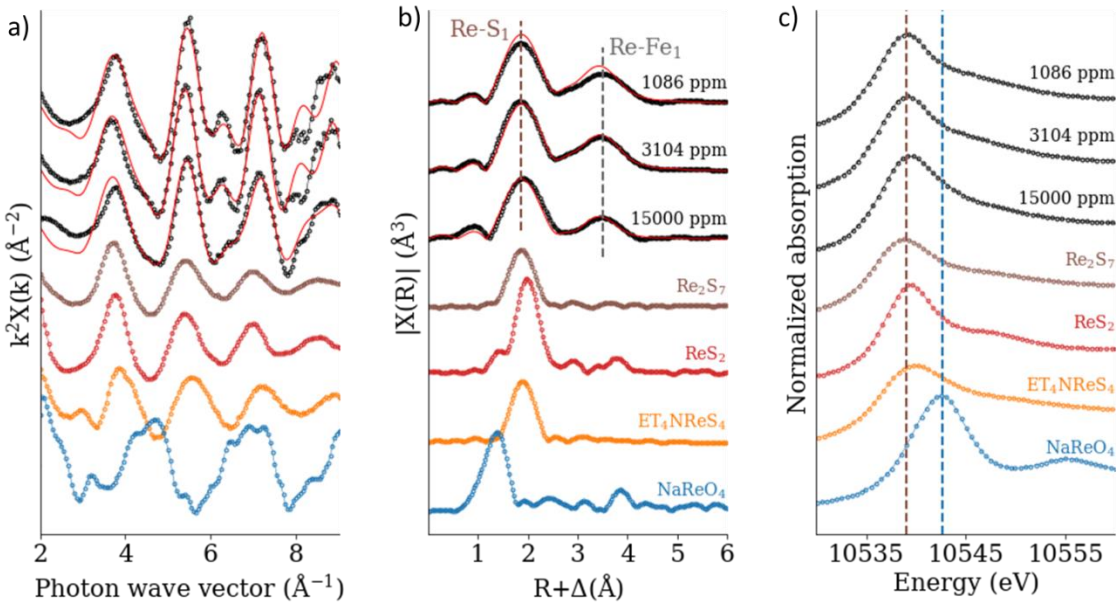

Figure 15 k^2-weighted chi functions EXAFS spectra (a) and its Fourier transform magnitudes (b) of Re L_3-EXAFS spectra of samples doped pyrite. Red lines represent the fit. c) Rhenium L_3-edge XANES for Re(VII) coprecipitation with pyrite experiments at different concentrations.

Table 4 EXAFS Parameters and interatomic distances calculated for Re(VII) doped pyrite samples

Sample	**Path**	**N [a]**	**R [b] [Å]**	**σ^2 [c] [Å^2]**	**ΔE_0 [d] [eV]**	**S_0^2 [e]**	**R-factor**
1086 ppm	Re-S.1	6[a]	2.32 (0.01)	0.006 (0.001)	6.7[a]	1[a]	0.012
R-range: 1.55:4	Re-Fe.1	12[a]	3.88 (0.01)	0.007 (0.011)	6.7[a]	1[a]	
3104 ppm	Re-S.1	6[a]	2.34 (0.01)	0.006 (0.001)	6.7[a]	1[a]	0.017
R-range: 1.55:4	Re-Fe.1	12[a]	3.91 (0.01)	0.007 (0.002)	6.7[a]	1[a]	
15000 ppm	Re-S.1	6[a]	2.34 (0.08)	0.007 (0.001)	6.7[a]	1[a]	0.03
R-range: 1.55:4	Re-Fe.1	12[a]	3.87 (0.04)	0.014 (0.002)	6.7[a]	1[a]	

[a]Coordination number for single paths, fixed value. [b]Interatomic distance. [c]Debye–Waller factor. [d]Shift of energy threshold. [e]Passive electron reduction factor.

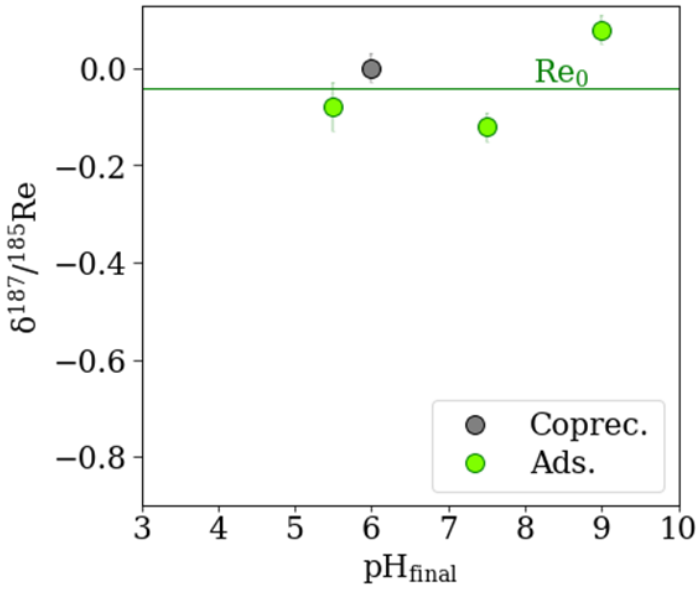

Figure 16 Re isotope compositions for selected pyrite samples for the adsorption and coprecipitation systems.

Chapter 4: Other interacting systems: Se-Pyrite and Gd-Magnetite

This chapter is constructed based on two articles. The first corresponds to "Revisiting the selenium interactions with pyrite: from adsorption to coprecipitation" which was published in *ACS Earth Space Chemistry* (https://doi.org/10.1021/acsearthspacechem.3c00219). The second article, titled "Characterisation of Magnetite Superparamagnetic Iron Oxide Nanoparticles Containing Gd: Dependence on the Fe(III)/Gd(III) Ratio" was submitted to *Environmental Science: Nano* Journal.

4.1 Revisiting the selenium interactions with pyrite: from adsorption to coprecipitation

Carolina Guida [1,2,3,‡], Vivien Ramothe [1,‡], Anthony Chappaz [2*], Pauline Simonnin [4], Kevin M. Rosso [4], Rong-Rong Ding [1,5], Damien Prieur [6,7], Andreas C. Scheinost [6,7], Laurent Charlet [1*]

[1] Univ. Grenoble Alpes, Univ. Savoie Mont Blanc, CNRS, IRD, Univ. Gustave Eiffel, ISTerre, 38058 Grenoble, France
[2] STARLAB, Central Michigan University, 48859 Mount Pleasant, Michigan, USA
[3] Grupo geología médica y forense, Universidad Nacional de Colombia, 111321 Bogotá, Colombia.
[4] Physical Sciences Division, Physical and Computational Sciences Directorate, Pacific Northwest National Laboratory, Richland, 99352 Washington, United States
[5] CAS Key Laboratory of Urban Pollutant Conversion, Department of Environmental Science and Engineering, University of Science and Technology of China, 230026 Hefei, China
[6] The Rossendorf Beamline at ESRF, 71 avenue des Martyrs, 38043 Grenoble, France
[7] HZDR Institute of Resource Ecology, 01328 Dresden, Germany.
[‡] co-first authors
[*] Corresponding author. E-mail address: charlet38@gmail.com & anthony.c@cmich.edu

Abstract

Interactions of selenium (Se), a trace element bio-essential at low concentrations but highly toxic at high concentrations, with the most abundant sulfide mineral in the Earth's crust, namely pyrite, was investigated over a wide range of time scales from nanosecond to days. At the nanosecond scale, selenate $Se(VI)O_4^{2-}$ adsorption onto the neat pyrite surface is shown by *ab-initio* computations to proceed via the formation of a chemical bond between an oxyanion oxygen atom and a surface Fe atom, weakening the other Se-O bonds and reducing Se atom oxidation state. At the hour-to-day scale, adsorption and coprecipitation of selenate $Se(VI)O_4^{2-}$ and selenite, $Se(IV)O_3^{2-}$, were investigated through wet chemical batch experiments at various pH values at different sulfide concentrations. Selenium removal from solution is slower and weaker for selenate than for selenite. After 24h, only 10% of selenate, against 60% of selenite (up to 100% in the presence of sulfide), is removed by the pyrite surface. Independently of its original oxidation state, adsorbed Se is completely reduced to elemental trigonal selenium via adsorption, precipitation or coprecipitation, as shown by XANES spectroscopy. Our EXAFS results, compared to published data on Se-rich pyrite, show a Se to S substitution within the pyrite structure. The reductive coprecipitation mechanism of selenium with pyrite represents valuable new insights for improving our understanding of modern and ancient biogeochemical cycles involving Se. In addition, several industries can benefit from direct applications of our findings, such as water treatment, green technologies, and sustainable mining.

4.1.1 Introduction

Positioned underneath sulfur (S) in the periodic table, selenium (Se), a redox-sensitive metalloid, shares similar features with this major element. Like S, it is enriched in geological settings buried under anoxic conditions (shales, coal (Fernández-Martínez and Charlet, 2009)) and displays a wide range of oxidation states ranging from -II to +VI with Se(-II), Se(-I), Se(0), Se(IV) and Se(VI) being the most predominant under natural conditions (Fernández-Martínez and Charlet, 2009; Fordyce, 2013). In aquatic systems, Se(IV) and Se(VI) species are usually dissolved, while Se(0) and Se(-I), and Se(-II) in the presence of iron minerals exhibit low solubilities (Chen et al., 1999; Scheinost and Charlet, 2008b). Its use as a paleo-redox proxy has been considered because of its different oxidation states and the occurrence of several stable isotopes in the environment (Stüeken and Kipp, 2020). The annual average production of Se is ~3,355 tons[9]. The main application is in metallurgy for producing electrolytic manganese as an additive in the steel manufacturing industry. Selenium is an essential nutrient fulfilling biological functions that cannot be substituted by any other elements. It is also used in the agricultural, food and pharmaceutical industries as an additive, fertilizer, dietary supplement, and fungicide to control dermatitis[9]. Some plants can uptake and metabolize Se as the ion selenate via the sulfate transporters (El-Ramady et al., 2016). For humans, the required Se intake is between 50 and 400µg/day(WHO, 1996). Se represent a bio-essential trace element involved in the enzyme glutathione peroxidase that converts peroxide into water and catalyzes the scavenging of free radicals, preventing oxidative damage to biological tissues (Chapman et al., 2004; Reich and Hondal, 2016). In contrast, Se can induce severe toxic effects on aquatic life at intake reaching 800 µg/day(WHO, 1996), causing deformities, lower reproduction rate, and higher mortality (Balistrieri and Chao, 1990).

The main natural sources releasing Se into aquatic systems are shale weathering processes and volcanoes (Fernández-Martínez and Charlet, 2009). The flux of Se from the ocean to the atmosphere represents, with volcanoes, the major source of atmospheric Se ($0.4 – 9 \times 10^3$ Se tons/year), with almost equal amounts released from the continents ($0.15 – 5.25 \times 10^3$ Se tons/year)(Wen and Carignan, 2007). Several industries also contribute to the release of anthropogenic Se in natural waters: coal mining, glassmaking, irrigation, pigment production, petroleum refining, coal combustions, and disposal of radioactive waste (Cao et al., 2014; Etteieb et al., 2021; Grambow, 2008). The latter is, in fact, a major source of the radioisotope ^{79}Se, a subproduct generated in nuclear power plants.

In aquatic systems, the speciation of Se controls its reactivity, transport, bioavailability, and potential toxicity. The predominant species in oxic waters are the oxyanions: selenate [$Se(VI)O_4^{2-}$], selenite [$Se(IV)O_3^{2-}$], and biselenite [$HSe(IV)O_3^-$] (Mason et al., 2018). Selenite is particularly bioavailable for most algae and cyanobacteria via the phosphate transporters(Vriens et al., 2016). Once internalized, it is converted to organic and volatile selenides (Simmons and Wallschläger, 2005; Vriens et al., 2016). Two volatile Se species: dimethyl selenide (DMSe) and dimethyl diselenide (DMDSe), are the main forms present in the atmosphere(Mason et al., 2018; Wen and Carignan, 2007). Selenium (VI) and Se(IV) can be sequestrated by adsorption and reduction reactions down to Se(0, -I, and -II) by several minerals (clay, iron oxyhydroxides, iron sulfide) and natural organic matter(Perrone et al., 2015). Selenium speciation in aquatic systems is governed by changes in pH and redox potential (E_H) (Figure 17). The chemical composition of the system, the type and amount of organic matter, and the microbiological activity also control the distribution of Se species in the environment (Simmons and Wallschläger, 2005). Thermodynamic calculations predict that selenate predominates in fully

oxygenated water, while selenite and biselenite are predominant species of hypoxic water (Belzile et al., 2000). Under reducing conditions, a large region of the E_H-pH diagram is occupied by reduced Se(0) species abiotically or biotically produced (Simmons and Wallschläger, 2005).

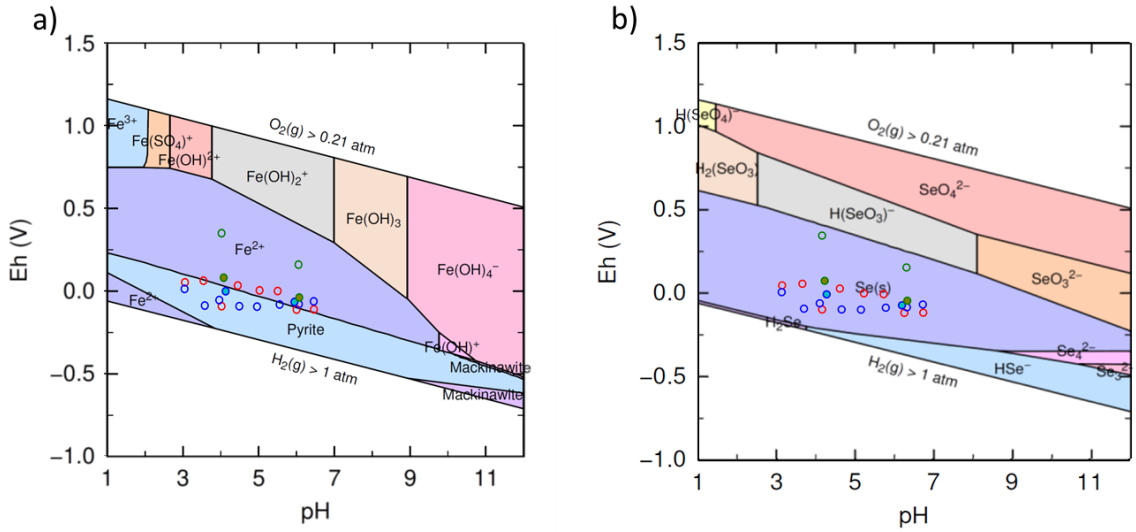

Figure 17 EH-pH values collected in Se-pyrite experiments plotted in the Fe-O-H (a) and Se-O-H (b) EH-pH diagrams.

The E_H values for the experiments were plotted with empty red dots for pyrite titration data, empty blue dots for the Selenate experimental data, empty green dots for Selenite experimental data, and the blue and green filled dots for experimental sorption data of selenate and selenite in the presence of added sulfide, respectively. The predominance diagrams were generated with the public domain code Phreeplot (Kinniburgh and Cooper, 2009), using the version 10a Thermodynamic database ThermoChimie (www.thermochimie-tdb.com). Eh-pH diagrams were constructed with 0.1 mM Se(VI), 1 mM Fe(II), 2 mM S(-II), and 10 mM NaCl.

Pyrite is the most abundant sulfide mineral and can be found in igneous, metamorphic, and marine sedimentary rocks as well as in submarine hydrothermal vents (Berner, 1984). The wide range of crystal chemical and surface properties displayed by pyrite – surface complexation, electron transfer, secondary mineral phases, short-range order, and structure sensitivity – makes this mineral an important redox catalyst for a multitude of reactions involving trace elements (Rickard and Luther, 2007), such as uranium (Descostes et al., 2010), molybdenum (Chappaz et al., 2014), arsenic (Nyström et al., 2021), Se (Manceau et al., 2020), and Tc (Rodríguez et al., 2020). A major environmental issue associated with the oxidation of pyrite is coal acid mine drainage. That process can release toxic trace elements in aquatic systems (Nyström et al., 2021). In natural pyrite, different reduced Se species are present within or at the surface, like ferroselite ($FeSe_2$) and dzharkenite (FeSe) (Ryser et al., 2005). Experimental studies demonstrated Se(IV) can be reduced to Se(0) in contact with a pyrite surface under anoxic and acidic conditions (Charlet et al., 2012; Kang et al., 2013). Probably, the electrons required for the reduction of Se(IV) are provided by the oxidation of Fe(II) and S(-II) phases (Jung et al., 2016; Kang et al., 2013, 2011). Few studies investigated the reduction of Se(VI) by pyrite. Selenate adsorbs weakly on pyrite making it challenging to characterize the Se(VI) – pyrite interactions. The reduction of Se(VI) to Se(0) involves the transfer of six electrons and the breakdown of four oxygen bonds; consequently, the reductive sorption process is very slow, and pyrite might have a low reactivity with selenate ions (Curti et al., 2013; Kang et al., 2013). A complete and detailed understanding of the mechanisms involved in reducing Se(VI) and Se(IV) when reacting with pyrite is still lacking.

To fill this knowledge gap, our goal was to thoroughly explore the Se(VI) and Se(IV) interactions with pyrite to meticulously characterize all the potential mechanisms involved, such as reductive adsorption and coprecipitation over different times scales. Furthermore, the role of dissolved sulfide during the Se reduction and adsorption processes when reacting with pyrite was investigated.

4.1.2 Materials and methods

4.1.2.1 Chemicals

Sodium selenite, 99% (Ref. 214485), sodium selenate, BioXtra (Ref. S8295), zinc acetate dihydrate, ≥98% (Ref. 383058), carbon disulfide, anhydrous, 99+% (Ref. 180173), sodium sulfide nonahydrate, ≥98% (Ref. 208043), sodium hydrosulfide hydrate (Ref. 161527), iron (III) chloride hexahydrate, ≥99% (Ref. 31232) and sodium chloride, ≥99.5% (Ref. 71379) were obtained from Sigma-Aldrich. Sodium hydroxide, ≥98% (Ref. 6771.3), was purchased from Roth, and hydrochloric acid, 32 % Extra Pure, SLR (Ref. 10458790) and nitric acid, 67 to 70% trace metal grade (Ref. A509P500) from Fisher Chemical.

All solutions were prepared with boiled, nitrogen-degassed Millipore 18.2 MΩ/cm water and stored in an oxygen-free glove box. All recipients were soaked in 5% HNO_3 for 24h, cleaned for 10 minutes in an ultrasonic bath, and rinsed three times with deionized water previously used. All experiments were done at room temperature in a Jacomex glove box filled with Ar, with a controlled oxygen partial pressure below 5 ppm.

4.1.2.2 Pyrite and Se-doped pyrite synthesis

Fresh pyrite was synthesized following the method proposed in previous literature (Wei and Osseo-Asare, 1996). Sixty mL of 0.05 M of Fe(III) solution was added drop by drop into 60 mL of 0.15 M HS^- solution. Then, 1 M NaOH solution drops were added to maintain a pH value of ~4. The final solution was agitated for five days. The FeS_2 precipitate was decanted and washed by replacing the supernatant with 0.2 M HCl solution six times, followed by acetone and carbon disulfide, to remove residual sulfur entirely from the solid surface. All the washing solutions were in contact with pyrite for a one-hour minimum. Finally, the suspension was washed, vacuum filtered with a 0.22 µm filter with degassed water six times, dried in the anaerobic chamber, and kept in degassed ultrapure water at 100 g/L solid concentration.

Se-doped pyrite synthesis was made according to the method proposed by Diener and Neumann (2011) (Diener and Neumann, 2011). A precise amount of Se(VI) and Se(IV) stock solutions were added to the HS^- solution before being mixed with Fe(III) solution. Then, following the same steps, Se coprecipitated with pyrite was synthesized similarly to the protocol described above. The final concentrations used in synthesizing Se-pyrite samples were 50, 75, 100, 130, and 150 µM for Se(IV) and 50, 75, and 100 µM for Se(VI). The supernatant was acidified with 100 µL 65 % HNO_3 prior to elemental analysis.

4.1.2.3 Pyrite titration and Se sorption on pyrite experiments

Several batch experiments were conducted at different pH (3 – 7.5), including a blank, which was prepared in glass bottles within Ar anoxic atmosphere. The initial concentration of pyrite was fixed to 2 g/L, and the ionic strength was adjusted to 10 mM with NaCl. pH was adjusted to selected values by either adding HCl or NaOH and was measured by a pH meter with pH/°C probe with 1 m cable (VWR pH110) calibrated with VWR buffers. After 24h of equilibrium, the solution was decanted. Then, 2 x 10 mL were taken from all solutions and filtered with a 0.45 µm pore size membrane filter. The first volume was stored in a tube with 100 µL of 100 mM Zinc acetate dihydrate (ACZn) stock solution for Fe(II) and ΣS(-II). The second volume was acidified with 100 µL of 65 % HNO_3 for ICP-AES measurements. Similar experiments were carried out for Se(VI) sorption experiments, adding a concentration of 100 µM selenate and including a blank with the initial concentration of selenate.

Nine experiments were carried out following the same experimental protocol: 6 with Se(IV) and 3 with Se(VI). A sulfide solution of 1 mM was added from a stock solution of sulfide that was prepared by dissolving washed transparent crystals of $Na_2S.9H_2O$ with degassed water. At the end of all batch experiments, pH and ORP values are measured (Figure 1). For all experiments, solid samples were collected after filtration, dried overnight, and preserved under an anoxic atmosphere.

4.1.2.4 Elemental analysis

ICP-AES. Total Se and Fe concentrations in the supernatant samples were determined by inductively coupled plasma atomic emission spectroscopy (ICP-AES, Varian 720 ES) at wavelengths 234,350 and Fe 238.204 nm for Fe and 196,026 nm for Se. 1000 ppm Fe and Se ROTH standards were used to prepare an external calibration with a range of 0.01 ppm - 25 ppm for Fe and Se concentration. Analytical precision (RSD) and recovery (CMS) were determined from replicate analyses (n=5 and n=2, respectively). The RSD calculated of 5 ppm standard was 1% for Fe and 1% for Se. The CMS was 97% for Fe and 99% for Se. The detection limits (DLs) for Fe and Se were 0.1 µM and 0.7 µM, respectively. The quantification limits (QLs) for Fe and Se were 0.4 µM and 2.2 µM, respectively.

Colorimetric methods. The ACZn solution samples were analyzed by colorimetric methods to measure the concentration of Fe(II) with the O-phenanthroline method (Fortune and Mellon, 1938) and ΣS(-II) with Sodium thiosulfate titration and Methylene blue method (Cline, 1969). Samples were analyzed at 513 nm and 670 nm for Fe(II) and ΣS(-II), respectively, with an Agilent Cary 300 UV-VIS. The DLs for Fe(II) and ΣS(-II) were 15.2 µM and 0.47 µM, respectively. The QLs for Fe(II) and ΣS(-II) were 46.1 µM and 1.47 µM, respectively.

4.1.2.5 Solid characterization

XRD. X-ray powder diffraction (XRD) patterns were collected in the 20° to 70° 2-theta range at room temperature using a laboratory Bruker D8 diffractometer with Cu radiation (λ = 1.54 Å), a SolX Si(Li) solid-state detector, and a step size of 0.026°. Into the air-tight polymethyl methacrylate (PMMA) sample holder with a transparent dome to avoid any possible oxidation, samples were placed inside the glovebox. For all samples, the lattice parameters and the average crystallite sizes were calculated using the Debye-Scherrer equation and the Profex software (Doebelin and Kleeberg, 2015), with a free lattice parameter.

SEM. SEM images were collected with a Scanning Electron Microscope with 16 kV at ISTerre, Grenoble, France. The sample was prepared by gently spreading a tiny quantity of pyrite on the surface of an electrically conductive carbon double-sided tape placed on the mount. The image detection mode used was backscattered electrons (BSE) and secondary electrons (SE).

BET. The specific surface area (SSA) was determined by the Brunauer−Emmett−Teller adsorption method (BET-N_2) at 77 K, using a Belsorp-Max (Bel Japan) volumetric gas sorption instrument. Inside the glovebox, 50 mg of pyrite was put in a glass cell and then dried under vacuum at 80 ^{o}C for 12 h. The SSA was calculated from the BET equation in the P/P0 range 0.05 – 0.31.

XANES, EXAFS and HERFD. X-ray Absorption Near-Edge Structure (XANES) and Extended X-Ray Absorption Fine Structure (EXAFS) were collected at the Rossendorf Beamline operated by Helmholtz-Zentrum Dresden Rossendorf (HZDR, Germany) (Scheinost et al., 2021). High-Energy-Resolution Fluorescence-Detected (HERFD) x-ray absorption spectroscopy was obtained at the French absorption spectroscopy beamline for ultra-high dilution samples (FAME-UHD). For XANES and EXAFS samples, 100 mg solid was homogenized with an agate mortar and then used to fill Kapton-sealed holders. For HERFD measurements, homogenized 40 mg of the solid samples and at least 10 mg of boron nitride were used to prepare 5 mm diameter pellets. All data collection was performed in a closed-cycle He cryostat with the atmosphere at 15 K to avoid photon-induced oxidation and to limit thermal disorder. XANES and EXAFS data were collected in fluorescence mode with an 18-element solid-state Germanium detector (Ultra-LEGe, GUL0055, Mirion Technologies), and the Se references were in a transmission mode recorded with ionization chamber filled with suitable gas mixture. HERFD, with a resolution of about 1-2 eV, used a beam with a size of 100*200 μm^2 and a 14-Si crystal analyzer spectrometer detection system. XANES and EXAFS spectra were calibrated with the simultaneous measurement of Au foil at L3 edge energy at 11902.9 eV. For HERFD data calibration, a Se foil was used before and after each sample scan at 12658.1 eV energy reference. The data collected was processed with the open-source software ATHENA program (Ravel and Newville, 2005). Linear Combination Fit (LCF) was performed using the Se spectra of standards collected in the beamtime and previous beamtimes conducted in the same line. Data from the EXAFS region was analyzed using the Artemis software package. Theoretical models based on the structures of trigonal (gray) Se, ferroselite ($FeSe_2$), and S-atom-centered pyrite were generated using the FEFF6 and ATOMS software packages to test for the existence of Se within or at the surface of pyrite.

4.1.2.6 Theoretical calculations

All calculations were carried out with periodic boundary conditions (PBC) in the plane-wave Vienna Ab initio Software Package (VASP) (Hafner and Kresse, 1997; Paier et al., 2005) electronic structure code. The simulations were performed within the generalized gradient approximation (GGA) with the exchange−correlation functional of Perdew, Burke, and Ernzerhof (PBE) (Perdew et al., 1996). The plane-wave calculations were carried out under the projector-augmented wave method with a kinetic energy cutoff of 400 eV (Blöchl et al., 1994). The total energy convergence criteria were set to be within 10^{-5} eV with a Gaussian smearing width of 0.05 eV to improve the convergence of orbital energies. The vacuum region between the two (100) pyrite surfaces was set to 30 Å (unless stated otherwise) to remove spurious interactions between the adsorbate and the periodic image of the bottom layer of the surface (Figure 18).

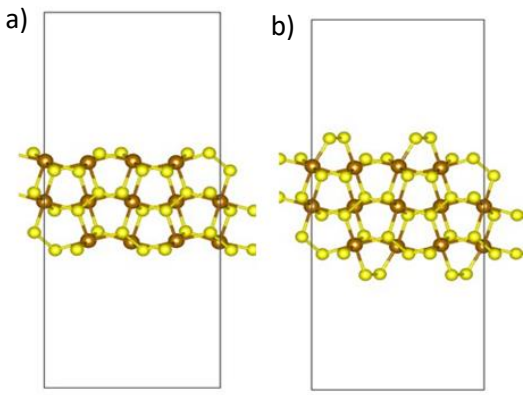

Figure 18 Side view of the two different (100) pyrite surfaces: a) The neat surface without disulfide terminations and b) with disulfide terminations.

The adsorption energy of the adsorbate species, ΔE, was calculated using the following expression:

$$\Delta E = E\_(\text{pyrite slab}) + E\_\text{adsorbate} - E\_\text{total} \quad (1)$$

where E_total represents the total energy of the pyrite slab with the molecule adsorbed on the surface, E_(pyrite slab) the total energy of the slab, and E_adsorbate the total energy of adsorbate in the gas phase (SeO_4^{2-}, SeO_3^{2-}…). Based on this definition, the larger the ΔE is, the more thermodynamically favorable the adsorption.

To investigate changes in the electronic structure when the molecule is adsorbed on the surface, the deformation charge density, Δρ(r), was calculated, which includes a direct comparison to the non-sorbed state:

$$\Delta\rho(r) = \rho\_\text{total}(r) - (\rho\_(\text{pyrite slab})(r) + \rho\_\text{adsorbate}(r)) \quad (2)$$

where ρ_total (r), ρ_(pyrite slab) (r), and ρ_adsorbate (r) are electron densities of the total system, the silver slab and the adsorbate in gas phase, respectively.

The charge transfer was studied by comparing the Bader charges (Henkelman et al., 2006; Sanville et al., 2007; Tang et al., 2009; Yu and Trinkle, 2011) between the slab surface and the gas phase molecule with the adsorbed state. The strength of bonds between the adsorbates and the surface was evaluated by calculating the charge density at (3,–1) bond critical points 〖∇ρ(r)〗_cp, corresponding to the zero-values of the gradient: ∇ρ(r)=0. These saddle points correspond to a minimum charge density along a bond path, providing a measure of the bonding strength in terms of the electronic overlap.

4.1.3 Results

4.1.3.1 *AB-Initio* calculations

According to our calculations, the neat surface has the lowest adsorption energy (3.46 eV vs. 1.44 eV) and therefore is a steadier adsorption surface. A bond appears to form between the selenate

and an iron atom of the pyrite surface in the adsorption process (Figure 19a). Thus, the remaining calculations were made on the selenate electronic properties adsorbed on the (100) neat surface.

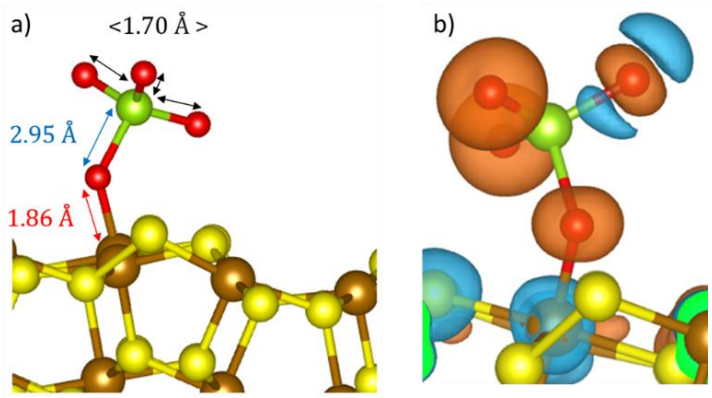

Figure 19 a) Most stable adsorption configuration of selenate on pyrite surface with the corresponding bond length. b) Close-up of the charge deformation of the electron in the energy range between -2.5eV and -0.5 eV at an isosurface value of 3.7×10-2 e-.Å-3.

Once adsorbed, the selenate ion undergoes a deformation induced by the 74 % elongation of the Se-O bond involving the oxygen atom interacting with the pyrite surface, while the remaining part of the oxygen atoms does not experience a significant change in bond length (0.6 % elongation). Interestingly, the Fe-O bond occurring at 1.86 Å is comparable to the original Se-O bond length found in selenate in the gas phase (see Table S 2), reflecting the strength of the Fe-O interaction. Neither the non-interacting O nor the Se show a significant loss of Bader charges (< 4 %). Thus, the absence of significant differences in these Se-O bond lengths is not surprising.

Geometrically, the selenate molecule is slightly inclined regarding the pyrite surface with an angle of 130.31°, while the remaining oxygen atoms form an O-Se-O angle (113.88°), very similar to the SeO_3^{2-} molecule (113.78°). Moreover, the interacting O atom experiences a loss of charge of 0.55 e-, one order of magnitude higher than the other O atoms, allowing the formation of a covalent Fe-O bond (Figure 19b). In Figure 19a, the blue area corresponds to a decrease in charge density, and the orange area is an increase in charge density at an isosurface value of 3.7×10^{-2} $e^-.Å^{-3}$, only observed in the oxygen atom furthest away from the pyrite surface. Interestingly this O atom does not display a significant change in Bader charge.

The projected density of states (PDOS) of both pyrite surface and selenate ion shows that the adsorption phenomena shift the whole spectra to lower energies (Figure 20). The pyrite's PDOS peaks at -14.80, 12.15, -3.53, -0,75, 0.54, and 1.82 are shifted on average by -0.27 eV to the corresponding peaks at -15.11, -12.40, -3.77, -0.98, 0.20 and 1.55 eV. Few gas phase peaks disappear at -13.58, -9.88, and 2.60 eV when selenate is adsorbed. The pyrite PDOS is mostly shifted in lower energies, whereas the selenate s orbital PDOS is completely changed. The selenate s orbital does not exhibit any density in unpopulated states and displays a density increase in the lowest energy states with three sharp peaks at -21.12, -17.82, and -9.87 eV and a broader one at -5.22 eV. The p and d orbitals are the most revealing because they show a shift in the lower energies with minimal density unoccupied states. The shift amplitude is accompanied by a modification of the peak shape, which prevents an average estimation of the shift magnitude. However, both p and d orbitals experience in the energy range [-2.5 - -0.5] eV indicating for pyrite and selenate an increased state density following the adsorption.

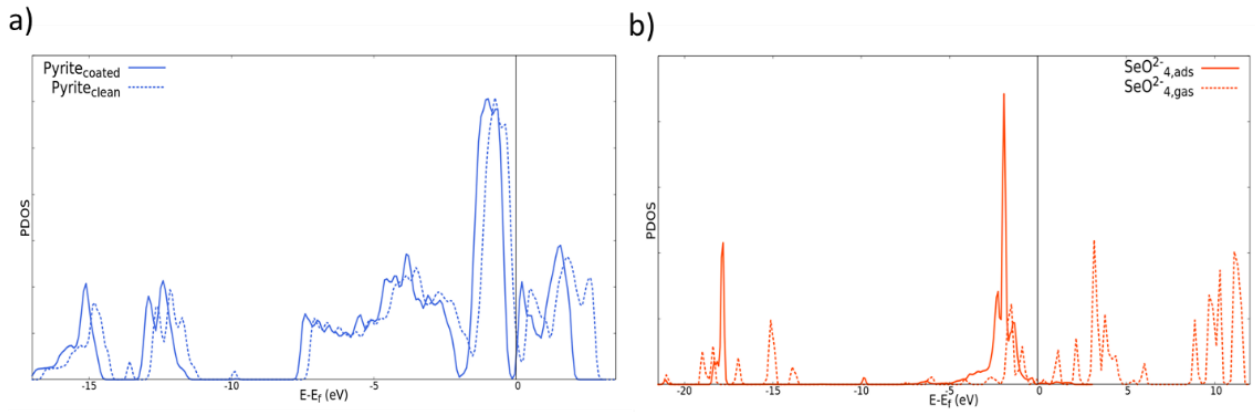

Figure 20 Projected density of states (PDOS) before (solid line) and after (dashed line) Selenate adsorption for all orbitals of a) the pyrite surface and b) Selenate ion.

Electrons for this energy range are the most susceptible to participate in a chemical bonding, therefore the spatial distribution of the electrons in this narrower energy range was examined. While the selenate ion forms a chemical bond with the pyrite surface, the bond between the O atom farthest from the surface and the rest of the molecule weakens as it loses electron density. This is consistent with the noticeable elongation of the Se-O of this involved O atom (1.70 Å) compared to the two others not participating in the chemical bonding with pyrite (1.69 Å) (Figure 19b).

Finally, the Nudge Elastic Band method was used to calculate the energy cost of dissociating an O atom from the selenate ion interacting with pyrite (Figure 20), creating a series of snapshots along the dissociation path. The calculated energy barrier of this process was 4.56 eV in the dissociation direction. However, the final image of the dissociation has higher energy than the first image (difference of 1.55 eV).

4.1.3.2 Experimental Se sorption on pyrite

4.1.3.2.1 Pyrite purity and solubility

The XRD spectra (Figure 21, blue line) show mainly typical reflexes of pure pyrite solid phase. Other peaks, displaying lower magnitude, demonstrate the presence of other minerals (up to ~20%), like marcasite, greigite, or mackinawite. The parameters obtained after the Rietveld refinements show a face-centered cubic unit cell parameter a = 5.4245 +/-1 Å (1) in good agreement with pyrite reference standards (00-037-0475 (*)). Crystallite sizes estimated from the Scherrer equation give values between 34.8 +/- 2.0 nm. The sharp diffraction peaks of the sample suggest good crystallinity. SEM image (Figure S 11) shows a large distribution of particles ranging from 500 nm to 2-3 µm. Finally, the specific surface area measured in the pyrite sample was 15 m^2/g.

SEM pictures show no changes in shape or size for pyrite equilibrated for 24 h at pH = 3, 5, or 7 (Figure S1). Fe(II) and ∑S(-II) concentrations for solutions equilibrated with pyrite at these different pH values are shown in Table S 3, Table S 4 and Figure 22. The measured Fe(II) concentrations ranged from 12 to 2985 µM, close to the total Fe concentration value measured with ICP-AES (Table S 3). The Fe(II) concentrations are higher at acidic pH. The ∑S(-II) values were below the detection limit for pH= 6.5 and 7.5, and equal to 105 µM at pH=4.5. Sulfide levels were higher for acidic pH and tend to decrease below pH=5. Measured E_H values ranged from -0.10 and 0.01 mV.

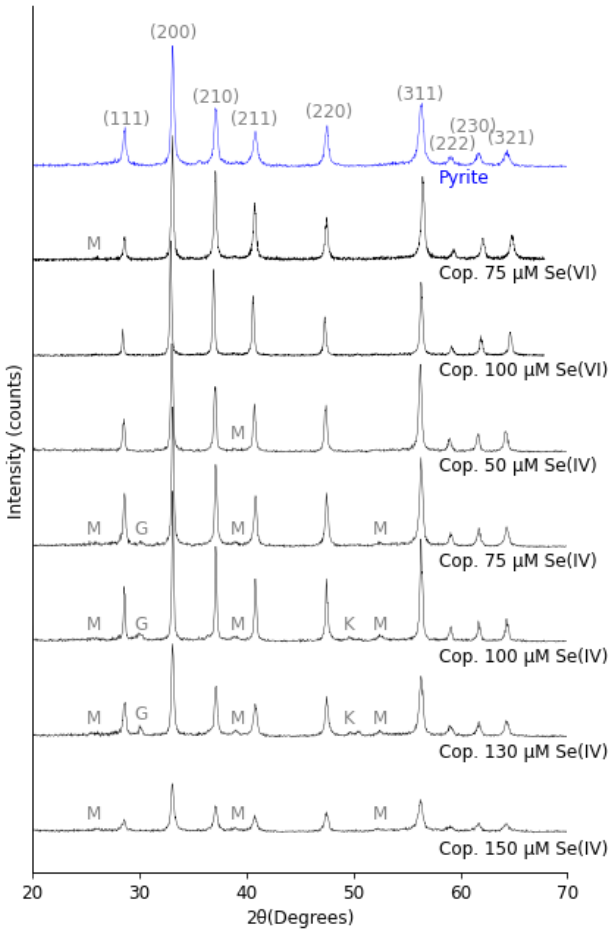

Figure 21 Raw data of XRD patterns measured from fresh pyrite and Se-doped pyrite synthesis (black line). The XRD peaks mainly show pyrite (blue line) and a minor fraction of marcasite (M), Greigite (G), and Machinawite (K). The references used correspond to 00-016-0713 (I) for greigite, 00-042-1340 (*) for pyrite, PDF 86-0389 for mackinawite, and 00-037-0475 (*) for marcasite.

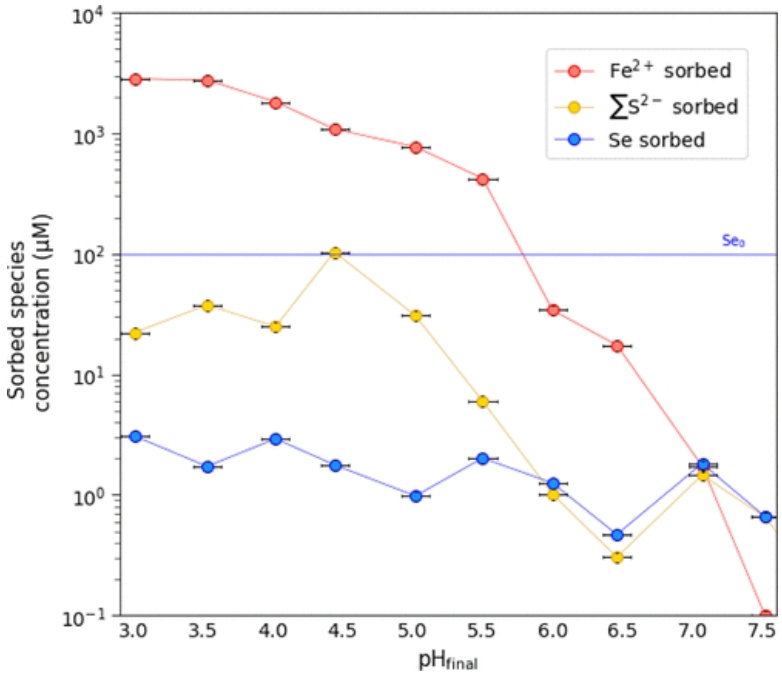

Figure 22 Sorbed measurement of Fe^{2+}, reduced sulfide species and total selenium, after 24 hours equilibrium time with fresh pyrite at different pHs between 3 and 7.5 in the presence of Se(VI), within sorption experiments. The error bar represents 0.1 pH measurement precision and 5 % of the standard error for ICP-AES and UV-VIS measurements.

4.1.3.2.2 Se(VI) adsorption on pyrite

In Se adsorption experiments, Fe(II) concentrations (Table S 3, Table S 4) were similar to total Fe concentrations for different pH values. The disparity between Fe(II) and total Fe measurements corresponds to a 5% standard error in both UV-VIS and ICP-AES measurements. In the Se-free experiments, the Fe(II) concentrations were 20 times higher at high pH and up to 50 times higher at low pH (Table S 3). As expected, the concentrations of Fe(II) are higher for lower pH values (3 – 6) than for neutral pH values (6.5 – 7.5). Sulfide concentrations ranged from ~0.5 to ~15 µM and were higher at acidic pH. They displayed lower concentrations for experiments where Se is present, indicating sorbed concentration in pyrite solid (Figure 22). The concentrations of adsorbed Se(VI) on pyrite varied between 1 (pH=5) and 6.4 µM (pH=3). Despite the low adsorption of Se(VI) within 24 hours (<2%), a slightly improved adsorption capacity is observed for acidic conditions (2-6% Se sorbed, pH<4.5). Finally, the measured E_H values were between -0.09 and 0.01 V (Figure 1).

No significant difference was observed for XANES-determined Se speciation for the samples equilibrated at pH 4 and 6. The white lines (E_{max}) for the XANES spectra for both samples are located between the E_{max} for the Se(IV) and Se(0) standards (Figure S 12a, Table S 6). The LCF results show these two samples are composed of trigonal, grey Se(0) (~80%) and Se(IV) (~20%) (Table S4). Similar results were found using XANES-HERFD for Se(VI) adsorbed on pyrite at pH=4 (See Figure S 12a, Table S 6).

4.1.3.2.3 Sulfide influence on Se adsorption

In the presence of sulfide, the Se(VI) adsorption on pyrite remains unchanged, and no enhancement is found. E_H values were 0.00 and -0.07 V for pH = 4 and 6, respectively. The XANES and HERFD-XANES findings additionally indicate that the samples primarily consist of trigonal grey Se(0) with a minor presence of Se(IV) (Figure S 12). In contrast with Se(VI), large Se(IV) adsorption on pyrite is observed (~40% improvement at pH=6 and ~60 % improvement at pH=4). The removal of Se(IV) when interacting with pyrite from both solutions (pH 4 and pH 6) was beyond 95% (Figure S 13). The speciation of Se was a mix of Se(IV) and Se(0) (Table S 5, Figure S 12). The measured E_H values for the experiments without sulfide and experiments with sulfide ranged from 0.35 to 0.16 V and from 0.08 to -0.04 V, respectively.

4.1.3.2.4 Selenium coprecipitation with pyrite

Similarly, to pure pyrite, the XRD diffractions show mainly peaks (~80%) associated with pure pyrite, yet with some impurities of marcasite, greigite, and mackinawite mineral phases (Figure 21). No significant difference between the mesh parameters or the particle size was found concerning the pyrite sample reference. Sharper peaks were observed for samples coprecipitated with 50, 75, and 100 µM of Se(IV) and with 75 and 100 µM of Se(VI). The samples with 130 and 150 µM of Se(IV) and 50 µM Se(VI) showed less pronounced peaks indicating a lower crystallinity than the pure pyrite.

All these samples display similar XANES features suggesting the Se speciation results from a mix of Se(IV) and Se(0) (Table S 5). HERFD-XANES spectra revealed distinct spectral features not observed in normal XANES spectroscopy. Notably, three additional features are evident in the co-precipitation samples: A form similar to the reference $FeSe_2$, a white line and shape of 100 µM Se(IV) co-precipitated sample resembling the reduced Se peak of Se(IV) adsorption sample equilibrated at pH 6 with sulfur addition; and analogous shape and energy characteristics between samples Se(IV)

adsorption equilibrated at pH 6 without sulfur addition and the 76 µM Se co-precipitated sample (Figure S 12, Figure S 14 and Table S 6).

For 50, 75 and 100 µM Se(IV) samples (about 1325, 1974 and 4037 ppm) measured with EXAFS (Figure 23), the crystal structures used for the fit are chosen considering (1) the sample matrix and (2) the possible choices of Se species that can be formed. The references used consisted of the pyrite structure (Rieder et al., 2007) involving a substitution of the central S atom by a Se atom (Manceau et al., 2020; Matamoros-Veloza et al., 2014), trigonal selenium (Se(0)), and Ferroselite (Se(-I)). The most appropriate fit of the spectra was using the five first single scattering paths of pyrite: Se-S.1 = 2.28 Å, Se-Fe.1 = 2.31 – 2.32 Å, Se-S.2 = 3.10 - 3.11 Å, Se-S.3 = 3.34 and Se-Fe.2 = 3.47 – 3.49 Å (Table 5). The atomic distances between the paths are similar to the values found by Manceau et al., 2020 in a natural pyrite with 500 ppm Se, and a little shorter than the values of Matamoros-Veloza et al., 2014 also in a natural euhedral pyrite with 670 ppm Se.

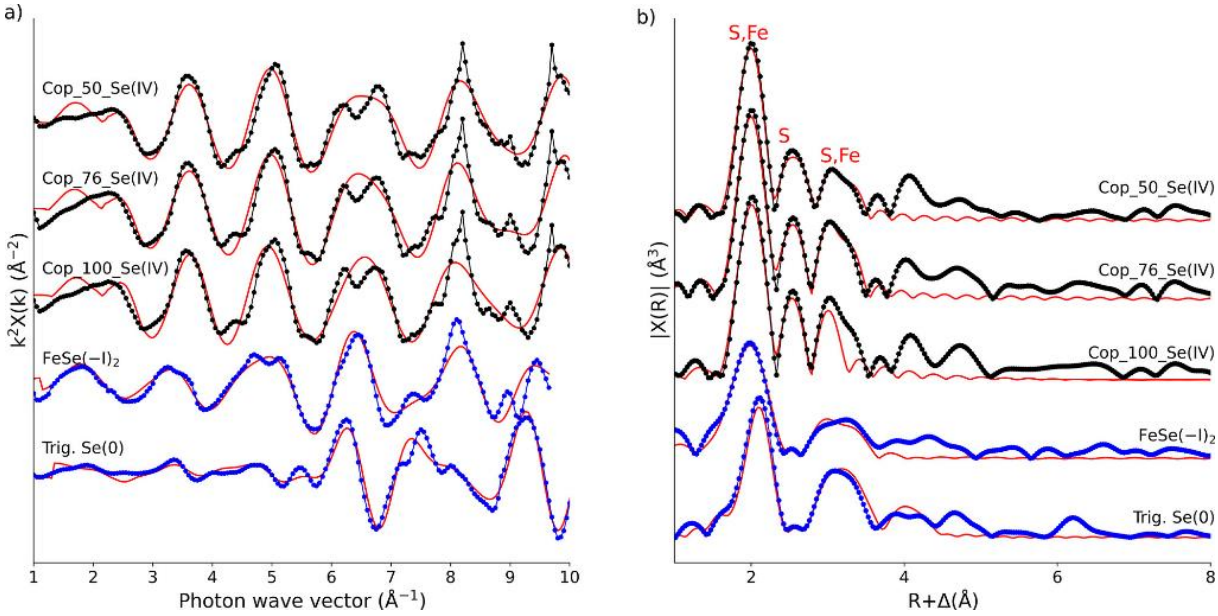

Figure 23 k_2-weighted chi functions EXAFS spectra (a) and its Fourier transform magnitudes (b) of Se K-EXAFS spectra measured at the Se K-edge of Se(IV) doped pyrite. The fit is represented by red lines.

Table 5 EXAFS Parameters and interatomic distances calculated for Se(IV) - pyrite coprecipitation samples

Sample	Path	N [a]	R [b] [Å]	σ^2 [c] [Å^2]	ΔE_0 [d] [eV]	S_0^2 [e]	R-factor
Cop_50 uM	Se-S.1	1.0	2.26 (0.04)	0.003[a]	6.58 (1.22)	0.898 (0.070)	0.014
r range: 1.45-3.5	Se-Fe.1	3.0	2.31 (0.01)	0.003[a]	6.58 (1.22)	0.898 (0.070)	
	Se-S.2	6.0	3.12 (0.02)	0.006 (0.002)	6.58 (1.22)	0.898 (0.070)	
	Se-S.3	6.0	3.36 (0.03)	0.006 (0.004)	6.58 (1.22)	0.898 (0.070)	
	Se-Fe.2	3.0	3.50 (0.03)	0.005 (0.003)	6.58 (1.22)	0.898 (0.070)	
Cop_76 uM	Se-S.1	1.0	2.25 (0.03)	0.003[a]	6.09 (0.77)	0.954 (0.064)	0.017
r range: 1.3-3	Se-Fe.1	3.0	2.31 (0.01)	0.003[a]	6.09 (0.77)	0.954 (0.064)	
	Se-S.2	6.0	3.10 (0.01)	0.005 (0.001)	6.09 (0.77)	0.954 (0.064)	
	Se-S.3	6.0	3.35 (0.01)	0.003[a]	6.09 (0.77)	0.954 (0.064)	
	Se-Fe.2	3.0	3.48 (0.01)	0.003[a]	6.09 (0.77)	0.954 (0.064)	
Cop_100 uM	Se-S.1	1.0	2.26 (0.04)	0.003[a]	6.51 (1.45)	0.900 (0.090)	0.024
r range: 1.1-3.3	Se-Fe.1	3.0	2.32 (0.01)	0.003[a]	6.51 (1.45)	0.900 (0.090)	
	Se-S.2	6.0	3.10 (0.02)	0.004 (0.003)	6.51 (1.45)	0.900 (0.090)	
	Se-S.3	6.0	3.33 (0.06)	0.003[a]	6.51 (1.45)	0.900 (0.090)	
	Se-Fe.2	3.0	3.41 (0.66)	0.023 (0.042)	6.51 (1.45)	0.900 (0.090)	
$FeSe_2$	Se-Fe.1	3.0	2.35 (0.01)	0.003[a]	5.04 (0.03)	0.822 (0.058)	0.039
r range: 1.5 - 4	Se-Se.1	1.0	2.48 (0.04)	0.003[a]	5.04 (0.03)	0.822 (0.058)	
	Se-Se.2	1.0	3.12 (0.05)	0.003[a]	5.04 (0.03)	0.822 (0.058)	
	Se-Se.3	4.0	3.22 (0.03)	0.007[a]	5.04 (0.03)	0.822 (0.058)	
	Se-Se.4	4.0	3.35 (0.01)	0.003[a]	5.04 (0.03)	0.822 (0.058)	
	Se-Se.5	2.0	3.44 (0.04)	0.003[a]	5.04 (0.03)	0.822 (0.058)	
Se^0 triclinic	Se-Se.1	2.0	2.39 (0.01)	0.003[a]	6.44 (1.39)	0.887 (0.058)	0.035
r range: 1.5 - 4	Se-Se.2	4.0	3.38 (0.01)	0.006 (0.001)	6.44 (1.39)	0.887 (0.058)	
	Se-Se.3	6.0	3.75 (0.01)	0.003[a]	6.44 (1.39)	0.887 (0.058)	
	Se-Se.4	2.0	4.33 (0.03)	0.008 (0.003)	6.44 (1.39)	0.887 (0.058)	

[a]Coordination number for single paths, fixed value. [b]Interatomic distance. [c]Debye–Waller factor. [d]Shift of energy threshold. [e]Passive electron reduction factor.

4.1.4 Discussion

4.1.4.1 Se(VI) – pyrite interactions

4.1.4.1.1 Initial adsorption from AB Initio calculations

Two reactive cleavage surfaces can be studied in *Ab-Initio* calculations. The cleavages consist of one surface with disulfide atoms and one corresponding to a neat surface without disulfide. These two possible surfaces in the [100] plane cannot be compared due to the difference in electron number between the two systems. The surface with disulfide terminations is discarded for several reasons, such as the low energy found when the Fe-S sulfurs start to join and disulfide bonds are formed, which explains why there is no experimental evidence of pyrite surface with a non-negligible amount of single Fe-S terminations. Furthermore, analyzing the surface more suitable for adsorption, the disulfide surface presents the highest adsorption energy, which makes it less stable (3.46 eV vs 1.44 eV). The last argument discussed further down is related to the adsorption of selenate, where a bond with a Fe atom is most likely to be involved (Figure 19a).

Regarding the interaction of Se(VI) with pyrite, it is theoretically feasible in terms of energy that the neat pyrite surface adsorbs the selenate molecule with an energy of 3.46 eV, promoting the creation of a bond between a Fe atom from the pyrite surface with an O atom from the selenate. Selenate deforms due to the elongation caused by the strong interaction that Fe has with O, which corresponds to a covalent bond, with an energy loss of 0.55 e^- observed in the respective oxygen. The new selenate geometry corresponds to the angles detected in the reduced selenite molecule, which may indicate that once adsorption is done within the first nanoseconds, reduction to selenite and oxidation of the pyrite surface are likely to follow.

PDOS analysis shows that the O atom further away from the pyrite increases in charge density, but because there is no significant change in the Bader charge, it must be compensated either by the deeper orbitals or by weakening its Se-O bond. The Se-O bond of this distant atom appears to weaken and, consequently, elongate to a distance of 1.71 Å, compared to 1.69 Å for the other two O atoms that do not interact with pyrite. However, it should be noted that a single O atom in the gas phase is highly unstable. Provided the furthest O atom from the pyrite surface is removed from the water molecule, a strong reaction with the surrounding solvent will occur. In addition, PDOS results indicate significant changes, especially in the p and d orbitals of both pyrite and selenate: lower energies with very few unoccupied density states and an increase of the density of state in the energy range between -2.5 eV and -0.5 eV, the energy range most likely to participate in a chemical bond. Further analysis of the projected state density between a hydrated selenate molecule with a neat pyrite surface is strongly recommended for a better understanding.

4.1.4.1.2 Factors controlling Se(VI) reductive adsorption processes over 24 hours

As indicated above, the first reaction between selenate and pyrite occurs within nanoseconds. However, the minimum equilibrium time that can be experimentally considered is 24 hours, in line with the analytical methods used. After this 24-hour period, the final solid had a selenium concentration just above the detection limit.

The interaction of Se(VI) with pyrite is significantly influenced by the synthesized pyrite product. Pyrite formation at low temperatures consists of the dilution-precipitation pathway of

intermediate phases such as nano-mackinawite and nano-greigite (Hunger and Benning, 2007). This occurs via a reductive coprecipitation pathway where Fe(III) is reduced to Fe(II) by S(-II) which is first oxidized to S(0) polysulfides, then to S(-I). The high solubility of pyrite measured at acidic pH during the pyrite titration experiments suggests the precipitate corresponds to a "fresh pyrite" or a "poorly" crystalized pyrite and it may contain metastable nano-minerals from precursor phases. Similarly, previous research reported elevated Fe concentrations after dissolving synthesized pyrite (pH < 5) (Wang et al., 2020). These findings align with a prior study[53], demonstrating that the stability of iron sulfides and their dissolution in ferruginous waters vary as a function of crystal size, pH, E_H, and ageing time (Son et al., 2022). These nano-sized mineral phases can also explain the higher specific surface area found (15 m^2/g^{-1}) than those previously documented in natural pyrites (0.06-1 m^2/g^{-1} (Bonnissel-Gissinger et al., 1998; Borah and Senapati, 2006; Weerasooriya and Tobschall, 2005; Yang et al., 2014)) with a better crystallization. High concentrations of Fe(II) were not determined for alkaline conditions because iron sulfides are more soluble under acidic conditions, and Fe(II) is soluble below pH 7.

Due to its inert character and negative charge, it is not surprising that only less than 10 % of Se(VI) was adsorbed and that the highest observed removal occurred at pH < 6. Se adsorption appears to have decreased the dissolved concentrations of Fe(II) and ∑S(-II) compared to those measured in the absence of selenium as seen in Figure 22 and Table S 3 and Table S 4. Selenium(VI) reduction or complexation in solution is discarded because there is no evidence of direct selenate sequestration with aqueous S(-II) in previous studies to the best of our knowledge and, after performing some blanks with 250 mM ∑S(-II) and 250 µM SeO_4^{2-}, at pH= 6 and 7, no Se(VI) precipitation was observed over six months. It is possible that Se(VI) and Fe(II) could precipitate, complex or form ternary surface complexes. After comparing the ion product to the only constant found in literature for $FeSeO_{4(s)}$ (Essington, 1988; Séby et al., 2001) (K=0.0015), the Se(VI)-pyrite system is not sufficiently saturated to form the precipitate. The influence of adding sulfide regarding Se(VI) adsorption is negligible in terms of the percentage of Se(VI) adsorbed or speciation. Similar findings were found in a previous study but adding Fe(II) to Se(VI) sorption experiments on pyrite, where the presence of Fe(II) did not improve Se(VI) removal(Charlet et al., 2012). XANES spectroscopy results show a reduction of Se(VI) adsorbed adding or not sulfide on pyrite, mainly as Se(0), close to other studies (Charlet et al., 2012; Mitchell et al., 2013). This finding is further supported by the measured E_H values plotted in the Pourbaix diagrams located within the domains of stability of Se(0) and pyrite (Figure 17).

In the reductive adsorption processes of Se(VI), a slightly more soluble polymorph of pyrite, should not be neglected, even when it constitutes less than 20% of the composition. Previous studies on the reduction of Tc in marcasite-pyrite and natural pure pyrite have given different results, in which the presence of marcasite slowed down the reduction(Rodríguez et al., 2021). Consequently, it is strongly recommended that additional research be conducted to explore the reactivity of Se(VI) in conjunction with Fe(II) and marcasite.

Our coprecipitation experiment with Se(VI) was not successful. The removal was minimal, and the quality of the collected XANES data was poor. It seems the small amount of Se(VI) that reacted was reduced to Se(0).

4.1.4.2 Factors controlling Se(IV) interaction with pyrite

4.1.4.2.1 Se(IV) adsorption experiments

Sulfide enhances the removal of Se(IV). This enhancement is not surprising since prior work shows that after 30 min, 5 mM sulfide reduces and precipitates 97.3% (±3.7) from 0.11 mM Se(IV) to Se(0) (Jung et al., 2016). On the other hand, Fe(II) released by pyrite can also influence the amount Se(IV) removed. The concentration of dissolved Fe(II) (measured) saturated the batch solution according to the $FeSeO_3$ solubility constant ($K = 10^{-9.99}$) and could have led to the precipitate formation (as observed on clay; see (Charlet et al., 2007; Séby et al., 2001)). Supporting the potential formation of $FeSeO_3$, our new HERFD-XANES results do indicate the presence of Se(IV) and Se(0) only for the Se(IV) experimental products, independently of the presence of sulfide. Moreover, in the samples without sulfide, at pH=4, which display a higher concentration of dissolved Fe(II), the percentage of removed Se(IV) is higher. In agreement, the E_H values plotted on the Pourbaix diagrams indicate an equilibrium phase close to the boundaries between Se(0), $H(SeO_3)^-$, and Fe(II).

4.1.4.2.2 Se(IV) doped pyrite

The coprecipitation of Se(IV) with pyrite is a fast and efficient process, as demonstrated by prior studies (Diener et al., 2012; Diener and Neumann, 2011). Se(IV) coprecipitation at the three concentrations studied, as revealed by XANES and EXAFS results, exhibits indistinguishable local structural parameters. This suggests a consistency in both chemical composition and crystal structure even when examining samples doped with up to 4037 ppm Se. The XANES peak for all three samples investigated in our study is located between Se(IV) and Se(0) and with a similar shape to trigonal Se reference. On the other hand, HERFD-XANES mainly indicates the presence of a Se(-I) due to the similarity of the shape to the $FeSe(-I)_2$ reference. The correspondence between the white line HERFD-XANES spectra of pyrite doped with 100µM Se(IV) with the spectrum of the Se(IV) sample adsorbed at pH6 adding sulfur, suggests a possible formation of SeS_2 on the pyrite surface due to an excess of S. This observation can also be supported by the fact that the EXAFS fit obtained with 100 µM Se(IV) was less optimal, accompanied by a slightly elevated Debye-Waller factor and R-factor. Comparable findings were reported for samples prepared with a similar protocol (Diener et al., 2012). Nevertheless, it is unclear whether Se is reduced to Se(-I) or Se(0) (Diener et al., 2012). On the other hand, our EXAFS results suggest that Se replaces an S in the pyrite structure, analogous to the previous natural Se-pyrite studied by Manceau et al., 2020 and Matamoros-Veloza et al., 2014 where Se is reduced to Se(-I) based on stoichiometry. This is different from the Diener study that concluded the incorporation of Se as amorphous Se(0) with a Se neighbour in the coordination layer at ~ 2.3 Å (Diener et al., 2012). It remains uncertain if this disparity is due to a different EXAFS adjustment strategy or to different experimental conditions.

The main host for Se is iron minerals, predominantly pyrite found in shales. Selenate and Selenite become toxic at elevated concentrations, often originating from anthropogenic sources like coal mining or radioactive waste. Our new findings suggest that the addition of S(-II) enhances the adsorption of pyrite, proving to be an effective treatment for removing Se(IV) from polluted waters or mining waste. However, the pyrite reductive adsorption mechanism demonstrates significantly greater efficiency for Se(IV) compared to Se(VI). To address the reversible desorption of Se, the reduction of both Se(VI) and Se(IV) to low-solubility Se(0) or other reduced Se species (Se(-I), Se(-II)) offers a stable solution, surpassing the efficacy of mere complexation or adsorption of the original oxyanions. Furthermore, integrating Selenium within the pyrite stoichiometric structure may emerge as a more effective treatment avenue. This approach has the potential to minimize the mobility of precipitated, reduced Selenium species, as demonstrated by Poulain et al. in 2022 (Poulain et al., 2022). Considering the low reactivity of Se(VI) with pyrite, a promising strategy for future studies to enhance removal

involves incorporating zero-valent iron. Zero-valent iron appears to facilitate the conversion of Se(VI) into Se(IV) and Se(0), thereby enhancing Selenium reduction processes (Das et al., 2017).

Se has emerged as a promising paleo-redox proxy in marine sediments due to its heightened concentration in anoxic environments, elevated redox potential, and sensitivity to both global and regional perturbations over relatively short timescales (Kipp et al., 2020; Stüeken and Kipp, 2020). This study marks a significant advance in our understanding of ancient processes leading to selenium accumulation in pyrite within sulfidic environments. It reveals a pathway involving oxyanion reduction to Se(0) and Se(-I), shedding light on intricate mechanisms. The detailed mechanism explored in this study includes reductive adsorption, Se incorporation in the pyrite lattice, and sulfide precipitation, laying valuable groundwork for future Se isotopic studies in both natural and experimental samples. This forthcoming research, complementing our investigation, holds the potential to deepen our understanding of the mechanisms elucidated here and capture the occurrences of anoxic events, spanning from modern times to Earth's stepwise oxygenation.

4.1.5 Supplementary information

Table S 2 Bond length, bond angles, and Bader charges of atoms in the gas and hydrated phase for the selenate ion.

	Se-O bond length (Å)	O-Se-O angle (°)	Se charge (e-)	O charge (e-)
Gas	1.69	109.47	2.49	-1,12
Hydrated	1.68	109.47	2.67	-1.04

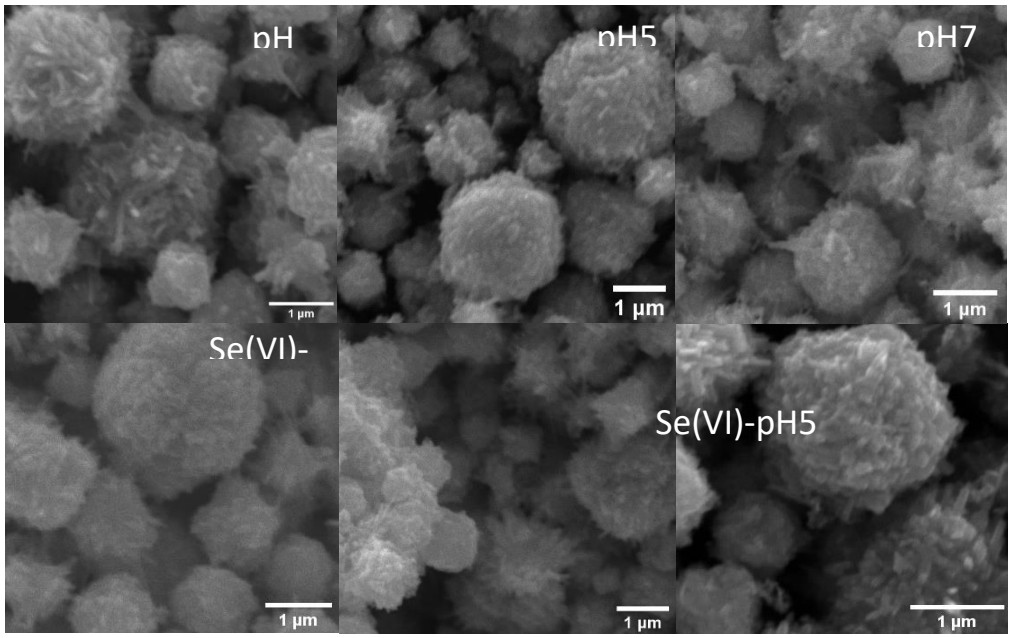

Figure S 11 SEM images of pyrite before and after Se(VI) sorption.

Table S 3 Fe(II), ΣS(-II), and Fe total from pyrite dissolution after equilibrium at different pH between pH=3 and 7.5

pH final	[ΣS(-II)] µM	[Fe total] µM	[Fe(II)] µM[a]
3.0	37	2956.1	2985
3.6	52	2831.9	2845
3.9	31	1891.0	1872
4.5	104	1143.8	1102
4.9	31	781.0	787
5.5	6	431.5	433
6.1	1	135.6	69
6.5	nd	43.8	40
7.1	2	14.3	14
7.5	1	17.6	12

[a] The disparity between Fe(II) and total Fe measurements corresponds to a 5% standard error in both UV-VIS and ICP-AES measurements.

Table S 4 pH, E_H, Fe(II), ΣS(-II), Fe total, and Se sorbed from pyrite after 24 hours equilibrium at different pH between pH=3 and 7.5

ID_Sample	pH final	E_H final V	[Fe total] µM	[Fe(II)] µM[a]	[ΣS(-II)] µM	[Se total] sorbed µM	Kd (mL/g)
pH3-Se(VI)	3.0	0.052	1220.9	1186	69	6.4	14.7
pH3.5-Se(VI)	3.5	0.062	87.9	84	14	1.7	8.2
pH4-Se(VI)	4.0	-0.092	624.2	626	64	4.6	6.0
pH4.5-Se(VI)	4.4	0.033	21.2	19	nd	1.8	8.5
pH5-Se(VI)	5.0	0.004	16.8	16	nd	1.0	4.7
pH5.5-Se(VI)	5.5	0	12.2	11	nd	2.0	9.6
pH6-Se(VI)	6	-0.112	23.9	35	nd	-	-
pH6.5-Se(VI)	6.5	-0.111	21.5	22	nd	-	-
pH7-Se(VI)	7.1	-0.128	11.8	12	nd	1.8	8.6
pH7.5-Se(VI)	7.5	-0.176	12.9	13	nd	0.7	3.1

[a] The disparity between Fe(II) and total Fe measurements corresponds to a 5% standard error in both UV-VIS and ICP-AES measurements.

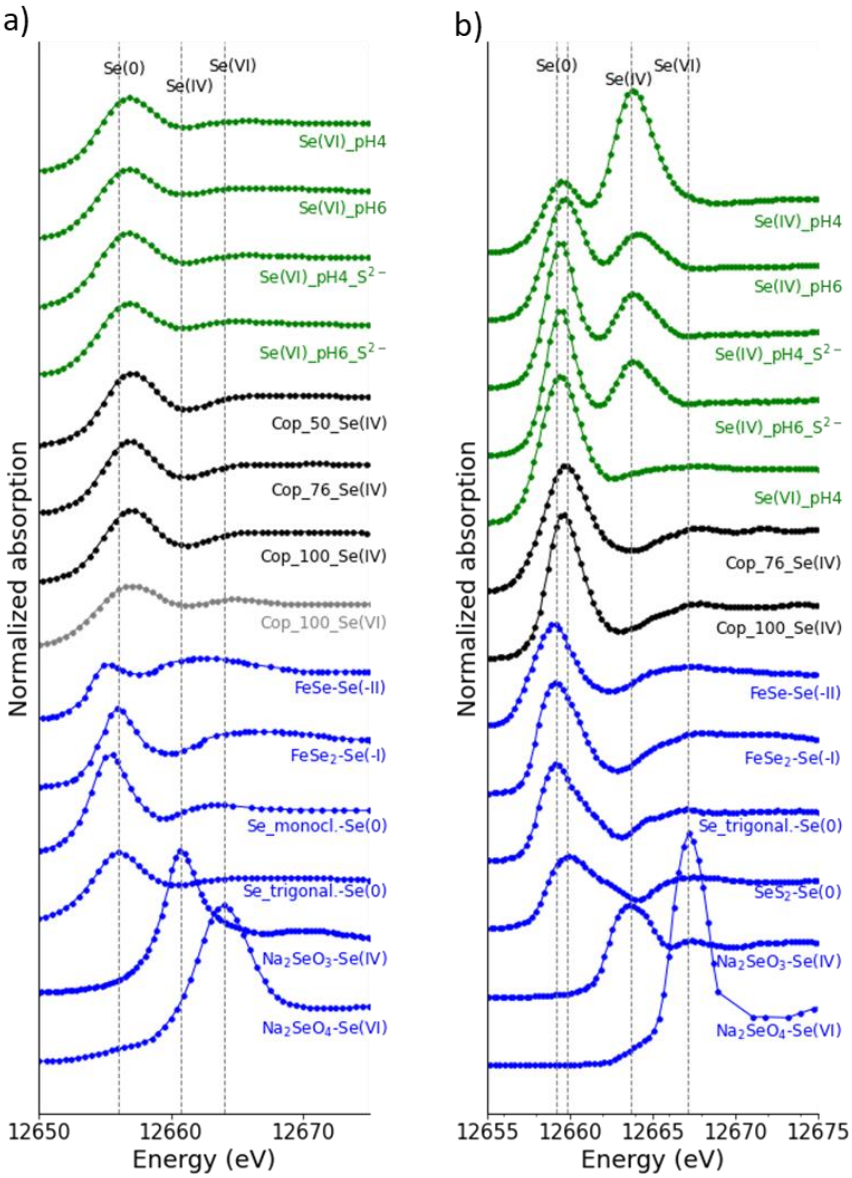

Figure S 12 Selenium K-edge XANES (a) and HERFD-XANES (b) spectra of Se(VI) sorption experiments with pyrite at pH 4 and 6 (green line), the coprecipitation Se(IV) (black line) and Se(VI) samples (grey line), and the standard spectra (blue line).

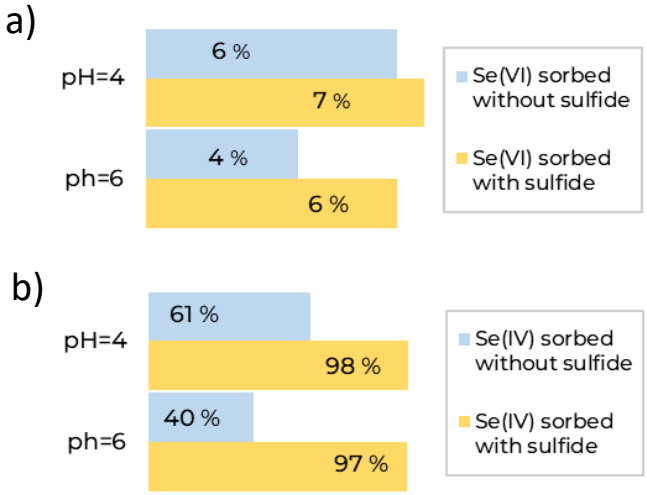

Figure S 13 The percentage of selenium sorption on pyrite with and without aqueous sulfide in solution and with different Se species: a) Selenate (Se(VI)). b) Selenite (Se(IV)). The percentage was calculated from ICP data in the supernatant after 24 hours of equilibrium and at pH=4 and 6.

Table S 5 Percentage of Se components of Selenium K-edge XANES spectra of Se sorption experiments calculated by the linear combination fitting method (LCF) in ATHENA code. The Linear Combination Fitting (LCF) analysis resulted in the best fit among all combinations tested, with the Se references plotted in Figure S 12**.**

Sample	**Se amorphous - Se(0)**	**Na_2SeO_3 - Se(IV)**	**Reduced chi-square**
Se(VI)-pH4	91%	9%	0.006
Se(VI)- pH6	89%	11%	0.01
Se(VI)-pH4 with sulphide	90%	10%	0.009
Se(VI)-pH6 with sulphide	86%	14%	0.01
Se(IV)-Cop-50 µM	98%	2%	0.0055
Se(IV)-Cop-75 µM	99%	1%	0.005
Se(IV)-Cop-100 µM	98%	2%	0.0048
Se(VI)-Cop-100 µM	92%	8%	0.0048

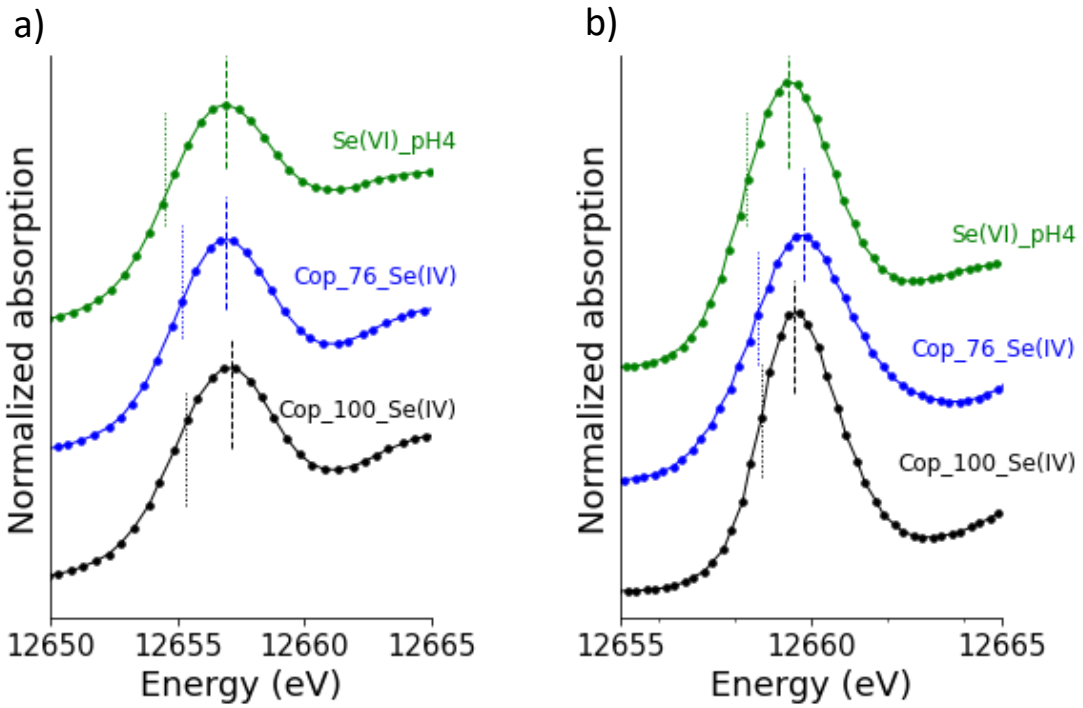

Figure S 14 Comparison of Selenium K-edge XANES (a) and HERFD-XANES (b) spectra of Se(VI) sorption experiment with pyrite at pH 4 (green line) and two coprecipitation Se(IV) (blue and black line) spectra. The white line and absorption edge are indicated by dashed and dotted lines, respectively.

Table S 6 White line and absorption edge of Selenium K-edge XANES and HERFD spectra of Se sorption experiments.

	XANES		HERFD	
Sample	**White line**	**Absorption edge**	**White line**	**Absorption edge**
Se(VI)-pH4	12656.9	12654.5	12659.4	12658.3
Se(VI)- pH6	12657.0	12654.5		
Se(VI)-pH4 with sulphide	12656.9	12654.4		
Se(VI)-pH6 with sulphide	12656.9	12654.9		
Se(IV)-pH4			12659.5	12658.5
Se(IV)- pH6			12659.8	12658.5
Se(IV)-pH4 with sulphide			12659.6	12658.5
Se(IV)-pH6 with sulphide			12659.5	12658.6
Se(IV)-Cop-50 µM	12656.9	12655.4		
Se(IV)-Cop-76 µM	12656.9	12655.2	12659.8	12658.6
Se(IV)-Cop-100 µM	12657.1	12655.3	12659.55	12658.7
Se(VI)-Cop-100 µM	12657.0	12654.6		
FeSe	12658.9	12657.2	12659.0	12657.8
$FeSe_2$	12659.0	12658.0	12659.1	12658.0
Monoclinical Se	12659.5	12657.9		
Trigonal Se	12659.3	12657.8	12659.2	12658.1
SeS_2			12660.0	12658.6
Na_2SeO_3	12663.5	12662.7	12663.6	12662.4
Na_2SeO_4	12667.9	12666.2	12667.2	12666.0

4.2 Characterisation of Magnetite Superparamagnetic Iron Oxide Nanoparticles Containing Gd: Dependence on the Fe(III)/Gd(III) Ratio

Carolina Guida,[*a,b,c] Agnieszka Poulain, [*a] Anthony Chappaz, [b†] Jean-Marc Grenèche, [d] Alexandre Gloter,[e] Nicolas Menguy,[f] Nathaniel Findling,[a] Philippe Le Bouteiller [g] and Laurent Charlet [a†]

[a] Univ. Grenoble Alpes, Univ. Savoie Mont Blanc, CNRS, IRD, Univ. Gustave Eiffel, ISTerre, 38000 Grenoble, France.
[b] STARLAB, Earth & Atmospheric Sciences, Central Michigan University, Mount Pleasant, Michigan 48859, USA.
[c] Grupo geología médica y forense, Universidad Nacional de Colombia. Apartado Aéreo, Bogotá, Colombia.
[d] Institut des Molécules et Matériaux du Mans, (IMMM CNRS UMR 6283), Le Mans Université, F-72085 Le Mans, France.
[e] Laboratoire de Physique des Solides, Université Paris-Saclay, CNRS UMR 8502, 91405, Orsay, France.
[f] Sorbonne Université, Muséum National d'Histoire Naturelle, IRD, Institut de Minéralogie, de Physique des Matériaux et de Cosmochimie (IMPMC UMR CNRS 7590), F-75005, Paris, France.
[g] HYMAG'IN, 38400, Saint Martin D'Hères, France.
* Equal first authors
[‡] Corresponding author. E-mail address: anthony.c@cmich.edu & charlet38@gmail.com

Environmental Significance

The use of Gadolinium-based contrast agents (GBCAs) in hospitals, and the presence of gadolinium as an emerging contaminant in hospital wastewater remain a global challenge for environmental science. By providing new insights into the sequestration mechanism of Gadolinium by magnetite by coprecipitation or adsorption, our research contributes both to the development of Gadolinium-based particles as an environmentally friendly medical device and to Gd trapping mechanism in waste sludge and sediments, allowing a better prediction of exposure and toxicity in aquatic environments.

4.2.1 Introduction

A promise superparamagnetic iron oxide nanoparticle synthesis containing Gd was characterized, revealing size and morphology independence from Gd content between 1 to 5% Gd replacing Fe(III). The size of Gd-doped nanoparticles ranged from 5 to 50 nm and exhibited a pure magnetite mineralogical phase.

Water is a crucial resource for the expanding global population. While new techniques for purifying water exhaust and drinking water are emerging, there is a need for the designing and synthesis of novel compounds that are versatile and adaptable for diverse industrial applications to prevent pollution. Gadolinium-based contrast agents (GBCAs) have been widely used in medical magnetic resonance imaging (MRI) since the 1980s.(Lux and Sherry, 2018) The new generation of Gd-complexes is very stable and non-reactive with the human body. However, their environmental impact remains poorly understood. Increasing levels of Gadolinium (Gd) have been reported in aquatic systems near major urban centers(Altomare et al., 2020; Rogowska et al., 2018; Souza et al., 2021). For example, the San Francisco Bay water experienced a ~70% increase in Gd concentration within a ~8-year interval.(Hatje et al., 2016) The release of Gd in the environment both in the United States of America and in the European Union is estimated to be equal to ~21 tons/year and ~19 tons/year, respectively.(Brünjes and Hofmann, 2020) It is expected that, due to the continuous growth of medical applications, the concentration of anthropogenic stable organic Gd complex in aquatic systems will keep increasing (Kaegi et al., 2021; Kümmerer and Helmers, 2000) and will have to be - poorly - removed by sorption and particle sedimentation, unless new retention techniques are implemented to treat hospital sewage waters or new non-bio-accumulable MRI contrasting agents are developed.

Magnetite is widely used as a powerful remediation agent due to its low production cost, redox-active behaviour, magnetic properties, and capability to adsorb contaminants efficiently(Cheng et al., 2018; Gorski and Scherer, 2010). GBCAs poorly adsorb on sediment iron particles, as could be observed after adsorption experiments of Dotarem® and Gadopentetic Gd-based acid contrast agents on industrial nanomagnetite particles (Figure 24, Figure S 21). In contrast, free Gd has a high affinity with magnetite nanoparticles and these particles could be used for medical applications.

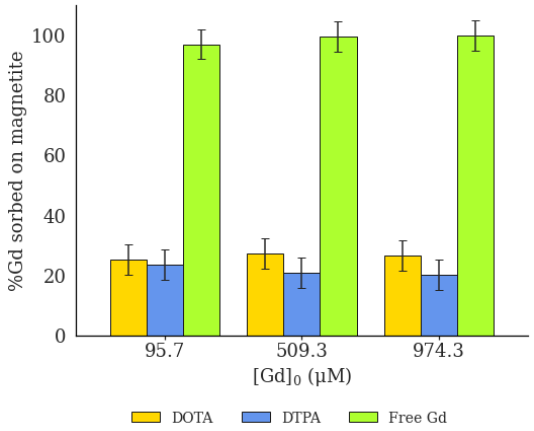

Figure 24 Adsorption percentage of Gd on magnetite in three chemical forms: Gadoteric acid or Dotarem (DOTA), Pentetic acid or diethylenetriaminepentaacetic acid (DTPA), and Gd(III) after $GdCl_3 \cdot 6H_2O$ dissolution, with three initial concentrations (95.7, 509.3, and 974.3 µM). Other experimental conditions include m/V = 5 g L^{-1}, [NaCl] = 0.1 mol L^{-1}, T = 25 ± 1 °C, equilibrium time: 24 hours, and a fixed pH of 7.5 with HEPES.

Gd-free magnetite nanoparticles are already used in biomedicine and in MRI imaging (Martins et al., 2021; Wallyn et al., 2019). Furthermore, commercially available magnetic particles MRI contrasting agents, are biodegradable in the environment and exhibit lower toxicity with proper surface coating than alternative contrast agents (Ghobril et al., 2013; Gupta and Gupta, 2005). However, the design of these iron nanoparticles (NPs) needs to be improved to allow the most effective combination of magnetic hyperthermia therapy and contrast imaging in the same nanoformulation in order to reduce the dose injected into the patient (Cotin et al., 2021).

Previous studies have shown that the stable incorporation of metals, such as Co(II), Zn(II), Cr(III), within the crystal lattice of magnetite is possible (He et al., 2015; Li et al., 2020). Only a limited number of studies have attempted to characterise synthesis pathways that incorporate Gd into the structure of nanomagnetite (He et al., 2015; Janani et al., 2021). Their characterisation is not fully clear, for example, it is unknown whether Gd can be incorporated into the magnetite structure or if it adsorbs on the surface. This information is crucial for planning an appropriate organic coating to protect against Gd release. Additionally, the impact of Gd substitution within magnetite on the synthesis of maghemite vs. magnetite needs to be precise. Maghemite is less interesting for industrial uses as partially oxidized magnetite reactivity and magnetic susceptibility decrease, following the decline or absence of structural Fe(II) (Jordan et al., 2014; Rebodos and Vikesland, 2010).

In this work, we synthesized Gd-doped magnetite/maghemite nanoparticles with Fe(III) substitution by Gd(III) at various loadings (1 to 12%) via a straightforward oxygen-free synthesis using the alkalizing aqueous Fe(II) and Fe(III) ions method (Jolivet et al., 1992). The purity of these nanoparticles was compared with oxidised nanomagnetite after equilibration at different acidic pH values. Characterization of the NPs by transmission electron microscopy (TEM), scanning transmission electron microscopy coupled with electron energy loss spectroscopy (STEM-EELS), X-ray powder diffraction (XRD) and ^{57}Fe Mössbauer spectrometry were performed.

4.2.2 Results and discussion

We explain the magnetite oxydation into maghemite due to acidic conditions that favor the release of Fe(II) into the solution (Equation 1) (Jolivet et al., 2004; Peng et al., 2018). A linear relationship was found for Fe concentration for pH values ranging from 5 to 10 (Figure S 15).

$$Fe_3O_4 + 2H^+ \rightarrow Fe_2O_3 + Fe^{2+} + H_2O \qquad \text{Eq. (1)}$$

Assuming reaction (1) is the only process releasing Fe in solution, the percentage of magnetite converted into maghemite can be determined. For pH values above ≥ 7, the magnetite conversion was stalled, and the amount of released iron remained below 0.07 mM throughout the experiment. At pH 6, only ~6 % of maghemite was produced, but for lower pH (≤ 5), more than half of the magnetite was transformed to maghemite, reaching up to 82 % at pH 3 (Figure S 15). The specific surface areas measured right after synthesizing nanomagnetites at pH 6 and 8 range from 62 to 70 m^2/g, in contrast to 92 m^2/g obtained for the Fe oxides stabilized at pH 4.

For the doped magnetites, no detectable levels of Gd were found in the supernatants after solid separation. The concentrations of Gd in the digestion solutions were found to be close to the predicted values (± 10%), confirming the complete immobilisation of Gd with the Fe iron oxide particles.

4.2.2.1 TEM and STEM

TEM images of all magnetite solids show a large distribution of particles ranging from 5 to 50 nm (Figure 25). From selected area electron diffraction (SAED) and high-resolution transmission electron microscopy (HRTEM) analyses, the presence of magnetite is confirmed (Figure S 16). No differences were observed in the size distribution or shape of magnetites stabilized at pH values of 8 and 4 and for nanomagnetites co-precipitated with Gd(III). The only noticeable difference was found for particles with 7 and 9% of Gd(III), where some crystals of goethite with elongated shapes measuring between 50 and 100 nm in length were observed.

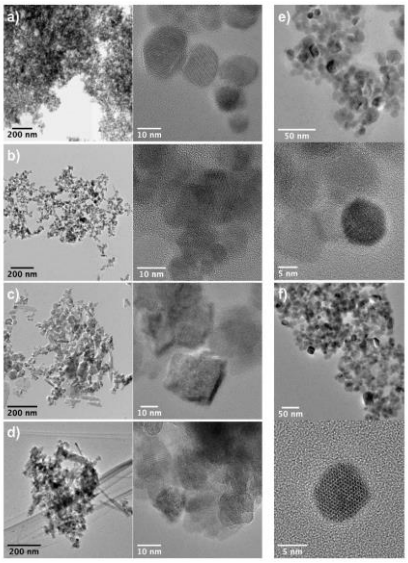

Figure 25 TEM bright field images of the magnetite doped with 3% (a) and 5% (b), 7% (c) and 9% (d) of Gd(III) as Fe(III) and magnetite stabilized at pH=4 (e) and pH=8 (f) samples. 3% (a) and 5% (b) of Gd(III) as Fe(III) magnetite samples equivalent to a pure magnetite phase. Samples 7% (c) and 9% (d) of Gd(III) as Fe(III) present magnetite and goethite phases mixture.

STEM-HAADF and STEM-XEDS elemental mapping (Figure 26) confirmed that Gd(III) was present and evenly distributed in the lattice. This distribution was also observed in the goethite crystals for syntheses with 7 and 9% of Gd(III). Additionally, XEDS measurements confirmed an increase in the concentration of Gd for the magnetite particles with the increased percentage of Gd(III) added during the synthesis (Figure S 17).

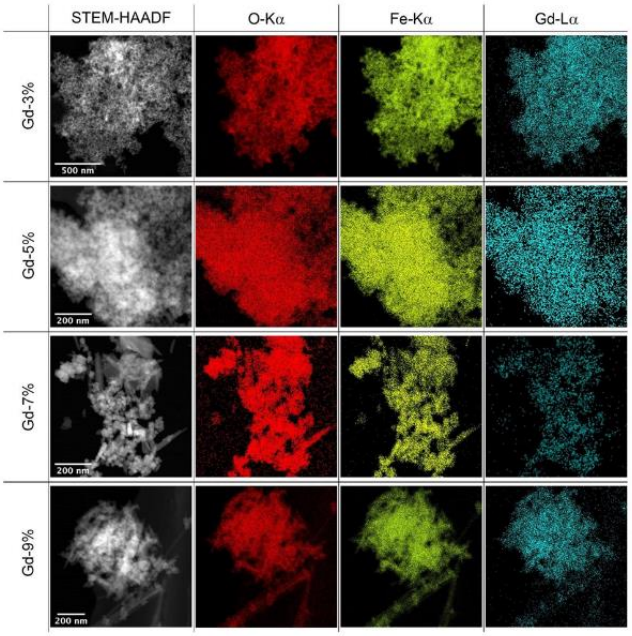

Figure 26 STEM-HAADF and STEM-XEDS elemental mapping of magnetite crystals with 3%; 5%, 7%, and 9% of Gd(III) as Fe(III). The elemental maps are not quantitative (not corrected from the background); they show that Gd is homogeneously distributed (at the scale of the analysis).

Since 1970, the STEM technique has revolutionized the imaging of individual metal atoms, leveraging the atomic number dependence of $Z^{1.7}$ in High-Angle Annular Dark Field (HAADF) imaging (Crewe and Wall, 1970). This innovative approach allows for the precise identification of atomic positions in both light and heavy element columns along the zonal axis of a crystal (Liu, 2021). In this particular study, we employ STEM-EELS to enhance the localization of Gd in co-precipitated samples. The images captured in pure magnetite reveal contrasting features between columns with varying iron density, such as distinct brightly coloured lines formed by iron in octahedral sites on crystals oriented to expose the (111) crystallographic planes. The technique facilitates the clear differentiation between Gd and Fe atoms based on their distinct atomic numbers (26 for Fe and 64 for Gd). Whether Gd is situated on the surface or within the structure becomes evident in the images. If on the surface, Gd should be visible in the thinnest part of the particle where iron atoms do not obstruct the view. Conversely, if Gd is within the structure, it should be observable throughout the particle. Figure 27 offers a comparative analysis of co-precipitated and adsorbed samples, revealing the identification of individual Gd atoms in both cases. As expected, the adsorbed sample predominantly displays Gd atoms at the particle's periphery, while in the doped sample, Gd atoms are distributed throughout the particle, seemingly aligning with sites corresponding to an octahedral Fe column.

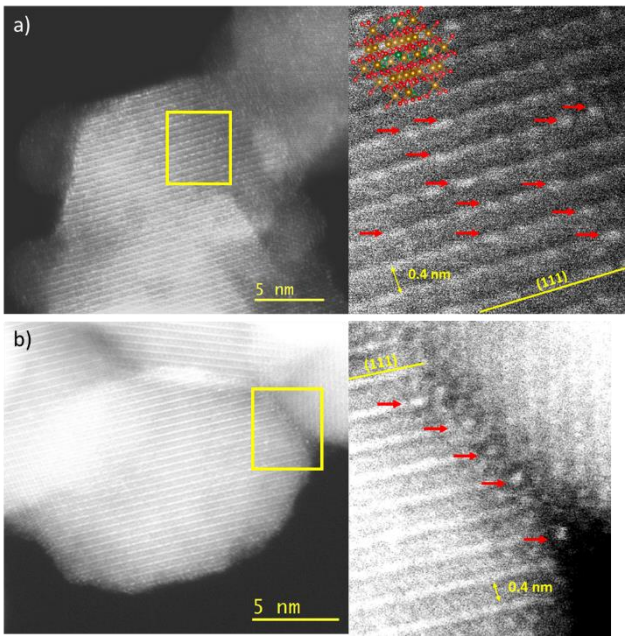

Figure 27 HAADF STEM images of (a) doped magnetite containing 4% Gd as Fe(III) and (b) Gd adsorbed on pure nanomagnetite. The adsorption experiment was performed with 0.001 M $NaNO_3$ for ionic background, 3 g/L solid solution, with an initial concentration of 100 µM Gd and equilibrated at pH 7.26 for 2 hours. The second image shows the focus of the observed Gd atom arrangement after background normalisation to enhance the sharp contrast associated with individual or small clusters of Gd atoms (yellow boxes).

4.2.2.2 XRD characterization of magnetite nanoparticles

XRD patterns of a dry, immediately synthesized magnetite show only peaks typical for the pure magnetite phase (Figure 28; face-centered cubic unit cell parameter a = 8.391(1) - 8.397(1) Å). The crystallite sizes estimated from the Scherrer equation give values between 12-17 nm (Table S 7). The width of the diffraction peaks of the three stabilized samples for pH = 3, 5, and 8 are similar (Figure 26), excluding a decrease in the magnetite crystal size, in agreement with prior studies (Moon et al., 2010). For a 16 nm spherical particle with 20% unmodified nanomagnetite, we estimated an inner diameter of 9.4 nm and an oxidized layer around the magnetite core of approximately 3 nm thickness. However, the TEM images (Figure 25f) show a large size distribution (approximately 5-50 nm). Thus, some small particles may be completely oxidised, while others may have only a thin layer of oxidation on the magnetite surface.

XRD results of nanomagnetites doped with Gd(III) indicate the presence of magnetite in all preparations (Figure 28, Figure S 18, and Figure S 19). The particle size of the Gd-magnetite samples showed no significant difference compared to pure nanomagnetites, supporting our TEM observations. Additionally, no shifted diffraction peak was observed, nor was a peak corresponding to a Gd hydroxide phase detected in the diffraction patterns. Nevertheless, in those samples containing more than 5% Gd(III), the solids show crystallised phases of goethite. Magnetite doped with 8% Gd appears to contain 5% of the green rust phase with a pyroaurite structure. For nano magnetites co-precipitated with 7% and 9% Gd, the presence of less than 3% green rust was less obvious because XRD has a detection limit of ~1%.

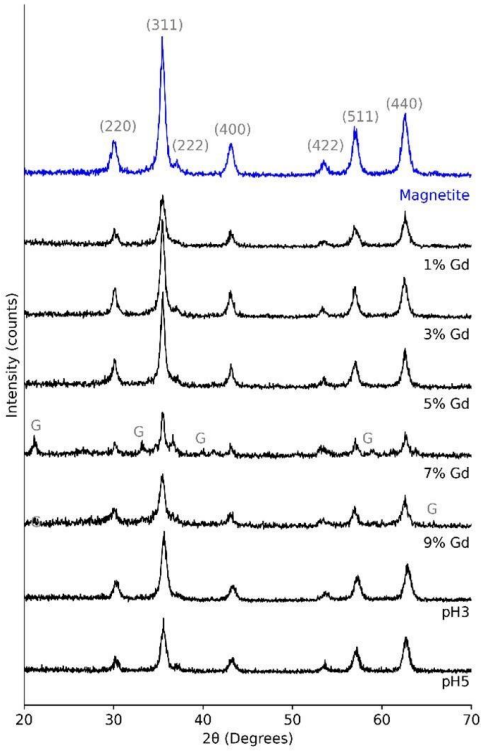

Figure 28 XRD patterns raw data from magnetite stabilized at pH 8 (blue), pH 3, and pH 5 (at the bottom) and magnetite with 1%, 3%, 5%, 7%, and 9% of Gd(III) as Fe(III). The XRD peaks mainly show magnetite and a minor fraction of goethite (G) phases in samples. The references used correspond to JCPDS PDF 00-019-0629 for magnetite and JCPDS PDF 00-029-0713 for goethite.

For magnetite to be formed, the Fe(II)/Fe(II)+Fe(III) ratio must be equal to 0.66 (pH range: 8.5-12; ionic strength: 0.5 -3M, (Jolivet et al., 2004)). Our nanomagnetite synthesis involved a high concentration of OH, which maintained the solution pH close to 12 for all preparations. For solutions containing 1 to 5% Gd(III), the Fe(II)/Fe(II)+Fe(III) ratio varies between 0.655 and 0.667 (Figure S 20). For concentrations between 6 and 12%, the Fe(II)/Fe(II)+Fe(III) ratio varies between 0.638 and 0.653 (values < 0.66), which is below the stoichiometric value required for the formation of magnetite. As a result, goethite and green rust are formed through the dissolution-crystallization process.

4.2.2.3 Mössbauer characterization

The Mössbauer spectra obtained at 300 and 77K for our magnetites are shown in Figure 29 and Figure 30, respectively, and the refined values of the hyperfine parameters are given in Table S 8. A typical magnetite spectrum at room temperature consists of two sextets: (1)Fe(III) in tetrahedral positions and (2)Fe(III) and Fe(II) in octahedral positions, which appear to average as $Fe^{2.5+}$ resulting from fast electron exchange. The magnetite spectra at 77 K, below the Verwey transition (~119 K) where electron hopping is absent, show the expected structural change from a cubic to a monoclinic system.(Doriguetto et al., 2003)

For the fresh magnetite sample (pH = 8; T= 300 and 77K), we collected a typical spectra expected for magnetite. The sextet lines are wider than expected for crystalline magnetite, and the broadening is therefore attributed to the presence of superparamagnetic relaxation effects due to the small size and size

distribution of particles, as concluded above from X-ray diffraction and TEM. The mean value of the isomer shift is typical of the exclusive presence of Fe(III) and, therefore, consistent with the presence of nano magnetites.

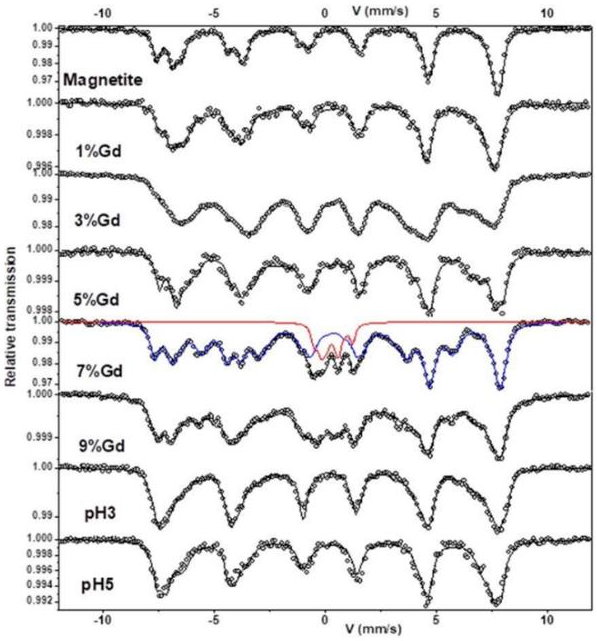

Figure 29 Mössbauer spectra were measured at 300 K of pure magnetite, magnetite equilibrated at pH 3 and 5, and magnetite doped with 1-9% of Gd as Fe(III) fitted with different components containing $Fe^{2.5+}$ (red line) and Fe(III) (blue line) species.

For the magnetite samples with Gd(III) ranging from 1 to 5 %, the spectra at 300K show broader lines than for fresh magnetite, while the hyperfine structures at 77K are rather similar. These features can be explained both by the presence of superparamagnetic nanoparticles and the additive role of Gd(III) ions introducing internal and/or surface structural disorder.

The magnetite-to-maghemite conversion ratios obtained from Mössbauer results and ICP-AES measurements are similar (see Figure S 15) and confirm prior findings.(Gorski and Scherer, 2010). For Gd-doped nanomagnetites (1 to 5%), the mean isomer shift values are consistent with the oxidation of some Fe species, allowing an estimate of the mean composition of the nanoparticles (Table S 8), in agreement with the XRD patterns. Furthermore, there were differences observed in the spectra between 300 K and 77 K, but the cause of this discrepancy is currently unknown.

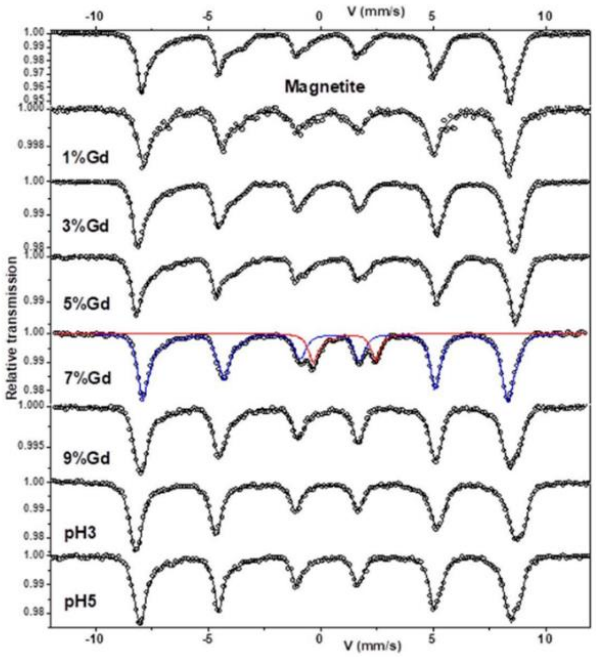

Figure 30 Mössbauer spectra measured at 77 K of the same samples

The incorporation of structural Gd can be possible if Gd replaces Fe(III) in an octahedral position because charge and size similarities (0.938 and 0.645 Å for Gd and Fe respectively (Shannon, 1976)). However, Gd has a much larger ionic radius than Fe (III) which may hinder or condition at low concentrations its incorporation into the magnetite lattice (Schock, 1979). This is supported by the analysis of co-precipitated nano magnetites with 7 and 9% of Gd. The Mössbauer spectra differ significantly from the spectra of fresh magnetite stabilized at pH = 8 (Figure 29 and Figure 30). Significant new quadrupolar doublets are observed in the central part (see red curve), suggesting the presence of some Fe-containing impurities. Indeed, the X-ray patterns indicate the presence of other mineral phases as goethite and green rust. The first phase generally contributes to a magnetic sextet with broadened lines and a specific value of quadrupolar shift (~0.20 mm/s) and/or quadrupolar doublet, depending on the size of the particles. The complexity of the hyperfine structure prevents the identification and estimation of any goethite content. But the red curve (quadrupolar doublets) could be attributed to some Fe species located in structurally and chemically disturbed green rusts.

Conversely, the hyperfine spectral structures for magnetites equilibrated at pH = 3 and 5 differ significantly from the previously discussed spectra for Gd-rich magnetites (Figure 5). These differences result from magnetic components with broadened and asymmetric lines that must be described employing a linearly correlated distribution of hyperfine fields and isomer shifts. The most relevant parameter is given by the average values of the isomeric shifts, which are intermediate between those typically observed in oxide phases containing Fe(II) and Fe(III) species. Such a description is consistent with a mixture of stoichiometric magnetite and maghemite phases (Table S 8 and Figure S 15;(Bogart et al., 2021; Greneche, 2013)) and confirms the absence of maghemite in Gd-rich particles. In general, increasing content of Gd is associated with an increasing complexity of the hyperfine structure at 300 and 77K.

4.2.3 Conclusion

In summary, Free Gd has a high affinity for magnetite, but Gd complexes such as DOTA and DTPA adsorb very poorly to this mineral. A potential solution to the problem of Gd contamination arising from the use of Gd complexes is the development of a new agent device. We produced magnetite nanoparticles with a stoichiometric ferrous-to-ferric ions ratio close to 0.5 and a size ranging from 5 to 50 nm. Our results show that maghemite is present in no more than 10% of the particles, and gadolinium is distributed uniformly throughout the particles and in Fe octahedral sites. Thus, Gd-doped nano magnetite samples form true $Fe_{(3-x)}Gd_xO_4$ solid solutions, with $0.02 < x < 0.1$, with Fe(III) being substituted by Gd(III) within the magnetite superparamagnetic iron oxide nanoparticles (SPION). Such trapping (or substitution) within the mineral structure prevents the release of Gd(III), a theragnostic agent within the cytoplasm or nucleus of the targeted cells. Thus, these nanoparticles present a strong potential in medical applications, combining the advantages of SPION nanoparticles and Gd-concentrates particles for imaging, therapeutic or theranostic applications. Moreover, this composite will be environmentally friendly as it can be readily eliminated through conventional wastewater treatment methods for future medical applications.

4.2.4 Supplementary information

4.2.4.1 Methods

4.2.4.1.1 Chemicals

Gadolinium (III) chloride hexahydrate (99.999%), sodium nitrate ACS reagent, ≥ 99.0%, nitric acid, ≥ 65 %, p.a., ISO, hydrazine hydrate (≥ 95%), iron (II) chloride tetrahydrate (99.99%), iron (III) chloride hexahydrate (≥ 99%), and ammonia solution, 25% (99%), were purchased from Sigma-Aldrich. Sodium hydroxide (≥ 99%) was bought from Roth, and hydrochloric acid, 48%, extra pure, SLR, from Fisher Chemical. All solutions were made with deionized Milli-Q water, and all experiments were performed under Ar atmosphere at room temperature within a glovebox. All containers were soaked in 5% HNO3 for 24h, cleaned for 10 minutes in an ultrasonic bath, and rinsed thoroughly with deionized water before use.

4.2.4.1.2 Nanomagnetite and Gd doped nanomagnetite synthesis

Nanomagnetites and Gd doped nanomagnetites were synthesized using the alkalizing aqueous Fe(II) and Fe(III) ions method(Jolivet et al., 1992; Scheinost and Charlet, 2008a). Briefly, 25 mL stock solutions of 0.8 M $FeCl_2$, 1.6 M $FeCl_3$, 1.6 M $GdCl_3$, and 60 mL of 6 M of NH_4OH were prepared. A drop of hydrazine hydrate was added to the $FeCl_2$ solutions to prevent ferrous oxidation. For co-precipitation experiments, a precise amount of Gd stock solution was added (0.25-1.8 mL) to replace the right amount of Fe(III) in the ferric solution. The Gd percentage calculated to replace Fe(III) ranged from 1 to 12%. As a first step, both ferrous and ferric chloride solutions were mixed. Then, the NH_4OH solution was slowly injected into the ferrous/ferric chloride solution (injection rate: 0.3mL/s) and stirred for 24 hours. Subsequently, the supernatant was separated and acidified with HNO_3 65% prior to ICP-AES measurements. Finally, the suspension was washed by replacing the supernatant with degassed water six times, vacuum filtered with a 0.22 µm filter, and dried under an anoxic atmosphere. Selected Gd-doped nanomagnetite samples were digested with 65% HNO_3 for elemental analysis.

4.2.4.1.3 Magnetite oxidation into maghemite

Structural changes and stability of magnetite were investigated across a wide pH range (3-10). Eight experiments were carried out, with the initial concentration of the magnetite fixed at 10 g/L and 0.1 mM NaCl background solution. pH was adjusted using HCl and NaOH solutions until the values remained stable within 0.2 units of pH over a 24 h period. After 3 weeks, a magnet was used to concentrate the magnetic solid at the bottom of the reactors to separate it from the liquid. All liquids were then filtered by a syringe filter (0.22 μm) to determine the iron concentration in the solution. The remaining solids were pre-dried using a vacuum filtration system (0.22 μm) and left overnight in the glovebox for a final drying step.

4.2.4.1.4 Elemental analysis

Total Gd and Fe concentrations in the liquid samples were determined by ICP-AES (Varian 720 ES) at wavelengths of 234,350 nm for Fe and 358,496 nm for Gd using external calibration. The RSD was 4% for Fe and 2% for Gd. The limits of detection were 4.96 μM for Fe and 0.05 μM for Gd. The limits of quantification were 15.02 μM for Fe and 0.16 μM for Gd.

4.2.4.1.5 Solid characterization

XRD. X-ray powder diffraction measurements were conducted with a diffractometer [CuKα radiation (λ = 1.54 Å); Bruker D8] using a Debye–Scherrer configuration with an elliptical mirror to obtain a high flux and parallel incident beam, and an a SolX Si(Li) solid-state detector to collect the diffracted beam. The patrons were collected with a step size of 0.026° in the 20° to 70° 2-theta range at room temperature. XRD pattern samples were loaded inside the glovebox into the airtight polymethyl methacrylate sample holder with a transparent dome to avoid any possible oxidation. The lattice parameters and the average crystallite sizes were calculated using the DebyeScherrer equation and the Profex software(Doebelin and Kleeberg, 2015). The refinement with a free lattice parameter was performed for all samples.

TEM and STEM-EELS. A few milligrams of nanomagnetite samples were placed in plastic vials, filled with 10 mL of ethanol, sealed with parafilm, and removed from the glovebox for 5 minutes for redistribution in an ultrasonic bath. These dilute suspensions were drop-casted on pure carbon, 200 mesh Cu TEM grids and dried. The samples were transferred for TEM and STEM measurement under anoxic conditions and were in contact with air only for a few minutes during mounting on the microscope sample holder. TEM observations (HRTEM, high-angle annular dark field imaging in scanning transmission electron microscope mode (STEM-HAADF) and X-ray energy-dispersive spectroscopy (XEDS) mapping experiments) were performed on a Jeol JEM 2100F microscope, operating at 200 kV, equipped with a Schottky emitter, a Jeol detector with an ultra-thin window allowing detection of light elements and a scanning TEM (STEM) device. STEM-EELS measurements were performed in a NION UltraSTEM200 operated at 100 kV and coupled with a high-sensitivity EELS spectrometer. Data was collected from clean GR plates; those that were considered free of contamination and/or visible stray iron (oxyhydr)oxide minerals.

BET. The specific surface area (SSA) was determined by the Brunauer−Emmett−Teller adsorption method (BET-N_2) at 77 K, using a Belsorp-Max (Bel Japan) volumetric gas sorption instrument. A small amount (0.418 g) of magnetite was loaded in a glass cell inside the glovebox and then dried under vacuum at 80 ^{o}C for 12 h. The SSA was calculated from the BET equation in the P/P_0 range 0.052 – 0.307.

^{57}Fe Mössbauer spectrometry. Mössbauer spectra were collected at 300 and 77 K using a conventional constant acceleration transmission spectrometer with a ^{57}Co(Rh) source and an α-Fe foil for calibration at room temperature. Samples containing 5 mg of Fe/cm^2 (~ 20 mg of the solids) were loaded in round plastic holders, sealed in glove box with epoxy glue to prevent possible oxidation, and then transported under oxygen-free conditions. The obtained spectra were fitted with an in-house program (MOSFIT). The description of the hyperfine structures consisted of a least-squares fit, including quadrupolar doublets and Zeeman magnetic sextets composed of Lorentzian lines.

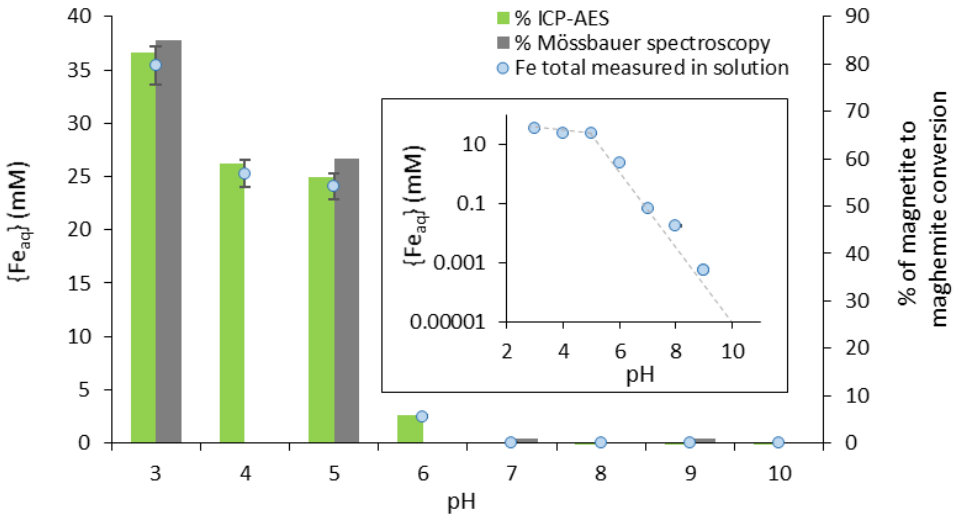

Figure S 15 Concentration of iron released in the solution during 3 weeks of stabilization experiments in the pH range 3-10 (blue dots), calculated magnetite to maghemite conversion from ICP-AES and Mössbauer spectroscopy (green and gray bars, respectively). Fe total measures are plotted in logarithmic scale in the inset graph.

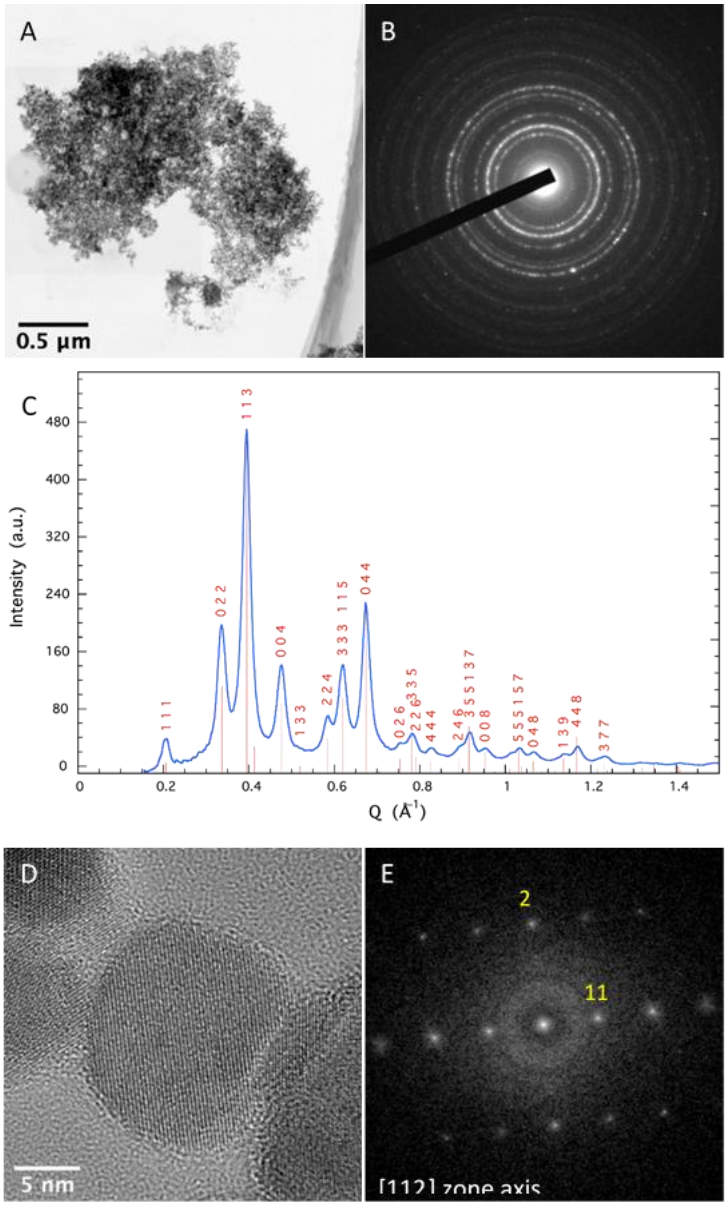

Figure S 16 TEM bright field image (A), selected area electron diffraction (B), and corresponding radial intensity (C). High-Resolution TEM image of a magnetite crystal and related fast Fourier transform (E). Diffraction pattern and FFT are indexed with magnetite structural parameters (a = 8.396 Å and Fd3m spacegroup)

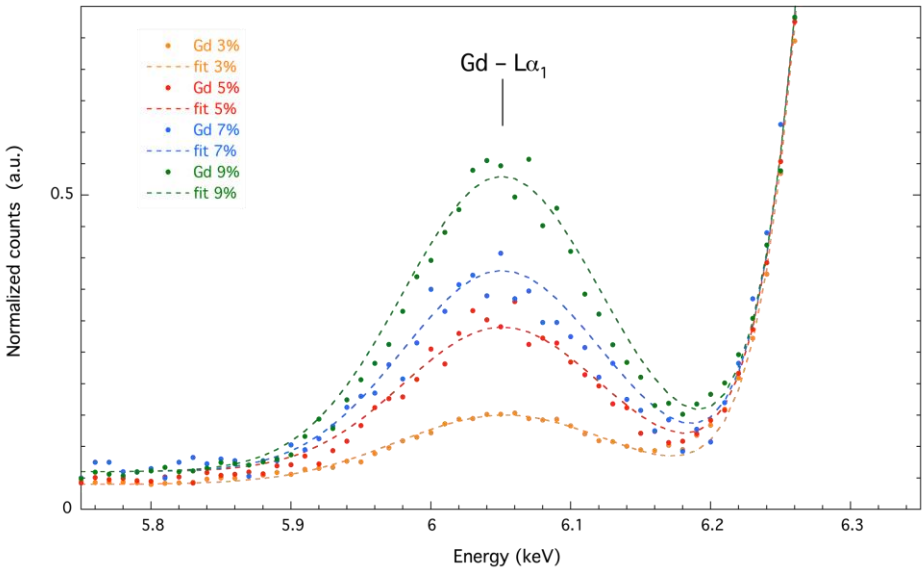

Figure S 17 Gadolinium Lα1 line profile as a function of Gd-content. Spectra have been normalized concerning the Fe-Kα line.

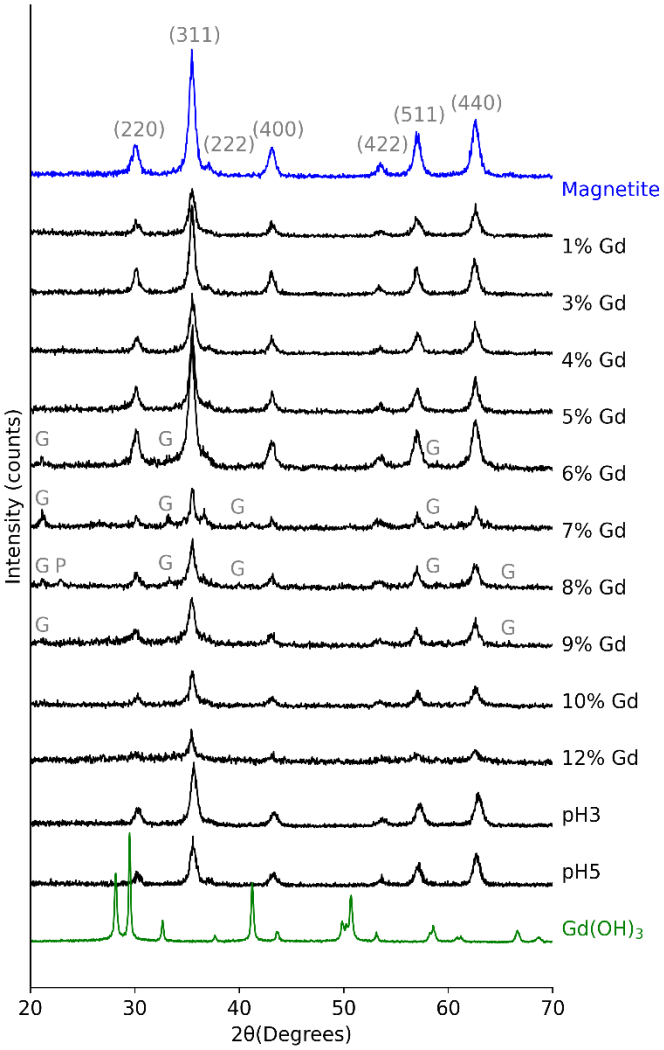

Figure S 18 XRD patterns data from all magnetite synthesis. XRD data of magnetite stabilized at pH 8, pH 3, and pH 5 and magnetite with 1-12% of Gd(III) as Fe(III). The references used correspond to JCPDS PDF 00-019-0629 for magnetite, JCPDS PDF 00-029-0713 for goethite (G), ICSD-80876, and PDF 01-086-0181 for green rust (P).

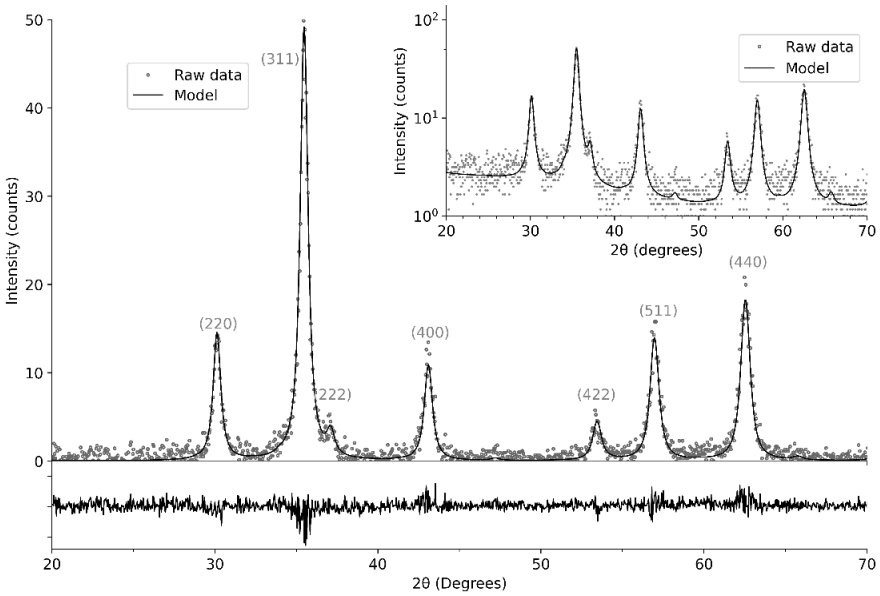

Figure S 19 Representative Rietveld analysis pattern of powder diffraction data of magnetite doped with 3% Gd(III) as Fe(III) for only cell parameters determination. The fit is made with magnetite (M) reference lattice parameters (JCPDS PDF 00-019-0629). The residue between the observed and calculated intensities is plotted below the profile. The same data is plotted on a logarithmic scale in the inset graph. Goethite and green rust phases are not present in this sample.

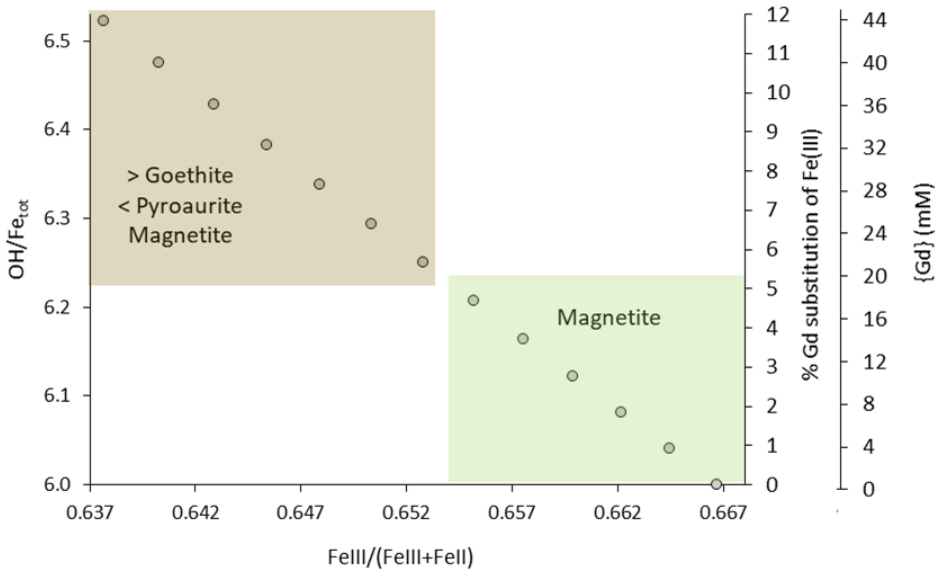

Figure S 20 The plot of ratios of iron and OH concentrations used to prepare Gd-doped magnetites. OH/Fetotal, Fe(III)/(Fe(III)+Fe(II)) and %Gd(III) substitution of Fe(III) were calculated with 3272.73 mM OH, the estimated total iron concentration for each sample, 181.82 mM Fe(II) and the calculated Fe(III) and Gd(III) values utilized for the coprecipitated sample preparation. The data are grouped into two groups Fe(III)/(Fe(III)+Fe(II)): values lower than 0.665 where the syntheses have phases like goethite and green rust in addition to magnetite and higher than 0.665, where only nano magnetite particles are observed.

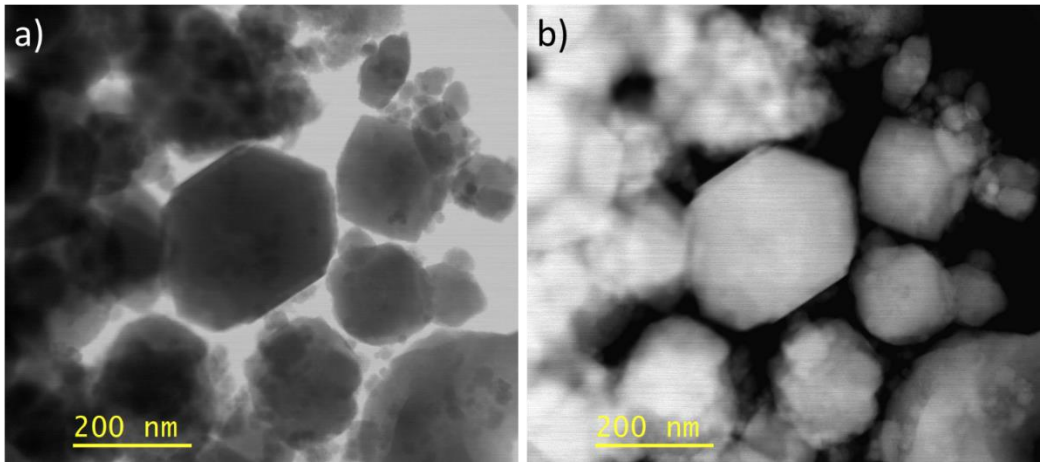

Figure S 21 Bright-field (a) and dark-field (b) STEM images of industrial magnetite nanoparticles obtained from HYMAG'IN company.

Table S 7 Gd(III) doped magnetite solids calculated parameters after Rietveld refinements of the recorded XDR, performed with the BGMN software and Profex user interface.

ID	XDR calculated parameters		Mineral phases detected (% mass)			
	[b]unit cell length (a)	Grain Size magnetite ± 2 (nm)	[a]Magnetite and maghemite ± 2	Goethite ± 2	Green rust ± 2	Amorphous ± 2
Magnetite	0.8390 (0.0001)	13	100	-	-	-
1% Gd	0.8398 (0.0003)	13	100	-	-	-
3% Gd	0.8409 (0.0002)	15	100	-	-	-
4% Gd	0.8403 (0.0002)	13	100	-	-	-
5% Gd	0.8402 (0.0002)	14	100	-	-	-
6% Gd	0.8393 (0.0002)	12	95	5	-	-
7% Gd	0.8398 (0.0003)	18	55	42	3	-
8% Gd	0.8404 (0.0003)	13	79	16	5	-
9% Gd	0.8396 (0.0003)	11	87	11	2	-
10% Gd	0.8405 (0.0004)	13	92	8	-	-
12% Gd	0.8398 (0.0007)	10	84	-	-	16
Mag_pH3	0.8369 (0.0002)	13	100	-	-	-
Mag_pH5	0.8400 (0.0003)	13	100	-	-	-

[a] The magnetite reference position is a=8.3958 A (ICDD: 04-005-4319), and for maghemite (cubic) is a=8.336 A (ICSD: 250541).

[b] The measurement error is shown in brackets.

Table S 8 ^{57}Fe Mossbauer parameters for magnetite samples recorded at 300 and 77 K. IS is isomer shift relative to αFe; 2ε quadrupole shift and $B_{hf,}$ the hyperfine field.

Sample	T (K)	<IS> ± 0.01 (mm s^{-1})	<2ε> ± 0.01 (mm s^{-1})	<B_{hf}> ± 1 (T)	% Magnetite ± 4
Magnetite	300	0.52_3	0.01	45.3	100
	77	0.60_5	0.02	49.2	100
1% Gd	300	0.51_9	0.00	33.1	100
	77	0.60_7	0.03	50.1	83
3% Gd	300	0.50_6	-0.05	33.2	100
	77	0.64_2	0.03	50.1	84
5% Gd	300	0.50_6	0.02	36.0	95
	77	0.64_2	0.05	50.4	100
7% Gd	300	0.47_6	-.07	39.2	80
	77	0.57_2	-0.07	49.4	65
9% Gd	300	0.42_2	0.09	26.4	52
	77	0.54_1	0.12	47.5	51
Mag_pH3	300	0.34_9	0.026	42.7	14
	77	0.47_6	0.02	51.6	18
Mag_pH5	300	0.41_2	-0.00	44.8	47
	77	0.52_6	0.06	50.3	43

Chapter 5: Conclusions and Perspectives

The formation of anoxia environments in ancient and modern settings is a major driver of the evolution of the Earth's surface through geological time (Rickard, 2012). Metal and metalloid sequestration processes in oxygen-depleted v.s. oxygen-rich aquatic environments allow to follow Earth's climate evolution. The anoxic trapping mechanism can also be used to concentrate contemporary resources and in decontamination management. This thesis is dedicated to describe the main mechanisms involved in the sequestration of trace elements, specifically Re, Se, and Gd, and thereby to improve our understanding of their biogeochemistry. We used a multi-analytical approach including mineral synthesis, adsorption experiments, wet chemistry, Se and Re speciation, Re stable isotope fractionation measurements and Gd imaging analyses in both aqueous and solid samples to address the following research questions.

How does trace element geochemistry differ in different environments and thus among different redox states? In particular, when interacting within anoxic, sulfidic-rich environments which insights can we get of their reactivity and binding with sulfur ligands?

What is the reduction pathway of Re(VII) within sulphidic waters, and how does it depend on pH, Re/S saturation ratio and kinetics?

Which are the key surface and structural processes governing the sequestration of Re(VII), Se(VI and IV) and Gd(III) in anoxic sediments, by magnetite in low sulfidic environment and by pyrite in high sulfidic environment?

This chapter provides a summary of the main results of the thesis and their implications. Additionally, it suggests ideas for future research development that will complement the limitations of the present study and will further enhance our understanding of trace element immobilisation in sedimentary environments.

5.1 Primary outcomes

The experimental studies in Chapters 2-4 build on each other. They investigate the sorption process of Re(VII) (Chapters 2 and 3), Se(VI), Se(IV) and Gd(III) (Chapter 4) using comparative experimental conditions to characterise the adsorption and surface redox process vs. coprecipitation in high Fe^{2+} or high $\sum S^{2-}$ systems. Within this context, Chapter 1 mainly served to put in perspective previous investigations of Se, Re and other oxyanions geochemistry. This review allows to understand the complex redox reactivity of ReO_4^-, SeO_4^{2-} and SeO_3^{2-} in sulfidic water developed in Chapter 2, and with magnetite and pyrite as investigated in Chapters 3 and 4. We show that Vanadium (V), Arsenic (As), Molybdenum (Mo), Tungsten (W), Technetium(Tc) and Rhenium (Re) have a less hard acidic character in their higher redox state, when compared to Chromium (Cr) and Selenium (Se) suggesting why there is more experimental evidence and natural thiospecies formation for the first above-mentioned oxyanions than for Se and Cr. This comparison is based on the HSAB principle, which describes the reaction of hard acid (A_H), such as Se or Cr or other soft acid (A_S); such as Re when bound to a hard base (B_H), such as O^{2-}, with a soft base (B_S), represented by S^{2-} ions (Sposito, 1981). In the following reaction, the arrow indicates the direction in which the reaction is more favourable.

(1) $A_HB_S + B_H \rightarrow A_HB_H + B_S$

(2) $A_SB_H + B_S \rightarrow A_SB_S + B_H$

Chapter 1 extends the HSAB principle to oxyanions usually applied to free metal ions. The greater affinity (or softer character) of metals and metalloids to $\sum S^{2-}$ ligands is observed for their lower redox states. The natural and synthetic sulfide materials containing those chemicals are further investigated by XAS spectroscopy for Se and Re in chapters 2 to 4.

Chapter 2 shows that, in highly saturated sulfidic systems, Re stepwise thiolation and subsequently reduction processes lead to final Re(III, IV, V)$_2S_7$ nanoparticles in the pH6 to pH8 ranges. A new pathway is introduced for the Re-S nanoparticle formation in a system at low temperatures in aqueous solutions; namely:

(3) $ReO_4^-{}_{(aq)} + HS^-{}_{(aq)} + H^+ \rightarrow ReO_3S^-{}_{(aq)} + H_2O$

(4) $ReO_3S^-{}_{(aq)} + 3HS^-{}_{(aq)} + H^+ \rightarrow ReS_4^- + 3H_2O$

(5) $H^+ + 2\ ReS_4^- \rightarrow Re_2S_7 + HS^-$

The data from Chapter 2 also suggest the nucleation rate dependency on initial pH and ionic strength. Two phenomena were observed: faster kinetics of Re-S nanoparticle formation at higher alkaline pH levels and ionic strength, and faster nanoparticle aggregation at acidic pH.

The surface sorption mechanisms by which magnetite and pyrite interact with ReO_4^-, are less efficient than co-precipitation mechanisms, and are kinetically slower as shown in Chapter 3. The adsorption of Re(VII) at a 100 µM concentration level and a 2g/L solid, involved only less than 20% of total perrhenate on magnetite and less than 0.1% on pyrite, whereas when Re doped minerals are formed, up to 250 µM for pyrite and up to 1800 µM for magnetite, i.e. >95% of perrhenate was removed during the precipitation of 3 and 42 g/L solid respectively. After measuring the sorbed Fe(II), Fe(III) and $\sum S^{2-}$ before and after the addition of Re to the system, we concluded that Re(VII) removal by magnetite and pyrite was also influenced by the dissolved species of the mineral crystal. The surface sequestration mechanisms in both pyrite and magnetite are heterogeneous processes. Surface reactions are dominated by the reactivity of crystal surface defects (Rosso et al., 2000), which may provide possible adsorption sites for Re. Furthermore, the metal may be integrated into the external layers, whether old or new, through a process of dilution-precipitation of the mineral. This occurs through competition and substitution of Fe(III) atoms, as well as co-precipitation with the dilute cations originating from the solid. On the other hand, it has been suggested that during coprecipitation experiments following pyrite synthesis procedure Re_2S_7 nanoparticles are formed on pyrite surface Fe sites. In magnetite coprecipitation samples, Re atoms appear to replace octahedral Fe(III) atoms within the surface crystal structure and to be completely reduced to Re(IV). This contrasts with surface sorption experiments where XANES spectra suggest the presence of Re(V), Re(VI) or a mix between Re(IV) and Re(VII) as surface species. The isotopic ratio measured after digestion and column purification showed greater fractionation for magnetite adsorption or coprecipitation samples, compared to Re(VII)-Fe(II) precipitates (-0.6 vs -0.2 ‰). These results confirm the enrichment of heavier isotopes during reduction experiments as predicted by ab initio calculations (Miller et al., 2015).

The same mechanisms were studied in the selenate or selenite–pyrite experiments described in Chapter 4. In particular, the pyrite surface presented a different adsorption reactivity and a different speciation of the two oxyanions in the final product. Pyrite adsorption is significantly more efficient for

Se(IV) than for Se(VI) (40-60% v.s. <10% Se removal) and, when we added $\sum S^{2-}$ to enhance the Se removal, only Se(IV) sorption was enhanced to >95% removal rate. Though XAS studies indicated that both Se(VI) and Se(IV) were reduced to Se(0) in the final solid product. Additionally, for Se(IV), we also observed the presence of Se(IV) in the particles, which could be formed by precipitation of $FeSeO_3$ (Charlet et al., 2007) using the Fe(II) released by the pyrite. In similitude with Re experiments, coprecipitation experimental approach was more efficient only for Se(IV) (>99% Se removal). The spectral results obtained for pyrite doped with Se(IV) indicate complete reduction of Se down to Se(-I) (based on HERFD-XANES) and a perfect fit of EXAFS using a model of pyrite that includes Se atoms in some S(-I) sites in the structure.

Given that Gd(III) has a hard Lewis acidic character like other trivalent lanthanide ions (Pearson, 1988; Sherry et al., 2009; Wulfsberg, 1987), this cation has a strong affinity for OH^- and not for S^{2-}, we only studied the sorption affinity of Fe_3O_4 nanoparticles for Gd in Chapter 4. The results obtained showed a longer efficiency for free Gd^{3+} ion removal by magnetite surface experiments a pH 7 (>95%). Gd-doped nano magnetite samples are shown to form true $Fe_{(3-x)}Gd_xO_4$ solid solutions for $0.02 < x < 0.1$, as expected for Gd affinity to oxide solids. The incorporation of Gd in the lattice of magnetite is based on charge and size similarities between Gd^{3+} and Fe^{3+} ions in an octahedral position. However, the larger ionic radius of Gd^{3+} compared to Fe^{3+} may hinder or condition its incorporation into the magnetite lattice at low concentrations.

5.2 Significance and suggestions for future research

5.2.1 Trace elements in anoxic sedimentary geological deposits

The transition to a low-carbon global economy could result in a sulfur supply shortfall of 100-320 million tonnes by 2040 (Maslin et al., 2022). This is because 80% of sulfur raw material is derived from fossil fuel desulfurisation. The rapid expansion of green technologies is predicted to significantly increase the requirement for non-renewable raw materials sourced from primary geological resources (Herrington, 2021). Geological deposits contain vast theoretical reserves of sulfur (USGS, 2023) that can be extracted from mining copper and other sulfide minerals. However, the extraction practices are both costly and environmentally damaging. Sulfide mineral mining main environmental concern is the acidification of local surface and ground waters, as well as the increase of concentration in these waters of numerous toxic elements with no commercial interest. A safe alternative solution is recycling sewage water and other wastes that contain critical metals and sulfur and give water a second life (Voulvoulis, 2018). By recognising the need for recycling and extraction in the near future, a more complete understanding of the origin of metal ores, specifically ore sulfide sediments, can help to develop national and international policies to manage this future demand.

The present dissertation investigates the affinity of three chemical elements to anoxic marine sediment components through adsorption and coprecipitation processes. Specifically, pyrite is examined as a representative of sulfide-rich environments, while magnetite is studied for its association with iron-rich settings, encompassing a diverse range of critical metals and raw minerals. The coprecipitation mechanism emerges as an important phenomenon, as it appears to be the most favourable for the natural incorporation of metal ions into minerals. In magnetite, studies showed that iron ions can be substituted by various metals like Co^{2+}, Mn^{2+}, Mg^{2+}, Zn^{2+}, Al^{3+} and Cr^{3+}, Ti^{3+} (Li et al., 2020). However, in-situ studies or investigations are scarce into the metal incorporation effect in magnetite, similar to those conducted for Gd^{3+} in this thesis.

In pyrite, concepts such as the degree of trace element pyritization (DTPA) (Huerta-Diaz and Morse, 1990) and the degree of pyritization (DOP) (Berner, 1970) have been proposed as a measure of the trace element affinity within pyrite. Earlier work studied the incorporation of Mn, Co, Ni, Cu, Zn, As, Se and Mo during pyrite formation via the polysulfide pathway synthesis at ambient temperature used in the present dissertation (Baya et al., 2022). The authors show a kinetic pyrite formation dependence on metal/metalloid type and also a selective sorption affinity Cu ≥ Ni ≥ Co > Se > V > Mo >> As > Zn >> Mn (See Figure 31). However, this concept and previous studies rely on selective dissolution of iron and metal fractions from natural pyrites, lacking an explanation for the chemical and crystallographic aspects of the incorporation within certain trace metals or their exclusion from pyrite lattice. In our Se results, some questions remain open regarding the initial stages of metal sequestration. It is unclear whether this process starts with nano-clusters containing SeS_2 or with the initial incorporation of metastable precursor phases of the mineral pyrite. Additionally, the dissolution processes occurring under varying pH or oxygen contents are not well understood. This lack of clarity is significant as metal(loid) release is directly linked to their contamination of surface water environments and toxicity for organisms, as well as for the effectiveness of element trapping process by pyrite and magnetite.

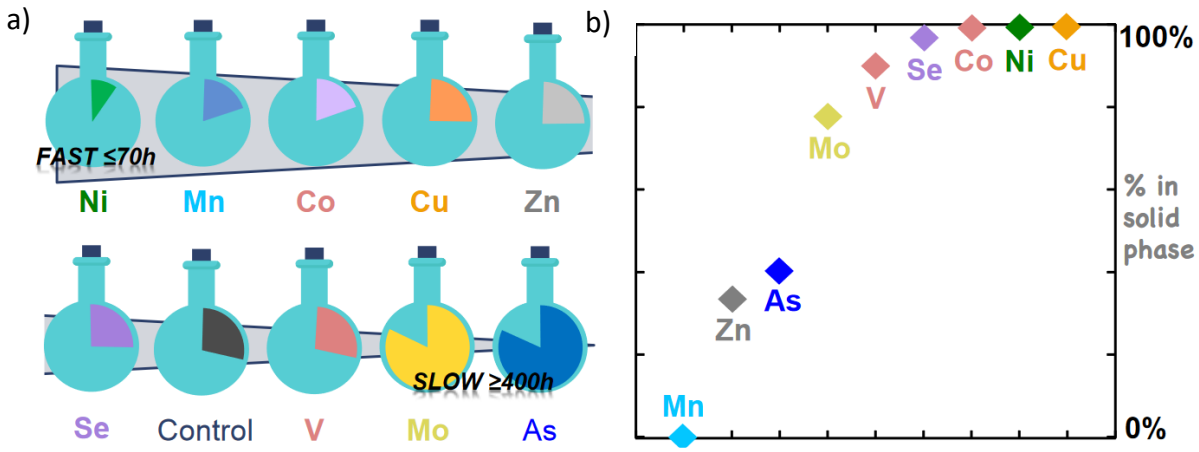

Figure 31 Schematic representation of results published in Baya et al (2022). a) Representation of some trace elements' influence on kinetic pyrite precipitation. b) Trace element solid/liquid ratio, where 100% represents total sequestration on the element and 0%, all trace element concentration has remained in solution. Syntheses were conducted by reacting a $FeCl_3$ with Na_2S and aqueous V, Mn, Co, Ni, Cu, Zn, As, Se and Mo in a trace element/total Fe molar ratio of 0.5 mol%. (taken from (Baya et al., 2022)).

A future line of research on the understanding of the metal coprecipitation mechanism leading to doped magnetite and pyrite would be to follow the synthesis method used in the present thesis with adaptations according to the specific metal/metalloid inclusion. Such future study could expand the scope to include other oxyanions and specifically to study: Se, Re, Mo, V, As, W, Sb, Sn, and Cr, which present high economic interest. Such a new project could focus on four main objectives: (1) Conduct a comprehensive review of studies with natural and experimental samples related to the incorporation of trace metals into magnetite and pyrite. This will involve comparing their affinity levels based on the HASB concept done in the first chapter. (2) Perform Ab- Initio calculations to gain insights into the energy cost to incorporate given trace elements and to explore why certain metal ions can replace either Fe or S within the structure while others precipitate at the surface of pyrite. (3) Characterize the pathway of metal/metalloid incorporation in the pyrite structure using a kinetic approach (0, 2, 4, 8, 24, 48, and 96 hours). This could be achieved through XAS spectroscopy measurements on metal traces, X-ray diffraction and Raman spectroscopy. (4) Measure desorption and dissolution rates across a range of pH values, considering both short (24 h) and long periods (weeks to months) for previously doped pyrite synthesis.

5.2.2 Re and Se as alternate geochemical proxies for anoxia

In geological times, especially in the mid to late Proterozoic (2.3 to 1 Gyr), anoxic waters with elevated sulphur levels were present in the planet oceans (Canfield, 1998). This period begins with the sulphate enriched the oceans, resulting from the first large oxygenation event of the Earth's atmosphere (2.3±2.0 Gyr), during which rocks were weathered and oxidised present at the Earth's surface. The sulphate was then reduced by the oxidation of previously accumulated organic matter, leading to an anoxic ocean enriched with dissolved sulfide. Similar, global oceanic anoxic events could be induced by global warming and gulf stream interruption with long-lasting impacts on the occurrence of life and biogeochemical cycles in the Earth system.

Identifying ancient euxinic conditions has been a challenging task, as ancient oceans cannot be observed directly. Several redox-sensitive elements, including U, V, Mo, Re, Se, Cr, Ni, Cu, Cd, Zn and Co (Kendall et al., 2015; Mitchell et al., 2012; Tribovillard et al., 2006), do exhibit divers chemistry in sulfidic and non-sulfidic environments. Their high concentration in iron sulfide-rich sediments, their specific speciation (reduced redox state, bonding with sulfur atoms) and isotopic fractionation vary with environmental conditions and can lead to their use as paleoenvironmental reporters. Thus the comparive geochemistry of these redox-dependent trace elements can be used as proxy of the redox environments that formed the sedimentary system in which they occur. There is also a close correlation between organic carbon and pyrite sulphur content in marine sediments (C/S ratio about ~2.8 (Morse and Berner, 1995)), e.g., in Phanerozoic shales. As previously stated, the production of H_2S for pyrite formation is a result of the reduction of interstitial dissolved sulphate by bacteria; which use sedimentary organic matter as a reducing agent and energy source (See Figure 32) (Berner, 1984). However, metal sulfides have been studied without considering the reactivity of organic carbon in the system (Rickard, 2012). New studies of sulphide mineral formation must include organic carbon in order to gain a full understanding of anoxic sediment formation.

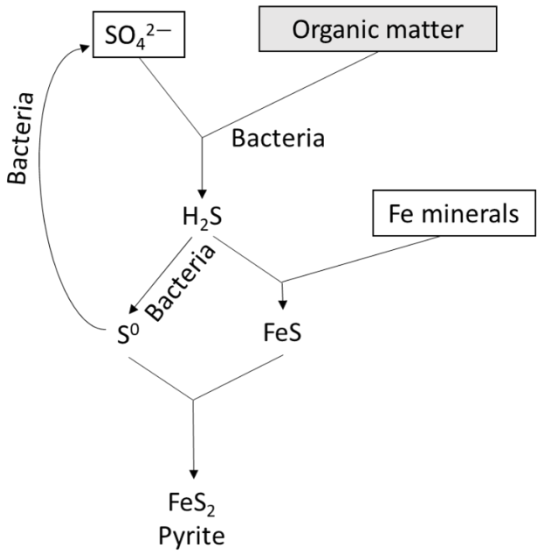

Figure 32 General model for the formation of sedimentary pyrite through a FeS precursor (after Berner, 1984) (Berner, 1984)

In oxic waters, the speciation of Re and Se is dominated by trace amounts of soluble perrenate, selenate, and selenite ions, each with their respective isotopic composition of +0.17 ± 0.12‰ for $\delta^{187/185}$Re (Dickson et al., 2020) and +0.3 ‰ for $\delta^{82/78}$Se (Chang et al., 2017). Highly reactive thioperrhenates are formed when Re complexes with sulphide in highly sulphidic waters. Se and Re are sequestered in iron- and sulphide-bearing ores, and their isotopic composition undergoes small

but measurable fractionation, depending on their degree of reduction and chemical environment. The residence time of Se and Re in the ocean is very different. Se persists in seawater for approximately 10-20 thousand years (Stüeken and Kipp, 2020), whereas Re remains for 720 thousand years (C. Miller et al., 2011). However, Se fractionates relatively much more than Re, with enrichment of light isotopes in the reduced phases between 0.1 to 11.8 ‰. In contrast, Re only shows a fractionation between -0.80‰ and +0.50‰, with the reduced phases enriched in heavy isotopes. Therefore, Se, which has a wider range of oxidation states, may be more sensitive to local redox processes than Re. In general, both elements have short residence times and are mainly restricted to local basins. Se and Re need protection from new disturbances caused by modern metamorphism and weathering because processes such as re-oxidation and re-reduction can significantly amplify the initial signal of compartment fractionation. However, the sensitivity of both elements to modern oxidative weathering makes them suitable for tracking contemporary processes, such as the weathering of carbonaceous rocks. This process releases CO_2 and is one of the causes of global warming.

Paleo-environmental studies have seldom investigated individual mineral phases in sediments. Limited observations have been made on experimental samples of both Se and Re, indicating considerable variability in measurements depending on the mineral type. This makes it challenging to interpret data resulting from the averaging of the isotopic composition of each constituent mineral in bulk rock measurements. In a previous study, $\delta^{82/76}$Se composition measurements have been performed in Se adsorption studies done on iron oxides (hematite, goethite and ferrihydrite), pyrite and mackinawite powders (Mitchell et al., 2013). This analysis was not extended to coprecipitated samples, as discussed in the preceding section, though this mechanism appears to be the primary mechanism for sequestering trace elements. The isotopic composition of our Re-pyrite and magnetite samples was compared to spectroscopic and microscopic analysis results. Fractionation was only observed in the magnetite samples, indicating that there was no fractionation during coprecipitation or adsorption to pyrite. The reason for this difference is unclear, but it may be related to the kinetic disparity between the two coprecipitation processes. Magnetite coprecipitation occurs faster (within 24 hours) than pyrite coprecipitation (which takes 6 days), and this may be due to the S/OH bonding type. The present study was limited to high concentrations of Re, as they allowed us to obtain XAS spectra data from the same samples. This limitation is due to the XAFS detection limit, which depends on the matrix. With a matrix rich in Fe, XAS measurements at the Re L_3-edge, a 100 ppm Re concentration is necessary, to date. However, these results suggest that it may be possible to trace past ocean chemistry directly by measuring isotopic fractionation only on magnetite minerals.

In summary, the study of the complementing Se and Re paleo-proxies is relatively new, and there are still many gaps in explaining the factors that generate the fractionation of their stable isotopes. To make interpretations more consistent, a greater understanding of molecular geochemistry is required to complement the recorded measurements in natural samples. Additionally, few if any geochemical studies in anoxic environments have considered the presence of organic carbon, which is key to the formation of sulphur-reducing species in the past oceans. For a forthcoming project, conducting $\delta^{187/185}$Re and $\delta^{82/76}$Se isotopic studies on pyrite and magnetite containing Re and Se could address the following objectives. (1) In order to characterize the speciation and mineralogy of Se- and Re-doped pyrites using a kinetic approach with and without the presence of organic carbon. One could repeat the synthesis of Se- and Re-doped pyrites, incorporating previously prepared organic matter content following the methodology presented in a previous study (MacKay and Canterbury, 2005) to mimic the organic carbon present in nature and see the OC v.s. pyrite effect on fractionation and sequestration. (2) Investigate the fractionation of Re and Se in experimental samples containing

low metalloid concentrations, close by to those found in nature (>1µM). For this purpose, the coprecipitation experimental procedure presented in the present thesis could be replicated, and at different reaction times (0, 2, 4, 8, 24, 48, and 96 hours) solid and remaining solution samples could be digested and isotopes separate on column in order to measure $\delta^{187/185}$Re and $\delta^{82/76}$Se isotopic ratios. (3) A literature review should be done to identify locations with sulfide and iron-rich sediments where to find high Re and Se concentrations. (4) Natural anoxic sediments rich in sulfide samples should be their Rhenium and Selenium content analysed, along with isotopic signatures, after magnetic separation of magnetite and pyrite mineralogical phases. Extracting these minerals can be achieved using separation methods proposed in the literature (Baer et al., 2010; Claff et al., 2010; Huerta-Diaz and Morse, 1990). Such a new study will help to enhance our understanding of affecting factors equilibrium isotope fractionation and to establish a direct correlation between laboratory systems and terrestrial material, with relatively low metalloid concentrations.

5.2.3 Towards an AMD remediation strategy

The impact of the release of selenate and selenite ions from coal mining or radioactive waste is an important issue, as these species become toxic at elevated concentrations. This study investigated the adsorption and co-precipitation mechanisms of selenium species with pyrite. Pyrite is a common sulfide mineral in the environment and is often discharged as solid waste by the mining industry. This material has emerged as a cost-effective sorbent for heavy metal control due to its high surface reactivity and environmental friendliness. However, the results obtained in the present study show a low reactivity of Se(VI), but high reactivity of Se(IV) with nano pyrite. The reactive sorption products, namely elemental selenium, SeS_2, $FeSe_2$ or $FeSe_xS_{(2-x)}$ particles, are all the most stable selenium compounds in nature, and this can greatly reduce the risk of secondary Se re-emission. A promising strategy for future studies is therefore to enhance Se(VI) removal by incorporating zero-valent iron (ZVI). ZVI appears to facilitate the conversion of Se(VI) into Se(IV) and Se(0), thereby enhancing Selenium reduction processes prior to its reductive precipitation (Das et al., 2017).

While ZVI is frequently employed for environmental remediation, its effectiveness is dependent on various factors, including the presence of oxygen and the pH of the solution (Naseri et al., 2017). These parameters have an impact on the oxidative dissolution of Fe(0). The ZVI particles dissolve into Fe(II) species that react with contaminants. The presence of excess oxygen leads to the formation of an oxide layer on the particles, which may reduce ZVI reactivity towards contaminants, particles cemented into aggregates that may reduce the permeability of the filtration system. The dissolution of ZVI increases the pH by consuming protons according to reaction (1) and this leads to a negative charge on formed Fe oxide particle surfaces and consequently to a reduced adsorption of oxyanions, such as selenate ions.

(1) $Fe(0) + 2H^+ \rightarrow Fe^{2+} + H_2$

Published studies suggest to use of pyrite together with ZVI, in order to enhance their respective individual remediation properties towards contaminants (Chen et al., 2020; Hu et al., 2021). As observed in the present thesis, pyrite also releases Fe(II) and generates H^+ upon contact with oxidants, as shown in reaction (2). This allows pyrite to buffer the pH increase induced by reaction (1), maintaining a high ZVI reactivity and inhibiting subsequent surface passivation.

(2) $FeS_2 + 7/2O_2 + H_2O \rightarrow Fe^{2+} + 2SO_4^{2-} + 2H^+$

The proposed project could thus aim at investigating the removal of Se(VI) using a ZVI and pyrite sorbent. The project could consist of two main parts. In the first part batch Se(VI) adsorption experiments using different ratios of ZVI and pyrite (5:1, 4:2, 3:3, 2:4, 1:5) could be conducted. Samples taken at various time intervals will be analyzed for their Se(VI), Fe(II), and ∑S(-II) soluble species content. Powder samples will be examined by TEM or STEM for newly formed mineralogical phases by EELS or XANES for their Se speciation. The second part would evaluate the optimal conditions for Se(VI) removal in waters which composition is similar to acid mine drainage (AMD) water. AMD water composition depends on the mine geology and can be rich in calcium, magnesium, bicarbonate, and/or sulphate. Both parts can be developed using two different experimental approaches: A batch reactor and a configuration mimicking a water treatment plant (see Figure 33).

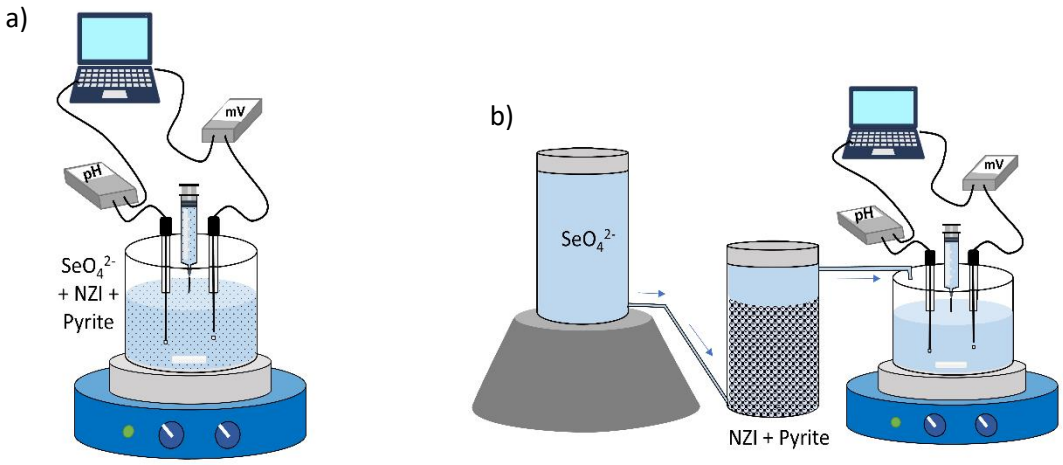

Figure 33 The diagram represents two experimental settings for the removal of Se(VI) using pyrite. A) Batch reactor with a solid concentration of pyrite mixed in water containing Se(VI). pH and EH conditions in situ during mixing. Sampling proposal at various equilibrium times: 0, 15 min, 30 min, 1 h, 2h, 4h, 8h and 24h, keeping solid and supernatant. b) Design of a low-cost treatment mine water plant on a small scale.

5.2.4 New materials

Advances in the synthesis of materials with new properties, or in the improvement of such properties is a major achievement in science and technology. Today, the development of new material should in low-cost, energy or time-efficient, easily scalable, operationally simple or safer than pre-existed synthesis methods. New materials must offer a sustainable future and thus allow to achieve sub-component recovery. The present study investigated the formation of Re_2S_7 nanoparticles under experimental conditions that closely mimic natural conditions. The characterisation of the nanoparticles is equivalent to that of 2D materials due to the highly controllable and precise atomic layer deposition (ALD) of the Re-S system.(Rahman et al., 2017). These Re-S composites have been proposed as excellent materials for flexible electronic devices (Hämäläinen et al., 2018), hydrogen evolution reactions and as candidate materials for lithium-sulphur batteries (Gao et al., n.d.). The benefits of developing and using new Re materials are also sustainable for the actual recycling of Re materials in superalloy and catalyst industries (Shen et al., 2021b) which suggests that the incorporation of 2D Re materials into a closed-loop system is feasible. However, the extraction of nanoparticles in our study encountered a limitation. In this investigation, Re_2S_7 powder was separated using $MgCl_2$ as a flocculating agent, which seemingly also precipitates and forms some crystals of magnesium hydroxide.

We have also presented magnetite nanoparticles with uniformly distributed gadolinium in the form of $Fe_{(3-x)}Gd_xO_4$ solid solutions for $0.02 < x < 0.1$. We propose that this first stage of nanoparticle synthesis can be a composite with strong potential in medical applications. This material combines the advantages of magnetite superparamagnetic iron oxide nanoparticles (SPIONs) and Gd-rich particles for imaging, therapeutic or theranostic applications, with easy recovery and recycling by conventional wastewater treatment methods.

The next phase for advancing these investigations should involve conducting two new studies. The first study entails preparing Re_2S_7 solutions once again at various time intervals (0, 2, 4, 8, 24, 48, 96, and 168 hours). This time, the nanoparticles will be separated using ultramicrofiltration. These additional experiments will contribute to a more comprehensive understanding of the nanoparticle formation of sulfide ion concentration in the solution.

The second study focuses on the design of organic coatings and toxicity assays for Gd-magnetite particles. The SPION composite requires surface functionalization and stabilization with an organic coating to render it more biocompatible and discreet at the nanoscale. This will enable selective attachment to specific biological entities, ensuring effective dispersion or solubilization and protection from environmental conditions such as oxidation or exposure to acids and bases (Cotin et al., 2021).

References

Afanasiev, P., 2008. Synthetic approaches to the molybdenum sulfide materials. Comptes Rendus Chimie 11, 159–182. https://doi.org/10.1016/j.crci.2007.04.009

Ahrland, S., 1973. Thermodynamics of the stepwise formation of metal-ion complexes in aqueous solution, in: Coordinative Interactions, Structure and Bonding. Springer, Berlin, Heidelberg, pp. 167–188. https://doi.org/10.1007/BFb0036786

Altomare, A.J., Young, N.A., Beazley, M.J., 2020. A preliminary survey of anthropogenic gadolinium in water and sediment of a constructed wetland. Journal of Environmental Management 255, 109897. https://doi.org/10.1016/j.jenvman.2019.109897

Anbar, A.D., Creaser, R.A., Papanastassiou, D.A., Wasserburg, G.J., 1992. Rhenium in seawater: Confirmation of generally conservative behavior. Geochimica et Cosmochimica Acta 56, 4099–4103. https://doi.org/10.1016/0016-7037(92)90021-A

Augsburger, F., Szabo, C., 2020. Potential role of the 3-mercaptopyruvate sulfurtransferase (3-MST)—hydrogen sulfide (H2S) pathway in cancer cells. Pharmacological Research, Country in focus: Pharmacology in Switzerland 154, 104083. https://doi.org/10.1016/j.phrs.2018.11.034

Baer, D.R., Grosz, A.E., Ilton, E.S., Krupka, K.M., Liu, J., Penn, R.L., Pepin, A., 2010. Separation, characterization and initial reaction studies of magnetite particles from Hanford sediments. Physics and Chemistry of the Earth, Parts A/B/C, MIGRATION 2009, 12th International Conference on the Chemistry and Migration Behaviour of Actinides and Fission Products in the Geosphere 35, 233–241. https://doi.org/10.1016/j.pce.2010.04.010

Balan, E., 2006. The oxidation state of vanadium in titanomagnetite from layered basic intrusions. American Mineralogist - AMER MINERAL 91, 953–956. https://doi.org/10.2138/am.2006.2192

Balistrieri, L.S., Chao, T.T., 1990. Adsorption of selenium by amorphous iron oxyhydroxide and manganese dioxide. Geochimica et Cosmochimica Acta 54, 739–751. https://doi.org/10.1016/0016-7037(90)90369-V

Bandoli, G., Tisato, F., Dolmella, A., Agostini, S., 2006. Structural overview of technetium compounds (2000–2004). Coordination chemistry reviews 250, 561–573.

Barnhart, J., 1997. Occurrences, Uses, and Properties of Chromium. Regulatory Toxicology and Pharmacology 26, S3–S7. https://doi.org/10.1006/rtph.1997.1132

Baya, C., Le Pape, P., Baptiste, B., Menguy, N., Delbes, L., Morand, M., Rouelle, M., Aubry, E., Ona-Nguema, G., Noël, V., Juillot, F., Morin, G., 2022. A methodological framework to study the behavior and kinetic influence of V, Mn, Co, Ni, Cu, Zn, As, Se and Mo during pyrite formation *via* the polysulfide pathway at ambient temperature. Chemical Geology 613, 121139. https://doi.org/10.1016/j.chemgeo.2022.121139

Belzile, N., Chen, Yu.-W., Xu, R., 2000. Early diagenetic behaviour of selenium in freshwater sediments. Applied Geochemistry 15, 1439–1454. https://doi.org/10.1016/S0883-2927(00)00011-1

Bennett, W.W., Canfield, D.E., 2020. Redox-sensitive trace metals as paleoredox proxies: A review and analysis of data from modern sediments. Earth-Science Reviews 204, 103175. https://doi.org/10.1016/j.earscirev.2020.103175

Berner, R.A., 1984. Sedimentary pyrite formation: An update. Geochimica et Cosmochimica Acta 48, 605–615. https://doi.org/10.1016/0016-7037(84)90089-9

Berner, R.A., 1970. Sedimentary pyrite formation. American Journal of Science 268, 1–23. https://doi.org/10.2475/ajs.268.1.1

Bernhardt, E., Herbst-Irmer, R., 2020. Phase transition and structures of the twinned low-temperature phases of $(Et_4N)[ReS_4]$. Acta Crystallogr C Struct Chem 76, 231–235. https://doi.org/10.1107/S205322961901725X

Berzina, A.N., Sotnikov, V.I., Economou-Eliopoulos, M., Eliopoulos, D.G., 2005. Distribution of rhenium in molybdenite from porphyry Cu–Mo and Mo–Cu deposits of Russia (Siberia) and Mongolia. Ore Geology Reviews 26, 91–113.

Birck, J.L., Barman, M.R., Capmas, F., 1997. Re-Os Isotopic Measurements at the Femtomole Level in Natural Samples. Geostandards Newsletter 21, 19–27. https://doi.org/10.1111/j.1751-908X.1997.tb00528.x

Blöchl, P.E., Jepsen, O., Andersen, O.K., 1994. Improved tetrahedron method for Brillouin-zone integrations. Phys. Rev. B 49, 16223–16233. https://doi.org/10.1103/PhysRevB.49.16223

Blowes, D.W., Ptacek, C.J., Jambor, J.L., Weisener, C.G., 2003. 9.05 - The Geochemistry of Acid Mine Drainage, in: Holland, H.D., Turekian, K.K. (Eds.), Treatise on Geochemistry. Pergamon, Oxford, pp. 149–204. https://doi.org/10.1016/B0-08-043751-6/09137-4

Bogart, L.K., Fock, J., Costa, G.M. da, Witte, K., Greneche, J.-M., Zukrowski, J., Sikora, M., Latta, D.E., Scherer, M.M., Hansen, M.F., Frandsen, C., Pankhurst, Q.A., 2021. Prenormative verification and validation of a protocol for measuring magnetite–maghemite ratios in magnetic nanoparticles. Metrologia 59, 015001. https://doi.org/10.1088/1681-7575/ac36b6

Boni, M., Terracciano, R., Evans, N., Laukamp, C., Schneider, J., Bechstädt, T., 2007. Genesis of Vanadium Ores in the Otavi Mountainland, Namibia. Economic Geology 102, 441–469. https://doi.org/10.2113/gsecongeo.102.3.441

Bonnissel-Gissinger, P., Alnot, M., Ehrhardt, J.-J., Behra, P., 1998. Surface Oxidation of Pyrite as a Function of pH. Environ. Sci. Technol. 32, 2839–2845. https://doi.org/10.1021/es980213c

Borah, D., Senapati, K., 2006. Adsorption of Cd(II) from aqueous solution onto pyrite. Fuel 85, 1929–1934. https://doi.org/10.1016/j.fuel.2006.01.012

Boyle, R.W., Jonasson, I.R., 1973. The geochemistry of arsenic and its use as an indicator element in geochemical prospecting. Journal of Geochemical Exploration 2, 251–296. https://doi.org/10.1016/0375-6742(73)90003-4

Brauer, G., 1975. Handbuch der präparativen anorganischen Chemie: in drei Bänden, 3. umgearb. Aufl. ed. Ferdinand Enke Verlag, Stuttgart.

Briscoe, H.V.A., Robinson, P.L., Stoddart, E.M., 1931. CXCV.—The sulphides and selenides of rhenium. J. Chem. Soc. 0, 1439–1443. https://doi.org/10.1039/JR9310001439

Bruland, K.W., Middag, R., Lohan, M.C., 2014. 8.2 - Controls of Trace Metals in Seawater, in: Holland, H.D., Turekian, K.K. (Eds.), Treatise on Geochemistry (Second Edition). Elsevier, Oxford, pp. 19–51. https://doi.org/10.1016/B978-0-08-095975-7.00602-1

Brumsack, H.-J., 2006. The trace metal content of recent organic carbon-rich sediments: Implications for Cretaceous black shale formation. Palaeogeography, Palaeoclimatology, Palaeoecology 232, 344–361. https://doi.org/10.1016/j.palaeo.2005.05.011

Brünjes, R., Hofmann, T., 2020. Anthropogenic gadolinium in freshwater and drinking water systems. Water Research 115966.

Bunău, O., Joly, Y., 2009. Self-consistent aspects of x-ray absorption calculations. Journal of physics. Condensed matter : an Institute of Physics journal 21, 345501. https://doi.org/10.1088/0953-8984/21/34/345501

Canfield, D.E., 1998. A new model for Proterozoic ocean chemistry. Nature 396, 450–453. https://doi.org/10.1038/24839

Canfield, D.E., Thamdrup, B., 2009. Towards a consistent classification scheme for geochemical environments, or, why we wish the term ‘suboxic’ would go away. Geobiology 7, 385–392. https://doi.org/10.1111/j.1472-4669.2009.00214.x

Cao, S., Duan, X., Zhao, X., Ma, J., Dong, T., Huang, N., Sun, C., He, B., Wei, F., 2014. Health risks from the exposure of children to As, Se, Pb and other heavy metals near the largest coking plant in China. Science of The Total Environment 472, 1001–1009. https://doi.org/10.1016/j.scitotenv.2013.11.124

Cao, T., Xu, T., Xu, R., Shu, X., Liao, S., 2020. Decarboxylative thiolation of redox-active esters to free thiols and further diversification. Nat Commun 11, 5340. https://doi.org/10.1038/s41467-020-19195-w

Chang, Y., Zhang, J., Qu, J.-Q., Xue, Y., 2017. Precise selenium isotope measurement in seawater by carbon-containing hydride generation-Desolvation-MC-ICP-MS after thiol resin preconcentration. Chemical Geology 471, 65–73. https://doi.org/10.1016/j.chemgeo.2017.09.011

Chapman, L.M., Roling, J.A., Bingham, L.K., Herald, M.R., Baldwin, W.S., 2004. Construction of a subtractive library from hexavalent chromium treated winter flounder

(Pseudopleuronectes americanus) reveals alterations in non-selenium glutathione peroxidases. Aquatic Toxicology 67, 181–194. https://doi.org/10.1016/j.aquatox.2003.12.006

Chappaz, A., Gobeil, C., Tessier, A., 2008. Geochemical and anthropogenic enrichments of Mo in sediments from perennially oxic and seasonally anoxic lakes in Eastern Canada. Geochimica et Cosmochimica Acta 72, 170–184. https://doi.org/10.1016/j.gca.2007.10.014

Chappaz, A., Lyons, T.W., Gregory, D.D., Reinhard, C.T., Gill, B.C., Li, C., Large, R.R., 2014. Does pyrite act as an important host for molybdenum in modern and ancient euxinic sediments? Geochimica et Cosmochimica Acta 126, 112–122. https://doi.org/10.1016/j.gca.2013.10.028

Charlet, L., Kang, M., Bardelli, F., Kirsch, R., Géhin, A., Grenèche, J.-M., Chen, F., 2012. Nanocomposite Pyrite–Greigite Reactivity toward Se(IV)/Se(VI). Environ. Sci. Technol. 46, 4869–4876. https://doi.org/10.1021/es204181q

Charlet, L., Scheinost, A.C., Tournassat, C., Greneche, J.M., Géhin, A., Fernández-Martı´nez, A., Coudert, S., Tisserand, D., Brendle, J., 2007. Electron transfer at the mineral/water interface: Selenium reduction by ferrous iron sorbed on clay. Geochimica et Cosmochimica Acta, Physical Chemistry of Soils and Aquifers: A Special Issue in Honor of Garrison Sposito 71, 5731–5749. https://doi.org/10.1016/j.gca.2007.08.024

Chen, F., C. Burns, P., Ewing, R.C., 1999. 79Se: geochemical and crystallo-chemical retardation mechanisms. Journal of Nuclear Materials 275, 81–94. https://doi.org/10.1016/S0022-3115(99)00105-1

Chen, K., Han, L., Li, J., Lü, Y., Yao, C., Dong, H., Wang, L., Li, Y., 2020. Pyrite enhanced the reactivity of zero-valent iron for reductive removal of dyes. Journal of Chemical Technology & Biotechnology 95, 1412–1420. https://doi.org/10.1002/jctb.6326

Cheng, W., Marsac, R., Hanna, K., 2018. Influence of magnetite stoichiometry on the binding of emerging organic contaminants. Environmental science & technology 52, 467–473.

Claff, S., Sullivan, L., Burton, E., Bush, R., 2010. A sequential extraction procedure for acid sulfate soils: Partitioning of iron. Geoderma 155, 224–230. https://doi.org/10.1016/j.geoderma.2009.12.002

Cline, J.D., 1969. Spectrophotometric Determination of Hydrogen Sulfide in Natural Waters. Limnology and Oceanography 14, 454–458. https://doi.org/10.4319/lo.1969.14.3.0454

Colodner, D., Edmond, J., Boyle, E., 1995. Rhenium in the Black Sea: comparison with molybdenum and uranium. Earth and Planetary Science Letters 131, 1–15. https://doi.org/10.1016/0012-821X(95)00010-A

Cotin, G., Blanco-Andujar, C., Perton, F., Asín, L., De La Fuente, J.M., Reichardt, W., Schaffner, D., Ngyen, D.-V., Mertz, D., Kiefer, C., Meyer, F., Spassov, S., Ersen, O., Chatzidakis, M., Botton, G.A., Hénoumont, C., Laurent, S., Greneche, J.-M., Teran, F.J., Ortega, D., Felder-Flesch, D., Begin-Colin, S., 2021. Unveiling the role of surface, size, shape and defects of iron oxide nanoparticles for theranostic applications. Nanoscale 13, 14552–14571. https://doi.org/10.1039/D1NR03335B

Crans, D.C., Zhang, B., Gaidamauskas, E., Keramidas, A.D., Willsky, G.R., Roberts, C.R., 2010. Is Vanadate Reduced by Thiols under Biological Conditions? Changing the Redox Potential of V(V)/V(IV) by Complexation in Aqueous Solution. Inorg. Chem. 49, 4245–4256. https://doi.org/10.1021/ic100080k

Crewe, A.V., Wall, J., 1970. A scanning microscope with 5 Å resolution. Journal of Molecular Biology 48, 375–393. https://doi.org/10.1016/0022-2836(70)90052-5

Cui, M., Luther, G.W., Gomes, M., 2023. Constraining the major pathways of vanadium incorporation into sediments underlying natural sulfidic waters. Geochimica et Cosmochimica Acta 359, 148–164. https://doi.org/10.1016/j.gca.2023.08.008

Cui, M., Luther, G.W., Gomes, M., 2021. Cycling of W and Mo species in natural sulfidic waters and their sorption mechanisms on MnO2 and implications for paired W and Mo records as a redox proxy. Geochimica et Cosmochimica Acta 295, 24–48. https://doi.org/10.1016/j.gca.2020.12.007

Cui, M., Mohajerin, T.J., Adebayo, S., Datta, S., Johannesson, K.H., 2020. Investigation of tungstate thiolation reaction kinetics and sedimentary molybdenum/tungsten enrichments: Implication for tungsten speciation in sulfidic waters and possible applications for paleoredox studies. Geochimica et Cosmochimica Acta 287, 277–295. https://doi.org/10.1016/j.gca.2020.04.004

Curti, E., Aimoz, L., Kitamura, A., 2013. Selenium uptake onto natural pyrite. J Radioanal Nucl Chem 295, 1655–1665. https://doi.org/10.1007/s10967-012-1966-9

Cutter, G.A., Cutter, L.S., 2001. Sources and cycling of selenium in the western and equatorial Atlantic Ocean. Deep Sea Research Part II: Topical Studies in Oceanography, Trace Chemical Species in the Water Column and Atmosphere of the Atlantic Ocean 48, 2917–2931. https://doi.org/10.1016/S0967-0645(01)00024-8

Dadachova, E., Bouzahzah, B., Zuckier, L.S., Pestell, R.G., 2002. Rhenium-188 as an alternative to Iodine-131 for treatment of breast tumors expressing the sodium/iodide symporter (NIS). Nuclear Medicine and Biology 29, 13–18. https://doi.org/10.1016/S0969-8051(01)00279-7

Das, S., Lindsay, M.B.J., Essilfie-Dughan, J., Hendry, M.J., 2017. Dissolved Selenium(VI) Removal by Zero-Valent Iron under Oxic Conditions: Influence of Sulfate and Nitrate. ACS Omega 2, 1513–1522. https://doi.org/10.1021/acsomega.6b00382

De Yoreo, J.J., Gilbert, P.U.P.A., Sommerdijk, N.A.J.M., Penn, R.L., Whitelam, S., Joester, D., Zhang, H., Rimer, J.D., Navrotsky, A., Banfield, J.F., Wallace, A.F., Michel, F.M., Meldrum, F.C., Cölfen, H., Dove, P.M., 2015. Crystallization by particle attachment in synthetic, biogenic, and geologic environments. Science 349, aaa6760. https://doi.org/10.1126/science.aaa6760

Del Corso, A., Giuseppe Vilardo, P., Cappiello, M., Cecconi, I., Dal Monte, M., Barsacchi, D., Mura, U., 2002. Physiological Thiols as Promoters of Glutathione Oxidation and Modifying Agents in Protein S-Thiolation. Archives of Biochemistry and Biophysics 397, 392–398. https://doi.org/10.1006/abbi.2001.2678

Dellinger, M., G. Hilton, R., M. Nowell, G., 2020. Measurements of rhenium isotopic composition in low-abundance samples. Journal of Analytical Atomic Spectrometry 35, 377–387. https://doi.org/10.1039/C9JA00288J

Dellinger, M., Hilton, R.G., Baronas, J.J., Torres, M.A., Burt, E.I., Clark, K.E., Galy, V., Ccahuana Quispe, A.J., West, A.J., 2023. High rates of rock organic carbon oxidation sustained as Andean sediment transits the Amazon foreland-floodplain. Proceedings of the National Academy of Sciences 120, e2306343120. https://doi.org/10.1073/pnas.2306343120

Dellwig, O., Wegwerth, A., Schnetger, B., Schulz, H., Arz, H.W., 2019. Dissimilar behaviors of the geochemical twins W and Mo in hypoxic-euxinic marine basins. Earth-Science Reviews 193, 1–23. https://doi.org/10.1016/j.earscirev.2019.03.017

Descostes, M., Schlegel, M.L., Eglizaud, N., Descamps, F., Miserque, F., Simoni, E., 2010. Uptake of uranium and trace elements in pyrite (FeS2) suspensions. Geochimica et Cosmochimica Acta 74, 1551–1562. https://doi.org/10.1016/j.gca.2009.12.004

Dickson, A.J., Hsieh, Y.-T., Bryan, A., 2020. The rhenium isotope composition of Atlantic Ocean seawater. Geochimica et Cosmochimica Acta 287, 221–228. https://doi.org/10.1016/j.gca.2020.02.020

Diemann, E., Müller, A., 1970. Elektronenspektren des VOS33−-, MoOS32−- und WOS32−-ions. Spectrochimica Acta Part A: Molecular Spectroscopy 26, 215–219. https://doi.org/10.1016/0584-8539(70)80262-8

Diener, A., Neumann, T., 2011. Synthesis and incorporation of selenide in pyrite and mackinawite. Radiochimica Acta 99, 791–798. https://doi.org/10.1524/ract.2011.1883

Diener, A., Neumann, T., Kramar, U., Schild, D., 2012. Structure of selenium incorporated in pyrite and mackinawite as determined by XAFS analyses. Journal of Contaminant Hydrology 133, 30–39. https://doi.org/10.1016/j.jconhyd.2012.03.003

Do, Y., Simhon, E.D., Holm, R.H., 1985. Tetrathiovanadate(V) and tetrathiorhenate(VII): structures and reactions, including characterization of the VFe2S4 core unit. Inorg. Chem. 24, 4635–4642. https://doi.org/10.1021/ic00220a042

Doebelin, N., Kleeberg, R., 2015. Profex: a graphical user interface for the Rietveld refinement program BGMN. Journal of applied crystallography 48, 1573–1580.

Doriguetto, A.C., Fernandes, N.G., Persiano, A.I.C., Filho, E.N., Grenèche, J.M., Fabris, J.D., 2003. Characterization of a natural magnetite. Phys Chem Minerals 30, 249–255. https://doi.org/10.1007/s00269-003-0310-x

Drewniak, L., Sklodowska, A., 2013. Arsenic-transforming microbes and their role in biomining processes. Environmental science and pollution research international 20. https://doi.org/10.1007/s11356-012-1449-0

Duce, R.A., Hoffman, G.L., 1976. Atmospheric vanadium transport to the ocean. Atmospheric Environment (1967) 10, 989–996. https://doi.org/10.1016/0004-6981(76)90207-9

Duckworth, S., Gaona, X., Castaño, D., Park, S., Altmaier, M., Geckeis, H., 2021. Redox chemistry, solubility and hydrolysis of Re in reducing aquatic systems. Thermodynamic description and comparison with Tc. Applied Geochemistry 132, 105037. https://doi.org/10.1016/j.apgeochem.2021.105037

Duker, A., Carranza, E., Hale, M., 2005. Arsenic geochemistry and health. Environment International 31, 631–641. https://doi.org/10.1016/j.envint.2004.10.020

Earnshaw, A., Greenwood, N.N., 1997. Chemistry of the Elements. Butterworth-Heinemann Oxford.

El-Ramady, H., Abdalla, N., Taha, H.S., Alshaal, T., El-Henawy, A., Faizy, S.E.-D.A., Shams, M.S., Youssef, S.M., Shalaby, T., Bayoumi, Y., Elhawat, N., Shehata, S., Sztrik, A., Prokisch, J., Fari, M., Domokos-Szabolcsy, E., Pilon-Smits, E.A., Selmar, D., Haneklaus, S., Schnug, E., 2016. Selenium and nano-selenium in plant nutrition. Environ. Chem. Lett. 14, 123–147. https://doi.org/10.1007/s10311-015-0535-1

Emerson, S.R., Huested, S.S., 1991. Ocean anoxia and the concentrations of molybdenum and vanadium in seawater. Marine Chemistry 34, 177–196. https://doi.org/10.1016/0304-4203(91)90002-E

Essington, M.E., 1988. Estimation of the Standard Free Energy of Formation of Metal Arsenates, Selenates, and Selenites. Soil Science Society of America Journal 52, 1574–1579. https://doi.org/10.2136/sssaj1988.03615995005200060010x

Etteieb, S., Magdouli, S., Komtchou, S.P., Zolfaghari, M., Tanabene, R., Brar, K.K., Calugaru, Iuliana L., Brar, S.K., 2021. Selenium speciation and bioavailability from mine discharge to the environment: a field study in Northern Quebec, Canada. Environ Sci Pollut Res 28, 50799–50812. https://doi.org/10.1007/s11356-021-14335-1

Fang, Y., Rogge, T., Ackermann, L., Wang, S.-Y., Ji, S.-J., 2018. Nickel-catalyzed reductive thiolation and selenylation of unactivated alkyl bromides. Nat Commun 9, 2240. https://doi.org/10.1038/s41467-018-04646-2

Fernández-Martínez, A., Charlet, L., 2009. Selenium environmental cycling and bioavailability: a structural chemist point of view. Rev Environ Sci Biotechnol 8, 81–110. https://doi.org/10.1007/s11157-009-9145-3

Ferrier, M., 2014. Technetium Sulfide: Fundamental Chemistry for Waste Storage Form's Application.

Finkelman, R.B., Mrose, M.E., 1977. Downeyite, the first verified natural occurrence of SeO2. American Mineralogist 62, 316–320.

Foltyn, K., Bertrandsson Erlandsson, V., Zygo, W., Melcher, F., Pieczonka, J., 2022. New perspective on trace element (Re, Ge, Ag) hosts in the Cu-Ag Kupferschiefer deposit, Poland: Insight from a LA-ICP-MS trace element study. Ore Geology Reviews 143, 104768. https://doi.org/10.1016/j.oregeorev.2022.104768

Fordyce, F.M., 2013. Selenium Deficiency and Toxicity in the Environment, in: Selinus, O. (Ed.), Essentials of Medical Geology: Revised Edition. Springer Netherlands, Dordrecht, pp. 375–416. https://doi.org/10.1007/978-94-007-4375-5_16

Fortune, W.B., Mellon, M.G., 1938. Determination of iron with O-phenanthroline: a spectrophotometric study. Industrial & Engineering Chemistry Analytical Edition 10, 60–64.

Freund, C., Wishard, A., Brenner, R., Sobel, M., Mizelle, J., Kim, A., Meyer, D.A., Morford, J.L., 2016. The effect of a thiol-containing organic molecule on molybdenum adsorption onto pyrite. Geochimica et Cosmochimica Acta 174, 222–235. https://doi.org/10.1016/j.gca.2015.11.015

Gao, J., Li, L., Tan, J., Sun, H., Li, B., Idrobo, J.C., Veer, C., Lu, T.-M., Koratkar, N., n.d. Vertically Oriented Arrays of ReS2 Nanosheets for Electrochemical Energy Storage and Electro-Catalysis.

Gay, C., Collins, J., Gebicki, J.M., 1999. Determination of Iron in Solutions with the Ferric–Xylenol Orange Complex. Analytical Biochemistry 273, 143–148. https://doi.org/10.1006/abio.1999.4207

Gebreeyessus, G.D., Zewge, F., 2018. A review on environmental selenium issues. SN Appl. Sci. 1, 55. https://doi.org/10.1007/s42452-018-0032-9

Geoffroy, N., Demopoulos, G.P., 2011. The elimination of selenium(IV) from aqueous solution by precipitation with sodium sulfide. J Hazard Mater 185, 148–154. https://doi.org/10.1016/j.jhazmat.2010.09.009

Ghobril, C., Popa, G., Parat, A., Billotey, C., Taleb, J., Bonazza, P., Begin-Colin, S., Felder-Flesch, D., 2013. A bisphosphonate tweezers and clickable PEGylated PAMAM dendrons for the preparation of functional iron oxide nanoparticles displaying renal and hepatobiliary elimination. Chem. Commun. 49, 9158. https://doi.org/10.1039/c3cc43161d

Gorski, C.A., Scherer, M.M., 2010. Determination of nanoparticulate magnetite stoichiometry by Mossbauer spectroscopy, acidic dissolution, and powder X-ray diffraction: A critical review. American Mineralogist 95, 1017–1026.

Graedel, T., Reck, B., Miatto, A., 2022. Alloy information helps prioritize material criticality lists. Nature Communications 13. https://doi.org/10.1038/s41467-021-27829-w

Grambow, B., 2008. Mobile fission and activation products in nuclear waste disposal. Journal of Contaminant Hydrology 102, 180–186. https://doi.org/10.1016/j.jconhyd.2008.10.006

Grégoire, M., Garçon, V., Garcia, H., Breitburg, D., Isensee, K., Oschlies, A., Telszewski, M., Barth, A., Bittig, H.C., Carstensen, J., Carval, T., Chai, F., Chavez, F., Conley, D., Coppola, L., Crowe, S., Currie, K., Dai, M., Deflandre, B., Dewitte, B., Diaz, R., Garcia-Robledo, E., Gilbert, D., Giorgetti, A., Glud, R., Gutierrez, D., Hosoda, S., Ishii, M., Jacinto, G., Langdon, C., Lauvset, S.K., Levin, L.A., Limburg, K.E., Mehrtens, H., Montes, I., Naqvi, W., Paulmier, A., Pfeil, B., Pitcher, G., Pouliquen, S., Rabalais, N., Rabouille, C., Recape, V., Roman, M., Rose, K., Rudnick, D., Rummer, J., Schmechtig, C., Schmidtko, S., Seibel, B., Slomp, C., Sumalia, U.R., Tanhua, T., Thierry, V., Uchida, H., Wanninkhof, R., Yasuhara, M., 2021. A Global Ocean Oxygen Database and Atlas for Assessing and Predicting Deoxygenation and Ocean Health in the Open and Coastal Ocean. Frontiers in Marine Science 8.

Greneche, J.-M., 2013. The contribution of 57 Fe Mössbauer spectrometry to investigate magnetic nanomaterials, in: Mössbauer Spectroscopy. Springer, pp. 187–241.

Guda, S.A., Guda, A.A., Soldatov, M.A., Lomachenko, K.A., Bugaev, A.L., Lamberti, C., Gawelda, W., Bressler, C., Smolentsev, G., Soldatov, A.V., Joly, Y., 2015. Optimized finite difference method for the full-potential XANES simulations: application to molecular adsorption geometries in MOFs and metal-ligand intersystem crossing transients. Journal of Chemical Theory and Computation 4512–4521. https://doi.org/10.1021/acs.jctc.5b00327

Guida, C., Ramothe, V., Chappaz, A., Simonnin, P., Rosso, K.M., Ding, R.-R., Prieur, D., Scheinost, A.C., Charlet, L., 2023. Revisiting Selenium Interactions with Pyrite: From Adsorption to Coprecipitation. ACS Earth Space Chem. 8, 67–78. https://doi.org/10.1021/acsearthspacechem.3c00219

Gupta, A.K., Gupta, M., 2005. Synthesis and surface engineering of iron oxide nanoparticles for biomedical applications. Biomaterials 26, 3995–4021. https://doi.org/10.1016/j.biomaterials.2004.10.012

Haase, F.J., Vessey, C.J., Sekine, R., Dorean, N.J.C., Welsh, D.T., Otte, J.A., Hamilton, J., Canfield, D.E., Wang, Y., Lombi, E., Bennett, W.W., 2024. Reductive sorption of vanadium by iron monosulfide in seawater. Chemical Geology 649, 121983. https://doi.org/10.1016/j.chemgeo.2024.121983

Hafner, J., Kresse, G., 1997. The Vienna AB-Initio Simulation Program VASP: An Efficient and Versatile Tool for Studying the Structural, Dynamic, and Electronic Properties of Materials. https://doi.org/10.1007/978-1-4615-5943-6_10

Hageman, S.P.W., van der Weijden, R.D., Stams, A.J.M., van Cappellen, P., Buisman, C.J.N., 2017. Microbial selenium sulfide reduction for selenium recovery from wastewater. Journal of Hazardous Materials 329, 110–119. https://doi.org/10.1016/j.jhazmat.2016.12.061

Hämäläinen, J., Mattinen, M., Mizohata, K., Meinander, K., Vehkamäki, M., Räisänen, J., Ritala, M., Leskelä, M., 2018. Atomic Layer Deposition of Rhenium Disulfide. Advanced Materials 30, 1703622. https://doi.org/10.1002/adma.201703622

Han, D.S., Batchelor, B., Abdel-Wahab, A., 2011. Sorption of selenium(IV) and selenium(VI) to mackinawite (FeS): Effect of contact time, extent of removal, sorption envelopes. Journal of Hazardous Materials 186, 451–457. https://doi.org/10.1016/j.jhazmat.2010.11.017

Harmer, M.A., Sykes, A.G., 1980. Kinetics of the interconversion of sulfido- and oxomolybdate(VI) species MoOxS4-x2- in aqueous solutions. Inorg. Chem. 19, 2881–2885. https://doi.org/10.1021/ic50212a006

Hatje, V., Bruland, K.W., Flegal, A.R., 2016. Increases in Anthropogenic Gadolinium Anomalies and Rare Earth Element Concentrations in San Francisco Bay over a 20 Year Record. Environ. Sci. Technol. 50, 4159–4168. https://doi.org/10.1021/acs.est.5b04322

He, H., Zhong, Y., Liang, X., Tan, W., Zhu, J., Yan WANG, C., 2015. Natural Magnetite: an efficient catalyst for the degradation of organic contaminant. Sci Rep 5, 10139. https://doi.org/10.1038/srep10139

Helz, G.R., 2022. The Re/Mo redox proxy reconsidered. Geochimica et Cosmochimica Acta 317, 507–522. https://doi.org/10.1016/j.gca.2021.10.029

Helz, G.R., Adelson, J.M., 2013. Trace Element Profiles in Sediments as Proxies of Dead Zone History; Rhenium Compared to Molybdenum. Environ. Sci. Technol. 47, 1257–1264. https://doi.org/10.1021/es303138d

Helz, G.R., Dolor, M.K., 2012. What regulates rhenium deposition in euxinic basins? Chemical Geology 304, 131–141.

Henkelman, G., Arnaldsson, A., Jónsson, H., 2006. A fast and robust algorithm for Bader decomposition of charge density. Computational Materials Science 36, 354–360. https://doi.org/10.1016/j.commatsci.2005.04.010

Herath, I., Vithanage, M., Seneweera, S., Bundschuh, J., 2018. Thiolated arsenic in natural systems: What is current, what is new and what needs to be known. Environment International 115, 370–386. https://doi.org/10.1016/j.envint.2018.03.027

Herrington, R., 2021. Mining our green future. Nat Rev Mater 6, 456–458. https://doi.org/10.1038/s41578-021-00325-9

Hibble, S.J., Walton, R.I., 1996. X-Ray absorption studies of amorphous Re2S7. Chemical Communications 2.

Hibble, S.J., Walton, R.I., Feaviour, M.R., Smith, A.D., 1999. Sulfur–sulfur bonding in the amorphous sulfides WS3, WS5, and Re2S7 from sulfur K-edge EXAFS studies. J. Chem. Soc., Dalton Trans. 2877–2883. https://doi.org/10.1039/a903918j

Hilton, R.G., Gaillardet, J., Calmels, D., Birck, J.-L., 2014. Geological respiration of a mountain belt revealed by the trace element rhenium. Earth and Planetary Science Letters 403, 27–36. https://doi.org/10.1016/j.epsl.2014.06.021

Hlohowskyj, S.R., Chappaz, A., Dickson, A.J., 2021a. Molybdenum as a Paleoredox Proxy: Past, Present, and Future. Elements in Geochemical Tracers in Earth System Science. https://doi.org/10.1017/9781108993777

Hlohowskyj, S.R., Chen, X., Romaniello, S.J., Vorlicek, T.P., Anbar, A.D., Lyons, T.W., Chappaz, A., 2021b. Quantifying Molybdenum Isotopic Speciation in Sulfidic Water: Implications for the Paleoredox Proxy. ACS Earth Space Chem. 5, 2891–2899. https://doi.org/10.1021/acsearthspacechem.1c00247

Hooda, P., 2010. Trace Elements in Soils. pp. 4–8. https://doi.org/10.13140/RG.2.1.3377.1123

Hope, B.K., 2008. A dynamic model for the global cycling of anthropogenic vanadium. Global Biogeochemical Cycles 22. https://doi.org/10.1029/2008GB003283

Hu, R., Cui, X., Xiao, M., Gwenzi, W., Noubactep, C., 2021. Characterizing the impact of pyrite addition on the efficiency of Fe0/H2O systems. Sci Rep 11, 2326. https://doi.org/10.1038/s41598-021-81649-y

Huang, J.-H., Huang, F., Evans, L., Glasauer, S., 2015. Vanadium: Global (bio)geochemistry. Chemical Geology 417, 68–89. https://doi.org/10.1016/j.chemgeo.2015.09.019

Huerta-Diaz, M.A., Morse, J.W., 1990. A Quantitative Method for Determination of Trace Metal Concentrations in Sedimentary Pyrite.

Hunger, S., Benning, L.G., 2007. Greigite: a true intermediate on the polysulfide pathway to pyrite. Geochem. Trans. 8, 1. https://doi.org/10.1186/1467-4866-8-1

Janani, V., Induja, S., Jaison, D., Meher Abhinav, E., Mothilal, M., Gopalakrishnan, C., 2021. Tailoring the hyperthermia potential of magnetite nanoparticles via gadolinium ION substitution. Ceramics International 47, 31399–31406. https://doi.org/10.1016/j.ceramint.2021.08.015

Janssen, D.J., Gilliard, D., Rickli, J., Nasemann, P., Koschinsky, A., Hassler, C.S., Bowie, A.R., Ellwood, M.J., Kleint, C., Jaccard, S.L., 2023. Chromium stable isotope distributions in the southwest Pacific Ocean and constraints on hydrothermal input from the Kermadec Arc. Geochimica et Cosmochimica Acta 342, 31–44. https://doi.org/10.1016/j.gca.2022.12.010

Jellinek, F., 1957. The structures of the chromium sulphides. Acta Cryst 10, 620–628. https://doi.org/10.1107/S0365110X57002200

Johannesson, K.H., Lyons, W.B., Graham, E.Y., Welch, K.A., 2000. Oxyanion concentrations in eastern Sierra Nevada rivers–3. Boron, molybdenum, vanadium, and tungsten. Aquatic Geochemistry 6, 19–46.

Jolivet, J.P., Belleville, P., Tronc, E., Livage, J., 1992. Influence of Fe(II) on the formation of the spinel iron oxide in alkaline medium. Clays Clay Miner 531–539.

Jolivet, J.-P., Chanéac, C., Tronc, E., 2004. Iron oxide chemistry. From molecular clusters to extended solid networks. Chem. Commun. 477–483. https://doi.org/10.1039/B304532N

Jordan, N., Ritter, A., Scheinost, A.C., Weiss, S., Schild, D., Hübner, R., 2014. Selenium(IV) Uptake by Maghemite (γ-Fe_2O_3). Environ. Sci. Technol. 48, 1665–1674. https://doi.org/10.1021/es4045852

Juillot, F., Ildefonse, Ph., Morin, G., Calas, G., Kersabiec, A.M. de, Benedetti, M., 1999. Remobilization of arsenic from buried wastes at an industrial site: mineralogical and geochemical control. Applied Geochemistry 14, 1031–1048. https://doi.org/10.1016/S0883-2927(99)00009-8

Jung, B., Safan, A., Batchelor, B., Abdel-Wahab, A., 2016. Spectroscopic study of Se (IV) removal from water by reductive precipitation using sulfide. Chemosphere 163, 351–358.

Juniku, R.B., 2004. Designing chiral rhenium (VII) trioxo complexes [WWW Document].

Kabata-Pendias, A., 2000. Trace elements in soils and plants. CRC press.

Kaegi, R., Gogos, A., Voegelin, A., Hug, S.J., Winkel, L.H., Buser, A.M., Berg, M., 2021. Quantification of individual Rare Earth Elements from industrial sources in sewage sludge. Water research X 11, 100092.

Kang, M., Chen, F., Wu, S., Yang, Y., Bruggeman, C., Charlet, L., 2011. Effect of pH on Aqueous Se(IV) Reduction by Pyrite. Environ. Sci. Technol. 45, 2704–2710. https://doi.org/10.1021/es1033553

Kang, M., Ma, B., Bardelli, F., Chen, F., Liu, C., Zheng, Z., Wu, S., Charlet, L., 2013. Interaction of aqueous Se(IV)/Se(VI) with FeSe/FeSe2: Implication to Se redox process. Journal of Hazardous Materials 248–249, 20–28. https://doi.org/10.1016/j.jhazmat.2012.12.037

Kashiwabara, T., Takahashi, Y., Marcus, M.A., Uruga, T., Tanida, H., Terada, Y., Usui, A., 2013. Tungsten species in natural ferromanganese oxides related to its different behavior from molybdenum in oxic ocean. Geochimica et Cosmochimica Acta 106, 364–378. https://doi.org/10.1016/j.gca.2012.12.026

Kendall, B., Creaser, R.A., Reinhard, C.T., Lyons, T.W., Anbar, A.D., 2015. Transient episodes of mild environmental oxygenation and oxidative continental weathering

during the late Archean. Science Advances 1, e1500777. https://doi.org/10.1126/sciadv.1500777
Ketris, M.P., Yudovich, Y., 2009. Estimations of Clarkes for Carbonaceous biolithes: World averages for trace element contents in black shales and coals. International Journal of Coal Geology 78, 135–148. https://doi.org/10.1016/j.coal.2009.01.002
Kilber, A.W., Boyanov, M.I., Kemner, K.M., O'Loughlin, E.J., 2024. Interactions of Perrhenate (Re (VII) O4-) with Fe (II)-Bearing Minerals. Minerals 14, 181.
Kim, E., Boulègue, J., 2003. Chemistry of rhenium as an analogue of technetium: Experimental studies of the dissolution of rhenium oxides in aqueous solutions. Radiochimica Acta 91, 211–216. https://doi.org/10.1524/ract.91.4.211.19968
Kinniburgh, D.G., Cooper, D.M., 2009. Creating graphical output with PHREEQC.
Kinraide, T.B., Yermiyahu, U., 2007. A scale of metal ion binding strengths correlating with ionic charge, Pauling electronegativity, toxicity, and other physiological effects. Journal of Inorganic Biochemistry, Life and Living in the Aluminium Age 101, 1201–1213. https://doi.org/10.1016/j.jinorgbio.2007.06.003
Kipp, M.A., Algeo, T.J., Stüeken, E.E., Buick, R., 2020. Basinal hydrographic and redox controls on selenium enrichment and isotopic composition in Paleozoic black shales. Geochimica et Cosmochimica Acta 287, 229–250. https://doi.org/10.1016/j.gca.2019.12.016
Kishida, K., Sohrin, Y., Okamura, K., Ishibashi, J., 2004. Tungsten enriched in submarine hydrothermal fluids. Earth and Planetary Science Letters 222, 819–827. https://doi.org/10.1016/j.epsl.2004.03.034
Kobayashi, T., Scheinost, A.C., Fellhauer, D., Gaona, X., Altmaier, M., 2013. Redox behavior of Tc(VII)/Tc(IV) under various reducing conditions in 0.1 M NaCl solutions. Radiochimica Acta 101, 323–332. https://doi.org/10.1524/ract.2013.2040
Korzhinsky, M.A., Tkachenko, S.I., Shmulovich, K.I., Taran, Y.A., Steinberg, G.S., 1994. Discovery of a pure rhenium mineral at Kudriavy volcano. Nature 369, 51–52. https://doi.org/10.1038/369051a0
Koutsospyros, A., Braida, W., Christodoulatos, C., Dermatas, D., Strigul, N., 2006. A review of tungsten: From environmental obscurity to scrutiny. Journal of Hazardous Materials, Selected Proceedings of the Seventh Biennial Protection and Restoration of the Environment International Conference 136, 1–19. https://doi.org/10.1016/j.jhazmat.2005.11.007
Krivovichev, V.G., Krivovichev, S.V., Charykova, M.V., 2019. Selenium Minerals: Structural and Chemical Diversity and Complexity. Minerals 9, 455. https://doi.org/10.3390/min9070455
Kumar, N., Noël, V., Planer-Friedrich, B., Besold, J., Lezama-Pacheco, J., Bargar, J.R., Brown, G.E., Fendorf, S., Boye, K., 2020. Redox Heterogeneities Promote Thioarsenate Formation and Release into Groundwater from Low Arsenic Sediments. Environ. Sci. Technol. 54, 3237–3244. https://doi.org/10.1021/acs.est.9b06502
Kümmerer, K., Helmers, E., 2000. Hospital effluents as a source of gadolinium in the aquatic environment. Environmental science & technology 34, 573–577.
Kurzweil, F., Archer, C., Wille, M., Schoenberg, R., Münker, C., Dellwig, O., 2021. Redox control on the tungsten isotope composition of seawater. pnas. https://doi.org/10.1073/pnas.2023544118
Large, R.R., Halpin, J.A., Danyushevsky, L.V., Maslennikov, V.V., Bull, S.W., Long, J.A., Gregory, D.D., Lounejeva, E., Lyons, T.W., Sack, P.J., 2014. Trace element content of sedimentary pyrite as a new proxy for deep-time ocean–atmosphere evolution. Earth and Planetary Science Letters 389, 209–220.
Li, Y., Wei, G., Liang, X., Zhang, C., Zhu, J., Arai, Y., 2020. Metal Substitution-Induced Reducing Capacity of Magnetite Coupled with Aqueous Fe (II). ACS Earth and Space Chemistry 4, 905–911.
Liu, H., Xu, B., Liu, J.-M., Yin, J., Miao, F., Duan, C.-G., Wan, X.G., 2016. Highly efficient and ultrastable visible-light photocatalytic water splitting over ReS2. Phys. Chem. Chem. Phys. 18, 14222–14227. https://doi.org/10.1039/C6CP01007E

Liu, J. (Jimmy), 2021. Advances and Applications of Atomic-Resolution Scanning Transmission Electron Microscopy. Microscopy and Microanalysis 27, 943–995. https://doi.org/10.1017/S1431927621012125

Liu, J., Pearce, C.I., Qafoku, O., Arenholz, E., Heald, S.M., Rosso, K.M., 2012. Tc(VII) reduction kinetics by titanomagnetite (Fe3−xTixO4) nanoparticles. Geochimica et Cosmochimica Acta 92, 67–81. https://doi.org/10.1016/j.gca.2012.06.004

Liu, Y.-Y., Xu, L., Guo, X.-T., Lv, T.-T., Pang, H., 2020. Vanadium sulfide based materials: synthesis, energy storage and conversion. J. Mater. Chem. A 8, 20781–20802. https://doi.org/10.1039/D0TA07436E

Livens, F.R., Jones, M.J., Hynes, A.J., Charnock, J.M., Mosselmans, J.F.W., Hennig, C., Steele, H., Collison, D., Vaughan, D.J., Pattrick, R.A.D., Reed, W.A., Moyes, L.N., 2004. X-ray absorption spectroscopy studies of reactions of technetium, uranium and neptunium with mackinawite. Journal of Environmental Radioactivity, Papers from the International Conference on Radioactivity in the Environment, Monaco, 1-5 September 2002 74, 211–219. https://doi.org/10.1016/j.jenvrad.2004.01.012

Lohmayer, R., Reithmaier, G.M.S., Bura-Nakić, E., Planer-Friedrich, B., 2015. Ion-Pair Chromatography Coupled to Inductively Coupled Plasma–Mass Spectrometry (IPC-ICP-MS) as a Method for Thiomolybdate Speciation in Natural Waters [WWW Document]. ACS Publications. https://doi.org/10.1021/ac5046406

Lottermoser, B.G., 2010. Mine Wastes: Characterization, Treatment and Environmental Impacts, in: Lottermoser, B. (Ed.), Mine Wastes: Characterization, Treatment and Environmental Impacts. Springer, Berlin, Heidelberg, pp. 1–41. https://doi.org/10.1007/978-3-642-12419-8_1

Lu, Z., Lu, W., Rickaby, R.E.M., Thomas, E., 2020. Earth History of Oxygen and the iprOxy, 1st ed. Cambridge University Press. https://doi.org/10.1017/9781108688604

Lunk, H.-J., Drobot, D.V., Hartl, H., 2021. Discovery, properties and applications of rhenium and its compounds. ChemTexts 7, 1–21.

Lux, J., Sherry, A.D., 2018. Advances in gadolinium-based MRI contrast agent designs for monitoring biological processes in vivo. Current Opinion in Chemical Biology, Molecular Imaging / Chemical Genetics and Epigenetics 45, 121–130. https://doi.org/10.1016/j.cbpa.2018.04.006

MacKay, A.A., Canterbury, B., 2005. Oxytetracycline Sorption to Organic Matter by Metal-Bridging. Journal of Environmental Quality 34, 1964–1971. https://doi.org/10.2134/jeq2005.0014

Manceau, A., Merkulova, M., Mathon, O., Glatzel, P., Murdzek, M., Batanova, V., Simionovici, A., Steinmann, S.N., Paktunc, D., 2020. The mode of incorporation of As (-I) and Se (-I) in natural pyrite revisited. ACS Earth and Space Chemistry 4, 379–390.

Marshall, T.A., Morris, K., Law, G.T.W., Mosselmans, J.F.W., Bots, P., Parry, S.A., Shaw, S., 2014. Incorporation and Retention of 99-Tc(IV) in Magnetite under High pH Conditions. Environ. Sci. Technol. 48, 11853–11862. https://doi.org/10.1021/es503438e

Martins, P.M., Lima, A.C., Ribeiro, S., Lanceros-Mendez, S., Martins, P., 2021. Magnetic Nanoparticles for Biomedical Applications: From the Soul of the Earth to the Deep History of Ourselves. ACS Appl Bio Mater 4, 5839–5870. https://doi.org/10.1021/acsabm.1c00440

Maslin, M., Van Heerde, L., Day, S., 2022. Sulfur: A potential resource crisis that could stifle green technology and threaten food security as the world decarbonises. The Geographical Journal 188, 498–505. https://doi.org/10.1111/geoj.12475

Mason, R.P., Soerensen, A.L., DiMento, B.P., Balcom, P.H., 2018. The Global Marine Selenium Cycle: Insights From Measurements and Modeling. Global Biogeochemical Cycles 32, 1720–1737. https://doi.org/10.1029/2018GB006029

Matamoros-Veloza, A., Peacock, C.L., Benning, L.G., 2014. Selenium Speciation in Framboidal and Euhedral Pyrites in Shales. Environ. Sci. Technol. 48, 8972–8979. https://doi.org/10.1021/es405686q

Materials Data on NaReO4 by Materials Project (No. mp-5558), 2020. . Lawrence Berkeley National Lab. (LBNL), Berkeley, CA (United States). LBNL Materials Project. https://doi.org/10.17188/1268996

McLennan, S.M., 2001. Relationships between the trace element composition of sedimentary rocks and upper continental crust. Geochemistry, Geophysics, Geosystems 2. https://doi.org/10.1029/2000GC000109

Middelburg, J.J., Levin, L.A., 2009. Coastal hypoxia and sediment biogeochemistry. Biogeosciences 6, 1273–1293.

Miller, C., Peucker-Ehrenbrink, B., Walker, B., Marcantonio, F., 2011. Re-assessing the surface cycling of molybdenum and rhenium. Geochimica et Cosmochimica Acta 75, 7146–7179. https://doi.org/10.1016/j.gca.2011.09.005

Miller, C.A., Peucker-Ehrenbrink, B., Ball, L., 2009. Precise determination of rhenium isotope composition by multi-collector inductively-coupled plasma mass spectrometry. J. Anal. At. Spectrom. 24, 1069. https://doi.org/10.1039/b818631f

Miller, C.A., Peucker-Ehrenbrink, B., Schauble, E.A., 2015. Theoretical modeling of rhenium isotope fractionation, natural variations across a black shale weathering profile, and potential as a paleoredox proxy. Earth and Planetary Science Letters 430, 339–348. https://doi.org/10.1016/j.epsl.2015.08.008

Miller, C.A., Peucker-Ehrenbrink, B., Walker, B.D., Marcantonio, F., 2011. Re-assessing the surface cycling of molybdenum and rhenium. Geochimica et Cosmochimica Acta 75, 7146–7179. https://doi.org/10.1016/j.gca.2011.09.005

Mindat.org [WWW Document], n.d. URL https://mindat.org/element/Chromium (accessed 3.1.24).

Misono, M., Ochiai, E., Saito, Y., Yoneda, Y., 1967. A new dual parameter scale for the strength of lewis acids and bases with the evaluation of their softness. Journal of Inorganic and Nuclear Chemistry 29, 2685–2691. https://doi.org/10.1016/0022-1902(67)80006-X

Mitchell, K., Couture, R.-M., Johnson, T.M., Mason, P.R.D., Van Cappellen, P., 2013. Selenium sorption and isotope fractionation: Iron(III) oxides versus iron(II) sulfides. Chemical Geology 342, 21–28. https://doi.org/10.1016/j.chemgeo.2013.01.017

Mitchell, K., Mason, P.R.D., Van Cappellen, P., Johnson, T.M., Gill, B.C., Owens, J.D., Diaz, J., Ingall, E.D., Reichart, G.-J., Lyons, T.W., 2012. Selenium as paleo-oceanographic proxy: A first assessment. Geochimica et Cosmochimica Acta 89, 302–317. https://doi.org/10.1016/j.gca.2012.03.038

Mohajerin, T.J., Helz, G.R., Johannesson, K.H., 2016. Tungsten–molybdenum fractionation in estuarine environments. Geochimica et Cosmochimica Acta 177, 105–119. https://doi.org/10.1016/j.gca.2015.12.030

Moon, J.-W., Rawn, C.J., Rondinone, A.J., Wang, W., Vali, H., Yeary, L.W., Love, L.J., Kirkham, M.J., Gu, B., Phelps, T.J., 2010. Crystallite Sizes and Lattice Parameters of Nano-Biomagnetite Particles. Journal of Nanoscience and Nanotechnology 10, 8298–8306. https://doi.org/10.1166/jnn.2010.2745

Moore, E.K., Hao, J., Spielman, S.J., Yee, N., 2020. The evolving redox chemistry and bioavailability of vanadium in deep time. Geobiology 18, 127–138. https://doi.org/10.1111/gbi.12375

Morford, J.L., Emerson, S., 1999. The geochemistry of redox sensitive trace metals in sediments. Geochimica et Cosmochimica Acta 63, 1735–1750. https://doi.org/10.1016/S0016-7037(99)00126-X

Morin, G., Juillot, F., Casiot, C., Bruneel, O., Personné, J.-C., Elbaz-Poulichet, F., Leblanc, M., Ildefonse, P., Calas, G., 2003. Bacterial Formation of Tooeleite and Mixed Arsenic(III) or Arsenic(V)−Iron(III) Gels in the Carnoulès Acid Mine Drainage, France. A XANES, XRD, and SEM Study. Environ. Sci. Technol. 37, 1705–1712. https://doi.org/10.1021/es025688p

Morse, J.W., Berner, R.A., 1995. What determines sedimentary C/S ratios? Geochimica et Cosmochimica Acta 59, 1073–1077. https://doi.org/10.1016/0016-7037(95)00024-T

Müller, A., Diemann, E., Jostes, R., Bögge, H., 1981. Transition Metal Thiometalates: Properties and Significance in Complex and Bioinorganic Chemistry. Angewandte Chemie International Edition in English 20, 934–955. https://doi.org/10.1002/anie.198109341

Müller, A., Wittneben, V., Diemann, E., Hormes, J., Kuetgens, U., 1994. Electronic structure of thiometalates [MS4]n− (M=Mo, W, Re). XANES spectra and SCF-Xα-SW

calculations. Chemical Physics Letters 225, 359–363. https://doi.org/10.1016/0009-2614(94)87094-2
Müller, J.H., Lande, W.A. la Jr., 1933. The Precipitation of Rhenium Sulfide from Ammoniacal Solution. A Separation of Rhenium and Molybdenum. J. Am. Chem. Soc. 55, 2376–2378. https://doi.org/10.1021/ja01333a023
Nameroff, T., Balistrieri, L., Murray, J., 2002. Suboxic trace metal geochemistry in the Eastern Tropical North Pacific. Geochimica Et Cosmochimica Acta - GEOCHIM COSMOCHIM ACTA 66, 1139–1158. https://doi.org/10.1016/S0016-7037(01)00843-2
Naseri, E., Ndé-Tchoupé, A.I., Mwakabona, H.T., Nanseu-Njiki, C.P., Noubactep, C., Njau, K.N., Wydra, K.D., 2017. Making Fe0-Based Filters a Universal Solution for Safe Drinking Water Provision. Sustainability 9, 1224. https://doi.org/10.3390/su9071224
Neikov, O.D., Naboychenko, S.S., Murashova, I.B., Yefimov, N.A., 2019. Chapter 23 - Production of Refractory Metal Powders, in: Neikov, O.D., Naboychenko, S.S., Yefimov, N.A. (Eds.), Handbook of Non-Ferrous Metal Powders (Second Edition). Elsevier, Oxford, pp. 685–755. https://doi.org/10.1016/B978-0-08-100543-9.00023-3
Nyström, E., Thomas, H., Wanhainen, C., Alakangas, L., 2021. Occurrence and Release of Trace Elements in Pyrite-Rich Waste Rock. Minerals 11, 495. https://doi.org/10.3390/min11050495
O'Connor, A.E., Canuel, E.A., Beck, A.J., 2022. Drivers and Seasonal Variability of Redox-Sensitive Metal Chemistry in a Shallow Subterranean Estuary. Frontiers in Environmental Science 9.
Osamu, W., 2004. What are Trace Elements? Trace Elements 351.
Paier, J., Hirschl, R., Marsman, M., Kresse, G., 2005. The Perdew–Burke–Ernzerhof exchange-correlation functional applied to the G2-1 test set using a plane-wave basis set. The Journal of Chemical Physics 122, 234102. https://doi.org/10.1063/1.1926272
Palumaa, P., 2009. Biological Redox Switches. Antioxidants & Redox Signaling 11, 981–983. https://doi.org/10.1089/ars.2009.2468
Pape, P.L., Blanchard, M., Brest, J., Boulliard, J.-C., Ikogou, M., Stetten, L., Wang, S., Landrot, G., Morin, G., 2017. Arsenic incorporation in pyrite at ambient temperature at both tetrahedral 2 S-I and octahedral Fe+II sites: evidence from EXAFS-DFT analysis. Environmental Science & Technology 51, 150–158.
Parr, R.G., Pearson, R.G., 1983. Absolute hardness: companion parameter to absolute electronegativity. J. Am. Chem. Soc. 105, 7512–7516. https://doi.org/10.1021/ja00364a005
Peacock, R.D., 1966. chemistry of technetium and rhenium.
Pearce, C.I., Liu, J., Baer, D.R., Qafoku, O., Heald, S.M., Arenholz, E., Grosz, A.E., McKinley, J.P., Resch, C.T., Bowden, M.E., 2014. Characterization of natural titanomagnetites (Fe3- xTixO4) for studying heterogeneous electron transfer to Tc (VII) in the Hanford subsurface. Geochimica et Cosmochimica Acta 128, 114–127.
Pearce, C.I., Qafoku, O., Liu, J., Arenholz, E., Heald, S.M., Kukkadapu, R.K., Gorski, C.A., Henderson, C.M.B., Rosso, K.M., 2012. Synthesis and properties of titanomagnetite (Fe3- xTixO4) nanoparticles: A tunable solid-state Fe (II/III) redox system. Journal of colloid and interface science 387, 24–38.
Pearson, R.G., 1997. Chemical Hardness, 1st ed. Wiley. https://doi.org/10.1002/3527606173
Pearson, R.G., 1988. Absolute electronegativity and hardness: application to inorganic chemistry. Inorg. Chem. 27, 734–740. https://doi.org/10.1021/ic00277a030
Pearson, R.G., 1963. Hard and soft acids and bases. Journal of the American Chemical society 85, 3533–3539.
Peng, H., I. Pearce, C., Huang, W., Zhu, Z., T. N'Diaye, A., M. Rosso, K., Liu, J., 2018. Reversible Fe(ii) uptake/release by magnetite nanoparticles. Environmental Science: Nano 5, 1545–1555. https://doi.org/10.1039/C8EN00328A
Perdew, J.P., Burke, K., Ernzerhof, M., 1996. Generalized Gradient Approximation Made Simple. Phys. Rev. Lett. 77, 3865–3868. https://doi.org/10.1103/PhysRevLett.77.3865
Perrone, D., Monteiro, M., Nunes, J., 2015. The Chemistry of Selenium. pp. 3–15. https://doi.org/10.1039/9781782622215-00003

Petersen, R.G., Hamilton, J.C., Myers, A.T., 1957. An occurrence of rhenium, associated with uraninite in Coconino County, Arizona (Report No. 651), Trace Elements Investigations. Washington, D.C. https://doi.org/10.3133/tei651

Pettine, M., Gennari, F., Campanella, L., Casentini, B., Marani, D., 2012. The reduction of selenium(IV) by hydrogen sulfide in aqueous solutions. Geochimica et Cosmochimica Acta 83, 37–47. https://doi.org/10.1016/j.gca.2011.12.024

Planer-Friedrich, B., Forberg, J., Lohmayer, R., Kerl, C.F., Boeing, F., Kaasalainen, H., Stefánsson, A., 2020. Relative Abundance of Thiolated Species of As, Mo, W, and Sb in Hot Springs of Yellowstone National Park and Iceland. Environ. Sci. Technol. 54, 4295–4304. https://doi.org/10.1021/acs.est.0c00668

Planer-Friedrich, B., Wallschläger, D., 2009. A Critical Investigation of Hydride Generation-Based Arsenic Speciation in Sulfidic Waters. Environmental science & technology. https://doi.org/10.1021/es900111z

Polyak, D.E., 2023. Rhenium in USGS Online Publications Directory, Mineral Commodity Summaries. U.S. Geological Survey.

Pósfai, M., Dunin-Borkowski, R.E., 2006. Sulfides in biosystems. Reviews in Mineralogy and Geochemistry 61, 679–714.

Poulain, A., Fernandez-Martinez, A., Greneche, J.-M., Prieur, D., Scheinost, A.C., Menguy, N., Bureau, S., Magnin, V., Findling, N., Drnec, J., Martens, I., Mirolo, M., Charlet, L., 2022. Selenium Nanowire Formation by Reacting Selenate with Magnetite. Environ. Sci. Technol. acs.est.1c08377. https://doi.org/10.1021/acs.est.1c08377

Rahman, M., Davey, K., Qiao, S.-Z., 2017. Advent of 2D Rhenium Disulfide (ReS2): Fundamentals to Applications. Advanced Functional Materials 27, 1606129. https://doi.org/10.1002/adfm.201606129

Ranade, A.C., Müller, A., Diemann, E., 1970. Übergangsmetallchalkogenverbindungen. Evidence for the existence of new Thioanions of Vanadium and Rhenium by their electronic spectra. Zeitschrift für anorganische und allgemeine Chemie 373, 258–264. https://doi.org/10.1002/zaac.19703730308

Ravel, B., Newville, M., 2005. ATHENA and ARTEMIS: interactive graphical data analysis using IFEFFIT. Physica Scripta 2005, 1007.

Rebodos, R.L., Vikesland, P.J., 2010. Effects of Oxidation on the Magnetization of Nanoparticulate Magnetite. Langmuir 26, 16745–16753. https://doi.org/10.1021/la102461z

Reich, H.J., Hondal, R.J., 2016. Why Nature Chose Selenium. ACS Chem. Biol. 11, 821–841. https://doi.org/10.1021/acschembio.6b00031

Rickard, D., 2012. Sulfidic sediments and sedimentary rocks. Newnes.

Rickard, D., Luther, G.W., 2007. Chemistry of Iron Sulfides. Chem. Rev. 107, 514–562. https://doi.org/10.1021/cr0503658

Rieder, M., Crelling, J.C., Šustai, O., Drábek, M., Weiss, Z., Klementová, M., 2007. Arsenic in iron disulfides in a brown coal from the North Bohemian Basin, Czech Republic. International Journal of Coal Geology 71, 115–121. https://doi.org/10.1016/j.coal.2006.07.003

Robbins, L.J., Lalonde, S.V., Planavsky, N.J., Partin, C.A., Reinhard, C.T., Kendall, B., Scott, C., Hardisty, D.S., Gill, B.C., Alessi, D.S., Dupont, C.L., Saito, M.A., Crowe, S.A., Poulton, S.W., Bekker, A., Lyons, T.W., Konhauser, K.O., 2016. Trace elements at the intersection of marine biological and geochemical evolution. Earth-Science Reviews 163, 323–348. https://doi.org/10.1016/j.earscirev.2016.10.013

Rochette, E.A., Bostick, B.C., Li, G., Fendorf, S., 2000. Kinetics of Arsenate Reduction by Dissolved Sulfide. Environ. Sci. Technol. 34, 4714–4720. https://doi.org/10.1021/es000963y

Rodríguez, D.M., Mayordomo, N., Scheinost, A.C., Schild, D., Brendler, V., Müller, K., Stumpf, T., 2020. New Insights into ^{99}Tc(VII) Removal by Pyrite: A Spectroscopic Approach. Environ. Sci. Technol. 54, 2678–2687. https://doi.org/10.1021/acs.est.9b05341

Rodríguez, D.M., Mayordomo, N., Schild, D., Shams Aldin Azzam, S., Brendler, V., Müller, K., Stumpf, T., 2021. Reductive immobilization of 99Tc(VII) by FeS2: The effect of

marcasite. Chemosphere 281, 130904. https://doi.org/10.1016/j.chemosphere.2021.130904
Rogowska, J., Olkowska, E., Ratajczyk, W., Wolska, L., 2018. Gadolinium as a new emerging contaminant of aquatic environments. Environmental toxicology and chemistry 37, 1523–1534.
Rooney, A.D., Macdonald, F.A., Strauss, J.V., Dudás, F.Ö., Hallmann, C., Selby, D., 2014. Re-Os geochronology and coupled Os-Sr isotope constraints on the Sturtian snowball Earth. Proceedings of the National Academy of Sciences 111, 51–56. https://doi.org/10.1073/pnas.1317266110
Rosso, K.M., Becker, U., Hochella Jr, M.F., 2000. Surface defects and self-diffusion on pyrite {100}: An ultra-high vacuum scanning tunneling microscopy and theoretical modeling study. American Mineralogist 85, 1428–1436.
Rubalcaba, J.G., Verberk, W.C., Hendriks, A.J., Saris, B., Woods, H.A., 2020. Oxygen limitation may affect the temperature and size dependence of metabolism in aquatic ectotherms. Proceedings of the National Academy of Sciences 117, 31963–31968.
Ryser, A.L., Strawn, D.G., Marcus, M.A., Johnson-Maynard, J.L., Gunter, M.E., Möller, G., 2005. Micro-spectroscopic investigation of selenium-bearing minerals from the Western US Phosphate Resource Area. Geochemical Transactions 6, 1–11.
Sanville, E., Kenny, S.D., Smith, R., Henkelman, G., 2007. Improved grid-based algorithm for Bader charge allocation. Journal of Computational Chemistry 28, 899–908. https://doi.org/10.1002/jcc.20575
Scheinost, A., Claussner, J., Exner, J., Feig, M., Findeisen, S., Hennig, C., Kvashnina, K., Naudet, D., Prieur, D., Rossberg, A., Schmidt, M., Qiu, C., Colomp, P., Cohen, C., Dettona, E., Dyadkin, V., Stumpf, T., 2021. ROBL-II at ESRF: a synchrotron toolbox for actinide research. Journal of Synchrotron Radiation 28, 333–349. https://doi.org/10.1107/S1600577520014265
Scheinost, A.C., Charlet, L., 2008a. Selenite Reduction by Mackinawite, Magnetite and Siderite: XAS Characterization of Nanosized Redox Products. Environ. Sci. Technol. 42, 1984–1989. https://doi.org/10.1021/es071573f
Scheinost, A.C., Charlet, L., 2008b. Selenite Reduction by Mackinawite, Magnetite and Siderite: XAS Characterization of Nanosized Redox Products. Environ. Sci. Technol. 42, 1984–1989. https://doi.org/10.1021/es071573f
Schock, H.H., 1979. Distribution of rare-earth and other trace elements in magnetites. Chemical Geology 26, 119–133. https://doi.org/10.1016/0009-2541(79)90034-2
Schwarz, D.E., Frenkel, A.I., Nuzzo, R.G., Rauchfuss, T.B., Vairavamurthy, A., 2004. Electrosynthesis of ReS4. XAS Analysis of ReS2, Re2S7, and ReS4. Chem. Mater. 16, 151–158. https://doi.org/10.1021/cm034467v
Séby, F., Potin-Gautier, M., Giffaut, E., Borge, G., Donard, O.F.X., 2001. A critical review of thermodynamic data for selenium species at 25°C. Chemical Geology 171, 173–194. https://doi.org/10.1016/S0009-2541(00)00246-1
Senesil, G.S., Baldassarre, G., Senesi, N., Radina, B., 1999. Trace element inputs into soils by anthropogenic activities and implications for human health. Chemosphere, Matter and Energy Fluxes in the Anthropocentric Environment 39, 343–377. https://doi.org/10.1016/S0045-6535(99)00115-0
Shaheen, S.M., Alessi, D.S., Tack, F.M.G., Ok, Y.S., Kim, K.-H., Gustafsson, J.P., Sparks, D.L., Rinklebe, J., 2019. Redox chemistry of vanadium in soils and sediments: Interactions with colloidal materials, mobilization, speciation, and relevant environmental implications- A review. Advances in Colloid and Interface Science 265, 1–13. https://doi.org/10.1016/j.cis.2019.01.002
Shannon, R.D., 1976. Revised effective ionic radii and systematic studies of interatomic distances in halides and chalcogenides. Acta Crystallographica Section A 32, 751–767. https://doi.org/10.1107/S0567739476001551
Sheen, A.I., Kendall, B., Reinhard, C.T., Creaser, R.A., Lyons, T.W., Bekker, A., Poulton, S.W., Anbar, A.D., 2018. A model for the oceanic mass balance of rhenium and implications for the extent of Proterozoic ocean anoxia. Geochimica et Cosmochimica Acta 227, 75–95. https://doi.org/10.1016/j.gca.2018.01.036

Shen, L., Tesfaye, F., Li, X., Lindberg, D., Taskinen, P., 2021a. Review of rhenium extraction and recycling technologies from primary and secondary resources. Minerals Engineering 161, 106719. https://doi.org/10.1016/j.mineng.2020.106719

Shen, L., Tesfaye, F., Li, X., Lindberg, D., Taskinen, P., 2021b. Review of rhenium extraction and recycling technologies from primary and secondary resources. Minerals Engineering 161, 106719. https://doi.org/10.1016/j.mineng.2020.106719

Sherry, A.D., Caravan, P., Lenkinski, R.E., 2009. A primer on gadolinium chemistry. J Magn Reson Imaging 30, 1240–1248. https://doi.org/10.1002/jmri.21966

Shiller, A.M., Boyle, E.A., 1987. Dissolved vanadium in rivers and estuaries. Earth and Planetary Science Letters 86, 214–224. https://doi.org/10.1016/0012-821X(87)90222-6

Shinto, A., Knapp, F.F. (Russ), 2017. Important Clinical Applications of ^{188}Rhenium for Radionuclide Therapy. Int. J. of Nuclear Medicine Research 16–38.

Simmons, D.B.D., Wallschläger, D., 2005. A critical review of the biogeochemistry and ecotoxicology of selenium in lotic and lentic environments. Environmental Toxicology and Chemistry 24, 1331–1343. https://doi.org/10.1897/04-176R.1

Smedley, P.L., Kinniburgh, D., 2017. Molybdenum in natural waters: A review of occurrence, distributions and controls. Applied Geochemistry. https://doi.org/10.1016/j.apgeochem.2017.05.008

Sohrin, Y., Isshiki, K., Kuwamoto, T., Nakayama, E., 1987. Tungsten in north Pacific waters.

Sohrin, Y., Isshiki, K., Nakayama, E., Kihara, S., Matsui, M., 1989. Simultaneous determination of tungsten and molybdenum in sea water by catalytic current polarography after preconcentration on a resin column. Analytica Chimica Acta 218, 25–35. https://doi.org/10.1016/S0003-2670(00)80279-2

Son, S., Hyun, S.P., Charlet, L., Kwon, K.D., 2022. Thermodynamic stability reversal of iron sulfides at the nanoscale: Insights into the iron sulfide formation in low-temperature aqueous solution. Geochimica et Cosmochimica Acta 338, 220–228. https://doi.org/10.1016/j.gca.2022.10.021

Souza, L.A., Pedreira, R.M.A., Miró, M., Hatje, V., 2021. Evidence of high bioaccessibility of gadolinium-contrast agents in natural waters after human oral uptake. Science of The Total Environment 793, 148506. https://doi.org/10.1016/j.scitotenv.2021.148506

Sposito, G., 1981. The thermodynamics of soil solutions, Oxford Science Publications. Clarendon Pr, Oxford.

Stauder, S., Raue, B., Sacher, F., 2005. Thioarsenates in Sulfidic Waters. Environ. Sci. Technol. 39, 5933–5939. https://doi.org/10.1021/es048034k

Stefánsson, A., Gunnarsson, I., Kaasalainen, H., Arnórsson, S., 2015. Chromium geochemistry and speciation in natural waters, Iceland. Applied Geochemistry, A Special Issue to Honor the Geochemical Contributions of D. Kirk Nordstrom 62, 200–206. https://doi.org/10.1016/j.apgeochem.2014.07.007

Stüeken, E.E., Kipp, M.A., 2020. Selenium Isotope Paleobiogeochemistry. Elements in Geochemical Tracers in Earth System Science. https://doi.org/10.1017/9781108782203

Stumm, W., Sulzberger, B., 1992. The cycling of iron in natural environments: considerations based on laboratory studies of heterogeneous redox processes. Geochimica et Cosmochimica Acta 56, 3233–3257.

Suess, E., Planer-Friedrich, B., 2012. Thioarsenate formation upon dissolution of orpiment and arsenopyrite. Chemosphere 89, 1390–1398. https://doi.org/10.1016/j.chemosphere.2012.05.109

Sun, F., Dempsey, B.A., Osseo-Asare, K.A., 2012. As(V) and As(III) reactions on pristine pyrite and on surface-oxidized pyrite. Journal of Colloid and Interface Science 388, 170–175. https://doi.org/10.1016/j.jcis.2012.08.019

Tagami, K., Uchida, S., 2008. Determination of bioavailable rhenium fraction in agricultural soils. Journal of environmental radioactivity 99, 973–80. https://doi.org/10.1016/j.jenvrad.2007.11.007

Tang, W., Sanville, E., Henkelman, G., 2009. A grid-based Bader analysis algorithm without lattice bias. Journal of Physics: Condensed Matter 21, 084204.

Thilo, E., Hertzog, K., Winkler, A., 1970. Über Vorgänge bei der Bildung des Arsen(V)-sulfids beim Ansäuern von Tetrathioarsenatlösungen. Zeitschrift anorg allge chemie 373, 111–121. https://doi.org/10.1002/zaac.19703730203

Tossell, J.A., 2005. Calculation of the UV-visible spectra and the stability of Mo and Re oxysulfides in aqueous solution. Geochimica et Cosmochimica Acta 69, 2497–2503. https://doi.org/10.1016/j.gca.2004.12.004

Tribovillard, N., Algeo, T.J., Lyons, T., Riboulleau, A., 2006. Trace metals as paleoredox and paleoproductivity proxies: An update. Chemical Geology 232, 12–32. https://doi.org/10.1016/j.chemgeo.2006.02.012

Tu, W., Denizot, B., 2007. Synthesis of small-sized rhenium sulfide colloidal nanoparticles. Journal of Colloid and Interface Science 310, 167–170. https://doi.org/10.1016/j.jcis.2007.01.054

USGS, 2023. Mineral commodity summaries 2023 (No. 2023), Mineral Commodity Summaries. U.S. Geological Survey. https://doi.org/10.3133/mcs2023

Vaughan, D.J., 2005. MINERALS | Sulphides, in: Selley, R.C., Cocks, L.R.M., Plimer, I.R. (Eds.), Encyclopedia of Geology. Elsevier, Oxford, pp. 574–586. https://doi.org/10.1016/B0-12-369396-9/00276-8

Vorlicek, T.P., Chappaz, A., Groskreutz, L.M., Young, N., Lyons, T.W., 2015. A new analytical approach to determining Mo and Re speciation in sulfidic waters. Chemical Geology 403, 52–57. https://doi.org/10.1016/j.chemgeo.2015.03.003

Vorlicek, T.P., Helz, G.R., 2002. Catalysis by mineral surfaces: implications for Mo geochemistry in anoxic environments. Geochimica et Cosmochimica Acta 66, 3679–3692.

Vorlicek, T.P., Helz, G.R., Chappaz, A., Vue, P., Vezina, A., Hunter, W., 2018. Molybdenum Burial Mechanism in Sulfidic Sediments: Iron-Sulfide Pathway. ACS Earth Space Chem. 2, 565–576. https://doi.org/10.1021/acsearthspacechem.8b00016

Voudouris, P.C., Melfos, V., Spry, P.G., Bindi, L., Kartal, T., Arikas, K., Moritz, R., Ortelli, M., 2009. Rhenium-rich molybdenite and rheniite in the Pagoni Rachi Mo–Cu–Te–Ag–Au prospect, northern Greece: implications for the Re geochemistry of porphyry-style Cu–Mo and Mo mineralization. The Canadian Mineralogist 47, 1013–1036.

Voulvoulis, N., 2018. Water reuse from a circular economy perspective and potential risks from an unregulated approach. Current Opinion in Environmental Science & Health 2, 32–45. https://doi.org/10.1016/j.coesh.2018.01.005

Vriens, B., Behra, R., Voegelin, A., Zupanic, A., Winkel, L.H.E., 2016. Selenium Uptake and Methylation by the Microalga *Chlamydomonas reinhardtii*. Environ. Sci. Technol. 50, 711–720. https://doi.org/10.1021/acs.est.5b04169

Wallschläger, D., Stadey, C.J., 2007. Determination of (oxy) thioarsenates in sulfidic waters. Analytical chemistry 79, 3873–3880.

Wallyn, J., Anton, N., Vandamme, T.F., 2019. Synthesis, Principles, and Properties of Magnetite Nanoparticles for In Vivo Imaging Applications—A Review. Pharmaceutics 11, 601. https://doi.org/10.3390/pharmaceutics11110601

Wang, N., Ye, Z., Huang, L., Zhang, C., Guo, Y., Zhang, W., 2023. Arsenic Occurrence and Cycling in the Aquatic Environment: A Comparison between Freshwater and Seawater. Water 15, 147. https://doi.org/10.3390/w15010147

Wang, T., Qian, T., Zhao, D., Liu, X., Ding, Q., 2020. Immobilization of perrhenate using synthetic pyrite particles: Effectiveness and remobilization potential. Science of The Total Environment 725, 138423. https://doi.org/10.1016/j.scitotenv.2020.138423

Weerasooriya, R., Tobschall, H.J., 2005. Pyrite–water interactions: Effects of pH and pFe on surface charge. Colloids and Surfaces A: Physicochemical and Engineering Aspects 264, 68–74. https://doi.org/10.1016/j.colsurfa.2005.05.012

Wei, D., Osseo-Asare, K., 1996. Particulate pyrite formation by the Fe3+ / H S - reaction in aqueous solutions: effects of solution composition. Colloids and Surfaces A: Physicochemical and Engineering Aspects 11.

Weiss, J., Möckel, H.J., Müller, A., Diemann, E., Walberg, H.-J., 1988. Retention of thio- and selenometalates in mobile-phase ion chromatography. Journal of Chromatography A 439, 93–108. https://doi.org/10.1016/S0021-9673(01)81678-2

Wells, R.C., Butler, B.S., 1917. Tungstenite, a new mineral. Journal of the Washington Academy of Sciences 7, 596–599.

Wen, H., Carignan, J., 2007. Reviews on atmospheric selenium: Emissions, speciation and fate. Atmospheric Environment 41, 7151–7165. https://doi.org/10.1016/j.atmosenv.2007.07.035

Wharton, M.J., Atkins, B., Charnock, J.M., Livens, F.R., Pattrick, R.A.D., Collison, D., 2000. An X-ray absorption spectroscopy study of the coprecipitation of Tc and Re with mackinawite (FeS). Applied Geochemistry 15, 347–354. https://doi.org/10.1016/S0883-2927(99)00045-1

WHO, 1996. Trace elements in human and health [WWW Document]. URL https://scholar.google.com/scholar_lookup?title=Trace%20elements%20in%20human%20nutrition%20and%20health&publication_year=1996 (accessed 10.12.21).

Wiley, J., Sons, I., 2002. Inorganic Syntheses, Volume 33 | Wiley.

Wolthers, M., Charlet, L., van Der Weijden, C.H., Van der Linde, P.R., Rickard, D., 2005. Arsenic mobility in the ambient sulfidic environment: Sorption of arsenic (V) and arsenic (III) onto disordered mackinawite. Geochimica et Cosmochimica Acta 69, 3483–3492.

Wu, D., Wang, H., Teng, T., Duan, S., Ji, A., Li, Y., 2018. Hydrogen sulfide and autophagy: A double edged sword. Pharmacological Research 131, 120–127. https://doi.org/10.1016/j.phrs.2018.03.002

Wu, G., Huang, L., Jiang, H., Peng, Y., Guo, W., Chen, Z., She, W., Guo, Q., Dong, H., 2017. Thioarsenate Formation Coupled with Anaerobic Arsenite Oxidation by a Sulfate-Reducing Bacterium Isolated from a Hot Spring. Frontiers in Microbiology 8.

Wu, W., Chen, B., Shen, H., Ding, Z., 2022. Molecular dynamics simulation of rhenium effects on creep behavior of Ni-based single crystal superalloys. Progress in Natural Science: Materials International 32, 259–266. https://doi.org/10.1016/j.pnsc.2022.01.010

Wulfsberg, G., 1987. Principles Of Descriptive Inorganic Chemistry. Brooks/Cole, Monterrey, California.

Xiong, Y., Wood, S.A., 2002. Experimental determination of the hydrothermal solubility of ReS2 and the Re–ReO2 buffer assemblage and transport of rhenium under supercritical conditions. Geochem Trans 3, 1. https://doi.org/10.1186/1467-4866-3-1

Xiong, Y., Wood, S.A., 1999. Experimental determination of the solubility of ReO2 and the dominant oxidation state of rhenium in hydrothermal solutions. Chemical Geology 158, 245–256. https://doi.org/10.1016/S0009-2541(99)00050-9

Yalçıntaş, E., Scheinost, A.C., Gaona, X., Altmaier, M., 2016. Systematic XAS study on the reduction and uptake of Tc by magnetite and mackinawite. Dalton Trans. 45, 17874–17885. https://doi.org/10.1039/C6DT02872A

Yang, Z., Kang, M., Ma, B., Xie, J., Chen, F., Charlet, L., Liu, C., 2014. Inhibition of U(VI) Reduction by Synthetic and Natural Pyrite. Environ. Sci. Technol. 48, 10716–10724. https://doi.org/10.1021/es502181x

Yu, M., Trinkle, D.R., 2011. Accurate and efficient algorithm for Bader charge integration. The Journal of chemical physics 134, 064111.

Zachara, J.M., Heald, S.M., Jeon, B.-H., Kukkadapu, R.K., Liu, C., McKinley, J.P., Dohnalkova, A.C., Moore, D.A., 2007. Reduction of pertechnetate [Tc(VII)] by aqueous Fe(II) and the nature of solid phase redox products. Geochimica et Cosmochimica Acta 71, 2137–2157. https://doi.org/10.1016/j.gca.2006.10.025

Zondervan, J.R., Hilton, R.G., Dellinger, M., Clubb, F.J., Roylands, T., Ogrič, M., 2023. Rock organic carbon oxidation CO2 release offsets silicate weathering sink. Nature 1–5. https://doi.org/10.1038/s41586-023-06581-9

Zuckier, L., Dohán, O., Li, Y., Chang, C., Carrasco, N., Dadachova, E., Dohan, O., 2004. Kinetics of perrhenate uptake and comparative biodistribution of perrhenate, pertechnetate, and iodide by NaI symporter-expressing tissues in vivo. Journal of nuclear medicine : official publication, Society of Nuclear Medicine 45, 500–7.

Appendices

Appendix 1 - Revisiting Selenium Interactions with Pyrite: FromAdsorption to Coprecipitation

ACS EARTH AND SPACE CHEMISTRY

http://pubs.acs.org/journal/aesccq Article

Revisiting Selenium Interactions with Pyrite: From Adsorption to Coprecipitation

Carolina Guida,[○] Vivien Ramothe,[○] Anthony Chappaz,* Pauline Simonnin, Kevin M. Rosso, Rong-Rong Ding, Damien Prieur, Andreas C. Scheinost, and Laurent Charlet*

Cite This: *ACS Earth Space Chem.* 2024, 8, 67−78 Read Online

ACCESS | Metrics & More | Article Recommendations | Supporting Information

ABSTRACT: Interactions of selenium (Se), a trace element bioessential at low concentrations but highly toxic at high concentrations, with the most abundant sulfide mineral in the earth's crust, namely, pyrite, were investigated over a wide range of time scales from nanoseconds to days. At the nanosecond scale, selenate $Se(VI)O_4^{2-}$ adsorption onto the neat pyrite surface is shown by *ab initio* computations to proceed via the formation of a chemical bond between an oxyanion oxygen atom and a surface Fe atom, weakening the other Se−O bonds and reducing the Se atom oxidation state. At the hour-to-day scale, the adsorption and coprecipitation of selenate $Se(VI)O_4^{2-}$ and selenite, $Se(IV)O_3^{2-}$, were investigated through wet chemical batch experiments at various pH values at different sulfide concentrations. Selenium removal from solution is slower and weaker for selenate than for selenite. After 24 h, only 10% of selenate, against 60% of selenite (up to 100% in the presence of sulfide), is removed by the pyrite surface. Independently of its original oxidation state, adsorbed Se is completely reduced to elemental trigonal selenium via adsorption, precipitation, or coprecipitation, as shown by XANES spectroscopy. Our EXAFS results, compared to published data on Se-rich pyrite, show a Se to S substitution within the pyrite structure. The reductive coprecipitation mechanism of selenium with pyrite represents valuable new insights for improving our understanding of modern and ancient biogeochemical cycles involving Se. In addition, several industries can benefit from direct applications of our findings, such as water treatment, green technologies, and sustainable mining.

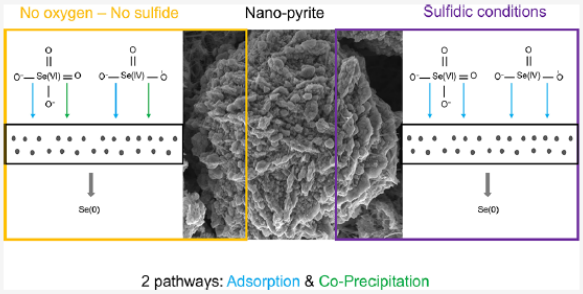

KEYWORDS: *selenium, pyrite, adsorption, coprecipitation, theoretical calculations, XANES*

■ INTRODUCTION

Positioned underneath sulfur (S) in the periodic table, selenium (Se), a redox-sensitive metalloid, shares features similar to those of this major element. Like S, it is enriched in geological settings buried under anoxic conditions (shales, coal[1]) and displays a wide range of oxidation states ranging from −II to +VI with Se(−II), Se(−I), Se(0), Se(IV), and Se(VI) being the most predominant under natural conditions.[1,2] In aquatic systems, Se(IV) and Se(VI) species are usually dissolved, while Se(0), Se(−I), and Se(−II) in the presence of iron minerals exhibit low solubilities.[3,4] The use of Se as a paleo-redox proxy has been considered because of its different oxidation states and the occurrence of several stable isotopes in the environment.[5] The annual average production of Se is ∼3355 tons.[9] The main application is in metallurgy for producing electrolytic manganese as an additive in the steel manufacturing industry. Selenium is an essential nutrient fulfilling biological functions that cannot be substituted by other elements. It is also used in the agricultural, food, and pharmaceutical industries as an additive, fertilizer, dietary supplement, and fungicide to control dermatitis.[9] Some plants can uptake and metabolize Se as the ion selenate via sulfate transporters.[6] For humans, the required Se intake is between 50 and 400 μg/day.[7] Se represents a bioessential trace element involved in the enzyme glutathione peroxidase that converts peroxide into water and catalyzes the scavenging of free radicals, preventing oxidative damage to biological tissues.[8,9] However, Se can induce severe toxic effects on aquatic life at an intake reaching 800 μg/day,[7] causing deformities, a lower reproduction rate, and higher mortality.[10]

The main natural sources releasing Se into aquatic systems are shale weathering processes and volcanoes.[1] The flux of Se from the ocean to the atmosphere represents, with volcanoes, the major source of atmospheric Se ($0.4–9 \times 10^3$ Se tons/year), with almost equal amounts released from the continents

Received: July 22, 2023
Revised: November 27, 2023
Accepted: November 27, 2023
Published: December 18, 2023

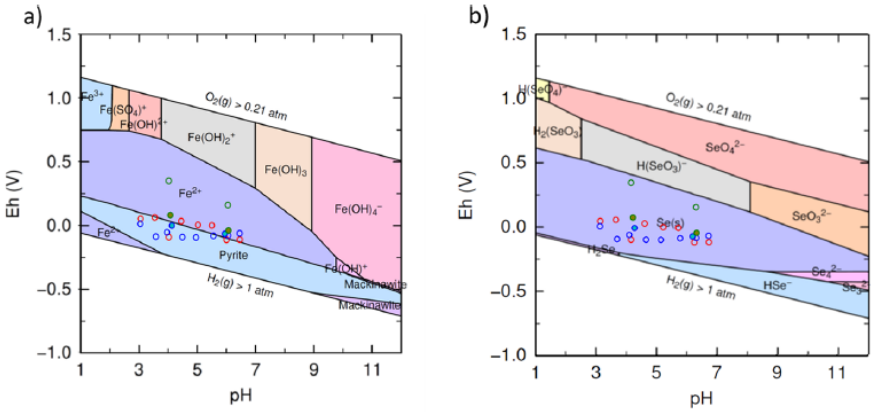

Figure 1. E_H–pH values collected in Se–pyrite experiments plotted in the (a) Fe–O–H and (b) Se–O–H E_H–pH diagrams. The E_H values for the experiments were plotted with empty red dots for pyrite titration data, empty blue dots for selenate experimental data, empty green dots for selenite experimental data, and blue and green filled dots for experimental sorption data of selenate and selenite in the presence of added sulfide. The predominance diagrams were generated with the public domain code PhreePlot,[20] using the version 10a of the thermodynamic database ThermoChimie (www.ThermoChimie-tdb.com). E_H–pH diagrams were constructed with 0.1 mM Se(VI), 1 mM Fe(II), 2 mM S(−II), and 10 mM NaCl.

(0.15–5.25 × 10^3 Se tons/year).[11] Several industries also contribute to the release of anthropogenic Se in natural waters: coal mining, glassmaking, irrigation, pigment production, petroleum refining, coal combustion, and disposal of radioactive waste.[12−14] The last one is, in fact, a major source of the radioisotope ^{79}Se, a subproduct generated in nuclear power plants.

In aquatic systems, speciation of Se controls its reactivity, transport, bioavailability, and potential toxicity. The predominant species in oxic waters are the oxyanions: selenate [Se(VI)O_4^{2-}], selenite [Se(IV)O_3^{2-}], and biselenite [HSe(IV)O_3^-].[15] Selenite is particularly bioavailable for most algae and cyanobacteria via phosphate transporters.[16] Once internalized, it is converted to organic and volatile selenides.[16,17] Two volatile Se species, dimethyl selenide (DMSe) and dimethyl diselenide (DMDSe), are the main forms present in the atmosphere.[11,15] Selenium(VI) and Se(IV) can be sequestrated by adsorption and reduction reactions down to Se(0, −I, and −II) by several minerals (clay, iron oxyhydroxides, iron sulfide) and natural organic matter.[18] Selenium speciation in aquatic systems is governed by changes in pH and redox potential (E_H) (Figure 1). The chemical composition of the system, the type and amount of organic matter, and the microbiological activity also control the distribution of Se species in the environment.[17] Thermodynamic calculations predict that selenate predominates in fully oxygenated water, while selenite and biselenite are predominant species of hypoxic water.[19] Under reducing conditions, a large region of the E_H–pH diagram is occupied by reduced Se(0) species abiotically or biotically produced.[17]

Pyrite is the most abundant sulfide mineral and can be found in igneous, metamorphic, and marine sedimentary rocks as well as in submarine hydrothermal vents.[21] The wide range of crystal chemical and surface properties displayed by pyrite—surface complexation, electron transfer, secondary mineral phases, short-range order, and structure sensitivity—makes this mineral an important redox catalyst for a multitude of reactions involving trace elements,[22] such as uranium,[23] molybdenum,[24] arsenic,[25] Se,[26] and Tc.[27] A major environmental issue associated with the oxidation of pyrite is coal acid mine drainage. That process can release toxic trace elements in aquatic systems.[25] In natural pyrite, different reduced Se species are present within or at the surface, like ferroselite ($FeSe_2$) and dzharkenite (FeSe).[28] Experimental studies demonstrated that Se(IV) can be reduced to Se(0) in contact with a pyrite surface under anoxic and acidic conditions.[29,30] Probably, the electrons required for the reduction of Se(IV) are provided by the oxidation of Fe(II) and S(−II) phases.[29,31,32] Few studies have investigated the reduction of Se(VI) by pyrite. Selenate adsorbs weakly on pyrite, making it challenging to characterize Se(VI)–pyrite interactions. The reduction of Se(VI) to Se(0) involves the transfer of six electrons and the breakdown of four oxygen bonds; consequently, the reductive sorption process is very slow, and pyrite might have a low reactivity with selenate ions.[29,33] A complete and detailed understanding of the mechanisms involved in reducing Se(VI) and Se(IV) upon reaction with pyrite is still lacking.

To fill this knowledge gap, our goal was to thoroughly explore Se(VI) and Se(IV) interactions with pyrite to meticulously characterize all of the potential mechanisms involved, such as reductive adsorption and coprecipitation, over different times scales. Furthermore, the role of dissolved sulfide during the Se reduction and adsorption processes when reacted with pyrite was investigated.

■ MATERIALS AND METHODS

Chemicals. Sodium selenite, 99% (ref. 214485); sodium selenate, BioXtra (ref. S8295); zinc acetate dihydrate, ≥98% (ref. 383058); carbon disulfide, anhydrous, 99+% (ref. 180173); sodium sulfide nonahydrate, ≥98% (ref. 208043); sodium hydrosulfide hydrate (ref. 161527); iron(III) chloride hexahydrate, ≥99% (ref. 31232); and sodium chloride, ≥99.5% (ref. 71379), were obtained from Sigma-Aldrich. Sodium hydroxide, ≥98% (ref. 6771.3), was purchased from Roth, and hydrochloric acid, 32% Extra Pure, SLR (ref. 10458790), and nitric acid, 67 to 70% trace metal grade (ref. A509P500), were from Fisher Chemical.

All solutions were prepared with boiled, nitrogen-degassed Millipore 18.2 MΩ/cm water and stored in an oxygen-free glovebox. All recipients were soaked in 5% HNO_3 for 24 h, cleaned for 10 min in an ultrasonic bath, and rinsed three times

https://doi.org/10.1021/acsearthspacechem.3c00219
ACS Earth Space Chem. 2024, 8, 67−78

with deionized water previously used. All experiments were done at room temperature in a Jacomex glovebox filled with Ar, with a controlled oxygen partial pressure below 5 ppm.

Pyrite and Se-Doped Pyrite Synthesis. Fresh pyrite was synthesized following the method proposed in previous literature.[34] Sixty milliliters of 0.05 M Fe(III) solution was added drop by drop into 60 mL of 0.15 M HS^- solution. Then, 1 M NaOH solution drops were added to maintain a pH value of ~4. The final solution was agitated for 5 days. The FeS_2 precipitate was decanted and washed by replacing the supernatant with a 0.2 M HCl solution six times, followed by acetone and carbon disulfide, to remove residual sulfur entirely from the solid surface. All of the washing solutions were in contact with pyrite for a 1 h minimum. Finally, the suspension was washed, vacuum filtered with a 0.22 μm filter with degassed water six times, dried in an anaerobic chamber, and kept in degassed ultrapure water at a 100 g/L solid concentration.

Se-doped pyrite synthesis was performed according to the method proposed by Diener and Neumann.[35] A precise amount of Se(VI) and Se(IV) stock solutions was added to the HS^- solution before being mixed with Fe(III) solution. Then, following the same steps, Se coprecipitated with pyrite was synthesized similarly to the protocol described above. The final concentrations used in synthesizing Se−pyrite samples were 50, 75, 100, 130, and 150 μM for Se(IV) and 50, 75, and 100 μM for Se(VI). The supernatant was acidified with 100 μL of 65% HNO_3 prior to elemental analysis.

Pyrite Titration and Se Sorption on Pyrite Experiments. Several batch experiments were conducted at different pH values (3−7.5), including a blank, which was prepared in glass bottles within an Ar anoxic atmosphere. The initial concentration of pyrite was fixed at 2 g/L, and the ionic strength was adjusted to 10 mM with NaCl. pH was adjusted to selected values by adding either HCl or NaOH and was measured by a pH meter with pH/°C probe with a 1 m cable (VWR pH110) calibrated with VWR buffers. After 24 h of equilibrium, the solution was decanted. Then, 2 × 10 mL was taken from all solutions and filtered with a 0.45 μm pore size membrane filter. The first volume was stored in a tube with 100 μL of a 100 mM zinc acetate dihydrate (ACZn) stock solution for Fe(II) and ΣS(−II). The second volume was acidified with 100 μL of 65% HNO_3 for inductively coupled plasma−atomic emission spectroscopy (ICP−AES) measurements. Similar experiments were carried out for Se(VI) sorption experiments, adding a concentration of 100 μM selenate and including a blank with the initial concentration of selenate.

Nine experiments were carried out following the same experimental protocol: six with Se(IV) and three with Se(VI). A sulfide solution of 1 mM was added from a stock solution of sulfide that was prepared by dissolving transparent crystals of $Na_2S{\cdot}9H_2O$ in degassed water. At the end of all batch experiments, pH and ORP values are measured (Figure 1). For all experiments, solid samples were collected after filtration, dried overnight, and preserved under an anoxic atmosphere.

Elemental Analysis. *ICP−AES.* Total Se and Fe concentrations in the supernatant samples were determined by ICP−AES (Varian 720 ES) at wavelengths of 234.350 and 238.204 nm for Fe and 196.026 nm for Se. 1000 ppm Fe and Se Roth standards were used to prepare an external calibration with a range of 0.01−25 ppm for Fe and Se concentrations, respectively. Analytical precision (RSD) and recovery (CMS) were determined from replicate analyses (n = 5 and n = 2, respectively). The RSDs calculated for the 5 ppm standard were 1% for Fe and 1% for Se. The CMSs were 97% for Fe and 99% for Se. The detection limits (DLs) for Fe and Se were 0.1 and 0.7 μM, respectively. The quantification limits (QLs) for Fe and Se were 0.4 and 2.2 μM, respectively.

Colorimetric Methods. The ACZn solution samples were analyzed by colorimetric methods to measure the concentration of Fe(II) with the *o*-phenanthroline method[36] and ΣS(−II) with the sodium thiosulfate titration and methylene blue method.[37] Samples were analyzed at 513 and 670 nm for Fe(II) and ΣS(−II), respectively, with an Agilent Cary 300 UV−vis spectrophotometer. The DLs for Fe(II) and ΣS(−II) were 15.2 and 0.47 μM, respectively. The QLs for Fe(II) and ΣS(−II) were 46.1 and 1.47 μM, respectively.

Solid Characterization. *XRD.* X-ray powder diffraction (XRD) patterns were collected in the 20 to 70° 2θ range at room temperature using a laboratory Bruker D8 diffractometer with Cu radiation (λ = 1.54 Å), a SolX Si(Li) solid-state detector, and a step size of 0.026°. Into an airtight poly(methyl methacrylate) (PMMA) sample holder with a transparent dome to avoid any possible oxidation, samples were placed inside the glovebox. For all samples, the lattice parameters and the average crystallite sizes were calculated using the Debye−Scherrer equation and the Profex software,[38] with a free lattice parameter.

SEM. SEM images were collected with a scanning electron microscope with 16 kV at ISTerre, Grenoble, France. The sample was prepared by gently spreading a tiny quantity of pyrite on the surface of an electrically conductive carbon double-sided tape placed on the mount. The image detection mode used was backscattered electrons (BSEs) and secondary electrons (SEs).

BET. The specific surface area (SSA) was determined by the Brunauer−Emmett−Teller adsorption method (BET-N_2) at 77 K, using a Belsorp-Max (Bel Japan) volumetric gas sorption instrument. Inside the glovebox, 50 mg of pyrite was put in a glass cell and then dried under a vacuum at 80 °C for 12 h. The SSA was calculated from the BET equation in the $P/P0$ range of 0.05−0.31.

XANES, EXAFS, and HERFD. X-ray absorption near-edge structures (XANES) and extended X-ray absorption fine structures (EXAFS) were collected at the Rossendorf Beamline operated by Helmholtz-Zentrum Dresden Rossendorf (HZDR, Germany).[39] High-energy-resolution fluorescence-detected (HERFD) X-ray absorption spectroscopy was performed at the French Absorption Spectroscopy Beamline in Material and Environmental Sciences at Ultra-High Dilution (FAME-UHD). For XANES and EXAFS samples, 100 mg of solid was homogenized with an agate mortar and then used to fill Kapton-sealed holders. For HERFD measurements, homogenized 40 mg of the solid samples and at least 10 mg of boron nitride were used to prepare 5 mm diameter pellets. All data collection was performed in a closed-cycle He cryostat with an atmosphere at 15 K to avoid photon-induced oxidation and to limit thermal disorder. XANES and EXAFS data were collected in fluorescence mode with an 18-element solid-state germanium detector (Ultra-LEGe, GUL0055, Mirion Technologies), and the Se references were in transmission mode recorded with an ionization chamber filled with a suitable gas mixture. HERFD, with a resolution of about 1−2 eV, used a beam with a size of 100 × 200 μm^2 and a 14-Si crystal analyzer spectrometer detection system. XANES and EXAFS spectra

https://doi.org/10.1021/acsearthspacechem.3c00219
ACS Earth Space Chem. 2024, 8, 67−78

were calibrated with the simultaneous measurement of Au foil at the L3 edge energy at 11,902.9 eV. For HERFD data calibration, a Se foil was used before and after each sample scan at a 12,658.1 eV energy reference. The data collected was processed with the open-source software ATHENA program.[40] Linear combination fit (LCF) was performed using the Se spectra of standards collected during the beamtime and previous beamtimes conducted in the same line. Data from the EXAFS region were analyzed using the Artemis software package. Theoretical models based on the structures of trigonal (gray) Se, ferroselite ($FeSe_2$), and S atom-centered pyrite were generated using the FEFF6 and ATOMS software packages to test for the existence of Se within or at the surface of pyrite.

■ THEORETICAL CALCULATIONS

All calculations were carried out with periodic boundary conditions (PBCs) in the plane-wave Vienna Ab initio Software Package (VASP)[41,42] electronic structure code. The simulations were performed within the generalized gradient approximation (GGA) with the exchange-correlation functional of Perdew, Burke, and Ernzerhof (PBE).[43] The plane-wave calculations were carried out under the projector-augmented wave method with a kinetic energy cutoff of 400 eV.[44] The total energy convergence criteria were set to be within 1×10^{-5} eV with a Gaussian smearing width of 0.05 eV to improve the convergence of orbital energies. The vacuum region between the two (100) pyrite surfaces was set to 30 Å (unless stated otherwise) to remove spurious interactions between the adsorbate and the periodic image of the bottom layer of the surface (Figure 2).

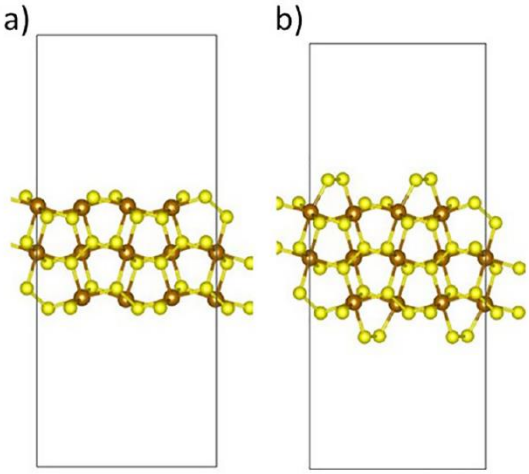

Figure 2. Side views of two different (100) pyrite surfaces: the neat surfaces (a) without disulfide terminations and (b) with disulfide terminations.

The adsorption energy of the adsorbate species, ΔE, was calculated using the following expression:

$$\Delta E = E\_(\text{pyrite slab}) + E\_\text{adsorbate} - E\_\text{total} \quad (1)$$

where $E_$total represents the total energy of the pyrite slab with the molecule adsorbed on the surface, $E\_$(pyrite slab) the total energy of the slab, and $E_$adsorbate the total energy of adsorbate in the gas phase (SeO_4^{2-}, SeO_3^{2-}, ...). Based on this definition, the larger the ΔE is, the more thermodynamically favorable the adsorption.

To investigate changes in the electronic structure when the molecule is adsorbed on the surface, the deformation charge density, $\Delta\rho(r)$, was calculated, which includes a direct comparison to the nonsorbed state:

$$\Delta\rho(r) = \rho\_\text{total}(r) - (\rho\_(\text{pyrite slab})(r) + \rho\_\text{adsorbate}(r)) \quad (2)$$

where $\rho_$total(r), $\rho\_$(pyrite slab)(r), and $\rho_$adsorbate(r) are electron densities of the total system, the silver slab, and the adsorbate in the gas phase, respectively.

The charge transfer was studied by comparing the Bader charges[45−48] between the slab surface and the gas-phase molecule with the adsorbed state. The strength of bonds between the adsorbates and the surface was evaluated by calculating the charge density at (3,−1) bond critical points $[\nabla\rho(r)]_$cp, corresponding to the zero values of the gradient: $\nabla\rho(r) = 0$. These saddle points correspond to a minimum charge density along a bond path, providing a measure of the bonding strength, in terms of the electronic overlap.

■ RESULTS

***Ab Initio* Calculations.** According to our calculations, the neat surface has the lowest adsorption energy (3.46 eV vs 1.44 eV) and therefore is a steadier adsorption surface. A bond appears to form between selenate and an iron atom of the pyrite surface in the adsorption process (Figure 3a). Thus, the remaining calculations were made on the selenate electronic properties adsorbed on the (100) neat surface.

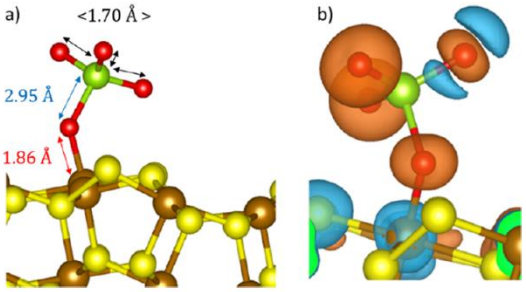

Figure 3. (a) Most stable adsorption configuration of selenate on the pyrite surface with the corresponding bond length. (b) Close-up of the charge deformation of the electron in the energy range between −2.5 and −0.5 eV at an isosurface value of 3.7×10^{-2} $e^{-}\cdot Å^{-3}$.

Once adsorbed, the selenate ion undergoes a deformation induced by the 74% elongation of the Se−O bond involving the oxygen atom interacting with the pyrite surface, while the remaining part of the oxygen atoms does not experience a significant change in bond length (0.6% elongation). Interestingly, the Fe−O bond occurring at 1.86 Å is comparable to the original Se−O bond length found in selenate in the gas phase (Table S1), reflecting the strength of the Fe−O interaction. Neither the noninteracting O nor the Se shows a significant loss of Bader charges (<4%). Thus, the absence of significant differences in these Se−O bond lengths is not surprising.

Geometrically, the selenate molecule is slightly inclined regarding the pyrite surface with an angle of 130.31°, while the remaining oxygen atoms form an O−Se−O angle (113.88°), which is very similar to that of the SeO_3^{2-} molecule (113.78°). Moreover, the interacting O atom experiences a loss of charge

https://doi.org/10.1021/acsearthspacechem.3c00219
ACS Earth Space Chem. 2024, 8, 67−78

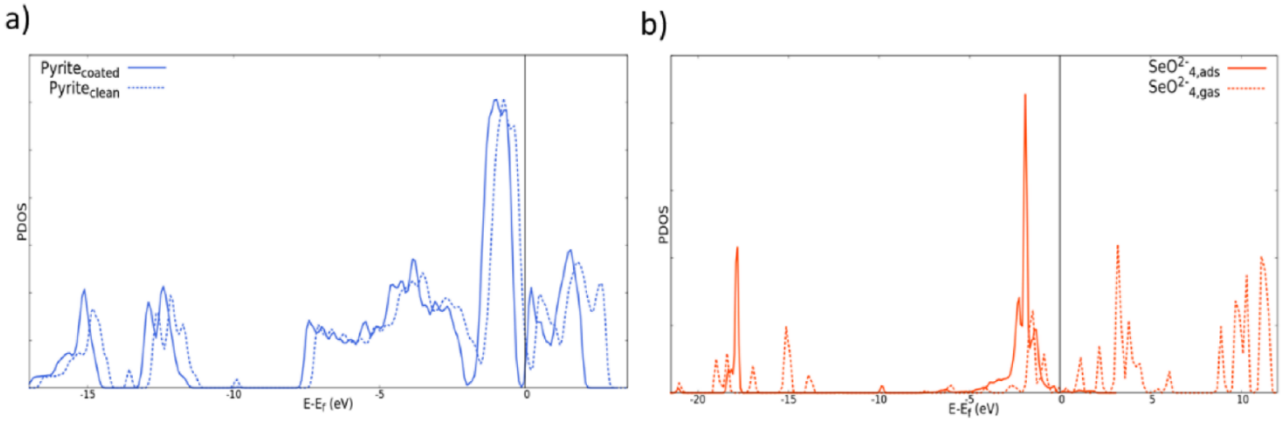

Figure 4. Projected density of states (PDOS) before (solid line) and after (dashed line) selenate adsorption for all orbitals of (a) the pyrite surface and (b) the selenate ion.

of 0.55 e^-, 1 order of magnitude higher than those of the other O atoms, allowing the formation of a covalent Fe−O bond (Figure 3b). In Figure 3a, the blue area corresponds to a decrease in charge density, and the orange area is an increase in charge density at an isosurface value of 3.7×10^{-2} $e^-\cdot Å^{-3}$, only observed in the oxygen atom furthest away from the pyrite surface. Interestingly, this O atom does not display a significant change in the Bader charge.

The projected density of states (PDOS) of both the pyrite surface and selenate ion shows that the adsorption phenomena shift the whole spectrum to lower energies (Figure 4). The pyrite's PDOS peaks at −14.80, 12.15, −3.53, −0,75, 0.54, and 1.82 are shifted on average by −0.27 eV to the corresponding peaks at −15.11, −12.40, −3.77, −0.98, 0.20, and 1.55 eV, respectively. Few gas-phase peaks disappear at −13.58, −9.88, and 2.60 eV when selenate is adsorbed. The pyrite PDOS is mostly shifted in lower energies, whereas the selenate s orbital PDOS is completely changed. The selenate s orbital does not exhibit any density in unpopulated states and displays a density increase in the lowest energy states with three sharp peaks at −21.12, −17.82, and −9.87 eV and a broader one at −5.22 eV. The p and d orbitals are the most revealing because they show a shift in the lower energies with minimal density unoccupied states. The shift amplitude is accompanied by a modification of the peak shape, which prevents an average estimation of the shift magnitude. However, both p and d orbitals experience in the energy range [−2.5 to −0.5] eV, indicating for pyrite and selenate an increased state density following the adsorption.

Electrons for this energy range are the most susceptible to participating in chemical bonding; therefore, the spatial distribution of the electrons in this narrower energy range was examined. While the selenate ion forms a chemical bond with the pyrite surface, the bond between the O atom farthest from the surface and the rest of the molecule weakens as it loses electron density. This is consistent with the noticeable elongation of the Se−O of this involved O atom (1.71 Å) compared to the two others not participating in the chemical bonding with pyrite (1.69 Å) (Figure 3b).

Finally, the nudge elastic band method was used to calculate the energy cost of dissociating an O atom from the selenate ion interacting with pyrite (Figure 4), creating a series of snapshots along the dissociation path. The calculated energy barrier of this process was 4.56 eV in the dissociation direction. However, the final image of the dissociation has a higher energy than the first image (difference of 1.55 eV).

Experimental Se Sorption on Pyrite. *Pyrite Purity and Solubility.* The XRD spectra (Figure 5, blue line) show mainly

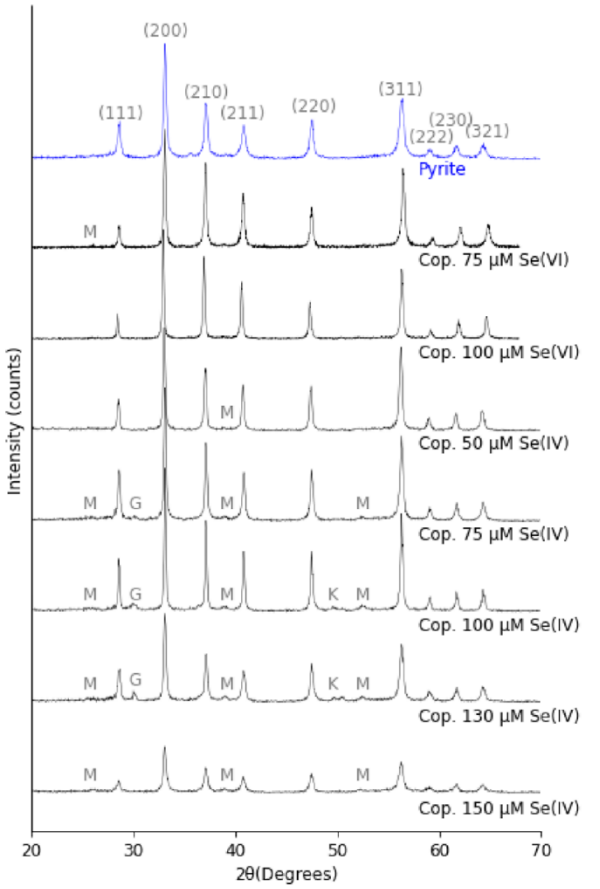

Figure 5. Raw data of XRD patterns measured from fresh pyrite and Se-doped pyrite syntheses (black line). The XRD peaks mainly show pyrite (blue line) and a minor fraction of marcasite (M), greigite (G), and mackinawite (K). The references used correspond to 00-016-0713 (I) for greigite, 00-042-1340 (*) for pyrite, PDF 86-0389 for mackinawite, and 00-037-0475 (*) for marcasite.

https://doi.org/10.1021/acsearthspacechem.3c00219
ACS Earth Space Chem. 2024, 8, 67−78

typical reflexes of the pure pyrite solid phase. Other peaks, displaying a lower magnitude, demonstrate the presence of other minerals (up to ~20%), like marcasite, greigite, or mackinawite. The parameters obtained after the Rietveld refinements show a face-centered cubic unit cell parameter a = 5.4245 ± 1 Å (1) in good agreement with pyrite reference standards (00-037-0475 (*)). Crystallite sizes estimated from the Scherrer equation give values between 34.8 ± 2.0 nm. The sharp diffraction peaks of the sample suggest good crystallinity. The SEM image (Figure S1) shows a large distribution of particles ranging from 500 nm to 2−3 μm. Finally, the SSA measured in the pyrite sample was 15 m^2/g.

SEM pictures show no changes in shape or size for pyrite equilibrated for 24 h at pH = 3, 5, or 7 (Figure S1). Fe(II) and ∑S(−II) concentrations for solutions equilibrated with pyrite at these different pH values are shown in Tables S2 and S3 and Figure 6. The measured Fe(II) concentrations ranged from 12

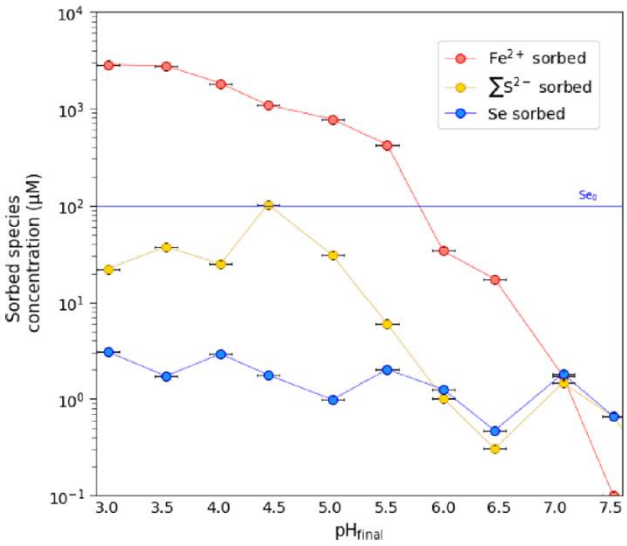

Figure 6. Sorbed measurement of Fe^{2+} (red dots), reduced sulfide species (yellow dots), and total selenium (blue dots), after 24 h equilibrium time with fresh pyrite at different pH between 3 and 7.5 in the presence of Se(VI), within sorption experiments. The error bar represents 0.1 pH measurement precision and 5% of the standard error for ICP−AES and UV−vis measurements.

to 2985 μM, close to the total Fe concentration value measured with ICP−AES (Table S2). The Fe(II) concentrations are higher at acidic pH. The ∑S(−II) values were below the DL for pH = 6.5 and 7.5 and equal to 105 μM at pH = 4.5. Sulfide levels were higher for acidic pH and tend to decrease below pH = 5. Measured E_H values ranged from −0.10 to 0.01 mV.

Se(VI) Adsorption on Pyrite. In Se adsorption experiments, Fe(II) concentrations (Tables S2 and S3) were similar to total Fe concentrations for different pH values. The disparity between Fe(II) and total Fe measurements corresponds to a 5% standard error in both UV−vis and ICP−AES measurements. In the Se-free experiments, the Fe(II) concentrations were 20 times higher at high pH and up to 50 times higher at low pH (Table S2). As expected, the concentrations of Fe(II) are higher for lower pH values (3−6) than for neutral pH values (6.5−7.5). Sulfide concentrations ranged from ~0.5 to ~15 μM and were higher at acidic pH. They displayed lower concentrations for experiments where Se was present, indicating sorbed concentration in the pyrite solid (Figure 6). The concentrations of adsorbed Se(VI) on pyrite varied between 1 (pH = 5) and 6.4 μM (pH = 3). Despite the low adsorption of Se(VI) within 24 h (<2%), a slightly improved adsorption capacity is observed for acidic conditions (2−6% Se sorbed, pH < 4.5). Finally, the measured E_H values were between −0.09 and 0.01 V (Figure 1).

No significant difference was observed for XANES-determined Se speciation for the samples equilibrated at pH 4 and 6. The white lines (E_{max}) for the XANES spectra for both samples are located between the E_{max} values for the Se(IV) and Se(0) standards (Figure S2a, Table S5). The LCF results show that these two samples are composed of trigonal, gray Se(0) (~80%) and Se(IV) (~20%) (Table S4). Similar results were found using HERFD−XANES for Se(VI) adsorbed on pyrite at pH 4 (see Figure S2b and Table S5).

Sulfide Influence on Se Adsorption. In the presence of sulfide, Se(VI) adsorption on pyrite remains unchanged, and no enhancement is found. E_H values were 0.00 and −0.07 V for pH = 4 and 6, respectively. The XANES and HERFD−XANES findings additionally indicate that the samples primarily consist of trigonal gray Se(0) with a minor presence of Se(IV) (Figure S2). In contrast with Se(VI), large Se(IV) adsorption on pyrite is observed (~40% improvement at pH = 6 and ~60% improvement at pH = 4). The removal of Se(IV) when interacting with pyrite from both solutions (pH 4 and 6) was beyond 95% (Figure S3). The speciation of Se was a mix of Se(IV) and Se(0) (Table S3 and Figure S2). The measured E_H values for the experiments without sulfide and experiments with sulfide ranged from 0.35 to 0.16 V and from 0.08 to −0.04 V, respectively.

Selenium Coprecipitation with Pyrite. Similarly, to pure pyrite, the XRD diffractions show mainly peaks (~80%) associated with pure pyrite yet with some impurities of marcasite, greigite, and mackinawite mineral phases (Figure 5). No significant difference between the mesh parameters or the particle size was found concerning the pyrite sample reference. Sharper peaks were observed for samples coprecipitated with 50, 75, and 100 μM Se(IV) and with 75 and 100 μM Se(VI). The samples with 130 and 150 μM Se(IV) and 50 μM Se(VI) showed less pronounced peaks, indicating a lower crystallinity than that of pure pyrite.

All of these samples display similar XANES features, suggesting that the Se speciation results from a mix of Se(IV) and Se(0) (Table S3). HERFD−XANES spectra revealed distinct spectral features not observed in normal XANES spectroscopy. Notably, three additional features are evident in the coprecipitation samples: a form similar to the reference $FeSe_2$, a white line and shape of the 100 μM Se(IV) coprecipitated sample resembling the reduced Se peak of the Se(IV) adsorption sample equilibrated at pH 6 with sulfur addition, and analogous shape and energy characteristics between samples of Se(IV) adsorption equilibrated at pH 6 without sulfur addition and the 76 μM Se coprecipitated sample (Figures S2 and S4 and Table S5).

For 50, 75, and 100 μM Se(IV) samples (about 1325, 1974, and 4037 ppm) measured with EXAFS (Figure 7), the crystal structures used for the fit are chosen considering (1) the sample matrix and (2) the possible choices of Se species that can be formed. The references used consisted of the pyrite structure[49] involving a substitution of the central S atom by a Se atom,[26,50] trigonal selenium (Se(0)), and ferroselite (Se(−I)). The most appropriate fit of the spectra used the

https://doi.org/10.1021/acsearthspacechem.3c00219
ACS Earth Space Chem. 2024, 8, 67−78

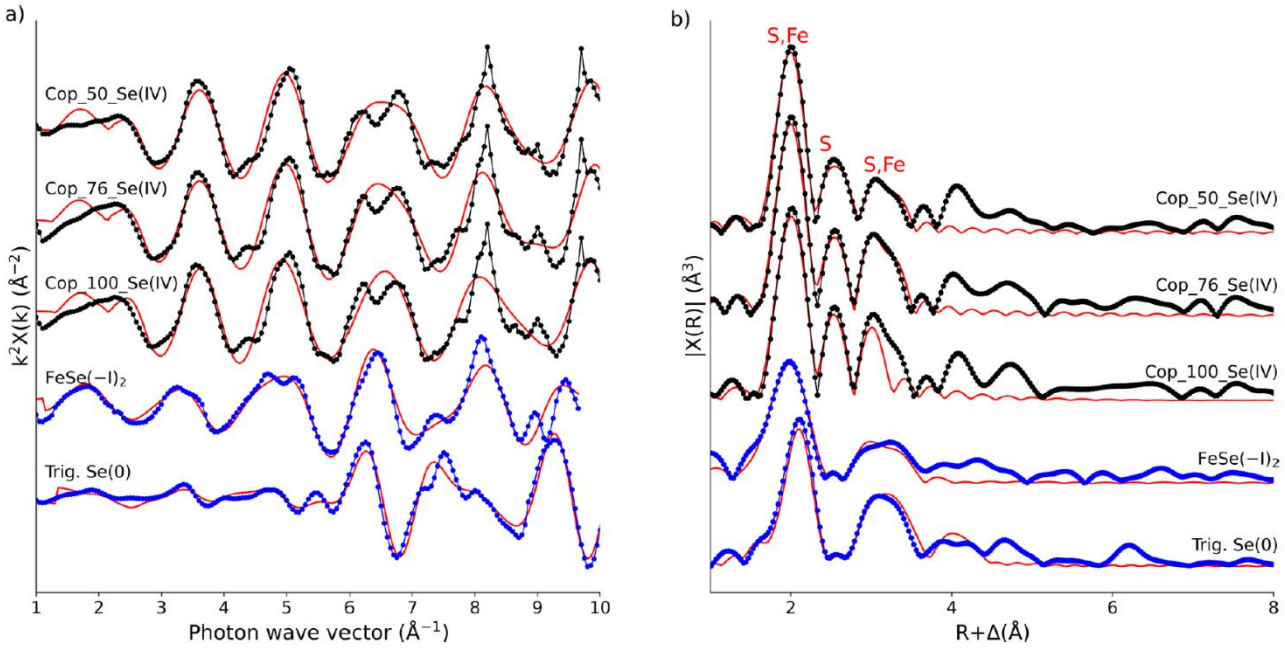

Figure 7. (a) k^2-weighted chi functions of EXAFS spectra and (b) the Fourier transform magnitudes of Se K-EXAFS spectra measured at the Se K edge of Se(IV)-doped pyrite. The fit is represented by red lines.

Table 1. EXAFS Parameters and Interatomic Distances Calculated for Se(IV)−Pyrite Coprecipitation Samples

sample	path	N^a	R^b (Å)	σ^{2c} (Å²)	$\Delta E_0{}^d$ (eV)	$S_0{}^{2e}$	R factor
Cop_50 μM r range: 1.45−3.5	Se−S.1	1.0	2.26 (0.04)	0.003[a]	6.58 (1.22)	0.898 (0.070)	0.014
	Se−Fe.1	3.0	2.31 (0.01)	0.003[a]	6.58 (1.22)	0.898 (0.070)	
	Se−S.2	6.0	3.12 (0.02)	0.006 (0.002)	6.58 (1.22)	0.898 (0.070)	
	Se−S.3	6.0	3.36 (0.03)	0.006 (0.004)	6.58 (1.22)	0.898 (0.070)	
	Se−Fe.2	3.0	3.50 (0.03)	0.005 (0.003)	6.58 (1.22)	0.898 (0.070)	
Cop_76 μM r range: 1.3−3	Se−S.1	1.0	2.25 (0.03)	0.003[a]	6.09 (0.77)	0.954 (0.064)	0.017
	Se−Fe.1	3.0	2.31 (0.01)	0.003[a]	6.09 (0.77)	0.954 (0.064)	
	Se−S.2	6.0	3.10 (0.01)	0.005 (0.001)	6.09 (0.77)	0.954 (0.064)	
	Se−S.3	6.0	3.35 (0.01)	0.003[a]	6.09 (0.77)	0.954 (0.064)	
	Se−Fe.2	3.0	3.48 (0.01)	0.003[a]	6.09 (0.77)	0.954 (0.064)	
Cop_100 μM r range: 1.1−3.3	Se−S.1	1.0	2.26 (0.04)	0.003[a]	6.51 (1.45)	0.900 (0.090)	0.024
	Se−Fe.1	3.0	2.32 (0.01)	0.003[a]	6.51 (1.45)	0.900 (0.090)	
	Se−S.2	6.0	3.10 (0.02)	0.004 (0.003)	6.51 (1.45)	0.900 (0.090)	
	Se−S.3	6.0	3.33 (0.06)	0.003[a]	6.51 (1.45)	0.900 (0.090)	
	Se−Fe.2	3.0	3.41 (0.66)	0.023 (0.042)	6.51 (1.45)	0.900 (0.090)	

[a]Coordination number for single paths, fixed value. [b]Interatomic distance. [c]Debye−Waller factor. [d]Shift of energy threshold. [e]Passive electron reduction factor.

five first single scattering paths of pyrite: Se−S.1 = 2.28 Å, Se−Fe.1 = 2.31−2.32 Å, Se−S.2 = 3.10−3.11 Å, Se−S.3 = 3.34, and Se−Fe.2 = 3.47−3.49 Å (Table 1). The atomic distances between the paths are similar to the values found by Manceau et al. (2020) in a natural pyrite with 500 ppm of Se, and a little shorter than the values of Matamoros-Veloza et al. (2014), also in a natural euhedral pyrite with 670 ppm of Se.

■ DISCUSSION

Se(VI)−Pyrite Interactions. *Initial Adsorption from Ab Initio Calculations.* Two reactive cleavage surfaces can be studied in *ab initio* calculations. The cleavages consist of one surface with disulfide atoms and one corresponding to a neat surface without disulfide. These two possible surfaces in the [100] plane cannot be compared due to the difference in the electron number between the two systems. The surface with disulfide terminations is discarded for several reasons, such as the low energy found when the Fe−S sulfurs start to join and disulfide bonds are formed, which explains why there is no experimental evidence of a pyrite surface with a nonnegligible amount of single Fe−S terminations. Furthermore, when the surface is more suitable for adsorption, the disulfide surface presents the highest adsorption energy, which makes it less stable (3.46 vs 1.44 eV). The last argument discussed further down is related to the adsorption of selenate, where a bond with a Fe atom is most likely to be involved (Figure 3a).

Regarding the interaction of Se(VI) with pyrite, it is theoretically feasible in terms of energy that the neat pyrite surface adsorbs the selenate molecule with an energy of 3.46 eV, promoting the creation of a bond between a Fe atom from

https://doi.org/10.1021/acsearthspacechem.3c00219
ACS Earth Space Chem. 2024, 8, 67−78

the pyrite surface and an O atom from selenate. Selenate deforms due to the elongation caused by the strong interaction that Fe has with O, which corresponds to a covalent bond, with an energy loss of 0.55 e^- observed in the respective oxygen. The new selenate geometry corresponds to the angles detected in the reduced selenite molecule, which may indicate that once adsorption is done within the first nanoseconds, reduction to selenite and oxidation of the pyrite surface are likely to follow.

PDOS analysis shows that the atomic distance of the O atom further away from the pyrite increases in charge density, but because there is no significant change in the Bader charge, it must be compensated for either by the deeper orbitals or by weakening its Se−O bond. The Se−O bond of this distant atom appears to weaken and, consequently, to elongate to a distance of 1.71 Å, compared to 1.69 Å for the other two O atoms that do not interact with pyrite. However, it should be noted that a single O atom in the gas phase is highly unstable. Provided that the furthest O atom from the pyrite surface is removed from the water molecule, a strong reaction with the surrounding solvent will occur. In addition, PDOS results indicate significant changes, especially in the p and d orbitals of both pyrite and selenate: lower energies with very few unoccupied density states and an increase of the density of states in the energy range between −2.5 and −0.5 eV, the energy range most likely to participate in a chemical bond. Further analysis of the projected state density between a hydrated selenate molecule and a neat pyrite surface is strongly recommended for a better understanding.

Factors Controlling Se(VI) Reductive Adsorption Processes over 24 h. As indicated above, the first reaction between selenate and pyrite occurs within nanoseconds. However, the minimum equilibrium time that can be experimentally considered is 24 h, in line with the analytical methods used. After this 24 h period, the final solid had a selenium concentration just above the DL.

The interaction of Se(VI) with pyrite is significantly influenced by the synthesized pyrite product. Pyrite formation at low temperatures consists of the dilution−precipitation pathway of intermediate phases such as nanomackinawite and nanogreigite.[51] This occurs via a reductive coprecipitation pathway where Fe(III) is reduced to Fe(II) by S(−II), which is first oxidized to S(0) polysulfides and then to S(−I). The high solubility of pyrite measured at acidic pH during the pyrite titration experiments suggests that the precipitate corresponds to a "fresh pyrite" or a "poorly" crystallized pyrite and it may contain metastable nanominerals from precursor phases. Similarly, previous research reported elevated Fe concentrations after dissolving synthesized pyrite (pH < 5).[52] These findings align with a prior study,[53] demonstrating that the stability of iron sulfides and their dissolution in ferruginous waters vary as a function of crystal size, pH, E_H, and aging time.[53] These nanosized mineral phases can also explain the higher SSA found (15 m^2/g^{-1}) than those previously documented in natural pyrites m^2/g^{-1}[54−57]) with a better crystallization. High concentrations of Fe(II) were not determined for alkaline conditions because iron sulfides are more soluble under acidic conditions and Fe(II) is soluble below pH 7.

Due to its inert character and negative charge, it is not surprising that only less than 10% of Se(VI) was adsorbed and that the highest observed removal occurred at pH < 6. Se adsorption appears to have decreased the dissolved concentrations of Fe(II) and ∑S(−II) compared to those measured in the absence of selenium, as seen in Figure 6 and Tables S2 and S3. Selenium(VI) reduction or complexation in solution is discarded because there is no evidence of direct selenate sequestration with aqueous S(−II) in previous studies to the best of our knowledge, and after performing some blanks with 250 mM ∑S(−II) and 250 μM SeO_4^{2-}, at pH = 6 and 7, no Se(VI) precipitation was observed over six months. It is possible that Se(VI) and Fe(II) could precipitate, complex or form ternary surface complexes. After comparing the ion product to the only constant found in literature for $FeSeO_{4(s)}$[58,59] (K = 0.0015), the Se(VI)-pyrite system is not sufficiently saturated to form the precipitate. The influence of adding sulfide regarding Se(VI) adsorption is negligible in terms of the percentage of Se(VI) adsorbed or speciation. Similar findings were found in a previous study but adding Fe(II) to Se(VI) sorption experiments on pyrite, where the presence of Fe(II) did not improve Se(VI) removal.[30] XANES spectroscopy results show a reduction of Se(VI) adsorbed adding or not sulfide on pyrite, mainly as Se(0), close to those from other studies.[30,60] This finding is further supported by the measured E_H values plotted in the Pourbaix diagrams located within the domains of stability of Se(0) and pyrite (Figure 1).

In the reductive adsorption processes of Se(VI), a slightly more soluble polymorph of pyrite should not be neglected, even when it constitutes less than 20% of the composition. Previous studies on the reduction of Tc in marcasite−pyrite and natural pure pyrite have given different results, in which the presence of marcasite slowed down the reduction.[61] Consequently, it is strongly recommended that additional research be conducted to explore the reactivity of Se(VI) in conjunction with Fe(II) and marcasite.

Our coprecipitation experiment with Se(VI) was not successful. The removal was minimal, and the quality of the collected XANES data was poor. It seems that the small amount of Se(VI) that reacted was reduced to Se(0).

Factors Controlling Se(IV) Interaction with Pyrite. Se(IV) Adsorption Experiments. Sulfide enhances the removal of Se(IV). This enhancement is not surprising since prior work shows that after 30 min, 5 mM sulfide reduces and precipitates 97.3% (±3.7) from 0.11 mM Se(IV) to Se(0).[32] On the other hand, Fe(II) released by pyrite can also influence the amount of Se(IV) removed. The concentration of dissolved Fe(II) (measured) saturated the batch solution according to the $FeSeO_3$ solubility constant ($K = 10^{-9.99}$) and could have led to the precipitate formation (as observed on clay; see refs 59 and 62). Supporting the potential formation of $FeSeO_3$, our new HERFD−XANES results do indicate the presence of Se(IV) and Se(0) only for the Se(IV) experimental products, independent of the presence of sulfide. Moreover, in the samples without sulfide, at pH = 4, which display a higher concentration of dissolved Fe(II), the percentage of removed Se(IV) is higher. In agreement, the E_H values plotted on the Pourbaix diagrams indicate an equilibrium phase close to the boundaries between Se(0), $H(SeO_3)^-$, and Fe(II).

Se(IV)-Doped Pyrite. The coprecipitation of Se(IV) with pyrite is a fast and efficient process, as demonstrated by prior studies.[35,63] Se(IV) coprecipitation at the three concentrations studied, as revealed by XANES and EXAFS results, exhibits indistinguishable local structural parameters. This suggests a consistency in both chemical composition and crystal structure even when examining samples doped with up to 4037 ppm of Se. The XANES peak for all three samples investigated in our study is located between Se(IV) and Se(0) and with a similar

https://doi.org/10.1021/acsearthspacechem.3c00219
ACS Earth Space Chem. 2024, 8, 67−78

shape to the trigonal Se reference. On the other hand, HERFD−XANES mainly indicates the presence of a Se(−I) due to the similarity of the shape to the $FeSe(-I)_2$ reference. The correspondence between the white line HERFD−XANES spectra of pyrite doped with 100 μM Se(IV) with the spectrum of the Se(IV) sample adsorbed at pH 6 adding sulfur suggests a possible formation of SeS_2 on the pyrite surface due to an excess of Se. This observation can also be supported by the fact that the EXAFS fit obtained with 100 μM Se(IV) was less optimal, accompanied by a slightly elevated Debye−Waller factor and *R* factor. Comparable findings were reported for samples prepared with a similar protocol.[63] Nevertheless, it is unclear whether Se is reduced to Se(−I) or Se(0).[63] On the other hand, our EXAFS results suggest that Se replaces a S in the pyrite structure, analogous to the previous natural Se−pyrite studied by Manceau et al. (2020) and Matamoros-Veloza et al. (2014)where Se is reduced to Se(−I) based on stoichiometry. This is different from the Diener et al. study that concluded the incorporation of Se as amorphous Se(0) with a Se neighbor in the coordination layer at ∼2.3 Å.[63] It remains uncertain if this disparity is due to a different EXAFS adjustment strategy or different experimental conditions.

The main host for Se is iron minerals, predominantly pyrite, found in shales. Selenate and selenite become toxic at elevated concentrations, often originating from anthropogenic sources such as coal mining or radioactive waste. Our new findings suggest that the addition of S(−II) enhances the adsorption of pyrite, proving to be an effective treatment for removing Se(IV) from polluted water or mining waste. However, the pyrite reductive adsorption mechanism demonstrates significantly greater efficiency for Se(IV) compared to Se(VI). To address the reversible desorption of Se, the reduction of both Se(VI) and Se(IV) to low-solubility Se(0) or other reduced Se species (Se(−I), Se(−II)) offers a stable solution, surpassing the efficacy of mere complexation or adsorption of the original oxyanions. Furthermore, integrating selenium within the pyrite stoichiometric structure may emerge as a more effective treatment avenue. This approach has the potential to minimize the mobility of precipitated, reduced Selenium species, as demonstrated by Poulain et al. in 2022.[64] Considering the low reactivity of Se(VI) with pyrite, a promising strategy for future studies to enhance removal involves incorporating zero-valent iron. Zero-valent iron appears to facilitate the conversion of Se(VI) into Se(IV) and Se(0), thereby enhancing selenium reduction processes.[65]

Se has emerged as a promising paleo-redox proxy in marine sediments due to its heightened concentration in anoxic environments, elevated redox potential, and sensitivity to both global and regional perturbations over relatively short time scales.[5,66] This study marks a significant advance in our understanding of ancient processes leading to selenium accumulation in pyrite within sulfidic environments. It reveals a pathway involving oxyanion reduction to Se(0) and Se(−I), shedding light on intricate mechanisms. The detailed mechanism explored in this study includes reductive adsorption, Se incorporation in the pyrite lattice, and sulfide precipitation, laying valuable groundwork for future Se isotopic studies in both natural and experimental samples. This forthcoming research, complementing our investigation, holds the potential to deepen our understanding of the mechanisms elucidated here and capture the occurrences of anoxic events, spanning from modern times to earth's stepwise oxygenation.

■ ASSOCIATED CONTENT

Supporting Information

The Supporting Information is available free of charge at https://pubs.acs.org/doi/10.1021/acsearthspacechem.3c00219.

Bond parameters of atoms in the gas and hydrated phases for the selenate ion; SEM images of the pyrite solid before and after Se(VI) sorption experiments; aqueous concentrations of selenium, iron, and sulfur in Se−pyrite experiments; XANES and HERFD−XANES selenium K-edge spectra and linear combination fitting of selenium K-edge XANES spectra (PDF)

■ AUTHOR INFORMATION

Corresponding Authors

Anthony Chappaz − *STARLAB, Central Michigan University, Mount Pleasant, Michigan 48859, United States;* orcid.org/0000-0001-8713-8456; Email: anthony.c@cmich.edu

Laurent Charlet − *ISTerre, Univ. Grenoble Alpes, Univ. Savoie Mont Blanc, CNRS, IRD, Univ. Gustave Eiffel, Grenoble 38058, France;* orcid.org/0000-0003-3669-7316; Email: charlet38@gmail.com

Authors

Carolina Guida − *ISTerre, Univ. Grenoble Alpes, Univ. Savoie Mont Blanc, CNRS, IRD, Univ. Gustave Eiffel, Grenoble 38058, France; STARLAB, Central Michigan University, Mount Pleasant, Michigan 48859, United States; Grupo geología médica y forense, Universidad Nacional de Colombia, Bogotá 111321, Colombia;* orcid.org/0000-0002-3181-7860

Vivien Ramothe − *ISTerre, Univ. Grenoble Alpes, Univ. Savoie Mont Blanc, CNRS, IRD, Univ. Gustave Eiffel, Grenoble 38058, France;* orcid.org/0000-0003-4614-2226

Pauline Simonnin − *Physical Sciences Division, Physical and Computational Sciences Directorate, Pacific Northwest National Laboratory, Richland, Washington 99352, United States;* orcid.org/0000-0002-6197-7435

Kevin M. Rosso − *Physical Sciences Division, Physical and Computational Sciences Directorate, Pacific Northwest National Laboratory, Richland, Washington 99352, United States;* orcid.org/0000-0002-8474-7720

Rong-Rong Ding − *ISTerre, Univ. Grenoble Alpes, Univ. Savoie Mont Blanc, CNRS, IRD, Univ. Gustave Eiffel, Grenoble 38058, France; CAS Key Laboratory of Urban Pollutant Conversion, Department of Environmental Science and Engineering, University of Science and Technology of China, Hefei 230026, China*

Damien Prieur − *The Rossendorf Beamline at ESRF, Grenoble 38043, France; HZDR Institute of Resource Ecology, Dresden 01328, Germany;* orcid.org/0000-0001-5087-0133

Andreas C. Scheinost − *The Rossendorf Beamline at ESRF, Grenoble 38043, France; HZDR Institute of Resource Ecology, Dresden 01328, Germany;* orcid.org/0000-0002-6608-5428

Complete contact information is available at: https://pubs.acs.org/10.1021/acsearthspacechem.3c00219

https://doi.org/10.1021/acsearthspacechem.3c00219
ACS Earth Space Chem. 2024, 8, 67−78

Author Contributions

[○]C.G. and V.R. are cofirst authors. The manuscript was written through the contributions of all authors. All authors have approved the final version of the manuscript.

Funding

The project funding and laboratory equipment have been supported by a grant from the French National Radioactive Waste Management Agency (ANDRA, Chatenay-Malabry). C.G. has received support funding from Convocatoria 885, Ministry of Science, Technology, and Innovation, Colombia. V.R. was supported by a SERENADE project award for the postdoctoral fellowship. The work was also funded by NSF-EAR Grant 2051199 awarded to A.C.

Notes

The authors declare no competing financial interest.

■ ACKNOWLEDGMENTS

The authors are thankful to the geochemistry−mineralogy platform of ISTerre (Grenoble, France) for laboratory support. The authors thank Valérie Magnin and Nathaniel Findling for performing BET and XRD measurements. K.M.R. and P.S. acknowledge the support from the US Department of Energy (DOE) Office of Science, Office of Basic Energy Sciences, Chemical Sciences, Geosciences, and Biosciences Division through its Geosciences programs at the Pacific Northwest National Laboratory (PNNL). V.R. thanks Dr. Ben Gilbert for support with *ab initio* calculations. The PNNL is a multiprogram national laboratory operated for DOE by the Battelle Memorial Institute under Contract DE-AC05-76RL0-1830. We acknowledge the European Synchrotron Radiation Facility (ESRF) for the provision of synchrotron radiation facilities, and we would like to thank beamline BM20 and BM16 for assistance and support. We thank Mauro Rovezzi for their invaluable help during our measurements at BM30. We would like to thank the anonymous reviewers for their valuable comments, which helped to improve the quality of this article.

■ ABBREVIATIONS

BET, Brunauer−Emmett−Teller adsorption method; ICP−AES, inductively coupled plasma−atomic emission spectroscopy; XRD, X-ray diffraction; RSD, relative standard deviation; DLs, detection limits; QLs, quantification limits; BSEs, backscattered electrons; SEs, secondary electrons; SSA, specific surface area; PMMA, poly(methyl methacrylate); XAS, X-ray absorption spectroscopy; XANES, X-ray absorption near-edge structure; EXAFS, extended X-ray absorption fine structure; HERFD, high-energy-resolution fluorescence-detected X-ray absorption spectroscopy; LCF, linear combination fit; PBC, periodic boundary conditions; VASP, Vienna Ab initio Software Package; GGA, generalized gradient approximation; PBE, Perdew, Burke, and Ernzerhof; ΔE, adsorption energy of the adsorbate species; $\Delta\rho(r)$, deformation charge density; PDOS, projected density of states

■ REFERENCES

(1) Fernández-Martínez, A.; Charlet, L. Selenium Environmental Cycling and Bioavailability: A Structural Chemist Point of View. *Rev. Environ. Sci. Biotechnol* **2009**, *8* (1), 81−110.

(2) Fordyce, F. M. Selenium Deficiency and Toxicity in the Environment. In *Essentials of Medical Geology: Revised Edition*; Selinus, O., Ed.; Springer Netherlands: Dordrecht, 2013; pp 375−416. DOI: 10.1007/978-94-007-4375-5_16.

(3) Chen, F.; Burns, C. P.; Ewing, R. C. 79Se: Geochemical and Crystallo-Chemical Retardation Mechanisms. *J. Nucl. Mater.* **1999**, *275* (1), 81−94.

(4) Scheinost, A. C.; Charlet, L. selenite Reduction by mackinawite, Magnetite and Siderite: XAS Characterization of nanosized Redox Products. *Environ. Sci. Technol.* **2008**, *42* (6), 1984−1989.

(5) Stüeken, E. E.; Kipp, M. A. Selenium Isotope Paleobiogeochemistry; Elements in Geochemical Tracers in Earth System Science. Cambridge University Press 2020. DOI: 10.1017/9781108782203.

(6) El-Ramady, H.; Abdalla, N.; Taha, H. S.; Alshaal, T.; El-Henawy, A.; Faizy, S. E.-D. A.; Shams, M. S.; Youssef, S. M.; Shalaby, T.; Bayoumi, Y.; Elhawat, N.; Shehata, S.; Sztrik, A.; Prokisch, J.; Fari, M.; Domokos-Szabolcsy, E.; Pilon-Smits, E. A.; Selmar, D.; Haneklaus, S.; Schnug, E. Selenium and Nano-Selenium in Plant Nutrition. *Environ. Chem. Lett.* **2016**, *14* (1), 123−147.

(7) WHO. *Trace elements in human and health*. https://scholar.google.com/scholar_lookup?title=Trace%20elements%20in%20human%20nutrition%20and%20health&publication_year=1996 (accessed 2021−10−12).

(8) Reich, H. J.; Hondal, R. J. Why Nature Chose Selenium. *ACS Chem. Biol.* **2016**, *11* (4), 821−841.

(9) Chapman, L. M.; Roling, J. A.; Bingham, L. K.; Herald, M. R.; Baldwin, W. S. Construction of a Subtractive Library from Hexavalent Chromium Treated Winter Flounder (Pseudopleuronectes Americanus) Reveals Alterations in Non-Selenium Glutathione Peroxidases. *Aquatic Toxicology* **2004**, *67* (2), 181−194.

(10) Balistrieri, L. S.; Chao, T. T. Adsorption of Selenium by Amorphous Iron Oxyhydroxide and Manganese Dioxide. *Geochim. Cosmochim. Acta* **1990**, *54* (3), 739−751.

(11) Wen, H.; Carignan, J. Reviews on Atmospheric Selenium: Emissions, Speciation and Fate. *Atmos. Environ.* **2007**, *41* (34), 7151−7165.

(12) Cao, S.; Duan, X.; Zhao, X.; Ma, J.; Dong, T.; Huang, N.; Sun, C.; He, B.; Wei, F. Health Risks from the Exposure of Children to As, Se, Pb and Other Heavy Metals near the Largest Coking Plant in China. *Science of The Total Environment* **2014**, *472*, 1001−1009.

(13) Etteieb, S.; Magdouli, S.; Komtchou, S. P.; Zolfaghari, M.; Tanabene, R.; Brar, K. K.; Calugaru, l. L.; Brar, S. K. Selenium Speciation and Bioavailability from Mine Discharge to the Environment: A Field Study in Northern Quebec, Canada. *Environ. Sci. Pollut. Res.* **2021**, *28* (36), 50799−50812.

(14) Grambow, B. Mobile Fission and Activation Products in Nuclear Waste Disposal. *Journal of Contaminant Hydrology* **2008**, *102* (3−4), 180−186.

(15) Mason, R. P.; Soerensen, A. L.; DiMento, B. P.; Balcom, P. H. The Global Marine Selenium Cycle: Insights From Measurements and Modeling. *Global Biogeochemical Cycles* **2018**, *32* (12), 1720−1737.

(16) Vriens, B.; Behra, R.; Voegelin, A.; Zupanic, A.; Winkel, L. H. E. Selenium Uptake and Methylation by the Microalga *Chlamydomonas Reinhardtii*. *Environ. Sci. Technol.* **2016**, *50* (2), 711−720.

(17) Simmons, D. B. D.; Wallschläger, D. A Critical Review of the Biogeochemistry and Ecotoxicology of Selenium in Lotic and Lentic Environments. *Environ. Toxicol. Chem.* **2005**, *24* (6), 1331−1343.

(18) Perrone, D.; Monteiro, M.; Nunes, J. The Chemistry of Selenium; 2015; pp 3−15. DOI: 10.1039/9781782622215-00003.

(19) Belzile, N.; Chen, Yu.-W.; Xu, R. Early Diagenetic Behaviour of Selenium in Freshwater Sediments. *Appl. Geochem.* **2000**, *15* (10), 1439−1454.

(20) Kinniburgh, D. G.; Cooper, D. M. *Creating Graphical Output with PHREEQC*; NERC Open Research Archive 2009.

(21) Berner, R. A. Sedimentary Pyrite Formation: An Update. *Geochim. Cosmochim. Acta* **1984**, *48* (4), 605−615.

(22) Rickard, D.; Luther, G. W. Chemistry of Iron Sulfides. *Chem. Rev.* **2007**, *107* (2), 514−562.

(23) Descostes, M.; Schlegel, M. L.; Eglizaud, N.; Descamps, F.; Miserque, F.; Simoni, E. Uptake of Uranium and Trace Elements in Pyrite (FeS2) Suspensions. *Geochim. Cosmochim. Acta* **2010**, *74* (5), 1551−1562.

(24) Chappaz, A.; Lyons, T. W.; Gregory, D. D.; Reinhard, C. T.; Gill, B. C.; Li, C.; Large, R. R. Does Pyrite Act as an Important Host for Molybdenum in Modern and Ancient Euxinic Sediments? *Geochim. Cosmochim. Acta* **2014**, *126*, 112−122.
(25) Nyström, E.; Thomas, H.; Wanhainen, C.; Alakangas, L. Occurrence and Release of Trace Elements in Pyrite-Rich Waste Rock. *Minerals* **2021**, *11* (5), 495.
(26) Manceau, A.; Merkulova, M.; Mathon, O.; Glatzel, P.; Murdzek, M.; Batanova, V.; Simionovici, A.; Steinmann, S. N.; Paktunc, D. The Mode of Incorporation of As (-I) and Se (-I) in Natural Pyrite Revisited. *ACS Earth and Space Chemistry* **2020**, *4* (3), 379−390.
(27) Rodríguez, D. M.; Mayordomo, N.; Scheinost, A. C.; Schild, D.; Brendler, V.; Müller, K.; Stumpf, T. New Insights into ^{99}Tc(VII) Removal by Pyrite: A Spectroscopic Approach. *Environ. Sci. Technol.* **2020**, *54* (5), 2678−2687.
(28) Ryser, A. L.; Strawn, D. G.; Marcus, M. A.; Johnson-Maynard, J. L.; Gunter, M. E.; Müller, G. Micro-Spectroscopic Investigation of Selenium-Bearing Minerals from the Western US Phosphate Resource Area. *Geochem. Trans.* **2005**, *6* (1), 1−11.
(29) Kang, M.; Ma, B.; Bardelli, F.; Chen, F.; Liu, C.; Zheng, Z.; Wu, S.; Charlet, L. Interaction of Aqueous Se(IV)/Se(VI) with FeSe/FeSe2: Implication to Se Redox Process. *Journal of Hazardous Materials* **2013**, *248*−*249*, 20−28.
(30) Charlet, L.; Kang, M.; Bardelli, F.; Kirsch, R.; Géhin, A.; Grenèche, J.-M.; Chen, F. Nanocomposite Pyrite−greigite Reactivity toward Se(IV)/Se(VI). *Environ. Sci. Technol.* **2012**, *46* (9), 4869−4876.
(31) Kang, M.; Chen, F.; Wu, S.; Yang, Y.; Bruggeman, C.; Charlet, L. Effect of pH on Aqueous Se(IV) Reduction by Pyrite. *Environ. Sci. Technol.* **2011**, *45* (7), 2704−2710.
(32) Jung, B.; Safan, A.; Batchelor, B.; Abdel-Wahab, A. Spectroscopic Study of Se (IV) Removal from Water by Reductive Precipitation Using Sulfide. *Chemosphere* **2016**, *163*, 351−358.
(33) Curti, E.; Aimoz, L.; Kitamura, A. Selenium Uptake onto Natural Pyrite. *J. Radioanal Nucl. Chem.* **2013**, *295* (3), 1655−1665.
(34) Wei, D.; Osseo-Asare, K. Particulate Pyrite Formation by the Fe3+/H S - Reaction in Aqueous Solutions: Effects of Solution Composition. *Colloids Surf., A* **1996**, 11.
(35) Diener, A.; Neumann, T. Synthesis and Incorporation of selenide in Pyrite and mackinawite. *Radiochim. Acta* **2011**, *99* (12), 791−798.
(36) Fortune, W. B.; Mellon, M. G. Determination of Iron with O-Phenanthroline: A Spectrophotometric Study. *Industrial & Engineering Chemistry Analytical Edition* **1938**, *10* (2), 60−64.
(37) Cline, J. D. Spectrophotometric Determination of Hydrogen Sulfide in Natural Waters. *Limnology and Oceanography* **1969**, *14* (3), 454−458.
(38) Doebelin, N.; Kleeberg, R. Profex: A Graphical User Interface for the Rietveld Refinement Program BGMN. *Journal of applied crystallography* **2015**, *48* (5), 1573−1580.
(39) Scheinost, A.; Claussner, J.; Exner, J.; Feig, M.; Findeisen, S.; Hennig, C.; Kvashnina, K.; Naudet, D.; Prieur, D.; Rossberg, A.; Schmidt, M.; Qiu, C.; Colomp, P.; Cohen, C.; Dettona, E.; Dyadkin, V.; Stumpf, T. ROBL-II at ESRF: A Synchrotron Toolbox for Actinide Research. *Journal of Synchrotron Radiation* **2021**, *28*, 333−349.
(40) Ravel, B.; Newville, M. ATHENA and ARTEMIS: Interactive Graphical Data Analysis Using IFEFFIT. *Phys. Scr.* **2005**, *2005* (T115), 1007.
(41) Hafner, J.; Kresse, G. The Vienna AB-Initio Simulation Program VASP: *An Efficient and Versatile Tool for Studying the Structural, Dynamic, and Electronic Properties of Materials*; Springer 1997. DOI: 10.1007/978-1-4615-5943-6_10.
(42) Paier, J.; Hirschl, R.; Marsman, M.; Kresse, G. The Perdew−Burke−Ernzerhof Exchange-Correlation Functional Applied to the G2−1 Test Set Using a Plane-Wave Basis Set. *J. Chem. Phys.* **2005**, *122* (23), 234102.
(43) Perdew, J. P.; Burke, K.; Ernzerhof, M. Generalized Gradient Approximation Made Simple. *Phys. Rev. Lett.* **1996**, *77* (18), 3865−3868.
(44) Blöchl, P. E.; Jepsen, O.; Andersen, O. K. Improved Tetrahedron Method for Brillouin-Zone Integrations. *Phys. Rev. B* **1994**, *49* (23), 16223−16233.
(45) Tang, W.; Sanville, E.; Henkelman, G. A Grid-Based Bader Analysis Algorithm without Lattice Bias. *J. Phys.: Condens. Matter* **2009**, *21* (8), No. 084204.
(46) Sanville, E.; Kenny, S. D.; Smith, R.; Henkelman, G. Improved grid-based algorithm for Bader charge allocation. *J. Comput. Chem.* **2007**, *28* (5), 899−908.
(47) Henkelman, G.; Arnaldsson, A.; Jónsson, H. A Fast and Robust Algorithm for Bader Decomposition of Charge Density. *Comput. Mater. Sci.* **2006**, *36* (3), 354−360.
(48) Yu, M.; Trinkle, D. R. Accurate and Efficient Algorithm for Bader Charge Integration. *J. Chem. Phys.* **2011**, *134* (6), No. 064111.
(49) Rieder, M.; Crelling, J. C.; Šustai, O.; Drábek, M.; Weiss, Z.; Klementová, M. Arsenic in Iron Disulfides in a Brown Coal from the North Bohemian Basin, Czech Republic. *International Journal of Coal Geology* **2007**, *71* (2), 115−121.
(50) Matamoros-Veloza, A.; Peacock, C. L.; Benning, L. G. Selenium Speciation in Framboidal and euhedral Pyrites in Shales. *Environ. Sci. Technol.* **2014**, *48* (16), 8972−8979.
(51) Hunger, S.; Benning, L. G. greigite: A True Intermediate on the Polysulfide Pathway to Pyrite. *Geochem. Trans.* **2007**, *8*, 1.
(52) Wang, T.; Qian, T.; Zhao, D.; Liu, X.; Ding, Q. Immobilization of Perrhenate Using Synthetic Pyrite Particles: Effectiveness and Remobilization Potential. *Science of The Total Environment* **2020**, *725*, 138423.
(53) Son, S.; Hyun, S. P.; Charlet, L.; Kwon, K. D. Thermodynamic Stability Reversal of Iron Sulfides at the Nanoscale: Insights into the Iron Sulfide Formation in Low-Temperature Aqueous Solution. *Geochim. Cosmochim. Acta* **2022**, *338*, 220−228.
(54) Bonnissel-Gissinger, P.; Alnot, M.; Ehrhardt, J.-J.; Behra, P. Surface Oxidation of Pyrite as a Function of pH. *Environ. Sci. Technol.* **1998**, *32* (19), 2839−2845.
(55) Weerasooriya, R.; Tobschall, H. J. Pyrite−Water Interactions: Effects of pH and pFe on Surface Charge. *Colloids Surf., A* **2005**, *264* (1−3), 68−74.
(56) Borah, D.; Senapati, K. Adsorption of Cd(II) from Aqueous Solution onto Pyrite. *Fuel* **2006**, *85* (12−13), 1929−1934.
(57) Yang, Z.; Kang, M.; Ma, B.; Xie, J.; Chen, F.; Charlet, L.; Liu, C. Inhibition of U(VI) Reduction by Synthetic and Natural Pyrite. *Environ. Sci. Technol.* **2014**, *48* (18), 10716−10724.
(58) Essington, M. E. Estimation of the Standard Free Energy of Formation of Metal Arsenates, Selenates, and Selenites. *Soil Science Society of America Journal* **1988**, *52* (6), 1574−1579.
(59) Séby, F.; Potin-Gautier, M.; Giffaut, E.; Borge, G.; Donard, O. F. X. A Critical Review of Thermodynamic Data for Selenium Species at 25°C. *Chem. Geol.* **2001**, *171* (3−4), 173−194.
(60) Mitchell, K.; Couture, R.-M.; Johnson, T. M.; Mason, P. R. D.; Van Cappellen, P. Selenium sorption and Isotope Fractionation: Iron(III) Oxides versus Iron(II) Sulfides. *Chem. Geol.* **2013**, *342*, 21−28.
(61) Rodríguez, D. M.; Mayordomo, N.; Schild, D.; Shams Aldin Azzam, S.; Brendler, V.; Müller, K.; Stumpf, T. Reductive Immobilization of 99Tc(VII) by FeS2: The Effect of marcasite. *Chemosphere* **2021**, *281*, 130904.
(62) Charlet, L.; Scheinost, A. C.; Tournassat, C.; Greneche, J. M.; Géhin, A.; Fernández-Martínez, A.; Coudert, S.; Tisserand, D.; Brendle, J. Electron Transfer at the Mineral/Water Interface: Selenium Reduction by Ferrous Iron Sorbed on Clay. *Geochim. Cosmochim. Acta* **2007**, *71* (23), 5731−5749.
(63) Diener, A.; Neumann, T.; Kramar, U.; Schild, D. Structure of Selenium Incorporated in Pyrite and mackinawite as Determined by XAFS Analyses. *Journal of Contaminant Hydrology* **2012**, *133*, 30−39.
(64) Poulain, A.; Fernandez-Martinez, A.; Greneche, J. M.; Prieur, D.; Scheinost, A. C.; Menguy, N.; Bureau, S.; Magnin, V.; Findling,

https://doi.org/10.1021/acsearthspacechem.3c00219
ACS Earth Space Chem. 2024, 8, 67−78

N.; Drnec, J.; Martens, I.; Mirolo, M.; Charlet, L. Selenium Nanowire Formation by Reacting Selenate with Magnetite. *Environ. Sci. Technol.* **2022**, 14817.
(65) Das, S.; Lindsay, M. B. J.; Essilfie-Dughan, J.; Hendry, M. J. Dissolved Selenium(VI) Removal by Zero-Valent Iron under Oxic Conditions: Influence of Sulfate and Nitrate. *ACS Omega* **2017**, *2* (4), 1513−1522.
(66) Kipp, M. A.; Algeo, T. J.; Stüeken, E. E.; Buick, R. Basinal Hydrographic and Redox Controls on Selenium Enrichment and Isotopic Composition in Paleozoic Black Shales. *Geochim. Cosmochim. Acta* **2020**, *287*, 229−250.

https://doi.org/10.1021/acsearthspacechem.3c00219
ACS Earth Space Chem. 2024, 8, 67−78

Tables

List of figures

List of tables

List of publications

Guida, C., Chappaz, A., Scheinost, A. C. and Charlet, L., (2024). Oxyanions HSAB behaviour: Thiolation, mineral ores, criticality and paleoenvironmental implications. *To be submitted to Earth Sci. Rev.*

Guida, C. Chappaz, A., Fernandez-Martinez, A., Menguy N., Prieur, D., Scheinost, A. C and Charlet, L., (2024). Rhenium geochemistry under sulfidic conditions: When does sulfide act as both ligand and reducing agent? *To be submitted to EST journal.*

Guida, C., Chappaz, A., Dickson, A., Gloter, A., Grenèche, J-M., Poulain, A., Scheinost, A. C. and Charlet, L. (2024). Isotopic fractionation, reduction and structure of Rhenium at the water magnetite interface. *To be submitted to PNAS as a brief report.*

Guida, C., Chappaz, A., Dickson, A., Montes-Hernandez, G., Scheinost, A. C. and Charlet, L. Rhenium reductive adsorption and co-precipitation by pyrite. *In preparation*.

Guida, C.*, Ramothe, V.*, Chappaz, A., Simonnin, P., Rosso, K-M, Ding. R-R*, Prieur, D., Scheinost, A. and Charlet, L., (2023). Revisiting the selenium interactions with pyrite: from adsorption to coprecipitation. ACS Earth Space Chem. 8, 67-78. https://doi.org/10.1021/acsearthspacechem.3c00219

Guida, C. *, Poulain, A.*, Chappaz, A., Grenèche, A., Gloter, J-M., Menguy, N., Findling, N. Le Bouteiller, P. and Charlet, L. Characterisation of Magnetite Superparamagnetic Iron Oxide Nanoparticles Containing Gd: Dependence on the Fe(III)/Gd(III) Ratio. *To be submitted to Environmental Science: Nano.*